# THÈSE

**En vue de l'obtention du**

# DOCTORAT DE L'UNIVERSITÉ DE TOULOUSE

**Délivré par :**

Institut National Polytechnique de Toulouse (INP Toulouse)

**Discipline ou spécialité :**

Micro Nano Systèmes

---

**Présentée et soutenue par :**

Mme LAVINIA-ELENA CIOTIRCA

le mardi 23 mai 2017

**Titre :**

## System design of a low-power three-axis underdamped MEMS accelerometer with simultaneous electrostatic damping control

---

**Ecole doctorale :**

Génie Electrique, Electronique, Télécommunications (GEET)

**Unité de recherche :**

Laboratoire d'Analyse et d'Architecture des Systèmes (L.A.A.S.)

**Directeur(s) de Thèse :**

MME HELENE TAP

**Rapporteurs :**

M. JEROME JUILLARD, SUPELEC
M. PASCAL NOUET, UNIVERSITE MONTPELLIER 2

**Membre(s) du jury :**

M. PHILIPPE BENECH, INP DE GRENOBLE, Président
Mme HELENE TAP, INP TOULOUSE, Membre
M. OLIVIER BERNAL, INP TOULOUSE, Membre

# Acknowledgement

The research work presented in this thesis was carried out between 2014 and 2017 at the Laboratory for Analysis and Architecture of Systems (LAAS) in Toulouse with collaboration of the Sensors Solutions Design (SSD) Team at NXP Semiconductors (previously Freescale Semiconductors).

Firstly, I would like to express my sincere gratitude to Prof. Hélène Tap and Mr. Philippe Lance for offering me the opportunity to carry out this research and for supervising this project. I would like to thank Hélène for her continuous support and guidance and for always being positive towards my work. Her motivation and patience helped me in all the time of research and writing of this thesis. I would also like to thank Philippe for his constant support and for the worthy advice on both research as well as on my career development.

Further, I would also like to thank the rest of my thesis committee Prof. Pascal Nouet, Prof. Jérôme Juillard and Prof. Philippe Benech for taking the time to review this thesis and for their insightful comments.

This thesis would not have been possible without the close guidance of Dr. Olivier Bernal, Mr. Jérôme Enjalbert and Mr. Thierry Cassagnes. I would like to express my gratitude for all their help, technical expertise and constant encouragement. I will always appreciate and remember their patience and kindness.

I am grateful to Dr. Robert Dean and Dr. Chong Li for offering me the opportunity to develop this research work within their facilities during my stay at Auburn University, USA.

I would also like to thank Ms. Peggy Kniffin, Mr. Aaron Geisberger and Mr. Bob Steimle for the MEMS modeling guidance and Mr. Clément Tronche, Mr. Francis Jayat and Mr. Philippe Calmettes for providing their help with the experimental set up and my samples demands.

Likewise, I want to hereby acknowledge the contributions of my colleagues at NXP Semiconductors as well as all the OSE (LAAS) group members. In particular, my sincere thanks go to all the doctoral students I had the chance to meet during this research work, for all their help and day to day support: Antonio Luna Arriaga, Evelio Ramirez Miquet, Jalal Al Roumy, Laura Le Barbier, Mohanad Albughdadi, Raül da Costa Moreira, Lucas Perbet, Blaise Mulliez, Yu Zhao, Fernando Urgiles, Harris Apriyanto and Mengkoung Veng.

I have no words to express my gratitude to all the friends I had or have made during these last three years. Their permanent encouragement, motivation, attention and care helped me to successfully complete this work. I would like to thank all of them for the special moments we have shared together and for never letting me down. Infinite thanks!

Last but not the least, I would like to present my deepest gratitude to my parents, Mia and Mircea, who have always encouraged and supported me to follow my dreams! I would like to thank them, and my little brother, Liviu, for the unconditioned love, trust, kindness and for being a constant source of inspiration. To them I dedicate this thesis!

# Abstract

Recently, consumer electronics industry has known a spectacular growth that would have not been possible without pushing the integration barrier further and further. Micro Electro Mechanical Systems (MEMS) inertial sensors (e.g. accelerometers, gyroscopes) provide high performance, low power, low die cost solutions and are, nowadays, embedded in most consumer applications.

In addition, the sensors fusion has become a new trend and combo sensors are gaining growing popularity since the co-integration of a three-axis MEMS accelerometer and a three-axis MEMS gyroscope provides complete navigation information. The resulting device is an Inertial measurement unit (IMU) able to sense multiple Degrees of Freedom (DoF).

Nevertheless, the performances of the accelerometers and the gyroscopes are conditioned by the MEMS cavity pressure: the accelerometer is usually a damped system functioning under an atmospheric pressure while the gyroscope is a highly resonant system. Thus, to conceive a combo sensor, a unique low cavity pressure is required. The integration of both transducers within the same low pressure cavity necessitates a method to control and reduce the ringing phenomena by increasing the damping factor of the MEMS accelerometer. Consequently, the aim of the thesis is the design of an analog front-end interface able to sense and control an underdamped three-axis MEMS accelerometer.

This work proposes a novel closed-loop accelerometer interface achieving low power consumption. The design challenge consists in finding a trade-off between the sampling frequency, the settling time and the circuit complexity since the sensor excitation plates are multiplexed between the measurement and the damping phases. In this context, a patented damping sequence (simultaneous damping) has been conceived to improve the damping efficiency over the state of the art approach performances (successive damping).

To investigate the feasibility of the novel electrostatic damping control architecture, several mathematical models have been developed and the settling time method is used to assess the damping efficiency. Moreover, a new method that uses the multirate signal processing theory and allows the system stability study has been developed. This very method is used to conclude on the loop stability for a certain sampling frequency and loop gain value.

Next, a CMOS implementation of the entire accelerometer signal chain is designed. The functioning has been validated and the block may be further integrated within an ASIC. Finally, a discrete components system is designed to experimentally validate the simultaneous damping approach.

# Résumé

L’intégration de plusieurs capteurs inertiels au sein d’un même dispositif de type MEMS afin de pouvoir estimer plusieurs degrés de liberté devient un enjeu important pour le marché de l’électronique grand public à cause de l’augmentation et de la popularité croissante des applications embarquées.

Aujourd’hui, les efforts d'intégration se concentrent autour de la réduction de la taille, du coût et de la puissance consommée. Dans ce contexte, la co-intégration d’un accéléromètre trois-axes avec un gyromètre trois-axes est cohérente avec la quête conjointe de ces trois objectifs. Toutefois, cette co-intégration doit s’opérer dans une même cavité basse pression afin de préserver un facteur de qualité élevé nécessaire au bon fonctionnement du gyromètre. Dans cette optique, un nouveau système de contrôle, qui utilise le principe de l’amortissement électrostatique, a été conçu pour permettre l’utilisation d’un accéléromètre sous-amorti naturellement. Le principe utilisé pour contrôler l’accéléromètre est d’appliquer dans la contre-réaction une force électrostatique générée à partir de l’estimation de la vitesse du MEMS. Cette technique permet d’augmenter le facteur d’amortissement et de diminuer le temps d’établissement de l’accéléromètre.

L’architecture proposée met en œuvre une méthode novatrice pour détecter et contrôler le mouvement d’un accéléromètre capacitif en technologie MEMS selon trois degrés de liberté : x, y et z. L'accélération externe appliquée au capteur peut être lue en utilisant la variation de capacité qui apparaît lorsque la masse se déplace. Lors de la phase de mesure, quand une tension est appliquée sur les électrodes du MEMS, une variation de charge est appliquée à l’entrée de l’amplificateur de charge (Charge-to-Voltage : C2V). La particularité de cette architecture est que le C2V est partagé entre les trois axes, ce qui permet une réduction de surface et de puissance consommée. Cependant, étant donné que le circuit ainsi que l’électrode mobile (commune aux trois axes du MEMS) sont partagés, on ne peut mesurer qu’un seul axe à la fois.

Ainsi, pendant la phase d'amortissement, une tension de commande, calculée pendant les phases de mesure précédentes, est appliquée sur les électrodes d'excitation du MEMS. Cette tension de commande représente la différence entre deux échantillons successifs de la tension de sortie du C2V et elle est mémorisée et appliquée trois fois sur les électrodes d’excitation pendant la même période d’échantillonnage.

Afin d’étudier la faisabilité de cette technique, des modèles mathématiques, Matlab-Simulink et VerilogA ont été développés. Le principe de fonctionnement basé sur l’amortissement électrostatique simultané a été validé grâce à ces modèles. Deux approches consécutives ont été considérées pour valider expérimentalement cette nouvelle technique : dans un premier temps l’implémentation du circuit en éléments discrets associé à un accéléromètre sous vide est présentée. En perspective, un accéléromètre sera intégré dans la même cavité qu’un gyromètre, les capteurs étant instrumentés à l’aide de circuits CMOS intégrés. Dans cette cadre, la conception en technologie CMOS 0.18µm de l’interface analogique d’amortissement est présentée et validée par simulation dans le manuscrit.

# CONTENTS

**Contents** ..... i
**List of Figures** ..... v
**List of Tables** ..... ix
**List of Abbreviations** ..... xi

**Introduction** ..... 1
A. Background and motivation ..... 1
B. Research direction and contributions ..... 1
C. Thesis organization ..... 2

**1. Inertial sensors** ..... 5
1.1 Introduction ..... 5
1.2 Degrees of freedom and types of motion in inertial sensors ..... 5
1.3 Consumer market MEMS inertial sensors ..... 6
1.4 Discrete inertial sensors ..... 8
1.4.1 Accelerometers ..... 9
A. Piezoresistive acceleration sensing ..... 9
B. Piezoelectric acceleration sensing ..... 10
C. Capacitive acceleration sensing ..... 10
D. Other acceleration sensing methods ..... 12
1.4.2 Gyroscopes ..... 13
1.5 Combo Sensors ..... 14
1.6 Summary ..... 16

**2. CMOS MEMS Accelerometers** ..... 17
2.1 Mechanical capacitive sensing element and second order mass spring damper model ..... 17
2.2 Physics of the capacitive sensing element ..... 19

2.3 Electrostatic actuation ........ 21
2.3.1 Electrostatic Actuation mechanism ........ 21
2.3.2 Static Pull-in voltage ........ 22
2.3.3 Spring Softening Effect ........ 23
2.4 CMOS Capacitive Accelerometers Interfaces ........ 24
2.4.1 Open-loop capacitive architectures for MEMS accelerometers ........ 25
2.4.2 Closed-loop capacitive architectures for MEMS accelerometers ........ 27
2.5 Summary ........ 30

**3. Three-axis high-Q MEMS accelerometer with electrostatic damping control – modelling ........ 33**
3.1 Introduction ........ 33
3.2 Three-axis Sensor Element ........ 34
3.2.1 Sensor Design ........ 34
3.2.2 Matlab-Simulink model and s-domain transfer function ........ 36
3.2.3 z-domain MEMS transfer function ........ 39
3.3 Analog interface: Charge-to-voltage amplifier modeling ........ 41
3.4 Voltage to force conversion ........ 43
3.4.1 Electrostatic damping linearity principle ........ 43
3.4.2 Linearity of the voltage-to-force conversion ........ 45
3.4.3 Bias calculation for electrostatic force optimization ........ 47
3.5 Discrete Controller: Derivative Block ........ 49
3.5.1 Derivative block – principle of operation ........ 49
3.5.2 Derivative block - modeling ........ 51
3.6 Damping approaches ........ 52
3.4.1 Successive damping ........ 53
3.4.2 Simultaneous damping ........ 56
3.4.3 Performances and choice of architecture ........ 57
3.7 Multirate controller modeling in z-domain ........ 59
3.8 Closed-loop transfer function and stability study ........ 61

3.9 Summary ........................................................................................................ 64

**4. Towards a CMOS interface for a three-axis high Q MEMS accelerometer with simultaneous damping control** ........................................ **65**

4.1 System design of a low-power three-axis underdamped MEMS accelerometer with simultaneous electrostatic damping control ........................................................ 65

4.2 MEMS Accelerometer Verilog A – Spectre Model ............................................ 66

4.3 Charge to voltage converter (C2V) ...................................................................... 69

4.3.1 Block diagram and clock diagram ..........................................................................69

4.3.2 Basics of CMOS Analog Design and C2V Architecture choice ............................71

4.3.3 Design and performances .......................................................................................74

4.4 Switched capacitor derivative block ..................................................................... 77

4.5 Derivative gain amplifier ...................................................................................... 82

4.6 CMOS Switches .................................................................................................... 88

4.7 Excitation signals block......................................................................................... 90

4.8 Closed-loop system validation .............................................................................. 91

4.9 Summary................................................................................................................ 92

**Conclusions and perspectives.........................................................................95**

**Bibliography ..............................................................................................97**

**Appendices ..............................................................................................109**

# List of Figures

Figure 1.1 A representation of the possible movements of an object in a three-dimensional space [Snyder, 2016] ....6
Figure 1.2 MEMS revenue forecast 2015-2021 per application [Yole, 2016] ....6
Figure 1.3 (a) Accelerometer applications vs. performances [Domingues, 2013] ....7
Figure 1.3 (b) Gyroscope applications vs. performances [Domingues, 2013] ....7
Figure 1.4 An illustration of a piezoresistive accelerometer ....9
Figure 1.5 An illustration of a piezoelectric accelerometer ....10
Figure 1.6 An illustration of a capacitive accelerometer with interdigitated fingers ....11
Figure 1.7 Typical structure of in-plane (left) and out-of-plane (right) capacitive MEMS accelerometer [Renaut, 2013] ....12
Figure 1.8 Functioning principle of in-plane (left) and out-of-plane capacitive MEMS accelerometer [Renaut, 2013] ....12
Figure 1. 9 A representation of the Coriolis gyroscope model ....13
Figure 1.10 Inertial sensors revenue forecast 2012-2019 [Yole, 2014] ....14
Figure 1.11 A plot of the Quality factor (Q) vs. MEMS cavity pressure (left) and the frequency response of a second order mass spring damper system (right) ....15
Figure 2.1 An illustration of a second order mass spring damper system ....17
Figure 2.2 An illustration of the capacitive sensing principle ....19
Figure 2.3 Capacitance variation dependency on MEMS displacement and the linear region of operation (highlighted in red) ....20
Figure 2.4 An illustration of a single electrode motion structure ....22
Figure 2.5. An illustration of a three-plate capacitive structure ....24
Figure 2.6 Conceptual block diagram of a closed-loop MEMS accelerometer ....25
Figure 2.7 Block diagram of the open-loop digital ΣΔ interface [Amini, 2004] ....26
Figure 2.8 Block diagram of an nth order ΣΔ digital closed-loop accelerometer ....28
Figure 2.9 Block diagram of an analogue closed-loop accelerometer ....30
Figure 3.1. Three-axis closed-loop underdamped MEMS accelerometer with electrostatic damping control ....34

Figure 3.2. An illustration of the dual-mass three-axis differential accelerometer with self-test capabilities and the analog frond end block diagram ....................35

Figure 3.3 An illustration of the Simulink model for the open loop MEMS accelerometer .........37

Figure 3.4. MEMS accelerometer response in open loop configuration to a 1g step acceleration for different quality factors: (a) Q=1, (b) Q=50 and (c) Q=2000 ....................38

Figure 3.5 Step response of the open loop accelerometer for Q=5....................39

Figure 3.6 Bode plot of the continuous-time MEMS transfer function (blue) and the associated discrete-time Euler approximated TF (red) for fs=30kHz and Q=2000 ....................40

Figure 3.7 Bode plot of the continuous-time MEMS transfer function (blue) and the associated discrete-time Tustin approximated TF (red) for fs=30kHz and Q=2000....................41

Figure 3.8 Block diagram of the capacitive sensing element and the AFE’s first stage with its chronograms ....................42

Figure 3.9 An illustration of the MEMS and the C2V simplified models....................42

Figure 3.10 An illustration of a parallel plate capacitive sensor and the electrostatic forces applied on the proof mass ....................43

Figure 3.11 Net electrostatic force simulation when the input acceleration varies from -8g to 8g and the control voltage Vctrl varies from -0.4V to 0.4V ....................46

Figure 3.12 Net electrostatic force nonlinearity when the input acceleration varies from -8g to 8g and the control voltage Vctrl varies from -0.4V to 0.4V ....................46

Figure 3.13 Excitation signals simulations using the optimal values found for VB and Vctrl......48

Figure 3.14 Net electrostatic forces simulation when VB varies from 0V to 0.8V ....................49

Figure 3.15 System block diagram ....................50

Figure 3.16 Derivative simulation for several sampling rates (a) Ts=2µs (b) Ts=5µs and (c) Ts=10µs (discrete derivative – green and continuous-time derivative red waveform) ....................50

Figure 3.17 Block diagram of the derivative model where S&H refers to sample and hold ........51

Figure 3.18 Simulation results of the derivative block ....................52

Figure 3.19 Classical approach: successive damping chronograms ....................53

Figure 3.20 (a) Block diagram model of the successive damping system ....................54

Figure 3.20 (b) Sensor model used in Figure 3.20 (a) to output the charge variation due to the acceleration variation ....................54

Figure 3.20 (c) Derivative model used in Figure 3.20 (a) to output the control voltage V_ctrlx ..55

Figure 3.21 Clock chronograms used to control the closed loop system implementing successive damping ....................55

Figure 3.22 Novel sequence: simultaneous damping chronograms ....................56

Figure 3.23 Clock chronograms used to control the closed loop system implementing simultaneous damping ....................57

Figure 3.24 Electrostatic force waveforms for both approaches: successive and simultaneous damping ....................58

Figure 3.25 Settling time simulation results for both approaches: successive and simultaneous damping ....................58

Figure 3.26 Simplified block diagram of the discretized system ....................59

Figure 3.27 Simplified discrete model using up-sampling and down-sampling blocks ....................60

Figure 3.28 Simplified Discrete model for the multirate controller ....................61

Figure 3.29 Equivalent open loop system ....................63

Figure 3.30. (kd, Ts) stable points ....................63

Figure 4.1. Block diagram of the accelerometer signal chain for x-axis ....................66

Figure 4.2. An illustration of the MEMS accelerometer Cadence symbol ....................67

Figure 4.3 Open-loop MEMS displacement for Q=2 and Q=2000 ....................68

Figure 4.4 Open-loop plates configuration for electrostatic force test ....................68

Figure 4.5 (a) Block diagram of the AFE's first stage (C2V) ....................70

Figure 4.5 (b) Chronograms of the C2V block and x-axis excitation signals....................70

Figure 4.6 (a) Telescopic-cascode amplifier and (b) folded-cascode amplifier [Johns – Martin, 1997] ....................71

Figure 4.7 (a) Folded-cascode amplifier with PMOS differential input pair (b) simplified folded-cascode amplifier to calculate the voltage gain [Razavi, 2001]....................72

Figure 4.8 (a) Basic current mirror (b) cascode current mirror [Razavi, 2001]....................73

Figure 4.9 Folded-cascode OTA with second stage and Miller compensation ....................75

Figure 4.10 Two stages Folded-cascode amplifier – biases generation ....................76

Figure 4.11 Amplifier Module and Phase – stability analysis ....................77

Figure 4.12 (a) and (b) An illustration of the derivative block ....................78

Figure 4.13 Chronograms of the derivative block ....................79

Figure 4.14 Chronograms of the derivative block ....................79

Figure 4.15 Derivative block simulation and illustration of the derivative block outputs during the reading phase ....................81

Figure 4.16 Derivative block simulation and illustration of the derivative outputs out of the reading phases ....................81

Figure 4.17 A representation of the switched-capacitors derivative gain block ....................82

Figure 4.18 A representation of the single stage fully-differential amplifier ....................83

Figure 4.19 Stage2 operating phases clocks: S1 (reset) and S2 (amplification)........................84
Figure 4.20 Transistor level schema of the Stage2 fully-differential amplifier........................85
Figure 4.21. Biases generation of the derivative gain block ........................86
Figure 4.22. Modulus and phase waveforms – Amplifier AC simulation ........................86
Figure 4.23 Switched-capacitors CMFB ........................87
Figure 4.24 PMOS switches to force the start-up output common mode ........................88
Figure 4.25 Transient analyze results of the overall derivative gain ........................88
Figure 4.26 Complementary CMOS switch ........................89
Figure 4.27 Switch Ron resistance simulation........................90
Figure 4.28 A representation of the excitation signals block ........................90
Figure 4.29 Sr and Sd control signals ........................91
Figure 4.30 Transient simulation results comparison between the open loop displacement response (no damping) and the closed loop displacement response (damping enabled) ........................92
Figure 5.1 Block diagram of the discrete circuit (printed board and microcontroller)........................94
Figure 5.2 Switched capacitor transimpedance amplifier (Texas Instruments, IVC102) ........................95
Figure 5.3. S1 charge injection vs. input capacitance (left) and S2 charge injection vs. input capacitance (right) [IVC102] ........................96
Figure 5.4. IVC102 configuration ........................97
Figure 5.5. IVC102 frequency response with Rfb=20MΩ connected between the amplifier inverting input and its output ........................98
Figure 5.6 IVC102 and analog gain stage configuration ........................99
Figure 5.7 Excitation signals chronograms ........................100
Figure 5.8. S1, -PWM1, -PWM2 and -PWM3 signals generation ........................101
Figure 5.9 (a) Vex+ Excitation signal generation ........................101
Figure 5.9 (b) Vex- Excitation signal generation........................102
Figure 5.10 C2V gain measurement when Cin =1pF ........................103
Figure 5.11 C2V high cut-off frequency measurement ........................103
Figure 5.12 PWM1, PWM2 and PWM3 signals generation ........................104
Figure 5.13 Vex- excitation signal to be applied on MEMS negative electrode ........................104

# List of Tables


Table 1.1 A comparison of several consumer accelerometer performances ................................8

Table 1.2 A comparison of several consumer gyroscope performances ......................................8

Table 1.3 A comparison of several combo inertial sensors performances ..................................15

Table 2.1 Performances summary of different open-loop topologies published in the literature 27

Table 2.2 Performances summary of different accelerometer topologies published in the literature ..........................................................................................................................32

Table 3.1 Nominal X, Y accelerometer transducer characteristics [Freescale Semiconductor, 2013] .............................................................................................................................36

Table 3.2 Brownian noise floor comparison between a damped and an underdamped MEMS accelerometer ...................................................................................................................36

Table 3.3 Open-loop settling times for different MEMS quality factors Q .................................38

Table 4.1 MEMS displacement under the effect of electrostatic forces and no extern acceleration .......................................................................................................................................69

Table 4.2 C2V amplifier performances ..........................................................................77

Table 4.3 CMOS interface performances .......................................................................77

# List of abbreviations

| | |
|---|---|
| MEMS | Micro Electro Mechanical System |
| IC | Integrated Circuit |
| ASIC | Application-Specific Integrated Circuit |
| CMOS | Complementary Metal Oxide Semiconductor |
| AFE | Analog Front End |
| DoF | Degrees of Freedom |
| IMU | Inertial Measurement Unit |
| ADC | Analog-to-Digital Converter |
| DAC | Digital-to-Analog Converter |
| ODR | Output Dynamic Range |
| NEMS | Nano Electro Mechanical System |
| QFN | Quad Flat No-leads |
| LGA | Land Grid Array |
| CSP | Chip Scale Package |
| CT | Continuous Time |
| SC | Switched Capacitors |
| CTV | Continuous Time Voltage |
| CTC | Continuous Time Current |
| BJT | Bipolar Junction Transistor |
| OTA | Operational Transimpedance Amplifier |
| SAR | Successive Approximation Register |
| SOI | Silicon on insulator |
| PD | Proportional Derivative |
| PID | Proportional Integral Derivative |
| C2V | Charge to Voltage converter |

# LIST OF ABBREVIATIONS

| | |
|---|---|
| CDS | Correlated Double Sampling |
| SNR | Signal to Noise Ration |
| BW | Bandwidth |
| GBW | Gain Bandwidth product |
| MPZ | Matched Pole-Zero |
| MMPZ | Modified Matched Pole-Zero |
| CMFB | Control Mode Feedback |
| TI | Texas Instruments |
| PWM | Pulse Width Modulation |

# INTRODUCTION

## A. Background and motivation

Over the past years, cutting-edge advances in electronics and in microfabrication have allowed the integration of multiple sensors within integrated analog and digital circuits to design Micro Electro Mechanical Systems (MEMS). MEMS are widely used in industries that include but are not limited to: medicine, automotive, aeronautic, aerospace and consumer electronics [Yole, 2016].

Nowadays, the devices are becoming smarter due to microelectronics progresses but also taking more and more advantage of integrated sensors. Among them, inertial sensors (e.g. accelerometers, gyroscopes) have known an important development and are employed in shock detection, healthcare (walking stability monitoring in Parkinson's disease patients), seismology, image and video stabilization, drop protection or motion control applications [Domingues, 2013].

Extensive consumer market growth, in terms of inertial sensors, has been possible due to continuous power, cost and surface reduction while maintaining high performances. Moreover, a trend that enables both cost and surface reduction, and came out recently, is the sensors fusion.

An accelerometer senses the linear motion of the device itself while the gyroscope measures the angular rotation, along one, two or three directions, often named Degrees of Freedom (DoF). To determine the dynamic behavior of a device, a three-axis accelerometer and a three-axis gyroscope can be fused to provide complete navigational information. The result is an inertial measurement unit (IMU) able to sense multiple DoF.

Freescale Semiconductor Inc. (acquired by NXP Semiconductors in December 2015) was one of the first semiconductors companies in the world and leader in automotive electronics, microcontrollers and microprocessors solutions. Further, NXP Semiconductors (45000 employees in 2016 and $6.1 billion revenue in 2015) provides strong expertise in security, near-field communication systems (NFC), sensors, radio frequency and power management systems. Consumer electronics have also gained its place in NXP Semiconductors portfolio, which includes accelerometers, gyroscopes, magnetometers, temperature and pressure sensors products. However, no accelerometer-gyroscope combo sensor is yet available in their portfolio.

In this context, the research carried out in this thesis, funded by NXP Semiconductors together with ANRT (Association Nationale Recherche Technologie), has as main objective the design of a combo six DoF sensor, compatible with a single MEMS cavity technology.

## B. Research direction and contributions

Inertial sensors, embedded in consumer electronics, are usually capacitive accelerometers and Coriolis vibratory gyroscopes. Their principle of operation and performances are conditioned

by the MEMS cavity pressure: the accelerometer is a damped system functioning under an atmospheric pressure while the gyroscope is a highly resonant system. To conceive a combo sensor, a unique low cavity pressure is required. The integration of both transducers within the same low pressure cavity necessitates a method to control and reduce the ringing phenomena by increasing the damping factor of the MEMS accelerometer. Hence, the goal of the thesis is the system design of an underdamped capacitive MEMS accelerometer.

The most used accelerometer control configurations are the digital closed loop ($\Sigma\Delta$ architecture) and the analog loop, enabling artificial damping by superimposing two electrostatic forces on the accelerometer proof mass to produce a linear feedback characteristic [Boser, 1996]. The former approach has a complex implementation and is not compatible with the actual transducer design (since the proof-mass is shared between the three-axis) while the latter provides good performances and can be used to control multiple DoF.

Firstly, this thesis proposes a novel closed-loop electrostatic damping architecture for a three-axis underdamped accelerometer. The circuit is a switched-capacitor low-power system that multiplexes the analog front-end (AFE) first stage between the three axes, to reduce both power and surface. Additionally, a new damping sequence (simultaneous damping), has been conceived to improve the damping efficiency over the state of the art approach performances (successive damping). The simultaneous damping sequence is implemented using a multirate control method.

Next, to validate the system operation, several behavioral and mathematical models have been designed and the settling time method is used to assess the damping efficiency.

In addition, a new approach that uses the multirate signal processing theory and allows the system stability study has been developed. This method is used to conclude on the loop stability for a certain sampling frequency and loop gain value.

Using the above techniques, a CMOS implementation of the entire accelerometer signal chain is designed. The functioning has been validated and the block may be further integrated within an ASIC. Finally, a discrete components system is designed to experimentally validate the simultaneous damping approach.

## C. Thesis organization

This thesis is organized as follows. Chapter 1 introduces the main inertial sensors applications, focusing on accelerometer and gyroscopes sensing principles and performances. This first chapter also highlights the consumer electronics continuous development and the increased combo sensors demand. In this context, this thesis research direction and main objective have been set.

Chapter 2 presents the fundamentals of the capacitive MEMS accelerometers including the physics of the mechanical sensing element, the second order mass spring damper model and the electrostatic actuation mechanism. A synopsis of the existing accelerometer CMOS interfaces is also briefly presented.

In Chapter 3, a new closed-loop accelerometer architecture that overcomes the underdamped MEMS oscillation issue is presented. The sensor control relies on the electrostatic damping principle and consists in estimating the proof mass velocity and in artificially increasing

the damping ratio. The Matlab-Simulink model for each block in the loop is described and the simulation results are shown. Then, a comparison between the novel simultaneous damping approach performances and the classical successive damping method is made. Finally, the multirate controller modeling and the system closed loop stability are analyzed.

Chapter 4 introduces a block by block transistor level design of the proposed damping architecture, adapted for a three-axis low power MEMS accelerometer. The switched capacitor technique is used to implement the read-out interface and the multirate controller block. The closed loop simulation results and performances are shown.

Finally, the thesis classically ends with a conclusion that summarizes the results and contributions, and suggests several future research directions and perspectives.

# CHAPTER 1
# INERTIAL SENSORS

## 1.1 Introduction

A sensor is a device that detects and converts any physical quantity (e.g. light, heat, pressure, motion, inertia, etc.) into a signal which can be electronically measured and further processed. Nowadays, sensors are widely used in applications that include but are not limited to: medicine, automotive, aeronautic and aerospace industries, but also in consumer electronics.

While the first sensor dates from the nineteenth century (a thermocouple), during the First and the Second World War, sensors as infrared, motion and inertial sensors, intended for strategical and tactical applications, have known an important development and improvement.

An inertial sensor is an observer who is caught within a completely shielded case and who is trying to determine the position changes of the case with respect to an outer inertial reference system [Kempe, 2011]. In other words, inertial sensors deal with the inertial forces to find the dynamic behavior of an object; these inertial forces modify the dynamic behavior and cause accelerations and angular velocities along one or several directions. Accordingly, the main inertial sensors are the accelerometer, which senses a linear motion and the gyroscope which measures the angular rotation.

Since the beginning of the 1990's, the inertial sensors are predominantly Micro Electro Mechanical Systems (MEMS) due to their low cost, high performances and high level of integration. Their advantages opened new markets and developed new applications, each one with its own specifications and constraints. The classical accelerometers and gyroscopes applications are: shock detection (airbag – automotive industry), seismology, aeronautics and space industry, healthcare (patient activity monitoring, disease identification), image and video stabilization, wearable computing, drop protection or motion control.

## 1.2 Degrees of freedom and types of motion in inertial sensors

The accelerations and the angular velocities, measured by an accelerometer or by a gyroscope, are vectors having an absolute value and an orientation. If only one vector component is measured, then the system is said to be a one-axis or one-DoF. If two vector components (acceleration or angular velocity) are measured, the system is a two-degree of freedom and so on. It is thus clear that in a three-dimensional space, one can measure six degrees of freedom as shown in Figure 1.1. Three of DoF are translational movements: surge, heave and sway (often noted $x$, $y$ and $z$) and can be measured using an accelerometer. The other three DoF represent rotational movements (yaw, pitch and roll) and can be sensed using a gyroscope sensor. Thus, the combination of the translational and rotational movements consists in a six DoF system requiring both a three-axis accelerometer and a three-axis gyroscope to determine its dynamic

behavior. Therefore, an inertial measurement unit (IMU) should embed a multiaxis accelerometer and a multiaxis gyroscope to provide all the required navigation information; the combination of an accelerometer and a gyroscope is often also called a combo sensor.

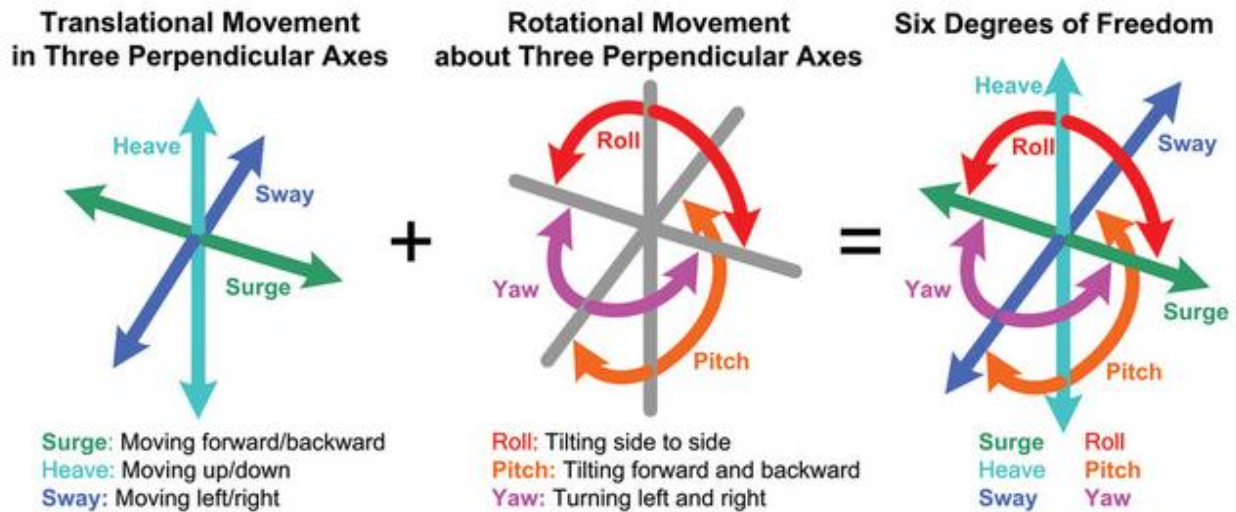


Figure 1.1 A representation of the possible movements of an object in a three-dimensional space [Snyder, 2016]

## 1.3 Consumer market MEMS inertial sensors

The consumer electronics industry is one of the markets that has continually grown over the past few years and this is mainly due to the technological progress and to consumer requests. Along with the overall market growth, consumer MEMS sensors also known an important development to enable cost, surface and power reductions while maintaining high performances. Figure 1.2 presents a MEMS revenue forecast which firstly, confirms the increasing revenue for the upcoming years and secondly, presents the consumer MEMS dominancy over the other sensor sectors as Aeronautics, Automotive, Defense, Industrial, Medical and Telecom.

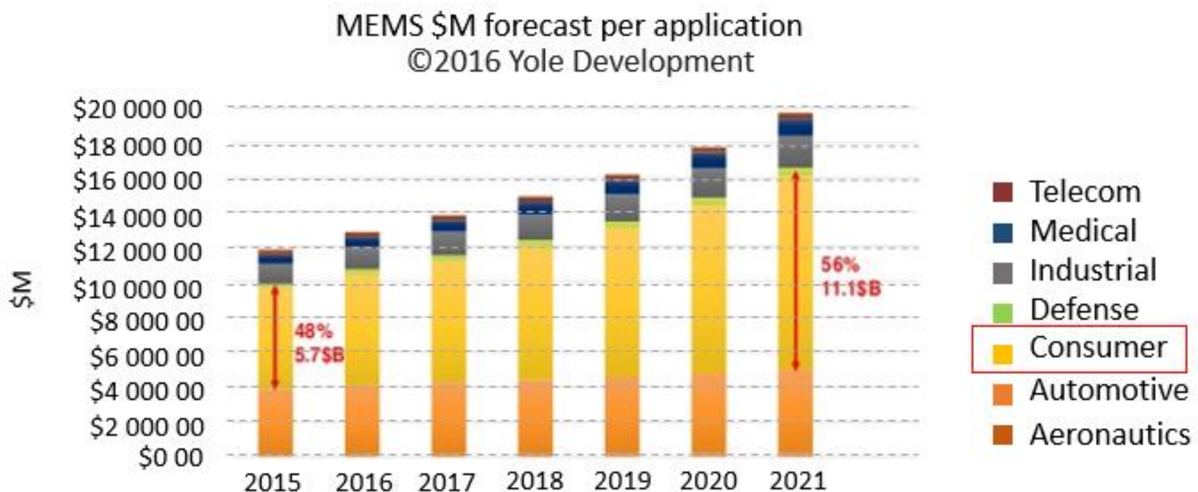


Figure 1.2 MEMS revenue forecast 2015-2021 per application [Yole, 2016]

Inertial MEMS sensors, the accelerometer as well as the gyroscope, are widely used in consumer market applications (smartphones, tablets, cameras, smart home devices, wearables, remote control, gaming, etc.). However, there is an important gap between the performances of an inertial sensor intended for consumer electronics and an automotive, medical or defense inertial sensor. Figure 1.3 (a) and (b) [Domingues, 2013] presents a sensor performances comparison for different applications.

For example, a consumer market accelerometer has an input range which can go up to $8g$ and requires a dynamic range between $60\ dB$ and $100\ dB$ while a seismology accelerometer, for the same input range, needs a much higher accuracy and a dynamic range between $140\ dB$ and $160\ dB$.

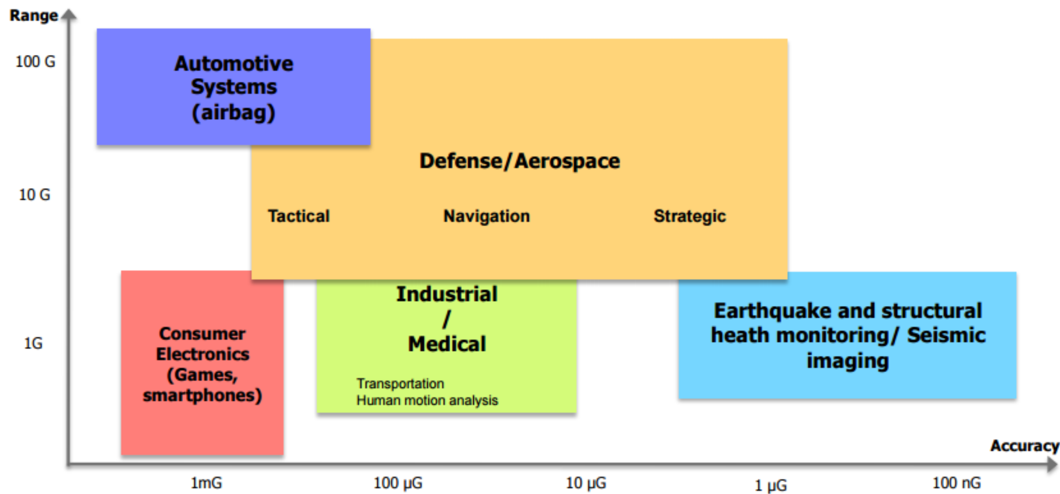


Figure 1.3 (a) Accelerometer applications vs. performances [Domingues, 2013]

A consumer market gyroscope is designed to measure up to $2000\ °/s$ of angular rate and needs an accuracy of $10\ °/s$ while a missile guidance gyroscope or an automotive gyroscope require an $0.1\ °/s$ accuracy.

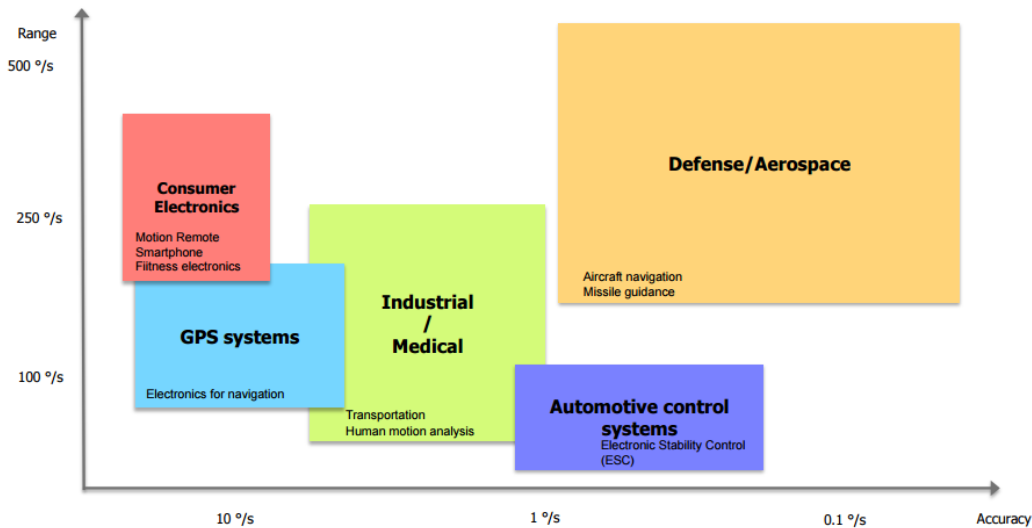


Figure 1.3 (b) Gyroscope applications vs. performances [Domingues, 2013]

On the other hand, the main constraints of a consumer market inertial sensor are the cost, the size and the power consumption. As it was shown, the industry targeting this market imposes high volume production thus the cost is very important. Silicon area and power consumption should also be considered to enable inertial sensors to be integrated within everyday user applications.

To have a better overview of the consumer market sensor performances, several three-axis consumer accelerometers and gyroscopes have been selected and are presented in Table 1.1 and Table 1.2, respectively.

| Part | NXP MMA8452Q | Analog Devices ADXL363 | Bosch BMA255 | STMicroelectronics LIS3DH |
|---|---|---|---|---|
| Size | $3mm\times3mm\times1mm$ | $3mm\times3.25mm\times1.06mm$ | $2mm\times2mm\times0.95mm$ | $3mm\times3mm\times1mm$ |
| $V_{dd}[V]$ | $1.6-3.6$ | $1.6-3.5$ | $1.62-3.6$ | $1.6-3.5$ |
| $I_{dd}[\mu A]$ | $6-165$ | $2(100Hz)$ | $130(2kHz)$ $6.5(40Hz)$ | $11(50kHz)$ $2(1Hz)$ |
| Noise floor $[\mu g/\sqrt{Hz}]$ | 99 | 550 | 150 | 220 |
| Output dynamic range (ODR) $[Hz]$ | $1.56-800$ | $12.5-400$ | $8-1000$ | $1-5300$ |
| ADC resolution $[bits]$ | 12 and 8 | 12 | 12 | 12 |

Table 1.1 A comparison of several consumer accelerometer performances

| Part | NXP FXAS21002C | Bosch BMG160 | STMicroelectronics L3GD20H | Invensense ITG-1010 |
|---|---|---|---|---|
| Size | $4mm\times4mm\times1mm$ | $3mm\times3mm\times0.95mm$ | $3mm\times3mm\times1mm$ | $3mm\times3mm\times0.9mm$ |
| $V_{dd}[V]$ | $1.95-3.6$ | $2.4-3.6$ | $2.2-3.6$ | $1.71-3.6$ |
| $I_{dd}[mA]$ | 2.7 | 5 | 5 | 3.2 |
| Noise floor $[mdps/\sqrt{Hz}]$ | 25 | $14(400Hz)$ | 11 | $10(10Hz)$ |
| Wake-up time $[ms]$ | 60 | 10 | 50 | 50 |
| Output dynamic range (ODR) $[Hz]$ | $12.5-800$ | 100,200,400, 1000,2000 | $11-757$ | – |
| ADC resolution $[bits]$ | 16 | 16 | 16 | 16 |

Table 1.2 A comparison of several consumer gyroscope performances

## 1.4 Discrete inertial sensors

Acceleration measurement accuracy depends on both the transducer performances and electronics design. This section, presents the main sensing methods and types of inertial sensors with their operation principle and applications.

### 1.4.1 Accelerometers

#### A. Piezoresistive acceleration sensing

The piezoresistive effect of semiconductors, such as silicon and germanium, is a phenomenon whereby the application of a stress induces a proportional variation of the material resistivity. A piezoresistive accelerometer detects the deformation of a structure from which the acceleration can be retrieved.

When an external acceleration $a$ is applied to the sensor (Figure 1.4), a certain force $F$ is exerted and the proof mass will be deflected from its rest position [Tan, 2012]. This deflection causes stress, which results in a resistance variation in the doped piezoresistor. This resistance variation is then usually converted to a voltage using a Wheatstone bridge.

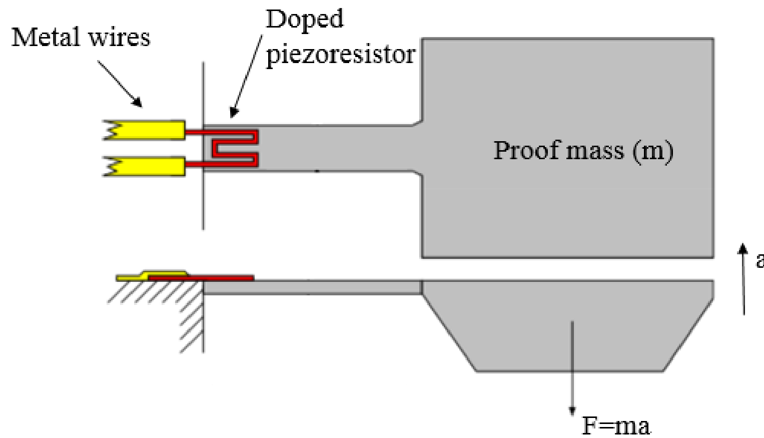


Figure 1.4. An illustration of a piezoresistive accelerometer

However, piezoresistive sensors are temperature dependent [Kim, 1983] and susceptible to self-heating [Doll, 2011]. Therefore, the main research efforts have been concentrated on decreasing the temperature dependency of the sensor sensitivity and offset [Partridge, 2000], [Sim, 1997].

The input signal range for a piezoelectric accelerometer can go up to $100000g$ [Ning, 1995] [Dong, 2008], [Huang, 2005], which makes from these sensors a suitable candidate for the automotive applications. The device presented by [Huang, 2005] achieves a sensitivity of $106\, mV/g$ and can measure from $0.25g$ to $25000g$. Several multi-axis accelerometers architectures have been presented in the literature: in [Chen, 1997] a two-axis piezoresistive accelerometer and in [Dong, 2008] a three-axis accelerometer where the achieved sensitivities are $2.17$, $2.25$ and $2.64\, \mu V/g$ for x, y and z, respectively.

Very new research in the field has conducted to a new approach for a 3D piezoresistive accelerometer using a NEMS-MEMS technology [Robert, 2009]. Due to a differential transducer

topology, the thermal sensitivity is reduced, but still, additional circuitry is required to compensate the thermal drift, which remains the most important drawback of the piezoresistive accelerometer.

Piezoresistive accelerometers have typically noise floors between $10$ and $100\ \mu g/\sqrt{Hz}$ for a bandwidth that ranges between 1 kHz and 10 kHz [Chatterjee, 2016].

### B. Piezoelectric acceleration sensing

A cross section of a piezoelectric accelerometer is presented in Figure 1.5. Its principle is also based on Newton's second law: an external acceleration applied to the proof mass will induce a force, proportional to the acceleration, which will deflect the mass.

When the proof mass is deflected, the piezoelectric layer bends and generates a charge that will then be read with a charge amplifier, for example. The most used materials for the piezoelectric layer are the zinc-oxide (ZnO) [DeVoe, 1997], [DeVoe, 2001], [Scheeper, 1996], aluminum nitride (AlN) [Wang, 2006], lead-zirconate-titanate (PZT) [Hewa-Kasakarage, 2013], [Wang, 2003] or a multi-layer structure [Zou, 2008], [Kobayashi, 2009] consisting in a piezoelectric-bimorph accelerometer.

The [Hewa-Kasakarage, 2013] devices sensitivity is $50\ pC/g$ with a noise floor of $1.74\ \mu g/\sqrt{Hz}$ @$30\ Hz$) while the [Zou, 2008] three-axis devices have a sensitivity of $0.93$, $1.13$ and $0.88\ mV/g$ for x, y and z, respectively. The minimum detectable signal is $0.04\ g$ for bandwidths ranging from subhertz to $100\ Hz$.

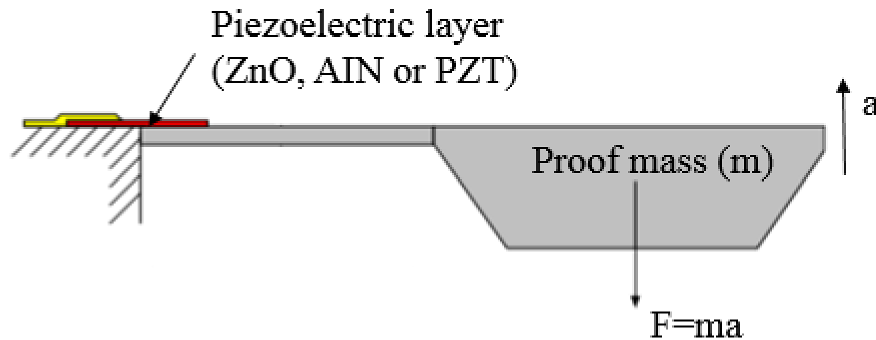


Figure 1.5 An illustration of a piezoelectric accelerometer

The most important advantages of the piezoelectric sensors are low power consumption due to the simple detection circuit, high sensitivity, low floor noise and temperature stability. Their most widely use is the vibration based applications since they can achieve high quality factor resonances without vacuum sealing [Denghua, 2010]. Finally, they can also be used in ultra-high dynamic range and linearity applications [Williams, 2010]. Regarding the microsystems technology, Figure 1.5 illustrates a bulk micromachined piezoelectric accelerometer, but the sensor can also be surface micromachined.

### C. Capacitive acceleration sensing

Capacitive sensing is one of the three most used acceleration detection methods, with the piezoresistive and piezoelectric sensing [Garcia-Valenzuela, 1994]. High performance

accelerometers are using a capacitive detection method since their fabrication cost is lower [Wu, 2002], they consume less power, they can be used in high sensitivity applications and are thermally stable.

The capacitive sensing principle (Figure 1.6) consists in measuring the proof mass displacement when an external acceleration is applied to the transducer. When the proof mass is deflected along the sensing direction, the capacitance value between the proof mass and the fixed electrodes changes. The capacitance change is then measured using an analog-front-end circuit, which can be more or less complex, depending on the specifications and the applications.

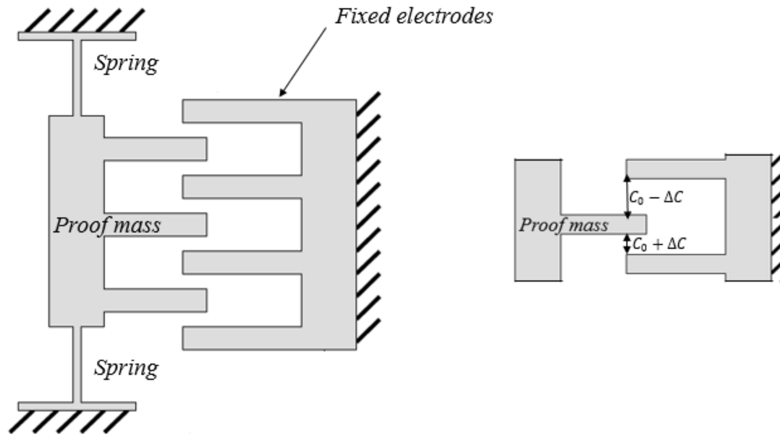


Figure 1.6 An illustration of a capacitive accelerometer with interdigitated fingers

In the 90s, important research was carried out to investigate the bulk and the surface micromachined structures. Even if the bulk micromaching was considered to be older and not so performant, [French, 1998] compares the two technologies and proves that both were developed in parallel and have their own advantages. For both technologies, the noise floor ranges between 1 to $100\ \mu g/\sqrt{Hz}$ .

Bulk-micromachined technology includes all the techniques that allows removing the silicon substrate (by wet or dry etching methods starting with the wafer back side, e.g.) since the micro-mechanical structure is created in the wafer thickness.

For a surface-micromachined sensor, the mechanical structure is built on the wafer surface by deposing thin films and selectively removing pieces of them [Boser, 1996]. The most common layer used in surface micromaching is polysilicon [Sugiyama, 1994], but also silicon nitride, silicon dioxide and aluminum sacrificial layers [Cole, 1994] were investigated.

The main advantage of the bulk micromachined technology lies in the proof mass size because the full silicon substrate is used to create the MEMS. This implies higher sensitivity and lower Brownian noise floor [Smith, 1994], [Tsai, 2012], [Tez, 2015]. On the other hand, surface micromachined technology cost is lower and the sensor along with the circuitry is easy to integrate [French, 1996]. Moreover, a combination of both technologies was used by Yazdi et al., [Yazdi, 2000], [Yazdi, 2003] to explore the benefits of the bulk-micromachined (high sensitivity) and of the surface-micromachined accelerometers. It results in a noise floor of $0.23\ \mu g/\sqrt{Hz}$.

There are two major configurations for the capacitive sensing element: in-plane designs, where the proof mass moves in plane of the device, and out-of-plane designs, where the proof mass is suspended and has an out-of-plane movement. Figure 1.7 shows a picture of the two capacitive sensing configurations: in-plane an out-of-place.

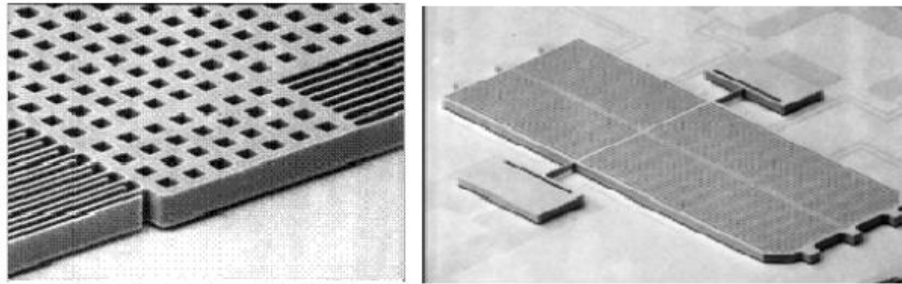

Figure 1.7 Typical structure of in-plane (left) and out-of-plane (right) capacitive MEMS accelerometer [Renaut, 2013]

For an in-plane design, the proof mass has a translational movement and is used to measure $x$ and $y$ accelerations; a teeter-tooter, out-of-plane, design is usually preferred to measure $z$-axis accelerations. When a $z$ - direction acceleration is applied to the teeter tooter system, the proof mass will rotate and will change the capacitances between the proof mass and the sense plates. The mass is attached to an anchor that is located away from the center of gravity though the transducer can be described in terms of rotational dynamics. A high-sensitivity $z$ -axis capacitive accelerometer with a torsional suspension was published by Selvakumar and Najafi [Selvakumar, 1998]. Both translational and rotational functioning principles are shown in Figure 1.8.

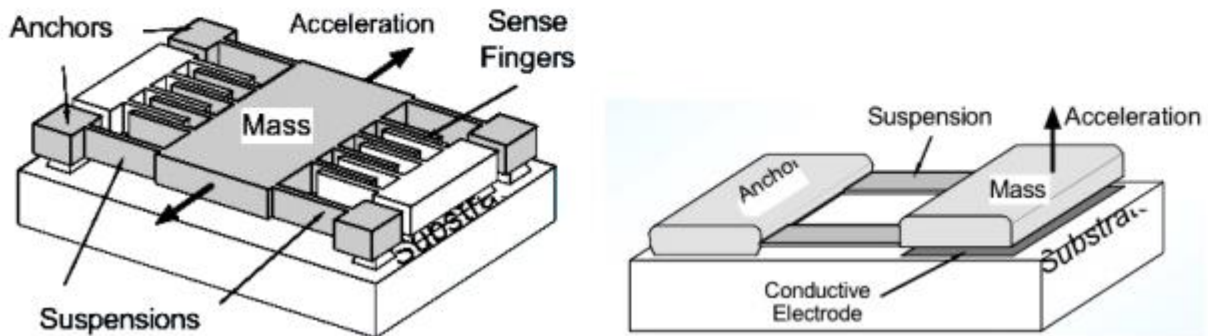


Figure 1.8 Functioning principle of in-plane (left) and out-of-plane capacitive MEMS accelerometer [Renaut, 2013]

The lower power consumption and small temperature dependency make from the capacitive MEMS accelerometer the most suitable candidate for the consumer market applications which demand low cost and robust sensors; capacitive MEMS accelerometers will be further detailed in Chapter 2.

## D. Other acceleration sensing methods

Resonance-based MEMS accelerometers exploits the oscillation amplitude-frequency dependency of a resonant system; for this kind of structure, around its resonance frequency, a small variation of the excitation frequency results in a high amplitude change. In the case of a resonant accelerometer, an extra-actuator is needed to excite the mechanical structure at its resonance frequency. Then, an acceleration force applied to the resonant structure results in a frequency shift and thus in an oscillation amplitude change. By measuring the oscillation amplitude, the level of

acceleration can be calculated [Roessig, 2002], [Li, 2012], [Zotov, 2015]. Resonant accelerometers usually require two systems: the read-out circuitry, which gives the acceleration measure, and a self-resonating structure that assures the MEMS oscillation [He, 2008].

Resonance-based accelerometers are radiation resistant and can be used in harsh environments as space exploration. They can have high resolutions ($150ng/\sqrt{Hz}$ – [Zou, 2015]) however they don't represent a suitable candidate for the consumer market electronics. The main limitation is given by the power consumption since the resonance-based accelerometers require the additional continuous time circuit to maintain the transducer oscillation. Comparing with a capacitive accelerometer, where the device can be completely turn-off, out of the measuring phases, a resonant accelerometer is continuous time excited with a certain amplitude oscillation. In [He, 2008] a CMOS readout for a SOI resonant accelerometer that consumes $6.96\,mA$ is reported. Consumer electronics require current consumptions as low as $1\,\mu A$ when operating in low-power modes.

Moreover, another resonant accelerometer design challenge is the proof mass size and the multiple axis (three) integration which is a main specification for the consumer electronics.

Another acceleration sensing method is based on the temperature change of the gas inside the MEMS cavity of a convective accelerometer, when an external acceleration is applied [Chatterjee, 2016]. The temperature change is measured using heat sensors which increases the cost of this sensing method and challenges the design of a single-die CMOS three-axis accelerometer [Milanovic, 2010], [Nguyen, 2014]. Convective accelerometers typically have a bandwidth of $10$ to $100\ Hz$ and a noise floor range of $100$ to $1000\ \mu g/\sqrt{Hz}$.

### 1.4.2 Gyroscopes

The first gyroscope (Foucault, 1852) was based on the conservation of the angular momentum of a spinning wheel and was used in the Second World War inertial navigation: submarines, aircrafts and missiles. The principle is still used to implement high performance gyroscopes for inertial navigation; however, they are costly [Allen, 2009].

Optical gyroscopes are based on the Sagnac effect (Sagnac, 1913) which measures the time difference between the clockwise and counterclockwise beams striking a detector located in the optical path and rotating with the optical path at a certain angular rate [Roland, 1981]. Optical gyroscopes can be implemented either using a fiber optic (fiber optic gyroscope) or a laser (ring laser gyroscope), both providing very high accuracy ($0.001\,°/s$, which is suitable for strategic market, seismology or astronomical observations.

Nowadays, Coriolis vibratory gyroscopes are widely used in consumer market applications. Their operating principle is based on the energy transfer between two oscillation modes using the Coriolis Effect. In a reference frame rotating with a certain angular velocity Ω and a proof mass $m$ moving with a certain linear velocity $V_x$, one can define the Coriolis force as:

$$\vec{F}_{Coriolis} = 2m\vec{\Omega}\,\vec{V_x} \quad (1.1)$$

Figure 1.9 shows the resonator model of a Coriolis accelerometer: the primary vibrating mode is induced electronically by a drive circuit while the secondary mode is driven by the Coriolis force. The secondary mode oscillation amplitude is proportional to the angular velocity (1.1).

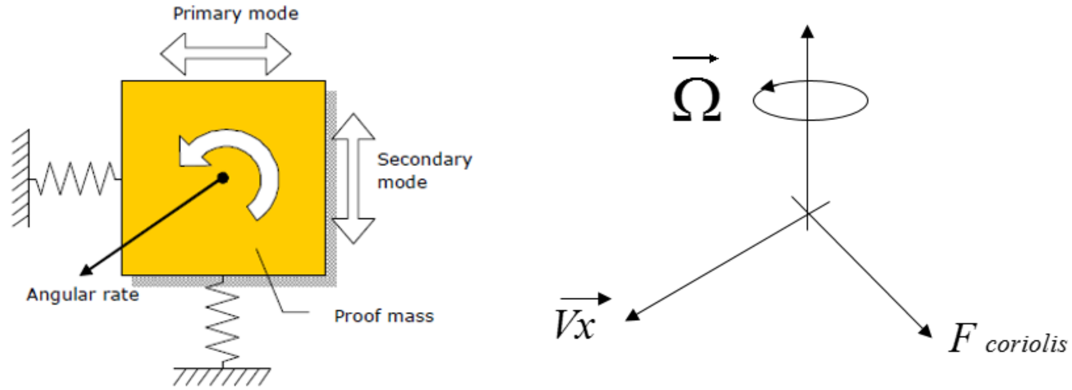


Figure 1.9 A representation of the Coriolis gyroscope model

Coriolis vibratory gyroscopes are fully-compatible with the MEMS technology and represent a successful candidate for the inertial measurement units required by the consumer market applications.

## 1.5 Combo sensors

As previously stated, the inertial sensor consumer market is a continually growing industry with big perspectives. In this context, it is clear that fast technological achievements, costly advantageous, have to be made.

The main characteristics and performances for both sensors: accelerometer and gyroscope, have been discussed in the previous sections; these sensors are discrete, meaning that they are QFN (quad-flat no-leads) or LGA (land grid array) separately packaged. Recently, but quickly increasing, a new trend came out in the industry: sensors fusion or combo packages. In other words, the accelerometer, the gyroscopes and even more sensors (e.g. magnetometer) are packaged within one single chip. The benefits of a combo sensor are the low cost, reduced footprint and qualification and testing easiness. It is no longer an inertial sensor design but a fully IMU solution.

Figure 1.10 proves the discrete to combo sensors market evolution and forecasts the combo market revenue supremacy over the discrete sensors in the next few years [Yole, 2014].

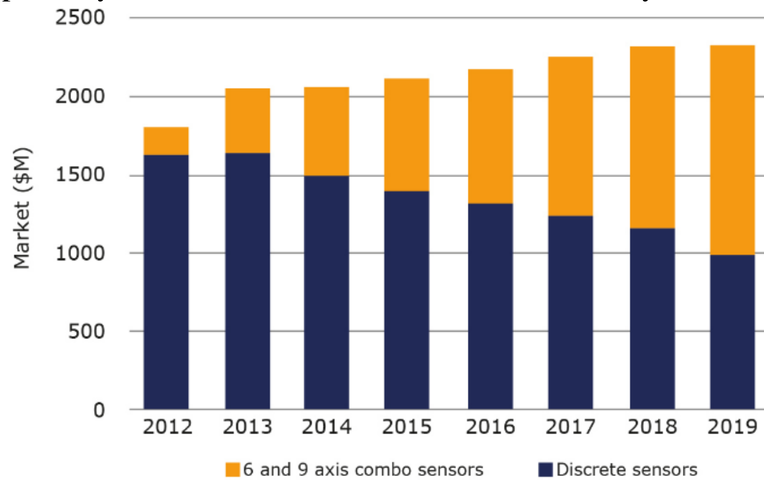


Figure 1.10 Inertial sensors revenue forecast 2012-2019 [Yole, 2014]

Consumer market combo sensors usually embed a capacitive accelerometer and a Coriolis gyroscope due to their high performances, low cost, low power consumption and robustness. Table 1.3 presents a performances comparison of several available combo inertial sensors available on the market. NXP Semiconductors, one of the larger semiconductor suppliers, offers discrete inertial sensors solutions and is further interested in developing combo sensors. In this context, this NXP Semiconductors funded work is concentrated on the accelerometer – gyroscope sensors fusion.

| Part | Bosch BMI055 | STMicroelectronics LSM6DLS | Invensense ICM-20600 | NXP Semiconductors |
|---|---|---|---|---|
| Size | $3mm \times 4.5mm \times 0.95mm$ | $2.5mm \times 3mm \times 0.83mm$ | $2.5mm \times 3mm \times 0.91mm$ | $To\ be\ developped$ |
| $V_{dd}[V]$ | $2.6 - 3.6$ | $1.71 - 3.6$ | $1.71 - 3.45$ | |
| $I_{dd}[mA]$ | $5.15$ | $0.45(208Hz)$ | $2.79(lownoisemode)$ | |
| Noise floor (A) $[\mu g/\sqrt{Hz}]$ (G) $[mdps/\sqrt{Hz}]$ | (A) 150 (G) 14 | (A) 130 (G) 4 | (A) 100 (G) 4 | |

Table 1.3 A comparison of several combo inertial sensors performances

A 6 DoF combo sensor integrates an accelerometer and a gyroscope. Two methods can be imagined in order to do so: the first one is to integrate the accelerometer (MEMS and ASIC) and the gyroscope (MEMS and ASIC) in the same package. It results in a 6 DoF IMU two-ASIC, two-MEMS (two cavities) single package that is certainly more robust and package costless than a discrete solution. The performances are the same with no additional design effort since each sensor has a separate MEMS cavity.

Going further, the second method that can be imagined for the sensor fusion, to reduce even more the cost and the footprint, is a one-MEMS (one cavity) one-ASIC solution. In this case, the two sensor performances are committed because they require different operating pressure in their cavities: the accelerometer is a damped system functioning under an atmospheric pressure while the Coriolis vibratory gyroscope is a highly resonant, high quality factor (Q) system in order to aid the drive oscillation. Figure 1.11 shows a plot of the quality factor dependency on the MEMS cavity pressure and the frequency response of a MEMS accelerometer. To enable the co-integration, a compromise should be made and a direction chosen:

- A low-Q gyroscope design – which is high challenging because the gyroscope primary resonance mode, the drive, requires a very high quality factor.
- A high-Q accelerometer design – which is achievable and makes the object of this research study. The goal is the system design of an underdamped MEMS accelerometer intended for consumer market applications.

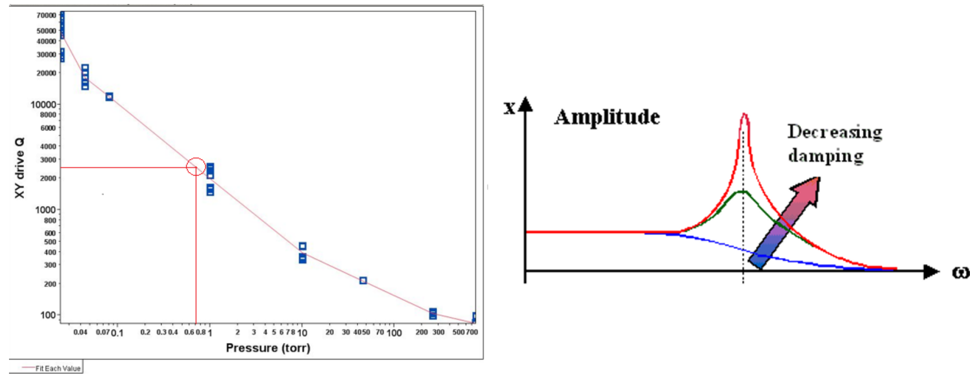


Figure 1.11 A plot of the Quality factor (Q) vs. MEMS cavity pressure (left) and the frequency response of a second order mass spring damper system (right)

From Figure 1.11, one can notice that a common cavity pressure lower than 1 torr is viable for both sensors and can lead to a successful 6 DoF combo sensor design. Consequently, the associated quality factor chosen for further designs and simulation, was considered to be superior to 2000.

## 1.6 Summary

This chapter introduced the main inertial sensors applications and different types of motion. Several accelerometer and gyroscope sensing principles with their associated performances have been presented. The chapter also highlights the consumer market continuous development and the increased combo sensors demand. Combo sensors usually embed a capacitive MEMS accelerometer and a Coriolis gyroscope to provide a 6 DoF IMU. Further, a solution that allows the accelerometer – gyroscope co-integration has been proposed and is based on the design of an underdamped MEMS accelerometer.

Next chapter details the capacitive accelerometers and the electrostatic actuation mechanism that appears in such transducers. A state of the art of the CMOS capacitive accelerometers interfaces is also presented in Chapter 2.

# CHAPTER 2
# CMOS MEMS ACCELEROMETERS

The integration of MEMS accelerometers is a topic extensively researched over the past years due to the sensors growing popularity and their new application fields. The integration efforts have been concentrated around the sensor robustness, cost and power consumption reduction.

Additionally, to their high performances, the interest for the capacitive MEMS accelerometers has also found its motivation in the electrostatic actuation capability. Whenever an electrical potential is applied across the plates of a capacitor, an attractive force is generated across the plates. For the accelerometers, this force is used to generate a force-balanced feedback, a damping control or in self-test configurations.

Therefore, this chapter introduces the physics of the mechanical capacitive sensing element, including the second order mass spring damper model, the electrostatic actuation mechanism and its nonlinearities and the electrostatic spring forces.

Finally, an overview of the capacitive CMOS interfaces in the literature implementing read-out techniques based on continuous-time voltage, continuous-time current and switched-capacitor architectures, as well as the advantages and drawbacks for both open-loop and closed-loop topologies using different control techniques, will be described in the next sections.

## 2.1 Mechanical capacitive sensing element and second order mass spring damper model

For a capacitive MEMS accelerometer, the mechanical sensing element consists in a proof mass that has a free movement along an axis direction between two fixed plates, also named excitation electrodes. Figure 2.1 shows a drawing of the mechanical sensing element which can be modeled with a second order mass spring damper system.

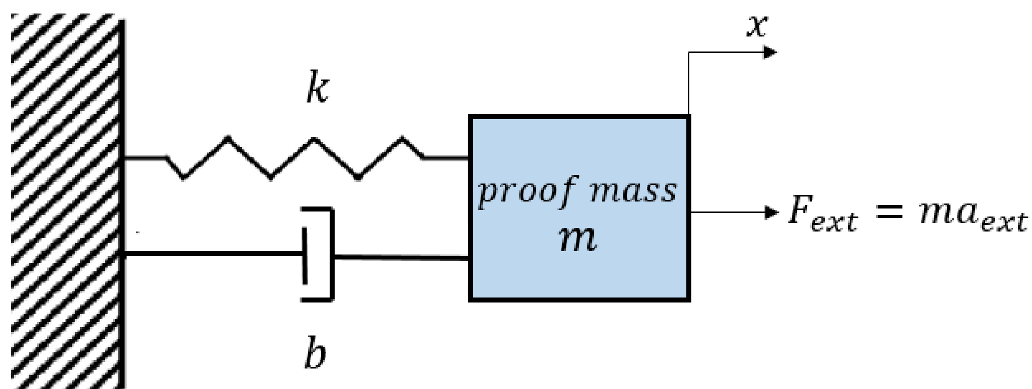


Figure 2.1 An illustration of a second order mass spring damper system

When an external acceleration $a_{ext}$ is applied on the proof mass $m$, an inertial force $F_{ext}$ induces the proof mass displacement. The parameter $k$ is the spring coefficient, which is a sensor design parameter and depends on the spring properties. The parameter $b$ is the mechanical damping coefficient and depends both on the sensor structure and on the air pressure inside the sensor cavity. Equation (2.1) can be derived from Figure 2.1, by applying the Newton's second law:

$$m\ddot{x}(t) + b\dot{x}(t) + kx(t) = ma_{ext}(t) = F_{ext}(t) \tag{2.1}$$

Where $\dot{x}(t)$ is the proof mass velocity and $\ddot{x}(t)$ the proof mass acceleration. When the steady state regime is reached, both $\dot{x}(t)$ and $\ddot{x}(t)$ terms will be null and thus, eq. (2.1) can be rewritten as:

$$kx = ma_{ext}$$

$$\frac{x}{a_{ext}} = \frac{m}{k} = Displacement\ sensitivity \tag{2.2}$$

The sensor has a continuous time movement, as expressed in equation (2.1), and therefore to obtain the s-domain equivalent equation or the transfer function, the Laplace Transform can be used. It will be shown later in this thesis that the mechanical sensing element transfer function can also be reduced to a discrete-time equation when the architecture requires this approximation. Equations (2.3) and (2.4) express the sensor transfer function when considering an inertial force as input or acceleration, respectively:

$$H_{MEMS(x\to F)}(s) = \frac{X(s)}{F_{ext}(s)} = \frac{1/m}{s^2+\frac{b}{m}s+\frac{k}{m}} \tag{2.3}$$

$$H_{MEMS(x\to a)}(s) = \frac{X(s)}{a_{ext}(s)} = \frac{1}{s^2+\frac{b}{m}s+\frac{k}{m}} \tag{2.4}$$

The natural pulsation of the transducer and the mechanical quality factor are:

$$\omega_n = \sqrt{\frac{k}{m}} \tag{2.5}$$

$$Q = \frac{\sqrt{km}}{b} \tag{2.6}$$

If considering $\xi = \frac{1}{2Q}$, the system transfer function becomes:

$$H_{MEMS(x\to a)}(s) = \frac{1}{s^2+2\xi\omega_n s+\omega_n^2} \tag{2.7}$$

Depending on the quality factor level, one can define:

- $Q > 0.5$ – the system is said underdamped or "high-Q". The oscillations caused by the high-quality factor are problematic when the oscillations amplitude is too large and the electronic interface saturates, when due to the oscillations the proof mass hits and sticks the sensor fingers but also when the proof mass settling times are too long for certain applications. All the above-mentioned drawbacks can be overcome with the aid of an artificial electrical damping mechanism.
- $Q = 0.5$ – the system is critically damped. For this specific case, the settling time is minimum.
- $Q < 0.5$ – the system is overdamped. No special caution needs to be taken to control the transducer.

Consequently, it was shown that the capacitive accelerometer sensor model can be reduced to a second order mass spring damper system with a continuous time transfer function which depends on several transducer design parameters. The behavior of the MEMS can be anticipated by evaluating its quality factor.

## 2.2 Physics of the capacitive sensing element

High-resolution applications are requiring MEMS capacitive sensors able to detect displacements in the order of $nm$ and capacitances down to $fF$ for $1g$ of acceleration. In addition to the imperfections caused by the process variations, the displacement to capacitance and the voltage to electrostatic force conversions are two other nonlinearity sources that will next be explained.

Figure 2.2 shows a two-plate capacitive structure. When the mass is in the rest position ($a = 0$), the gap between the proof mass and the fixed electrodes is symmetrical and equal to $d_0$.

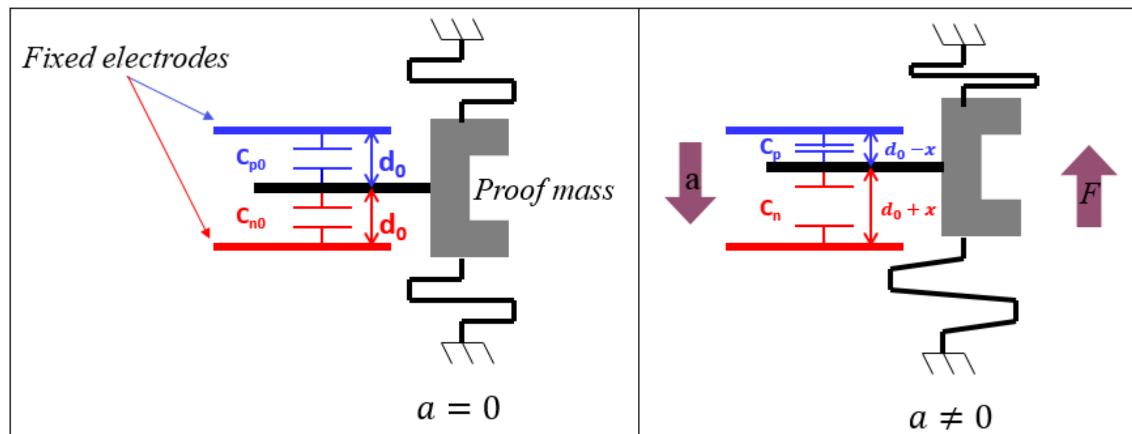


Figure 2.2 An illustration of the capacitive sensing principle

The two nominal capacitances $C_{p0}$ and $C_{n0}$ are fixed and depend on the electrodes surface, the gap between them and on their surface $A$:

$$C_{p0} = \frac{\varepsilon A}{d_0} + C_q \tag{2.8}$$

$$C_{n0} = \frac{\varepsilon A}{d_0} + C_q \tag{2.9}$$

where $\varepsilon$ is the air permittivity and $C_q$ a parasitic fixed capacitance.

When the proof mass is deflected under the effect of an extern acceleration, one of the fixed nominal capacitance will increase while the other decreases:

$$C_p = \frac{\varepsilon A}{d_0 - x} + C_q \tag{2.10}$$

$$C_n = \frac{\varepsilon A}{d_0 + x} + C_q \tag{2.11}$$

Then, the capacitance variations $\Delta C_p, \Delta C_n$ can be deduced as:

$$\Delta C_p = C_p - C_{p0} = \frac{\varepsilon A}{d_0} \times \frac{x}{d_0} \times \frac{1}{(1 - \frac{x}{d_0})} \tag{2.12}$$

$$\Delta C_n = C_n - C_{n0} = \frac{\varepsilon A}{d_0} \times \frac{x}{d_0} \times \frac{1}{(1 + \frac{x}{d_0})} \tag{2.13}$$

Using the Taylor development for the geometric series $\frac{1}{1 \pm \frac{x}{d_0}}$ and considering that the displacement $x$ is much smaller than the gap between the electrodes $d_0$, one can find that the overall capacitance variation is proportional to x as:

$$\Delta C = \Delta C_p + \Delta C_n \approx \frac{2\varepsilon A}{d_0} \times \frac{x}{d_0} \tag{2.14}$$

However, the relationship (2.14) is only an approximation and the capacitance variation $\Delta C$ is only proportional to the MEMS displacement within a limited range of operation where $\frac{x}{d_0} \ll 1$. Figure 2.3 illustrates the capacitance variation of a transducer with a sensitivity of $4.5 fF/g$ (or 15.45 $nm/g$) when the extern acceleration varies from $0g$ to $50g$. The linear region of operation is limited to 38.8% of the total acceleration variation interval.

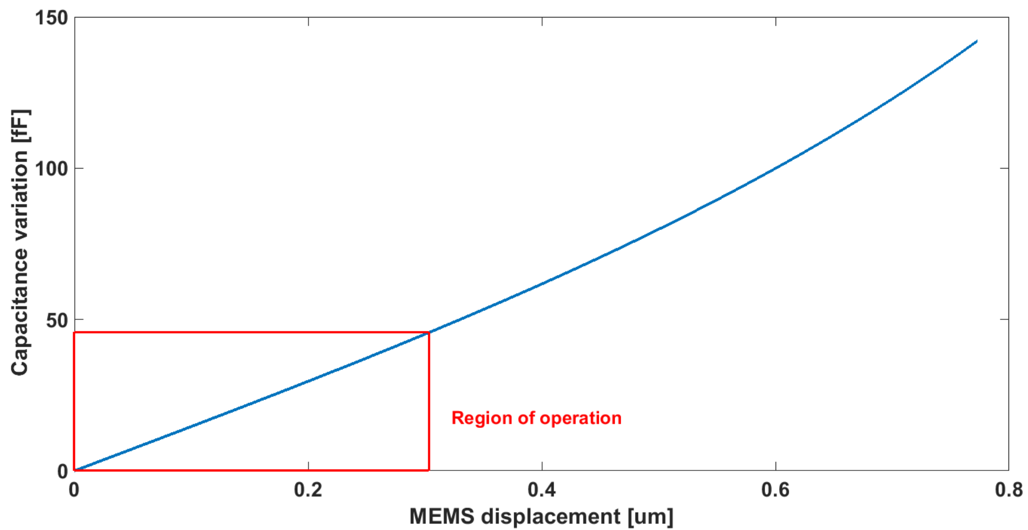


Figure 2.3 Capacitance variation dependency on MEMS displacement and the linear region of operation (highlighted in red)

In addition to the nonlinear capacitance, when the displacement is increasing the sensor can experience the spring softening effect, further explained.

## 2.3 Electrostatic actuation

During the past years, high performances micro actuators have been developed and integrated in many domains as the automotive industry or in biomedical applications [Park, 2011]. Several actuation mechanisms have been heavily researched due to the easiness they can be used within typical MEMS technologies and will be next be presented.

The electromagnetic actuation uses a ferromagnetic material to displace the microactuator [Iseki, 2006] and even if provides the highest displacement comparing with the others actuation methods, has a complicated fabrication process and consumes high power. The piezoelectric actuation occurs when an electric field is applied across a piezoelectric material [Robbins, 1991]. It consumes lower power and has a good linearity [Seo, 2005]. Another method is the electrothermal actuation that uses the expansion of some solids or fluids under the temperature effect to move the microactuator. The electrothermal actuation has a simple fabrication method but very slow responses times [Atre, 2006].

### 2.3.1 Electrostatic actuation mechanism

Finally, the electrostatic actuation uses the attraction force (e.g. electrostatic force) between two oppositely charged plates when a voltage $V$ is applied across them to displace the microactuator. The main advantages of the electrostatic actuation are the possibility to design both the sensing and microactuator device using typical CMOS and MEMS technologies, the low power consumption and also the high speed since it is based on the capacitors charge-discharge mechanism. The drawbacks are that the electrostatic force is inversely proportional to the square of the actuator displacement which leads to large force value only when the distance is small and a limited operation range due to the spring softening effect when high actuation voltage is applied resulting in nonlinear forces.

To find the electrostatic force $F_{el}$ expression, one has to consider the energy $E$ stored in the capacitance that exists between the two oppositely charged plates:

$$\mathrm{E} = \frac{1}{2}CV^2 = \frac{1}{2}\frac{\varepsilon A}{d}V^2 \tag{2.15}$$

$$F_{el} = \frac{\partial E}{\partial d} = -\,\frac{1}{2}\frac{\varepsilon A}{d^2}V^2 \tag{2.16}$$

The electrostatic actuation is also the most popular actuation method due to the diversity of the control techniques that can be used to implement the actuation. Conventional electrostatic actuation uses voltage and charge control [Seeger, 2003] but a combination of the voltage control with a feedback capacitor can also be considered [Chan, 2000], [Maithripala, 2003]. Further, more recent research works proved the efficiency of a parallel plate actuator driven by a resonant circuit [Kyynäräinen, 2001], [Cagdaser, 2005].

### 2.3.2 Static Pull-in voltage

The voltage controlled electrostatic actuation consists in generating an electrostatic force when a voltage is applied on microactuator plates. When the potential difference between the plates of the actuator increases, the electrostatic force also increases until it reaches a certain linearity limit, often called in the literature pull-in voltage [Chowdhury, 2003]. The dynamics and the nonlinearity sources for a single electrode motion structure with voltage control electrostatic actuation will next be derived.

Figure 2.4 shows a drawing of such a structure where $F_{el}$ is the electrostatic force and $F_s = kx$ is the spring force. When no acceleration is applied to the structure along the sensing direction, the system can be modeled using the equation (2.17).

$$m\ddot{x} + b\dot{x} + kx = F_{el} \tag{2.17}$$

However $\ddot{x}$ and $\dot{x}$ are null since no acceleration is applied. Hence, only the two opposite direction forces: $F_{el}$ and $F_s$ have to be considered. Equation (2.17) becomes:

$$kx = F_{el} \tag{2.18}$$

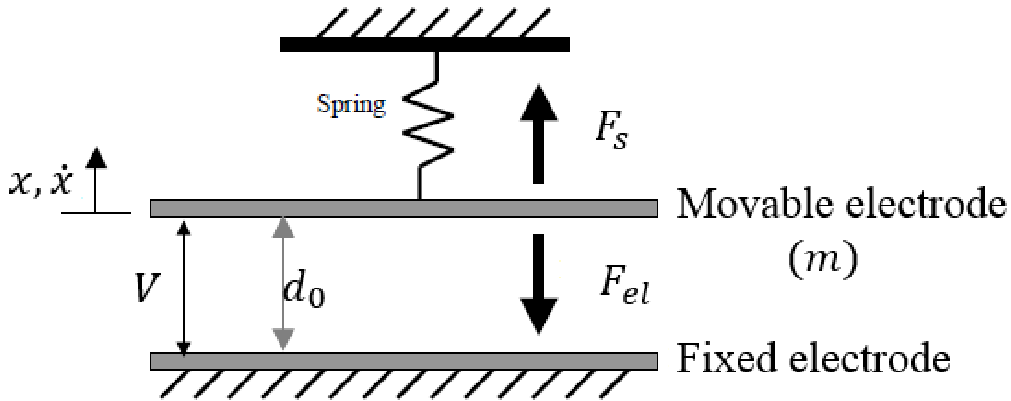


Figure 2.4 An illustration of a single electrode motion structure

Under the effect of the two forces, the movable electrode deflects from its neutral position by a certain displacement $x$.When the voltage $V$ is slowly increased, the system will stay stable until the movable electrode reaches the displacement value $x = x_0$ beyond which the system converges into an unstable equilibrium point. The voltage at which the instability occurs is called the pull-in voltage $V_{pi}$.

$$kx_0 = \frac{1}{2}\frac{\varepsilon A}{(d_0 - x_0)^2}V^2 \tag{2.19}$$

By solving the equation (2.19), the displacement stability limit $x_0$ and the pull-in voltage can be found:

$$x_0 = \frac{d_0}{3}; \quad V_{pi} = \sqrt{\frac{8kd_0^3}{27\varepsilon A}} \tag{2.20}$$

When the voltage $V$ is equal or greater than $V_{pi}$, the movable electrode snaps into contact with the fixed electrode. This happens because the electrostatic force is larger than the spring force. Therefore, for an open-loop architecture, with no control over the proof mass movement, the transducer has a limited linear range of operation reached once the displacement closes $x_0$. Several methods have been investigated to increase the linear range of operation [Seeger, 1997], [Chan, 2000], however they usually need higher operating voltage.

### 2.3.3 Spring softening effect

Another nonlinear effect that appears in capacitive MEMS sensors is the spring softening effect [Mukherjee, 2011] and consists in slightly modifying the spring mechanical constant $k$ due to the second order components of the electrostatic force. Hence, the spring softening effect leads to a sensitivity and resonance frequency alteration.

Equation (2.19) can be rewritten as:

$$kx = \frac{\varepsilon A}{2d_0^2}\frac{1}{(1-\frac{x}{d_0})^2}V^2 \qquad (2.21)$$

Where $x$ is the proof mass displacement under the effect of the electrostatic force.

After developing the series $\frac{1}{(1-\frac{x}{d_0})^2}$ using the Taylor relationship, the overall net force applied to the transducer becomes:

$$\Delta F = kx - \frac{\varepsilon A}{2d_0^2}V^2(1+\frac{2x}{d_0}) \qquad (2.22)$$

$$\Delta F = x\left(k - \frac{\varepsilon A V^2}{d_0^3}\right) + \frac{\varepsilon A}{2d_0^2}V^2 \qquad (2.23)$$

It can be noticed from equation (2.22) that the mechanical constant $k$ is decreased by a term called $k_{soft} = \frac{\varepsilon A V^2}{d_0^3}$.

Depending on the actuation voltage and on the gap between electrodes, the spring softening constant can slightly influence the sensitivity and the resonance pulsation:

$$\omega_{res} = \sqrt{\frac{1}{m}(k - k_{soft})} \qquad (2.24)$$

$$S = \frac{m}{k-k_{soft}} \qquad (2.25)$$

The spring softening effect appears also in a three-plate structure electrostatically actuated [Xie, 2003] since the spring softening constant results from the second-order terms of the electrostatic force. Figure 2.5 shows such a structure where $V_0$ is the actuation voltage and $V_x$ the voltage applied on the movable electrode. The difference of the two electrostatic forces applied on

the movable electrode $F_1$ and $F_2$ is approximately null if considering the displacement $x$ very small compared to the gap $d$.

However, if the second order terms are taken into account, one can observe:

$$F_2 - F_1 = \frac{\varepsilon A V_0^2}{2}\left[\frac{1}{(d_0+x)^2} - \frac{1}{(d_0-x)^2}\right] \cong -\frac{2\varepsilon A V_0^2}{d^3}x \quad (2.26)$$

In this case, the spring softening constant is $k_{soft} = \frac{2\varepsilon A V_0^2}{d_0^3}$, which is twice the softening constant for the single electrode motion structure.

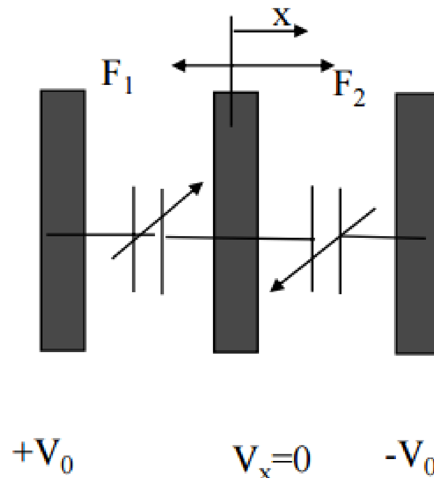


Figure 2.5. An illustration of a three-plate capacitive structure

## 2.4 CMOS Interface Circuits for Capacitive MEMS Accelerometers

The capacitance variation induced by the external acceleration, can be converted into an electrical signal using several techniques and capacitive sensing circuit architectures. They can be switched-capacitor or continuous time techniques but also open-loop or closed-loop interfaces [Borovic, 2005].

A closed-loop operation and a control system, even if optional in several situations and implemented only to increase performances and reduce nonlinearities, can be mandatory if the accelerometer sensor is operating in a low-vacuum cavity to reduce oscillations. The electrical signal at the front-end stage output can then be subject to analog filtering, noise-reduction techniques or other signal processing operations. Depending on the applications, both digital and analog output accelerometers have advantages therefore an ADC can be sometimes added at the output. Figure 2.6 illustrates the block diagram of a closed-loop MEMS accelerometer.

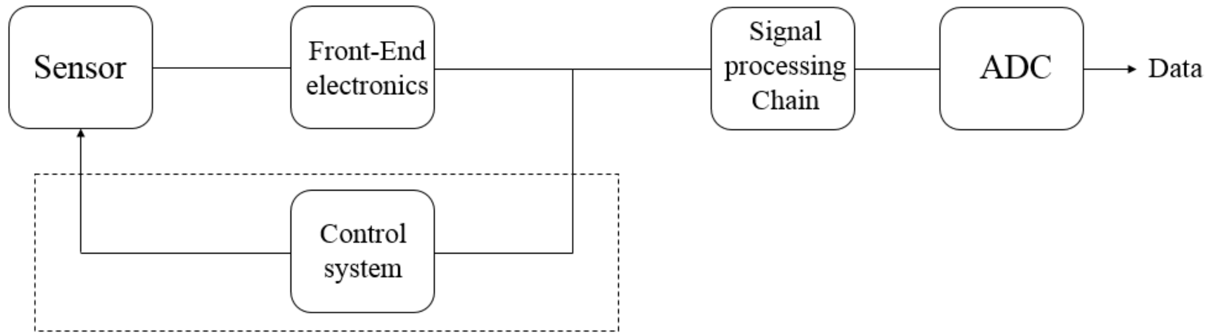


Figure 2.6 Conceptual block diagram of a closed-loop MEMS accelerometer

Noise and offset reduction techniques, as the autozero, the correlated double-sampling (CDS) and the Chopper Stabilization are often used for both topologies, open-loop and closed-loop, to improve the performances.

Open-loop architectures are usually easier to implement than the closed-loop due to less stability issues. In addition, open-loop interfaces are ratiometric since their output is directly proportional to the circuit reference. A switched-capacitor hybrid implementation using an open-loop read-out circuit and a force-feedback control system can be a trade off between the open-loop and the closed-loop accelerometers capacitive sensing circuits [Yucetas, 2012]. A literature summary and overview of all these different architectures will be presented in the following subsections.

### 2.4.1 Open-loop capacitive architectures for MEMS accelerometers

Open-loop architectures are usually chosen when no additional control is required over the sensor properties. Depending on the circuit specifications, the capacitance variation is measured using a single ended or fully-differential amplifier, that can be implemented either using a continuous-time voltage (CTV), a continuous-time current (CTC) or a discrete-time switching capacitor (SC) sensing technique. The SC technique has larger switching noise than continuous-time (CT) circuits; the noise sources for the SC circuits are: the thermal noise of the MOS on-resistances, the sampling noise (the $kT/C$ noise of the MOS switches) and also the noise folded by a sampled system. On the other hand, switched-capacitors architecture consumes usually lower power.

In [Wu, 2004] an open-loop topology with continuous-time voltage sensing, able to detect ultra-small capacitances is presented. The capacitance variation can be as low as $0.4\ fF/g$ thus the Chopper stabilization technique is used to minimize the sensing amplifier non-ideal effects.

Another open-loop architecture, but using a switched-capacitor technique, was developed by Paavola [Paavola, 2007]. Comparing with the system presented in [Wu, 2004] that can measure one single axis of acceleration, the circuit designed by Paavola is able to measure 3-axis of accelerations: $x, y$ and $z$. Hence the transducer comprises four masses and eight fixed-electrodes. The four capacitances between the proof masses and the fixed-electrodes will change their values when an acceleration occurs and will be read-out using a time-multiplexed sampling technique.

The choice of a switched-capacitor open-loop topology relies on power consumption as well as on the silicon area constraints. However, to compensate the electrostatic forces nonlinearities of an open-loop interface, a self-balancing bridge is implemented in the first stage of the front-end. This technique consists in biasing the sensor middle plate with a voltage updated constantly so that the charges flowing between the two fixed-electrodes and the mass, are equal on each side. Chopper stabilization and Correlated double sampling [Enz, 1996] are enabled to reduce the noise.

The two circuits mentioned above are analog open-loop interfaces. However, a digital ΣΔ open-loop architecture can also be used and was presented by Amini and Ayazi [Amini, 2004]. Figure 2.7 shows the overall input-output block diagram. The one mass full-differential transducer allows the integration within a full-differential front-end composed by a switched-capacitor (SC) charge amplifier. The back-end consists in an Anti-Aliasing-Filter (AAF), that filters the signal higher frequency components to avoid aliasing, and the SC modulator block. When the SC modulator is directly connected to the transducer ([Kulah, 2003a], [Jiangfeng, 2002], [Kajita, 2000]), the sensor capacitance directly influences the circuit performances. The advantage of this architecture, where the sensor and the SC modulator are separated by the charge amplifier [Amini, 2004], is that the front-end clock frequency is low, while the back-end stages can be clocked at a higher frequency to reduce the quantization noise.

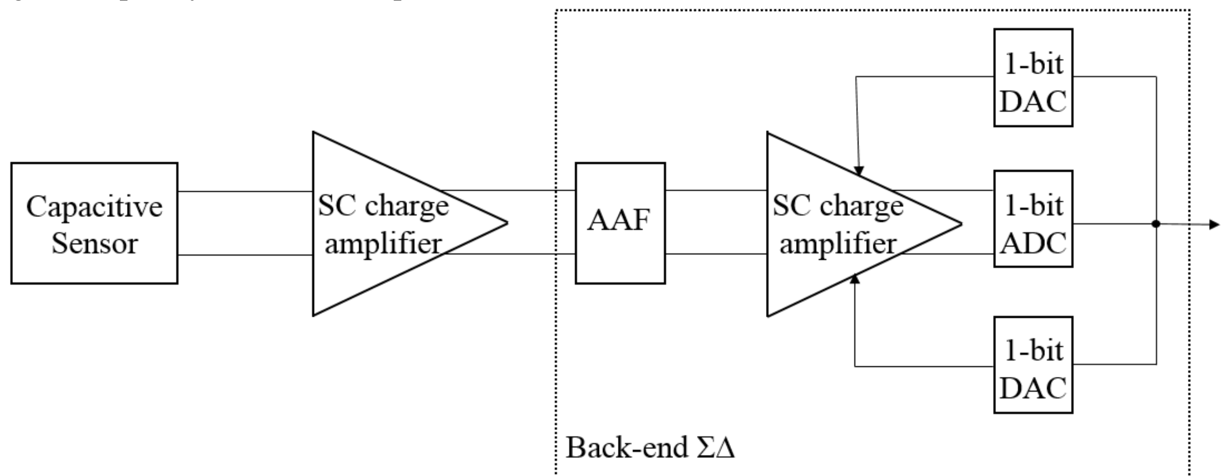


Figure 2.7 Block diagram of the open-loop digital ΣΔ interface [Amini, 2004]

Another open-loop architecture that implements Chopper stabilization and targets micro-gravity resolution applications, as GPS inertial navigation and sub atomic distances measurement systems, was presented in [Zhao, 2008].

The sensor is a one-axis fully differential MEMS accelerometer designed in a SOI technology. In this work, to achieve high resolution, the differential input stage transistors noise issue is addressed since in an open-loop system and at low frequency, the overall accelerometer performances are limited by the Flicker noise of the input transistors.

Lateral bipolar PNP transistors are used for the input pair of the first stage differential OTA amplifier due to their good matching, high transconductance and low Flicker noise. Moreover, they are fully compatible with conventional, low cost CMOS process [Zhao, 2009].

A more recent publication [Matteis, 2015] presents a low power continuous-time interface for a 3-axis capacitive accelerometer that includes a 10-bit Successive-Approximation-Register (SAR) ADC. Since the transducer has a large sensitive area, which results in large leakage currents (in the order of $pA$) that can saturate the analog-front-end first stage when it is DC coupled to the MEMS, an AC-coupling topology is implemented.

Table 2.1 summarizes the performances of the open-loop capacitive accelerometers architectures previously mentioned. Depending on the targeted application and circuit specifications, both continuous-time and switched-capacitors techniques can be used: CT systems have lower noise floors while switched-capacitor circuits consume less power. Another important aspect to be taken in consideration is either the circuit is designed to measure one or several degrees of freedom; in some situations, a 3-axis accelerometer will consume more power than a single-axis circuit because it can contain more blocks.

| Reference | Topology | CMOS technology/ chip area | Supply voltage/ input range | Power | Dynamic range/ Bandwidth |
|---|---|---|---|---|---|
| [Amini, 2004] | Open loop-SC | $0.25\ \mu m/2\ mm^2$ | $2.5\ V/\pm 2g$ | $6\ mW$ | $85\ dB/75\ Hz$ |
| [Wu, 2004] | Open loop-CT | $0.5\ \mu m/$ $8.75\ mm^2$ | $5\ V/\pm 6g$ | $30\ mW$ | $N/A$ |
| [Paavola, 2007] | Open loop-SC | $0.13\ \mu m/$ $0.5\ mm^2$ | $1.8\ V/\pm 4g$ | $113\mu W$ | $65\ dB$ $/100\ Hz$ |
| [Zhao, 2008] | Open loop-SC | $0.6\ \mu m/0.5\ mm^2$ | $3\ V/\pm 18g$ | $3.75\ mW$ | $105\ dB/3\ Hz$ |
| [Matteis, 2015] | Open loop-CT | $0.13\ \mu m/$ $1.24mm^2$ | $1.2\ V/N/A$ | $90\ \mu W$ | $66\ dB/4\ kHz$ |

Table 2.1 Performances summary of different open-loop topologies published in the literature

### 2.4.2 Closed-loop capacitive architectures for MEMS accelerometers

A capacitive MEMS accelerometer can also be driven using a closed-loop operation. A closed-loop implementation usually requires special attention to insure stability, and control knowledge to implement the feedback that can be relatively complicated if higher precision is targeted.

The accelerometers are often closed-loop controlled if the sensor cavity has a low-level vacuum pressure and the mechanical sensing element need to be damped prior to measurement; the high-Q packaging requires electrical artificial damping to limit the proof mass displacement that can oscillate and stick to the fixed electrodes. Furthermore, a closed-loop operation also overcomes the "pull-in" effect of the electrostatic force.

For the capacitive MEMS accelerometers, to improve the performances, two different directions have been followed lately: the first one is to optimize the mechanical sensing element design and to adopt a rudimental electronics interface, or the second one, to design a best-in-class

circuit interface for a given mechanical sensor performances. Therefore, one of the advantages of a closed-loop MEMS accelerometer is the control over the transducer properties (damping, bandwidth) due to the interaction between the sensor element and the interface performances.

The accelerometer sensor is a continuous time system but the controller can be either continuous-time or discrete-time resulting in a hybrid architecture which requires the same control method technique. In this case, if the controller sampling frequency is much higher than the signal bandwidth, the controller can be approximated to a continuous time system or contrary, the transducer must be sampled to the controller frequency. However, it can happen that the controller and the sampled transducer are functioning at different rates and the system is then called a multi-rate digital controller [Lee, 2006].

A reference paper in the literature is the work presented by Kraft [Kraft, 1998] which describes the two main closed-loop approaches for the MEMS accelerometer interfaces that can be either analog or digital. Digital closed interfaces usually refer to ΣΔ architectures while analog closed interfaces implement electrostatic damping. The research carried out in the domain and the measurement results showed good performances for each architecture but also revealed the analog transducer linearity limitation and the complexity that a higher order ΣΔ modulator requires. These are the two major topics further addressed in the specialty literature.

As for the digital transducer implementation, a ΣΔ converter modulator is placed in the feedback path. One sampling period consists in a sensing phase and a reset phase during which a feedback force is applied on the mass and nulls its displacement even for large input signals; the control system output is a digital signal. Figure 2.8 shows the general block diagram of an $nth$ order ΣΔ closed-loop accelerometer: the sensor is a second order integrator and its output is a capacitance variation measured by the analog front-end. Then, a number of integrators can be placed in the loop to implement a higher order modulation and to increase the performances. When the front end stage is directly connected to the quantizer, the noise in the comparator input is increased and so is the comparator's output quantization noise which can't be overcome by oversampling. Based on the comparator decision, a voltage will be applied on the sensor electrodes and will generate an electrostatic force in the opposite direction of the initial mass displacement. This way, the sensor is maintained in its equilibrium position and the digital output contains the information on the force that is required to keep the mass in the neutral position.

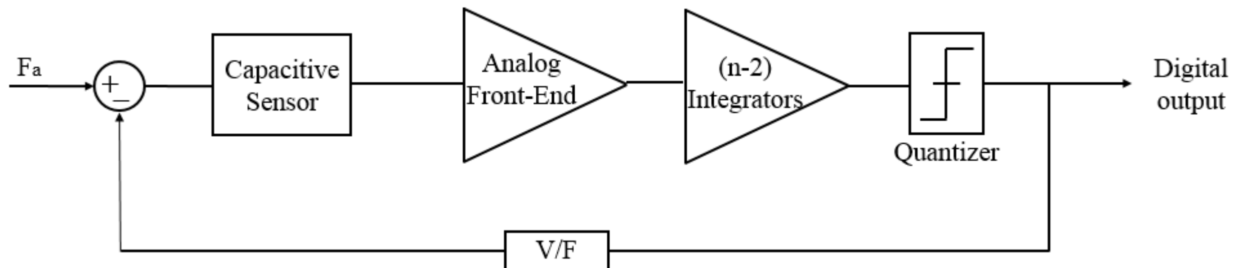


Figure 2.8 Block diagram of an nth order ΣΔ digital closed-loop accelerometer

Petkov and Boser presented a fourth-order ΣΔ architecture [Petkov, 2005] for a surface micromachined sensor; authors claim to achieve a noise floor of $150\ \mu g/\sqrt{Hz}$ and showed that the contribution of the quantization noise is negligible. The motivation of a higher-order ΣΔ

modulation is to decrease the quantization noise which is generally much larger than the analog-front end electronic noise [Kulah, 2006]. Comparing with a second order ΣΔ capacitive accelerometer ([Lu, 1995], [Lemkin, 1999], [Jiang, 2000], [Kulah, 2002]) that uses only the second-order sensor element as loop-filter, this work presents a single-loop high-order ΣΔ architecture, based on two integrators with feedforward summation.

A higher-order ΣΔ modulator for a closed-loop accelerometer was also reported by Chen [Chen, 2014]. The sensor has a low vacuum packaging which allows the co-integration within a gyroscope but requires a method to reduce the settling times and the ringing. The configuration proposed in this paper has the second order mechanical sensing element part of the loop, four electronic integrators cascaded in the multi-feedback loops and a quantizer block, which results in a sixth-order ΣΔ continuous time interface. The system output is digitalized and there is no need for an additional ADC. However, here, separate electrodes for the sensing and for the feedback are used to enable the design of a damping system that can reduce the oscillations due to vacuum packaging.

Another closed-loop, most recent, ΣΔ interface for a high Q capacitive surface micromachined sensor was reported by Xu [Xu, 2015]. $\text{Sub} - \mu g -$ resolution is obtained implementing the switching-capacitor technique and increasing the ΣΔ modulator order to three, resulting in an overall fifth-order system. The transducer does not have dedicated electrodes for the force feedback phase during which the sensor is damped, thus a time-multiplexing chronogram was conceived. Low-noise design techniques, as the CDS, have been used for the analog-front-end. Similar ΣΔ modulator interfaces with high performances can be found in the literature [Paavola, 2009], [Pastre, 2009], [Lang, 1999], [Lajevardi, 2012], [Petkov, 2014], [Wang, 2015], however, the main drawbacks of the digital loops remain the power consumption caused by the system complexity and the stability issue. Additionally, for a multiples degrees of freedom sensor, the ΣΔ interface can be used only if the movable electrode is not shared between several axes.

Furthermore, regarding the analog closed loop interfaces for capacitive accelerometers, the research interest has been concentrated around the electrostatic forces linearity for a higher input dynamic range but also the control over the sensor properties when low-vacuum operation is required. High resolution and low power applications can also be targeted with an analog loop implementation.

Considering now the analog transducer presented in Figure 2.9, when functioning in closed-loop, two electrostatic forces will be superimposed on the proof mass, to provide a linear operation. The net electrostatic force applied to the transducer is proportional to the output $V_{out}$ and to $V_B$ when the mass displacement is very small compared with the gap between the electrodes. To increase the linear operation range a higher DC voltage $V_B$ can be applied. The electrostatic damping principle will be detailed in the next chapter.

Analog closed-loop interfaces can also be continuous-time [Aaltonen, 2007] or switched-capacitors circuits [Yin, 2009], [Zhao, 2016]. In [Aaltonen, 2007] a proportional-integrator-derivative (PID) control block is used to damp the high Q transducer. Techniques as CDS or the use of n-type bipolar transistors for the input of the analog front-end first stage can be used for noise considerations.

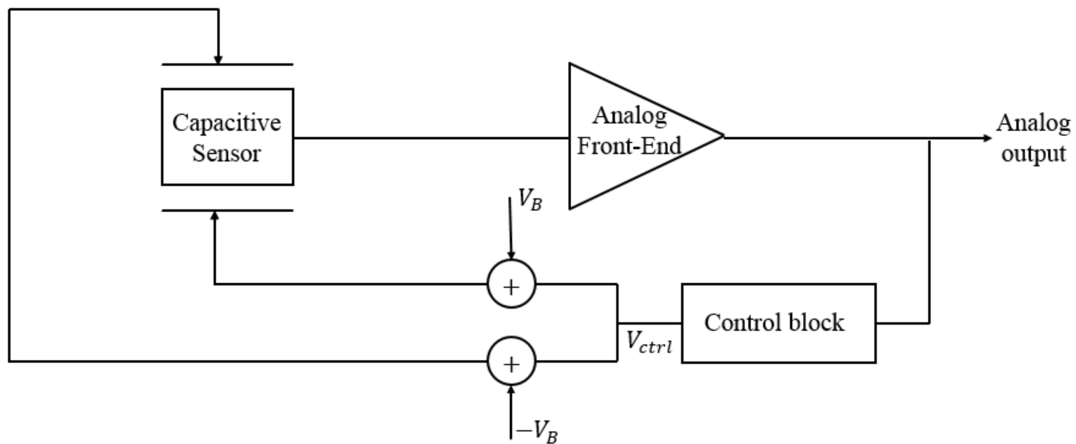


Figure 2.9 Block diagram of an analogue closed-loop accelerometer

For the analog closed-loop interfaces, the controllers are usually P.I.D. (Proportional Integral Derivative) blocks [Bose, 2014] but also P.D. architectures [Yucetas, 2010]. A P.I.D. controller nulls the proof mass displacement and implements a force-feedback system. On the other hand, the P.D. controller not only damps the sensor but will also change the system mechanical bandwidth by modifying the mechanical spring constant. Equations (2.27) resumes a P.D. continuous time controller transfer function and in eq. (2.28) the overall sensor and control block equation is given:

$$V_{ctrl}(t) = k_p x(t) + k_d \dot{x}(t) \tag{2.27}$$

$$ma(t) = m\ddot{x}(t) + (b + k_d)\dot{x}(t) + (k + k_p)x(t) \tag{2.28}$$

where $k_p$ and $k_d$ are controller design parameters. It can be noticed from eq. (2.28) that the damping factor $b$ as well as the spring constant $k$ values of the transducer are modified.

Another important aspect that must be considered for the control block design is where the feedback voltage will be applied. In [Yucetas, 2012] and [Ye, 2013], the control voltage is applied on the movable electrode (proof mass) since the chip senses only one axis of acceleration. Sometimes, the transducer design imposes the application of the feedback voltage on the fixed electrodes if the proof mass is shared between several axes and if the first stage of the front-end is also shared between multiple axes.

Using the electrostatic damping, the oscillations caused by the underdamped mechanical sensor can be reduced by enabling a control scheme which decreases the system settling time and provide full-control over the MEMS dynamic range. For carefully choosing the controller design parameters, s-domain, z-domain or state-space representations can be used to model the system [Tingting, 2012].

## 2.5 Summary

This chapter resumed the physics of the capacitive sensor as well as the electrostatic actuation mechanism and its associated nonlinearities. It was highlighted the importance of the mathematical modeling of each block, part of the CMOS MEMS accelerometer system.

The mechanical sensing element can be modeled using the second-order mass spring damper transfer function. The continuous-time model can then be transformed in a discrete-time system with a certain frequency rate if required. The mechanical damping ratio depends on the spring design and on the cavity pressure around the sensor. If the sensor is underdamped, it will start oscillating and in order to rapidly decrease the oscillations amplitude, the mechanical damping can be adjusted electrostatically.

The electrostatic actuation mechanism has been presented. The voltage applied across a charged capacitor will generate an electrostatic force which can be used to increase the mechanical damping. The electrostatic force has a second order dependency with the gap between the electrodes, the proof mass displacement and with the actuation voltage. The spring softening and the pull-in effect have been discussed. The pull-in effect can produce the snapping of the movable electrode onto the fixed plate if either the actuation voltage or the gap between the electrodes are not controlled; hence, the importance of the closed-loop systems.

Switched-capacitor, continuous time voltage or current techniques can be used for the capacitance read-out. Capacitive open-loop systems are easy to implement, they don't have stability issues and consume less power. Moreover, they have a ratiometric output. On the other hand, closed-loop systems can achieve larger signal bandwidth, high input range and higher linearity. Digital interfaces have the advantage of direct digitized data output while complex implementations. Analog interfaces are consuming less power but have linearity limitations. The main privilege of a closed-loop implementation is the artificial damping control which is highly recommended when the sensor is operating in high-vacuum cavity.

Table 2.2 presents a summary of the performances and architectures of the published capacitive MEMS accelerometers discussed in previous sections, where O refers to an open-loop architecture and C to a closed-loop architecture.

In next chapter, a novel closed-loop electrostatic damping architecture for a three-axis underdamped accelerometer will be presented. The system is a switched-capacitors discrete architecture with simultaneous electrostatic damping control. Matlab-Simulink models and z-Transform transfer functions have been developed for each block. Finally, a new approach to establish the system closed-loop transfer function and to study the stability is presented.

| Reference | Topology | CMOS technology/ chip area | Supply voltage/ input range | Power | Dynamic range/ Bandwidth |
|---|---|---|---|---|---|
| [Wu, 2004] | O | $0.5\ \mu m/$ $8.75\ mm^2$ | $5\ V/\pm 6g$ | $30\ mW$ | $N/A$ |
| [Amini, 2004] | O | $0.25\ \mu m/2\ mm^2$ | $2.5\ V/\pm 2g$ | $6\ mW$ | $85\ dB/75\ Hz$ |
| [Petkov, 2005] | C | $0.5\ \mu m/0.9\ mm^2$ | $5\ V/N/A$ | $13\ mW$ | $N/A$ |
| [Paavola, 2007] | O | $0.13\ \mu m/$ $0.5\ mm^2$ | $1.8\ V/\pm 4g$ | $113 \mu W$ | $65\ dB$ $/100\ Hz$ |
| [Aaltonen, 2007] | C | $0.7\ \mu m/16\ mm^2$ | $5\ V/\pm 1.5g$ | $0.24\ mW$ | $120\ dB$ $/300\ Hz$ |
| [Zhao, 2008] | O | $0.6\ \mu m/0.5\ mm^2$ | $3\ V/\pm 18g$ | $3.75\ mW$ | $105\ dB/3\ Hz$ |
| [Pastre, 2009] | C | $0.6 \mu m/9.7\ mm^2$ | $9\ V/\pm 11g$ | $12\ mW$ | $114\ dB$ $/300\ Hz$ |
| [Yin, 2009] | C | $2\ \mu m/15.2\ mm^2$ | $18\ V/\pm 15g$ | $N/A$ | $120\ dB/1\ Hz$ |
| [Sun, 2010] | O | $0.35\ \mu m/9\ mm^2$ | $N/$ $A/\pm 11.5g$ | $1\ mW$ | $95\ dB$ $/100\ Hz$ |
| [Yucetas, 2012] | C | $0.35\ \mu m/$ $6.66\ mm^2$ | $3.6\ V/$ $\pm 1.15g$ | $3.6\ mW$ | $91\ dB$ $/200\ Hz$ |
| [Ye, 2013] | C | $0.35\ \mu m/$ $0.5\ mm^2$ | $5\ V/\pm 1.2g$ | $58\ mW$ | $N/A$ |
| [Matteis, 2015] | O | $0.13\ \mu m/$ $1.24 mm^2$ | $1.2\ V/N/A$ | $90\ \mu W$ | $66\ dB/4\ kHz$ |
| [Xu, 2015] | C | $0.5\ \mu m/7.8\ mm^2$ | $7\ V/\pm 1.2g$ | $23 mW$ | $130\ dB/1\ Hz$ |
| [Zhao, 2016] | C | $0.35\ \mu m/$ $11.75\ mm^2$ | $15\ V/$ $3.3V/\pm 50g$ | $168\ mW/$ $6.97\ mW$ | $106.2\ dB$ $/200\ Hz$ |

Table 2.2 Performances summary of different accelerometer topologies published in the literature

From Table 2.2 two main conclusions can be stated: firstly, the closed-loop architectures consume more power since they have a more complex implementation than the open-loop circuits. Secondly, the closed-loop system has a higher dynamic range justified by the control over the sensor properties that a closed-loop operation provides. Therefore, for a closed-loop architecture imposed by the cavity level of vacuum, for example, the principal goal is the power consumption reduction by limiting the number of system blocks.

# CHAPTER 3

# THREE-AXIS HIGH-Q MEMS ACCELEROMETER WITH ELECTROSTATIC DAMPING CONTROL – MODELLING

To design a six-degree of freedom (6DOF) sensor for consumer electronics applications (e.g. inertial navigation), it would be interesting to co-integrate a three-axis accelerometer and a three-axis gyroscope within the same chip and the same low level vacuum cavity. The problems related to the accelerometer placement in a low-pressure cavity were shown in the previous chapter. Therefore, in this chapter, a new method based on a closed-loop accelerometer architecture is devised and presented in order to overcome the underdamped MEMS oscillation issue. The sensor control relies on the electrostatic damping principle by estimating the proof mass velocity and increasing the mechanical damping ratio. Here, the ΣΔ digital architecture can't be used because the proof mass is common to the three-axis and the movable electrode can't be maintained in the equilibrium position during the acceleration measurement phase.

Further, the circuit specifications require a low-power, low-cost and small area design. Hence, the analog front-end architecture and the electrostatic damping chronograms have to be optimally chosen. In order to define the architecture and to determine exhaustively all the variable design parameters, the system was modeled using Matlab-Simulink. Additionally, the overall closed-loop transfer function was found using an analytical model that required a block by block mathematical representation. Finally, the closed-loop transfer function was used to study the system stability.

This chapter presents the proposed new architecture, the sensor device, the analog front-end and the controller models, different methods for implementing the electrostatic damping for a 3-axis accelerometer and the efficiency of each method in terms of system settling time and sampling frequency. Finally, a novel approach that allows to study the multirate controller stability has been developed and applied in order to determine the design parameters of the 3-axis MEMS accelerometer for the CMOS implementation.

## 3.1 Introduction

The novel system architecture is presented in Figure 3.1. The sensor (MEMS) is a differential two masses three-axis accelerometer with two fixed plates per axis functioning in a high-level vacuum cavity. The fixed plates are often named excitation electrodes since they serve as excitation support during the acceleration measurement phase. The MEMS wafer has a cap-wafer used to seal the cavity and it is glass-fritted bonded with the ASIC wafer. The charge to voltage converter (C2V) is directly connected to the proof mass (movable electrode). In addition, the design specifications impose that the C2V is shared between the 3-axis and only one

acceleration direction can thus be measured at a time. During the measurement phase for an axis, no voltages (excitation or feedback) are allowed to be applied on the other axis fixed plates. Contrary to the C2V that is common to all the 3-axis, there are three different control units that implement the C2V output derivative, one for each axis, and that apply the required feedback voltage on the excitation plates at a specific predefined time during a certain period. It is clear then that the system is time-discretized and the sampling frequency can directly influence the loop performances. The sampling frequency as well as the derivative gain, are the two main design parameters that will be closely analyzed in this thesis since they play an important role in the damping efficiency and in the system stability. To estimate the damping efficiency, the settling time will be used as criteria. For this architecture, the settling time is defined as the time that is required by the C2V to reach the steady state and provide a valid measured acceleration value to the Signal Processing chain.

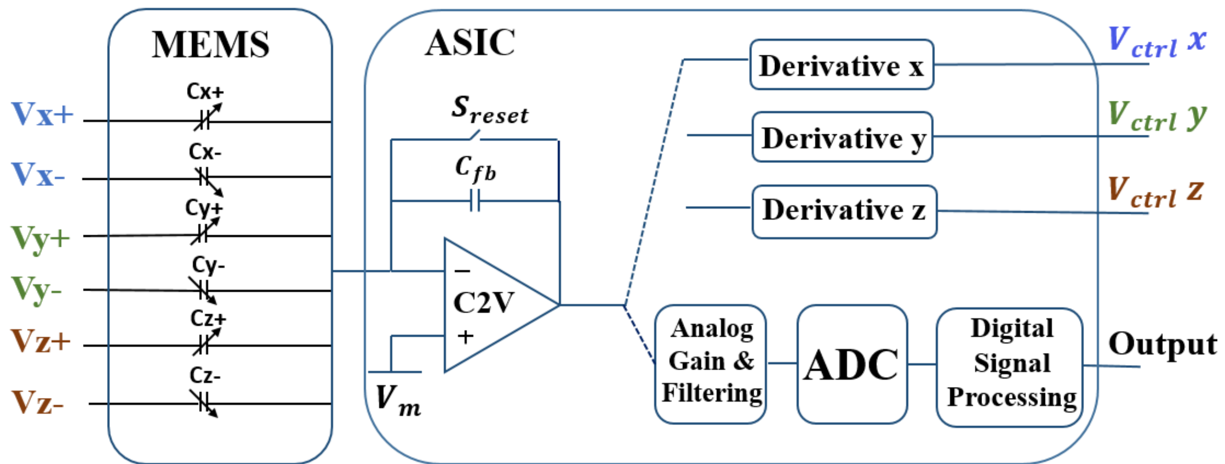


Figure 3.1. Three-axis closed-loop underdamped MEMS accelerometer with electrostatic damping control

## 3.2 Three-axis sensor element

This section presents in detail the structure, the Matlab-Simulink modeling and different mathematical representations in s and z-domains for the capacitive element sensor.

### 3.2.1 Sensor Design

As previously mentioned**,** the mechanical sensor element is able to sense accelerations along three-directions: $x$, $y$ and $z$. Translational motion laws apply to $x$ and $y$-axis while the $z$-axis can be described in terms of rotational dynamics. Figure 3.2. illustrates the three-axis sensor structure along with the C2V illustration.

To both reduce noise and to increase the sense area, the sensor structure comprises two proof masses thereby allowing the MEMS integration with a fully-differential CMOS interface. Nevertheless, for simplification reasons, one proof mass (red proof mass drawing in Fig. 3.2.) will be disregarded in the model, since the design is totally symmetric.

The proof masses are built on a substrate that can be biased through the $sh$ pad (shield bias). It is not desired to generate electrostatic forces between the shield and the proof mass, that may perturb the acceleration measurement, and hence the shield bias is usually kept the same as the proof mass bias. The design has also self-test capabilities ($st$ pad) which can be eventually used to test part of the circuit functions. Similarly, if the self-test is not enabled, the $st$ pad should be biased with the same voltage as the proof mass.

The pressure inside the MEMS cavity, obtained when sealing the MEMS-cap over the MEMS wafer, is a very high vacuum. The quality factor Q associated with this level of pressure is in the range of $1000 < Q < 3000$. Further models and simulations will be performed considering $Q = 2000$.

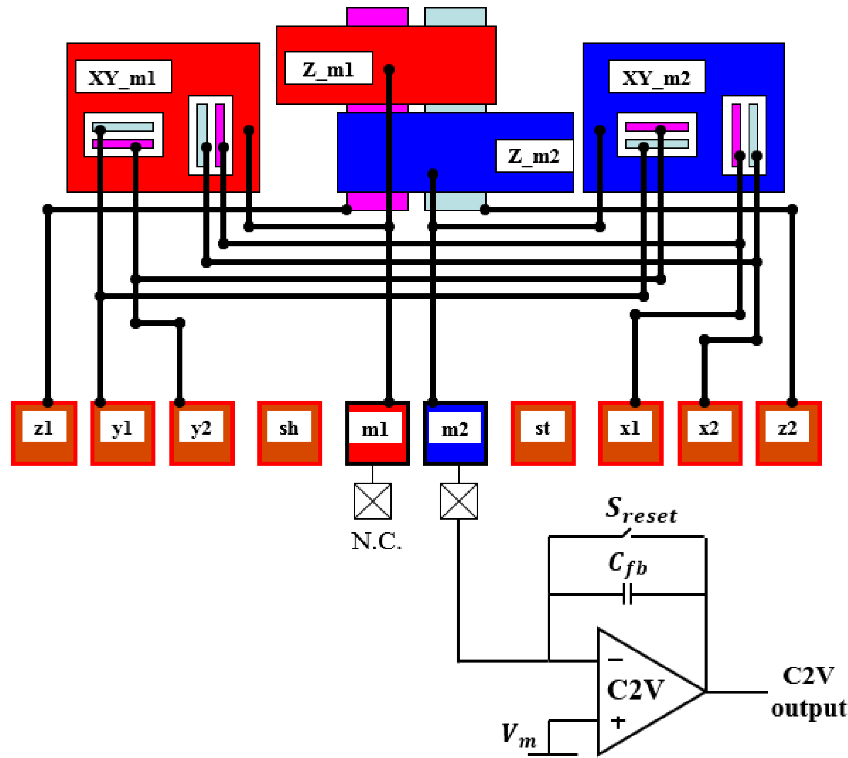


Figure 3.2. An illustration of the dual-mass three-axis differential accelerometer with self-test capabilities and the analog frond end block diagram

As it can be seen in Figure 3.2. there is no dedicated electrode for the electrostatic damping control and the fixed plates have to be shared between the measuring and the damping phase. The proof mass is also shared between the 3-axis which implies that only one amplifier can be connected to the $m2$ pad. This amplifier has two purposes: firstly, it allows to measure the capacitance variation due to the external acceleration applied to the transducer and to convert it into an electrical signal, and secondly to constantly bias the proof mass, through its feedback.

Table 3.1. resumes the transducer parameters where $1\text{g} = 1\text{m/s}^2$ is the gravitational acceleration. The characteristics differ from one axis to another due to process variations but also due to the different motion design for $x$, $y$ from $z$. Table 3.1. presents the nominal characteristics for $x$ and $y$-axis and as a second modeling simplification, it will be considered in the following

studies that the transducer parameters are identical for $x$, $y$ and $z$. For an underdamped second order system, the resonance frequency $f_r$ is calculated using the relationship (3.1) which leads to approximately the same value as $f_0$ hence, the transducer will have an oscillation frequency of $4\ kHz$.

$$f_r = f_0\sqrt{1-\left(\frac{1}{2Q}\right)^2} \tag{3.1}$$

| Sensitivity | $4.5\ fF/g$ (2 masses) |
|---|---|
| Mass of the proof mass $(m)$ | $5.52nkg$ |
| Spring constant $(k)$ | $3.5\ N/m$ |
| Natural frequency $(f_0)$ | $4.01kHz$ |
| Quality factor $(Q)$ | $2000$ |
| Sense area $(A)$ | $0.238\ mm^2$ |
| Sense gap $(d_0)$ | $1.7\ um$ |

Table 3.1. Nominal X, Y accelerometer transducer characteristics (Freescale Semiconductor, 2013)

Though in Table 3.1 the capacitance variation sensitivity is given, the sensor displacement sensitivity can also be calculated as:

$$Displacement\ Sensitivity = 9.8\frac{m}{k} = 15.45\ nm/g \tag{3.2}$$

The Brownian noise $(BN)$ of the transducer can be estimated using the parameters presented in Table 3.1 and the equation (3.3):

$$BN\left[g/\sqrt{Hz}\right] = \frac{1}{9.8}\sqrt{\frac{4k_B T\omega_0}{mQ}} \tag{3.3}$$

where $k_B$ is the Boltzmann constant ($k_B = 1.38e-23$), $T$ is the temperature in Kelvin, $\omega_0 = 2\pi f_0$ is the sensor natural pulsation, $m$ is the mass of the proof mass and $Q$ is the quality factor. Higher the quality factor is, lower the Brownian noise floor is. Usual accelerometers, not co-integrated with another sensor, have a pressure inside their cavities similar to the atmospheric pressure, which ensures a quality factor of 1 $(Q = 1)$. Table 3.2. presents a $BN$ comparison between two different sensors: an atmospheric accelerometer and a vacuum-packaged pressure accelerometer at a room temperature of 25℃. It clearly shows that the lower $BN$ is achieved by the underdamped accelerometer which is roughly 40 times smaller than for the damped transducer.

| $Q$ | $BN$ |
|---|---|
| 1 | $27.95\ \mu g/\sqrt{Hz}$ |
| 2000 | $0.625\ \mu g/\sqrt{Hz}$ |

Table 3.2. Brownian noise floor comparison between a damped and an underdamped MEMS accelerometer

### 3.2.2 Matlab-Simulink model and s-domain transfer function

In section 2.1, the accelerometer was modeled as a second order mass spring damper system. Applying the Newton second law to the system, one can write the equation (3.4) that describes the open-loop MEMS proof mass translational motion:

$$m\ddot{x}(t) + b\dot{x}(t) + kx(t) = ma_{ext}(t) \tag{3.4}$$

Equation (3.4) has been implemented in Simulink using two continuous time integrators because the external acceleration applied on the transducer has to be integrated twice to obtain the displacement $x$. In Figure 3.3. the continuous time Matlab-Simulink model of an open-loop accelerometer is presented.

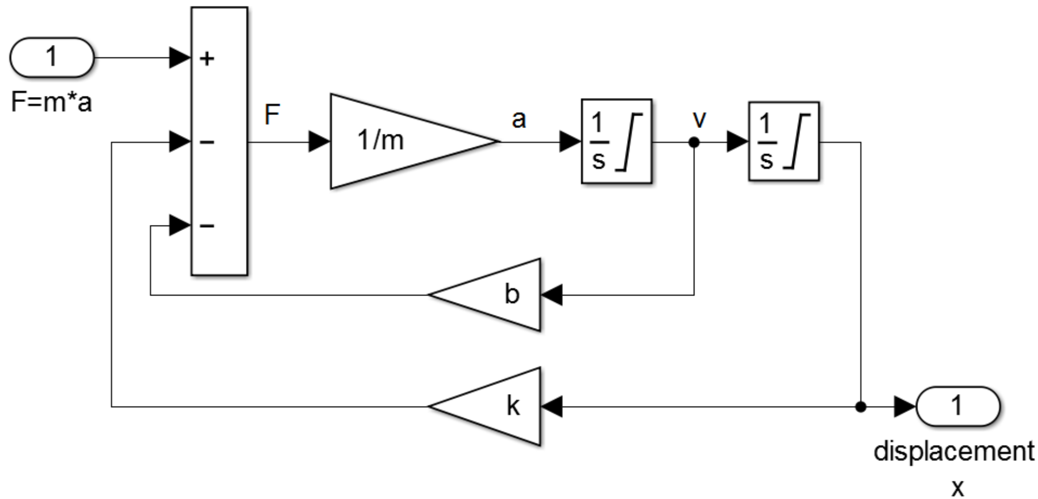


Figure 3.3 An illustration of the Simulink model for the open loop MEMS accelerometer

This model has an associated continuous-time transfer function between the acceleration force and the MEMS displacement given by the equation (3.5):

$$H_{MEMS(x \to F)}(s) = \frac{X(s)}{F_{ext}(s)} = \frac{1/m}{s^2 + \frac{b}{m}s + \frac{k}{m}} \tag{3.5}$$

By replacing (2.5) and (2.6) in (3.5), the mechanical element transfer function can also be written as:

$$H_{MEMS(x \to F)}(s) = \frac{X(s)}{F_{ext}(s)} = \frac{1}{k}\frac{\omega_0^2}{s^2 + \frac{\omega_0}{Q}s + \omega_0^2} \tag{3.6}$$

The continuous time model was simulated for different quality factor values in order to estimate the settling times when functioning in open-loop. Figure 3.4. shows the MEMS responses for a 1g input acceleration and a quality factor Q of (a) 1, (b) 50 and (c) 2000. In Table 3.3 the associated settling times are given. It can be noticed, as it was expected, that the settling time increases significantly when $Q$ increases.

Since the co-integration with the gyroscope sensor requires a high-quality factor, in the order of 2000 or higher, the accelerometer settling time becomes the main issue to be addressed.

| Q | Settling time $[ms]$ |
|---|---|
| 1 | 0.25 |
| 50 | 15 |
| 2000 | 350 |

Table 3.3. Open-loop settling times for different MEMS quality factors Q

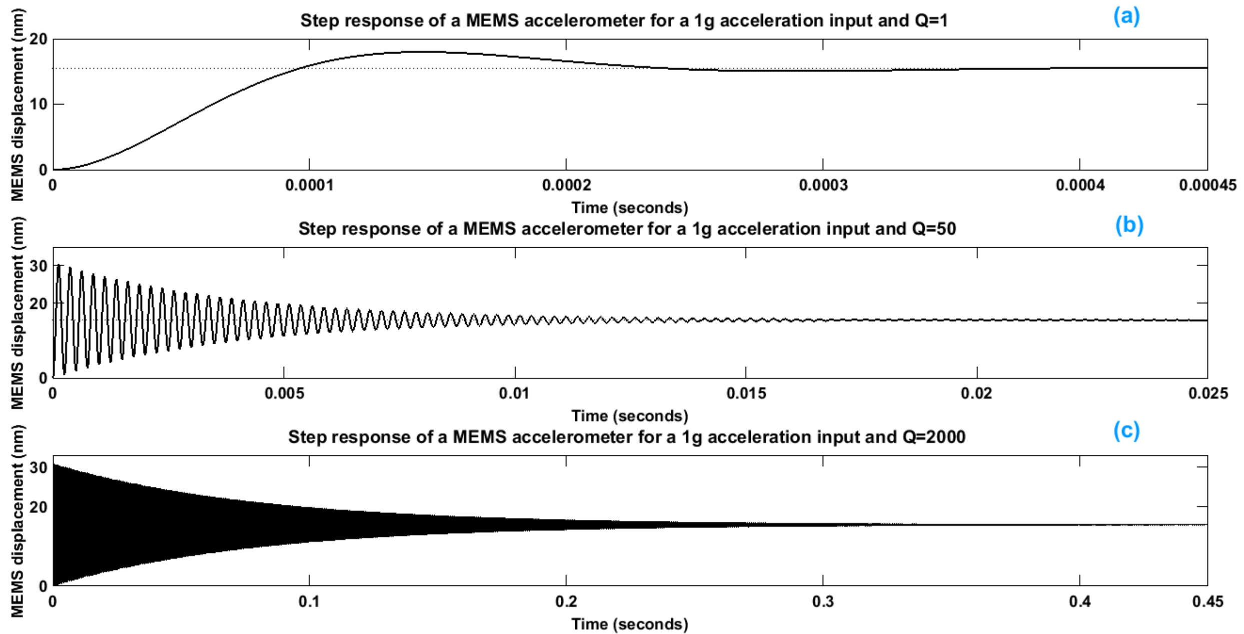


Figure 3.4. MEMS accelerometer response in open loop configuration to a 1g step acceleration for different quality factors: (a) Q=1, (b) Q=50 and (c) Q=2000

The second aspect to be taken into consideration is the oscillation amplitude. The proof mass is situated symmetrically between the fixed sensor fingers. As a result, under the effect of a sharp acceleration due to a shock for instance, the proof mass can oscillate with very large oscillation amplitude, which can ultimately lead to the destruction of the MEMS. For this reason, some transducer designs have stop-fingers that protect the sensors fixed plates.

Such a maximum oscillation amplitude can be derived for a high-Q MEMS accelerometer from its transfer function. This calculation is useful to estimate the signal that the first stage of the electronic interface will measure and how the first stage has to be designed in order not to be saturated by the proof mass large oscillation amplitude.

The maximum oscillation amplitude can be estimated from the MEMS step response (Figure 3.5) where $X_0$ is the steady-state displacement value and $X$ is the amplitude of the first oscillation.

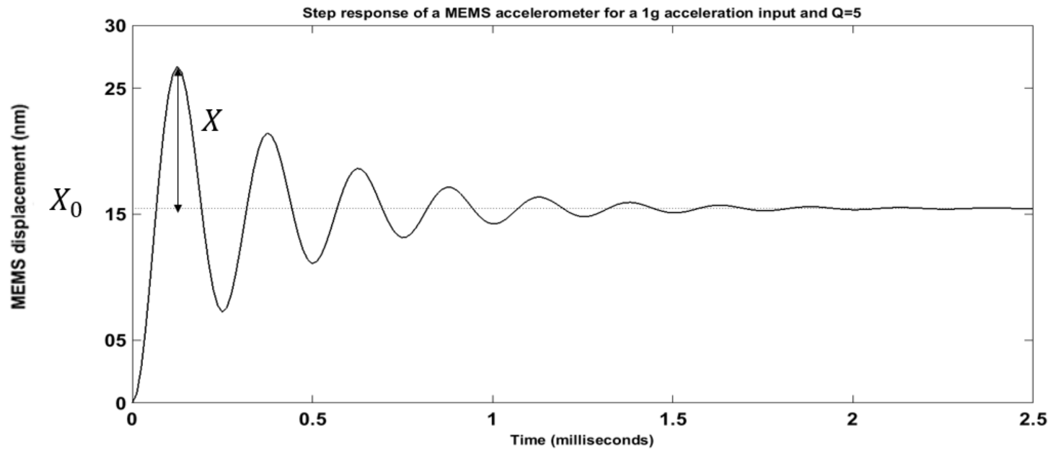


Figure 3.5 Step response of the open loop accelerometer for Q=5

In [San-Andres, 2015], it is shown that the ratio between $X$ and $X_0$ is:

$$\frac{X}{X_0} = e^{\frac{-\xi\pi}{\sqrt{1-\xi^2}}} \tag{3.7}$$

Where $\xi = \frac{1}{2Q}$.

The maximum oscillation value when $\xi \ll 1$ is:

$$X + X_0 = X_0\left(1 + e^{\frac{-\xi\pi}{\sqrt{1-\xi^2}}}\right) \cong 2X_0 \tag{3.8}$$

It can be concluded from (3.8) that for high-Q designs, the maximum oscillation is limited to twice the steady state displacement value thus the electronic interface will be designed in conformity.

The continuous time open-loop transfer function and model allow to estimate the settling time and the amount of signal that the electronic interface will have to deal with. As stated in section 3.1, the novel architecture proposed in this thesis is a discrete-time system and for a full input-to-output system modeling, the sensor continuous time model has to be transformed in a discrete-time model. The input-to-output discrete model is mandatory for the stability investigation of the closed-loop system. The MEMS discrete-time transfer function transformation will be explained in sub-section 3.2.3.

### 3.2.3 z-domain MEMS transfer function

Discrete-time systems often require discrete controllers or the discretization of existing continuous-time blocks. In this perspective, the transfer function transformation from s-domain to z-domain has been heavily researched over the past years [Cannon, 2014], [Tingting, 2012]. The s-to-z domain conversion usually uses an approximation method and the choice is usually based on both the sampling frequency and the transfer function to be converted since there are methods more efficient for certain filters. The most used s-to-z transformation methods are: the impulse invariant method, the Euler's approximation, the Tustin's method (bilinear approximation), the

matched Pole-Zero method (MPZ) and the modified matched pole-zero method (MMPZ) [Lian, 2010], [Doncescu, 2014].

For the MEMS continuous-time transfer function (3.6) the Euler approximation has firstly been used. If the continuous-time transfer function 3.6) has to be transformed in discrete-time system with a generic sampling period $T_s$, then (3.9) is the relationship between the s and the z domain when using the Euler approximation:

$$s \to \frac{z-1}{T_S} \tag{3.9}$$

The new discrete-time MEMS transfer function (TF) becomes:

$$H_{MEMS}(z) = \frac{1}{k}\frac{\gamma^2}{z^2+2z(\xi\gamma-1)+(1-2\xi\gamma+\gamma^2)} \tag{3.10}$$

Where $\gamma = \omega_0 T_S$.

The MEMS transfer function (3.10), obtained using the Euler approximation, has been implemented in Matlab and compared to the continuous-time behavior. Figure 3.6 shows the two waveforms for a transducer with $Q = 2000$ and the sampling frequency $f_s = 1/Ts = 30kHz$. The test sampling frequency was chosen accordingly with the system specifications that require a sampling frequency of $30\,kHz$ or thereabouts. In addition to the Shannon theorem, the discretization methods require also a sampling frequency 20 to 30 times higher than the system bandwidth to minimize the errors. It can be noticed from Figure 3.6 that the discretization doesn't fit the continuous-time model and this can be due to the fact that the ratio between the sampling and the signal frequencies is only 7.5.

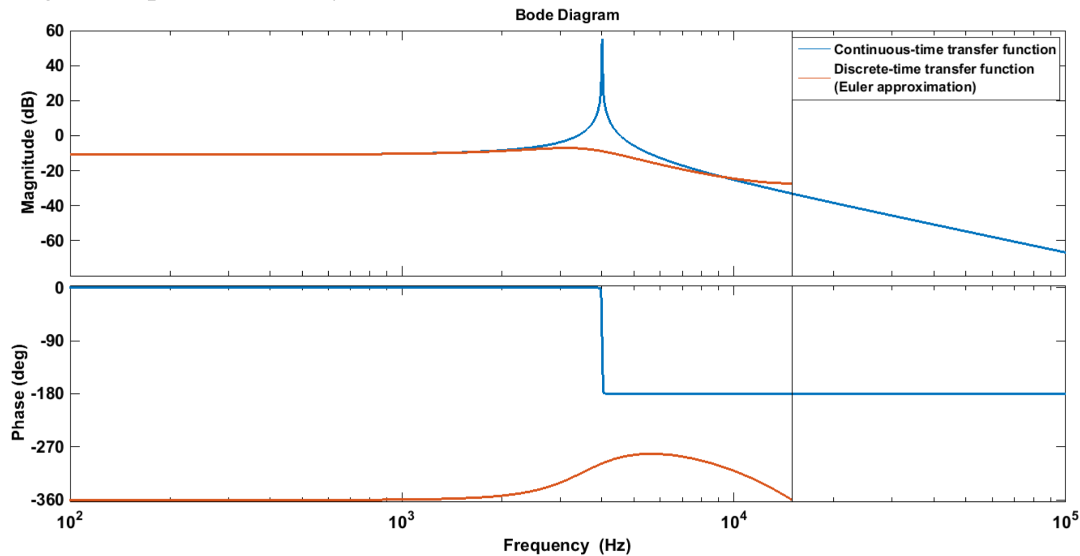


Figure 3.6 Bode plot of the continuous-time MEMS transfer function (blue) and the associated discrete-time Euler approximated TF (red) for $f_s = 30kHz$ and $Q = 2000$

Consequently, another discretization method will next be used for the MEMS transfer function. The Tustin's approximation is based on the frequency characteristic preservation [Roberts, 2006] and is often used for low-pass filters discretization.

For the Tustin method, the s-to-z conversion is done using the relationship (3.11):

$$s \rightarrow \frac{2}{T_s}\frac{1-z^{-1}}{1+z^{-1}} \tag{3.11}$$

The MEMS continuous-time transfer function (3.6) becomes:

$$H_{MEMS}(z) = \frac{1}{k}\frac{\gamma^2(1+z^2)}{z^2(\gamma^2+4\xi\gamma+4)+z(2\gamma^2-8)+(\gamma^2-1-4\xi\gamma+1)} \tag{3.12}$$

Figure 3.7 presents the simulation of the continuous and discrete-time models for the MEMS at the same sampling frequency $f_s = 30\ kHz$. It is clear that the waveforms fit better using the Tustin's approximation than using the Euler's one. Consequently the equation (3.12) will be kept for the MEMS discretization in this thesis.

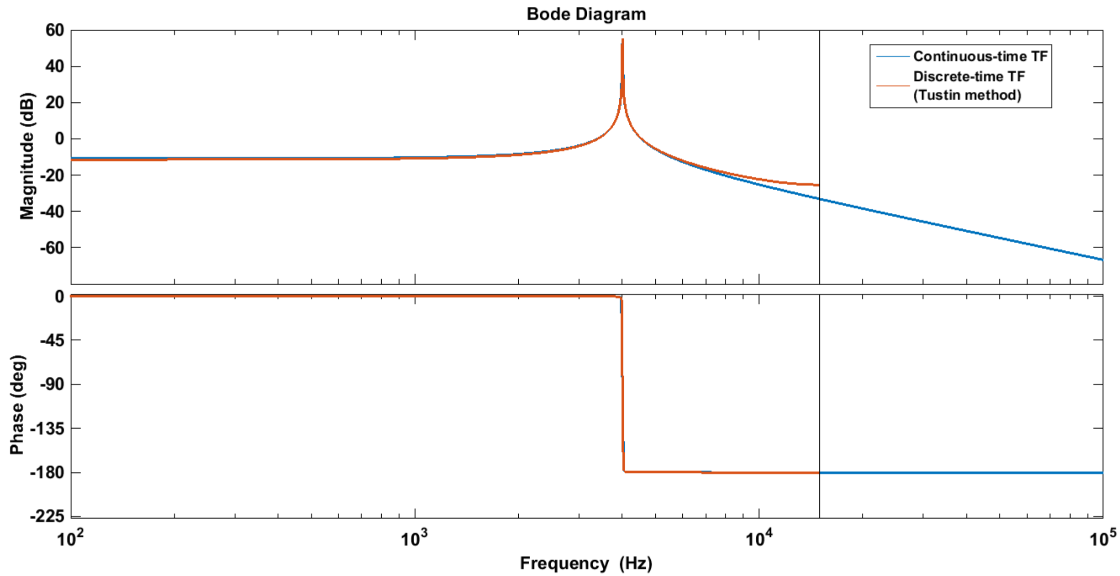


Figure 3.7 Bode plot of the continuous-time MEMS transfer function (blue) and the associated discrete-time Tustin approximated TF (red) for $f_s = 30kHz$ and $Q = 2000$

In this section, the three axis mechanical sensing element was described and its operation modeled. For design and stability considerations, the continuous-time transfer function is transformed in a discrete system with a certain sampling frequency. This approach will next be used to find the system closed-loop transfer function and to conclude on the stability.

## 3.3 Analog interface modeling: Charge-to-voltage amplifier

The analog front-end performances are critical aspects to consider in sensor design. Circuit noise generated in the front-end will dominate the sensor Signal-to-Noise Ratio (SNR) performance and the parasitic capacitances will result in an offset shift and non-linearities.

The Charge-to-Voltage (C2V) amplifier is the first stage of the AFE and its main role is to output an accurate amplified voltage that corresponds to the capacitance and charge variation caused by the external acceleration applied to the inertial transducer.

Depending on the mechanical sensing element design, the C2V can have a single-ended or a fully differential architecture. Further, for this specific design, as previously mentioned, the C2V is shared between the 3 axes since the movable electrode is common. The C2V must assure a constant voltage polarization on the sensor proof mass, during all phases and for the 3 axes, and this will mainly be possible due to the amplifier feedback.

The mechanical sensing element bandwidth is limited to $4\ kHz$ (Table 3.1). Consequently, the C2V amplifier must have a sampling frequency of at least $24\ kHz$ (Nyquist–Shannon sampling theorem).

In Figure 3.8, the block diagram of a single-ended capacitive sensing element with its AFE's first stage as well as with its chronograms, is shown. The C2V amplifier has basically two non-overlapping phases: Reset (1) and Integration (2). During the reset phase the feedback capacitor $C_{fb}$ is reset to zero when the switch $S_{reset}$ closes and the excitation signals $Ex_p$ and $Ex_n$ are equal to a $V_m$ DC bias. Then, during the integration phase the $S_{reset}$ switch opens and the charge variation from $C_1$ and $C_2$ is integrated by the feedback capacitor due the voltage step between $Ex_p$ and $Ex_n$. The voltage step between $Ex_p$ and $Ex_n$ is $2V_m$. This functioning is typical to a one-axis capacitive switched-capacitor accelerometer.

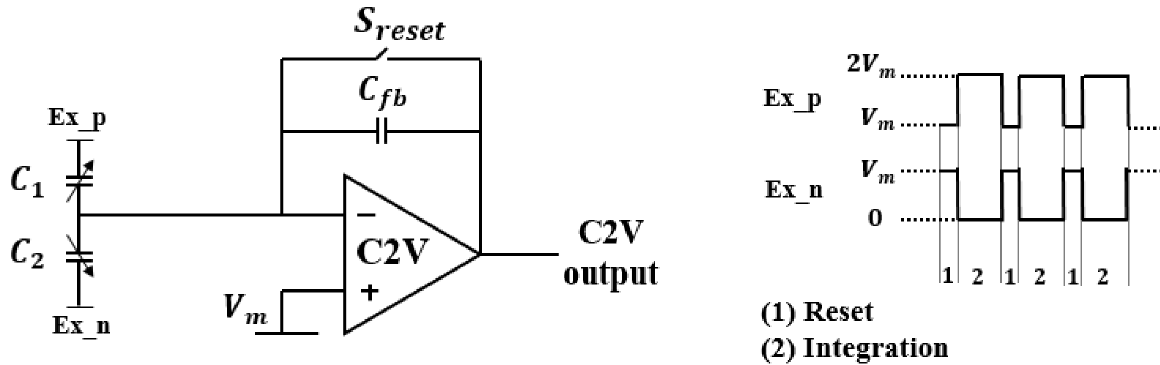


Figure 3.8 Block diagram of the capacitive sensing element and the AFE's first stage with its chronograms

Since no additional signal processing techniques, as filtering, are applied to the C2V during the integration phase, the amplifier will be modeled as a constant gain that reflects the acceleration (or the acceleration force) to voltage conversion.

If $\Delta C$, defined in (2.14), is the capacitance variation to be integrated into the amplifier, then the C2V output is:

$$V_{c2v_{out}} = \frac{-\Delta C}{C_{fb}} V_m \tag{3.13}$$

Considering the parameters from Table 3.1 for the mechanical sensing element, a feedback capacitor of $C_{fb} = 300\ fF$ and $V_m = 0.8\ V$ (compatible with a $1.6V$ CMOS technology), then the C2V is able to output $V_{c2v_{out}} = 12\ mV$ in a single ended topology for a $1g$ acceleration input when the system reaches the steady state.

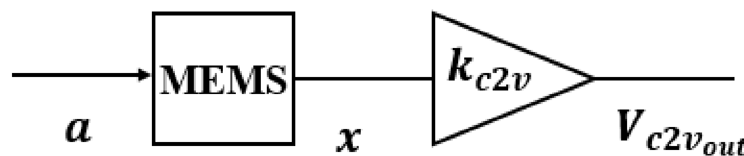


Figure 3.9 An illustration of the MEMS and the C2V simplified models

For the sake of simplicity, the C2V will next be modeled using a constant gain $k_{c2v}$ (Figure 3.9). The AFE's first stage has an important contribution to the SNR and circuit noise performances but for this part of the study, a macro model will be instead used for the C2V in order to find the suitable system architecture; then, the block by block design will be detailed.

# 3.4 Voltage-to-force-conversion

## 3.4.1 Electrostatic damping principle

It was previously stated (section 3.1) that three different control blocks have to apply control voltages on the sensor excitation plates in order to create an artificial electrical damping that assists the low mechanical damping of a high Q accelerometer.

This microactuator functioning is based on the electrostatic actuation mechanism. However, not every voltage applied on the excitation plates will produce an electrostatic force able to damp the transducer.

There has been an active research carried on the superimposition of two electrostatic forces on a proof mass to produce a linear feedback characteristic [Kraft, 1998], [Yucetas, 2010]. The main advantage of this approach is the implementation simplicity, compared with a digital loop. However, it has non-linearities issues and depending on the mechanical sensing element design parameters, the linear region of the feedback characteristic varies. In Figure 3.10, a MEMS capacitive structure with parallel excitation plates and the electrostatic forces applied on the proof mass is presented.

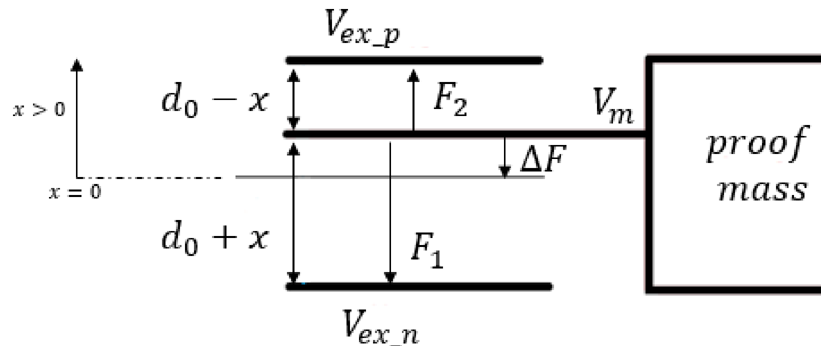


Figure 3.10 An illustration of a parallel plate capacitive sensor and the electrostatic forces applied on the proof mass

In the presence of external acceleration, the proof mass moves, which induces a capacitance variation between the transducer electrodes. Moreover, when a voltage ($V_{ex_p}$, $V_{ex_n}$ and $V_m$) is applied on the electrodes, an electrostatic force ($F_1$,$F_2$) is generated between the proof mass and the excitation electrodes. The net electrostatic force $\Delta F$, detailed using the equation (3.14) is an attraction force:

$$\Delta F = F_1 - F_2 = \frac{1}{2}\varepsilon_0\varepsilon_r A\left(\frac{\left(V_{ex_n}-V_m\right)^2}{(d_0+x)^2} - \frac{\left(V_{ex_p}-V_m\right)^2}{(d_0-x)^2}\right) \tag{3.14}$$

Note that $\Delta F$ should be null during the integration phase since an electrostatic force would disturb the acceleration measurement. Supposing now that on the fixed plates, a differential bias $V_B$ and a common control voltage $V_{ctrl}$ is superimposed on the common mode voltage $V_m$ as in (3.15), $\Delta F$ will depend both on $V_{ctrl}$ and $V_B$.

$$\begin{aligned} V_{ex_p} &= V_m + V_{ctrl} + V_B \\ V_{ex_n} &= V_m + V_{ctrl} - V_B \end{aligned} \tag{3.15}$$

Replacing (3.15) in (3.14), one can rewrite:

$$\Delta F = F_1 - F_2 = \frac{1}{2}\varepsilon_0\varepsilon_r A\left(\frac{(V_{ctrl}-V_B)^2}{(d_0+x)^2} - \frac{(V_{ctrl}+V_B)^2}{(d_0-x)^2}\right) \tag{3.16}$$

If the displacement $x$ is very small besides the gap between the electrodes $d_0$, $x \ll d_0$, then the net electrostatic force $\Delta F$ becomes:

$$\Delta F \cong -\frac{2\varepsilon_0\varepsilon_r A}{d_0^2} V_B V_{ctrl} \tag{3.17}$$

And:

$$\Delta F \cong -B V_{ctrl} \tag{3.18}$$

Where $B = \frac{2\varepsilon_0\varepsilon_r A}{d_0^2} V_B$.

The electrostatic force $\Delta F$ (3.18) represents another force to be added to the second order mass-spring damper system equation. In addition, if the control voltage $V_{ctrl}$ is proportional to the proof mass velocity $\dot{x}$, then it can clearly be noticed that the mechanical damping $b$ will be artificially increased with a certain value $B$, where $B$ is thus the electrostatic damping coefficient:

$$m\ddot{x} + (b + B)\dot{x} + kx = ma_{ext} \tag{3.19}$$

Therefore, the control blocks should apply on the proof mass the excitation signals (3.15) where $V_{ctrl}$ is proportional to the proof mass velocity. Since the electrodes are multiplexed and the damping phase is followed by another reset and integration phases, the net electrostatic force $\Delta F$ will be modulated with a ratio $\frac{t_{damp}}{T_s}$ where $t_{damp}$ is the damping phase period and $T_s$ the sampling frequency for a discrete system implementation.

Further, it is clear that from a net electrostatic force perspective, $V_{ctrl}$ and $V_B$ are symmetrical. If considering:

$$\begin{aligned} V_{ex_p} &= V_m + V_{ctrl} + V_B \\ V_{ex_n} &= V_m - V_{ctrl} + V_B \end{aligned} \tag{3.20}$$

Then the net electrostatic force $\Delta F$ becomes:

$$\Delta F = F_1 - F_2 = \frac{1}{2}\varepsilon_0\varepsilon_r A\left(\frac{(-V_{ctrl}+V_B)^2}{(d_0+x)^2} - \frac{(V_{ctrl}+V_B)^2}{(d_0-x)^2}\right) \tag{3.21}$$

Equation (3.21) is equivalent to equation (3.16) and will lead to the same electrostatic force linear characteristic (3.17). Depending on the design specifications, either solution for the excitation signals ((3.15) or (3.20)) can be considered and implemented since they are symmetrical and will have the same net electrostatic force result.

### 3.4.2 Linearity of the voltage-to-force conversion

From equation (3.17), the linear characteristic of the net electrostatic force both with $V_B$ and $V_{ctrl}$ can be noticed. However, this linearity has a limitation imposed by the ratio between the proof mass displacement $x$ and the gap between the electrodes $d_0$.

The electrostatic force nonlinearity has two main drawbacks. The first one is the electrostatic damping inefficiency if the electrostatic force is not proportional with the proof mass velocity estimation; consequently, in addition to the oscillation issue, the system will have a nonlinear behavior.

To check the voltage-to-electrostatic force nonlinearity for the design presented in this study, the transducer was excited with several acceleration values ranging from $-8g$ to $8g$ which is the input dynamic range targeted for this architecture. When the input acceleration increases, the proof mass displacement increases and it is expected to increase the net electrostatic force nonlinearity also. It was assumed a control voltage variation from $-0.4V$ to $0.4V$ and $V_B = 0.4V$. Figure 3.11 presents the model simulation results.

The nonlinearity depends on the proof mass displacement $x$ but also on $V_{ctrl}$ (equation 3.22). A higher $V_{ctrl}$ results in a higher electrostatic force and so in a larger electrical damping but also in a higher nonlinearity. It is clear from Figure 3.12 that the highest nonlinearity (7.7 %) is reached for $a_{ext} = \pm 8g$ and $V_{ctrl} = \pm 0.4V$. However, for the architecture implemented in this thesis, that is not based on the electrostatic force estimation to quantify the external acceleration (as in the case of ΣΔ digital interfaces) the nonlinearity is not a real issue. Moreover, the analog closed loop operation will reduce loop nonlinearities if the gain is high enough.

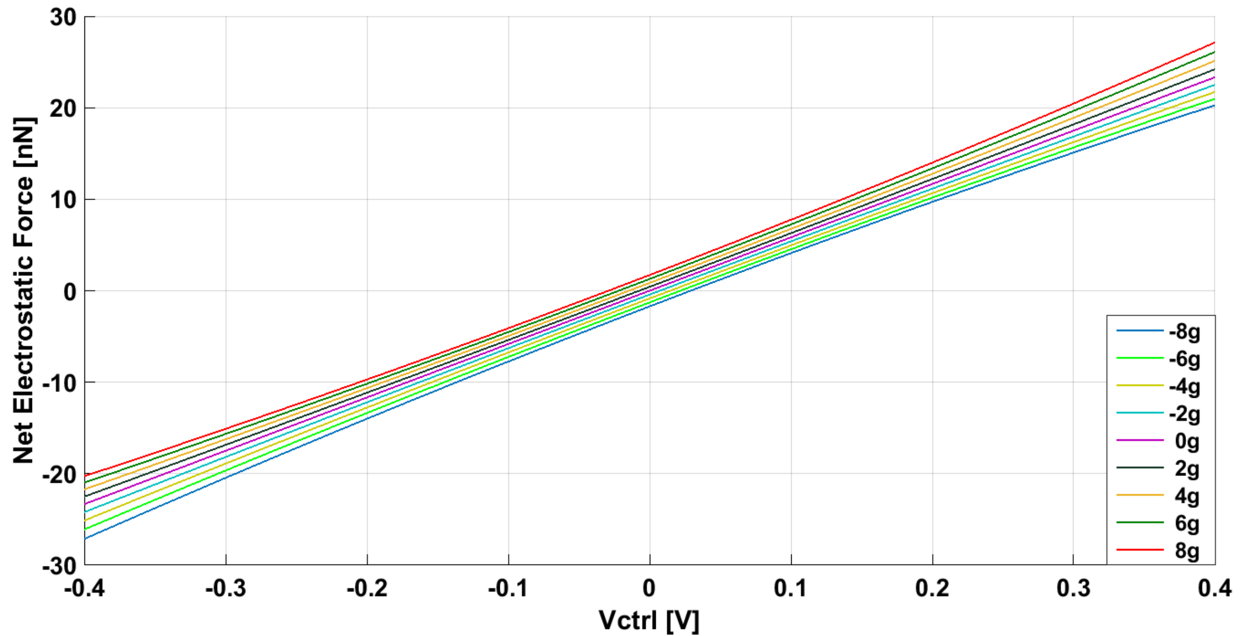


Figure 3.11 Net electrostatic force simulation when the input acceleration varies from $-8g$ to $8g$ and the control voltage $V_{ctrl}$ varies from $-0.4V$ to $0.4V$

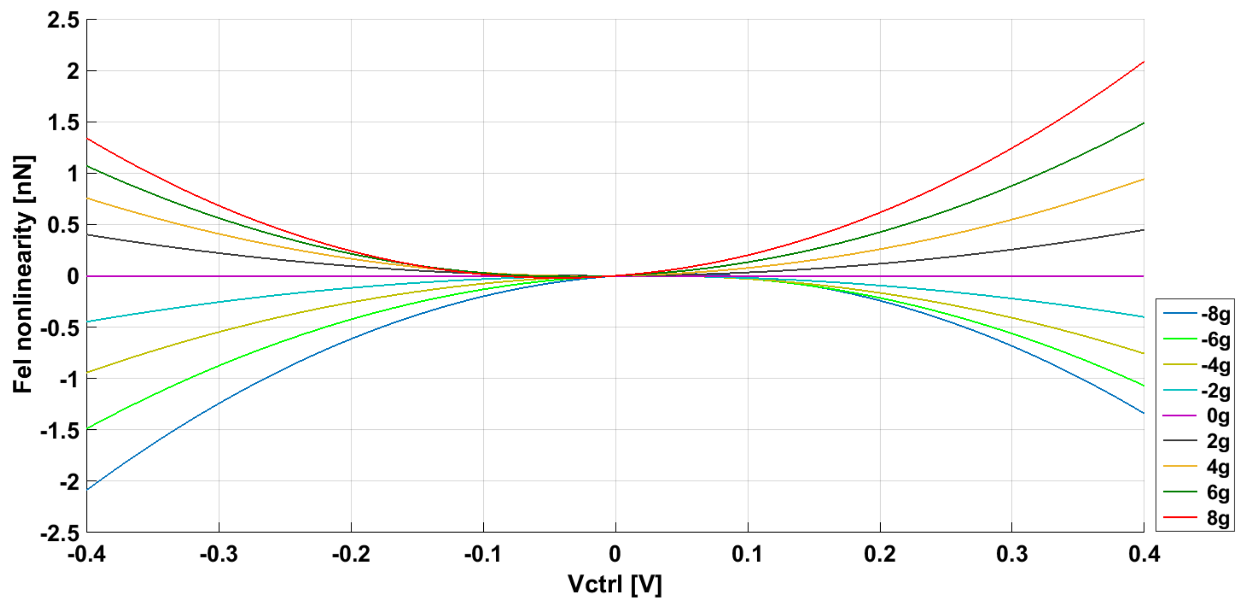


Figure 3.12 Net electrostatic force nonlinearity when the input acceleration varies from $-8g$ to $8g$ and the control voltage $V_{ctrl}$ varies from $-0.4V$ to $0.4V$

The second drawback can be noticed from the second term of the equation (3.22) which can be obtained by developing (3.16).

$$\Delta F = \frac{-2\varepsilon_0\varepsilon_r A}{d_0^2} V_{ctrl} V_B \frac{1+\left(\frac{x}{d_0}\right)^2}{\left(1-\left(\frac{x}{d_0}\right)^2\right)^2} - \frac{\varepsilon_0\varepsilon_r A}{d_0^2}\frac{x}{d_0}\left(V_{ctrl}^2 + V_B^2\right)\frac{1}{\left(1-\left(\frac{x}{d_0}\right)^2\right)^2} \tag{3.22}$$

It consists in adding a displacement-proportional term $k'$ in the second order mass spring damper equation (3.23) that will cause a change in the sensor resonance frequency ($f_{res}$). Since it is desired to modify only the proof mass velocity, the resonance frequency shift (3.24) can be considered a drawback.

$$m\ddot{x} + (b+B)\dot{x} + (k+k')x = ma_{ext} \tag{3.23}$$

$$f_{res} = \frac{1}{2\pi}\sqrt{\frac{k+k'}{m}} \tag{3.24}$$

Increasing the DC voltage $V_B$ and $V_{ctrl}$ will increase also the nonlinearity coefficient $k'$. In the same time, the net electrostatic force can be maximized by choosing the optimum value for $V_B$. The $V_B$ calculation for a maximum net electrostatic force generation will be next presented.

### 3.4.3 Bias calculation for electrostatic force optimization

In order to find the design parameter $V_B$, several design assumptions have to be made. The first one is the targeted CMOS process: the accelerometer architecture should be designed in a 0.18 $\mu m$ CMOS technology within a $V_{dd} = 1.6V$ power supply. Secondly, no additional charge pump circuit can be used since the CMOS technology is not high-voltage compatible and the system has to be low power and small area. Then, no negative voltage can be generated or applied with the IC. Finally, it was chosen to have a common mode voltage of $V_m = 0.8V$ to maximize the dynamic range.

In this conditions, equations (3.15) can be rewritten as:

$$\begin{aligned} V_{ex_p} &= 0.8 + V_{ctrl} + V_B \\ V_{ex_n} &= 0.8 + V_{ctrl} - V_B \end{aligned} \tag{3.25}$$

In addition, the positive excitation signal $V_{ex_p}$ can reach $V_{dd}$ at most and $V_{ex_n}$ can't be lower than the analog ground $0V$.

$$\begin{aligned} (V_{ctrl} + V_B)_{max} &= V_m \\ (V_{ctrl} - V_B)_{min} &= -V_m \end{aligned} \tag{3.26}$$

Depending on $V_B$, we can now define a maximum and a minimum for the net electrostatic force approximation:

$$\begin{aligned} \Delta F_{max} &\cong \frac{2\varepsilon_0\varepsilon_r A}{d_0^2}\times(V_B\times V_{ctrl})_{max} = \frac{2\varepsilon_0\varepsilon_r A}{d_0^2}\times V_B\times (V_{ctrl})_{max} = f_1(V_B) \\ \Delta F_{min} &\cong \frac{2\varepsilon_0\varepsilon_r A}{d_0^2}\times(V_B\times V_{ctrl})_{min} = \frac{2\varepsilon_0\varepsilon_r A}{d_0^2}\times V_B \times(V_{ctrl})_{min} = f_2(V_B) \end{aligned} \tag{3.27}$$

If replacing $(V_{ctrl})_{max}$ and $(V_{ctrl})_{min}$ from (3.26) in (3.27) and imposing the annulation of the first order derivative for $f_1$ and $f_2$ (

$\frac{\partial f_1}{\partial V_B} = 0$ and $\frac{\partial f_2}{\partial V_B} = 0$ ) then $V_B$ can be found as well as the maximum and minimum for the control voltage $V_{ctrl}$:

$$V_B = \frac{V_m}{2} = 0.4\ V$$
$$(V_{ctrl})_{max} = \frac{V_m}{2} = 0.4\ V;\ (V_{ctrl})_{min} = -\frac{V_m}{2} = -0.4\ V \qquad (3.28)$$

Using these parameter values (3.28) the excitation signals have been calculated and plotted (Figure 3.13). It can be noticed that excitation signals comply with the specifications as they do not exceed $V_{dd}$ or go below the analog ground and as they are symmetrical from the common mode.

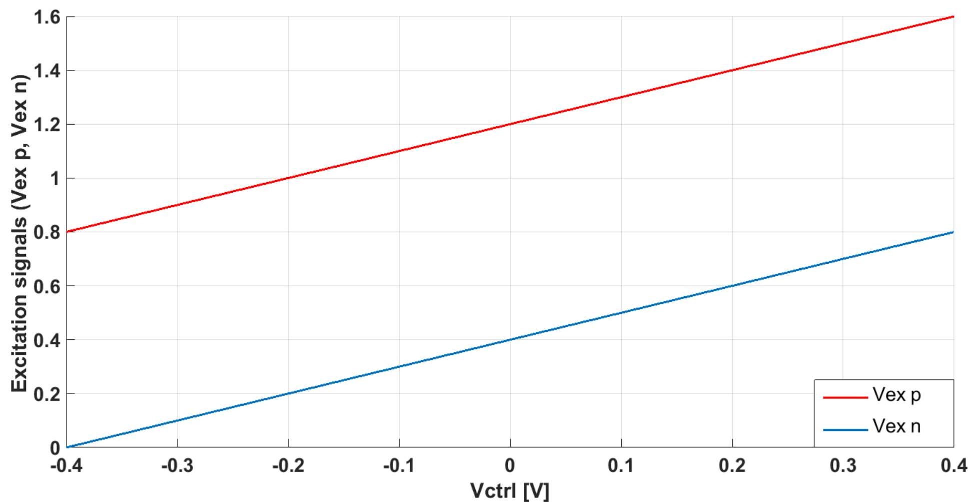


Figure 3.13 Excitation signals simulations using the optimal values found for $V_B$ and $V_{ctrl}$:$V_{ex_p}$ (red) and $V_{ex_n}$ (blue)

Moreover, it is necessary to check and validate the electrostatic forces maximum and minimum equations. When replacing (3.26) in (3.27), the net electrostatic forces expressions can be rewritten as:

$$\Delta F_{max} \cong \frac{2\varepsilon_0\varepsilon_r A}{d_0^2} \times V_B \times (V_m - V_B)$$
$$\Delta F_{min} \cong \frac{2\varepsilon_0\varepsilon_r A}{d_0^2} \times V_B \times (-V_m + V_B) \qquad (3.29)$$

The net electrostatic forces maximum and minimum equations are plotted in Figure 3.14. $V_B$ varies from $0V$ to $0.8V$ and for $V_B = 0.4V$ both waveforms have an inflexion point which proves that the optimal $V_B$ value is $0.4V$.

It is very important to find the optimal design parameters in order to increase the amount of electrostatic force applied to the proof mass and to decrease the system settling time. For this specific case, the optimal value for $V_B$ was found to be $0.4V$. It can be more generally inferred that $V_B$ should be half the common mode voltage applied on the proof mass.

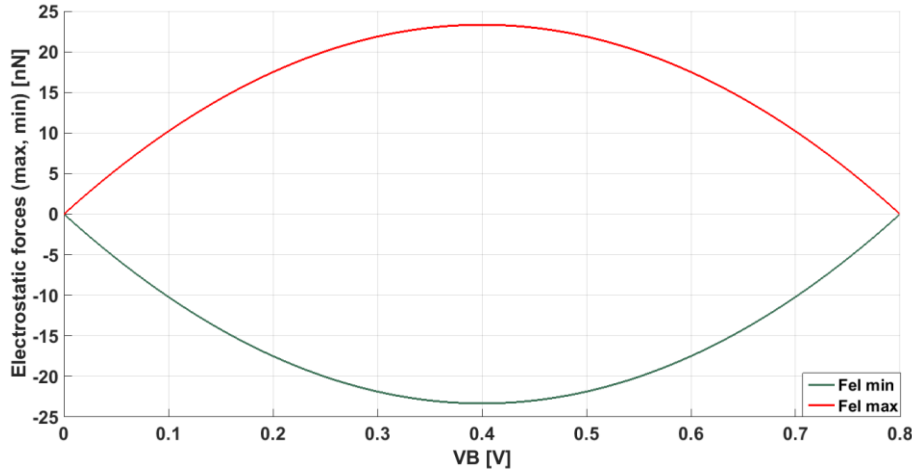


Figure 3.14 Net electrostatic forces simulation when $V_B$ varies from $0V$ to $0.8V$

## 3.5 Discrete Controller: Derivative block

### 3.5.1 Derivative block – principle of operation

The need of a control system for the underdamped MEMS accelerometer has been previously described and proved. Further, starting from the second order mass spring damper system equation, it has been observed and decided which term has to be increased (the mechanical damping) and which force can be used in order to do so (the electrostatic force). Additionally, the relationship between the excitation signals and the control voltage ($V_{ctrl}$) to allow a linear electrostatic force dependency has been found. It is clear now that a $V_{ctrl}$ that estimates the proof mass velocity is the most suitable candidate for the control voltage which is applied on the MEMS electrodes during the damping phase. Moreover, concerning the control block a Derivative-only approach has been chosen due to three axis common proof mass constraint and low power considerations; a force-feedback P.I.D. ($\sum\Delta$ approach) controller [Ye, 2013] can't be implemented if the mass is common to the three-axis and a P.D. [Yucetas, 2010] control block induces a resonance frequency shift and sensor sensitivity change which is not desired.

The simplest way to obtain the proof mass velocity estimation is to derivate the displacement (3.30). However, this approach can't be used if the system is not continuous-time controlled.

$$\acute{x}(t) = \frac{\partial x(t)}{\partial t} \tag{3.30}$$

A discrete derivative block will be used instead. The discrete controllers, one for each axis, are applying the control signals on the MEMS electrodes during the phase that follows the measurement, which is the *damping phase*.

The fundamentals of the discrete control theory state the necessity of an accurate control but also the system stability concerns. The control blocks usually add poles and zeros in the closed loop transfer function that can play an important role in the system stability.

Figure 3.15 presents the block diagram of a single-axis underdamped accelerometer where the reset phase is integrated within the measurement phase. During the first phase $\Phi_1$, two opposite excitation signals are applied onto the transducer electrodes to create a voltage step so as to measure the acceleration. The C2V output $V$ is then transferred to the *Derivative* block and stored during two successive sampling periods. The Derivative block calculates the difference between two successive C2V output samples and applies a derivation gain $k_d$; this way, $V_{ctrl}$ is the proof mass velocity estimation.

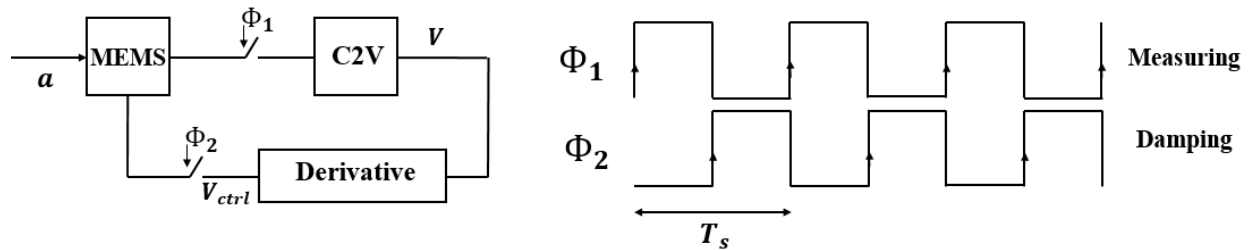


Figure 3.15 System block diagram

During the second phase $\Phi_2$, the control voltage, previously calculated, will be applied on the sensor electrodes using the (3.15) scheme. The sampling period $T_s$ has one measuring and one damping phase. This working principle can be translated into an input-output relation between $V$ and $V_{ctrl}$:

$$V_{ctrl}(nT_s) = k_d\left(V(nT_s) - V\big((n-1)T_s\big)\right) \tag{3.31}$$

It is clear that the velocity accuracy depends on the sampling frequency: a higher sampling frequency increases the chances to have a perfect reconstruction of the signal and minimizes the data loses. On the other hand, a lower system sampling frequency leads to a lower power consumption. Figure 3.16 shows the simulation results for the discrete derivative block when sampling at different frequencies; the red waveform corresponds to the continuous time derivative.

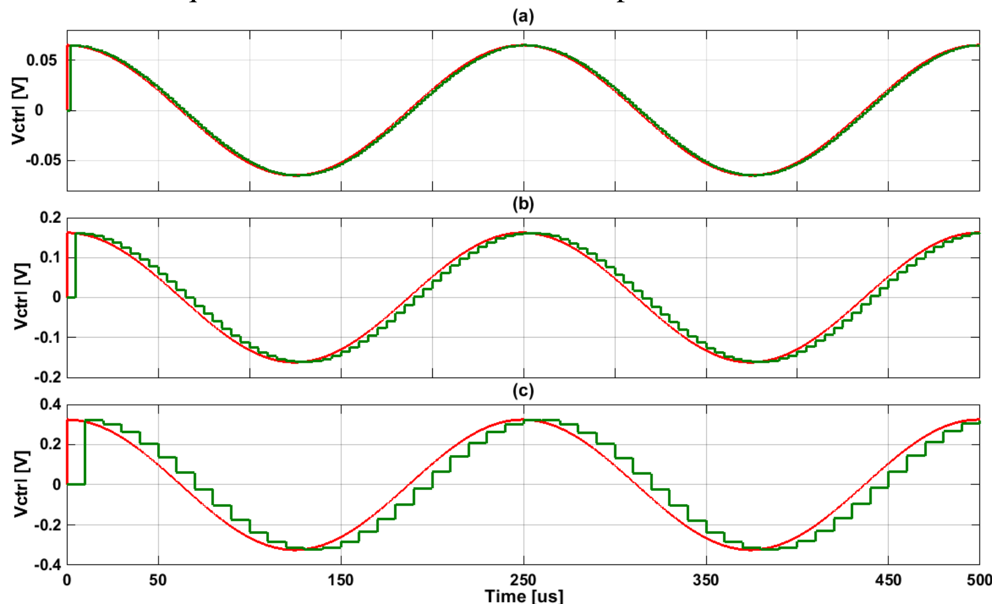


Figure 3.16 Derivative simulation for several sampling rates (a) $T_s = 2\mu s$ (b) $T_s = 5\mu s$ and (c) $T_s = 10\mu s$ (discrete derivative – green and continuous-time derivative red waveform)

Comparing to the continuous time derivative, it can be noticed that the discrete derivative approach error increases when the sampling frequency decreases.

Equation (3.31) can also be rewritten using the Z-transform as:

$$V_{ctrl}(z) = k_d(1 - z^{-1})V(z) \tag{3.32}$$

The discrete derivative sub-section revealed two other design parameters extremely important for the system performance: the sampling period $T_s$ and the derivative gain $k_d$ that can increase the net electrostatic force applied on the transducer but can also drive the system unstable since they are controller design parameters.

### 3.5.2 Derivative block - modeling

This sub-section details the modeling of the derivative block using both Matlab and Simulink for the system block presented in Figure 3.15. Here, it is supposed to have a continuous-time C2V voltage output ($V$). This voltage is then sampled twice: once on the rising-edge of the sampling clock and secondly on the falling-edge of the same sampling clock. The reason for doing so is the need of holding the C2V output for at least two successive sampling periods. Figure 3.17 shows the block diagram of the derivative model. The signals $V_1$ and $V_2$ are the two sampled versions of the C2V output voltage $V$.

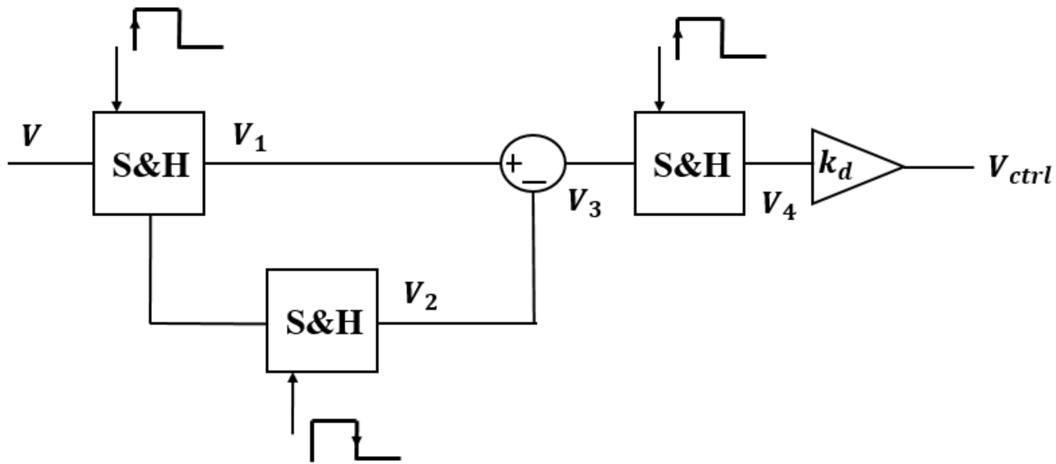


Figure 3.17 Block diagram of the derivative model where S&H refers to sample and hold circuits

Then, $V_3$ is the difference between $V_1$ and $V_2$; the difference has to be one more time sampled to reject the null $V_3$ samples and then amplified with the derivative gain parameter $k_d$. Figure 3.18 presents the model simulation results for the derivative block: the $V_1, V_2, V_3$ and $V_4$ waveforms help to have a better understanding of the controller operation during the damping phase.

The purpose of this model is to aid the full-architecture modeling and study. In a CMOS implementation, this block would be most likely designed using switched-capacitor techniques since its operation it is limited to sample and hold phases.

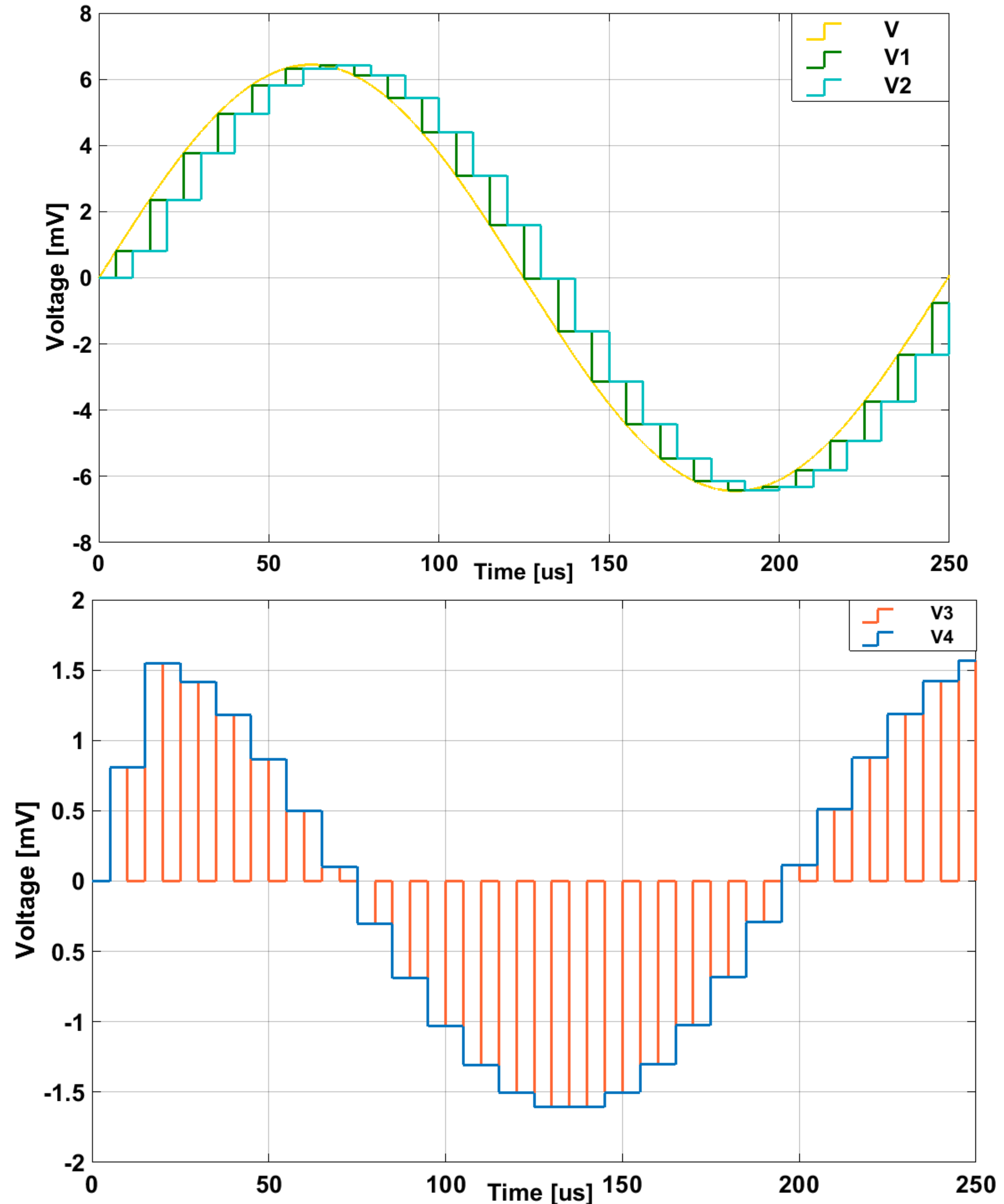


Figure 3.18 Simulation results of the derivative block

## 3.6 Damping approaches

### 3.6.1 Successive damping

After introducing the main blocks of the underdamped accelerometer with electrostatic damping control, it is time now to detail the chronograms and the overall system operation. To define a damping approach, one have to keep in mind that the C2V as well as the excitation electrodes are shared between the axes and the system phases (measuring and damping). In addition, to fulfill the circuit specifications, a maximum amount of electrostatic damping force has to be applied on the MEMS electrodes.

In a classical approach, the acceleration measurement (reading) and the damping phases are successive. Figure 3.19 shows the chronograms for the classical successive damping approach where 0 refers to a phase when no action is taken for that axis. During a sampling period $T_s$, there are three reading and three measuring phases. After an *x*-axis acceleration measurement during *Phase 1*, a new velocity estimation can then be calculated and a new $V_{ctrl_x}$ sample is thus generated and used to apply an updated electrostatic force value on the proof mass during *Phase 2* . During these *Phase 1* and *Phase 2*, no action is taken for *y* and *z*-axis. Then, when *Phase 3* occurs, the *y*-axis acceleration is measured and a new electrostatic force value is applied on the mass during *Phase 4*. Similarly, when the *y*-axis is measured and damped, no action is taken for the *x* and *z*-axis. And finally, during *Phase 5*, the *z*-axis is measured and a new damping force is applied on the proof mass during *Phase 6*. During these two last phases of the sampling period, no electrostatic force is applied on the *x* and *y* axis. No damping values are stored for the next sampling period.

| | Phase 1 | Phase 2 | Phase 3 | Phase 4 | Phase 5 | Phase 6 | Phase 1 | Phase 2 |
|---|---|---|---|---|---|---|---|---|
| X | Read x | Damp x[n] | - | - | - | - | Read x | Damp x[n+1] |
| Y | - | - | Read y | Damp y[n] | - | - | - | - |
| Z | - | - | - | - | Read z | Damp z[n] | - | - |

Figure 3.19 Classical approach: successive damping chronograms

The closed loop system implementing the successive damping sequence was fully modeled in Matlab-Simulink using the continuous time sensor model $H_{MEMS(s)}$ and ideal control clocks and sources. The top model is presented in Figure 3.20 (a) and then, Figure 3.20 (b) and Figure 3.20 (c) present the detailed models of each block. Figure 3.21 shows the control signals for the closed loop system.

The capacitance variation $\Delta C$ generated by the acceleration excitation, is converted into a charge variation $\Delta Q$ when a voltage is applied on the sensor electrodes. However, one would like to measure the charge variation only during the reading phase.

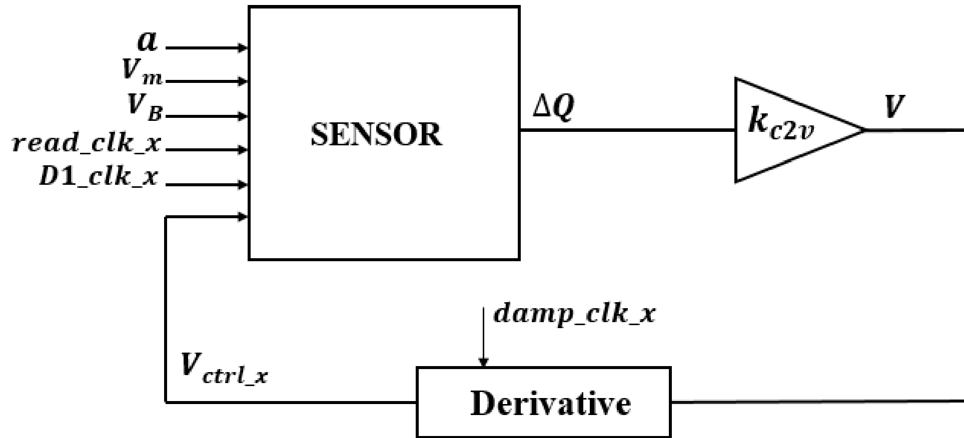


Figure 3.20 (a) Block diagram model of the successive damping system

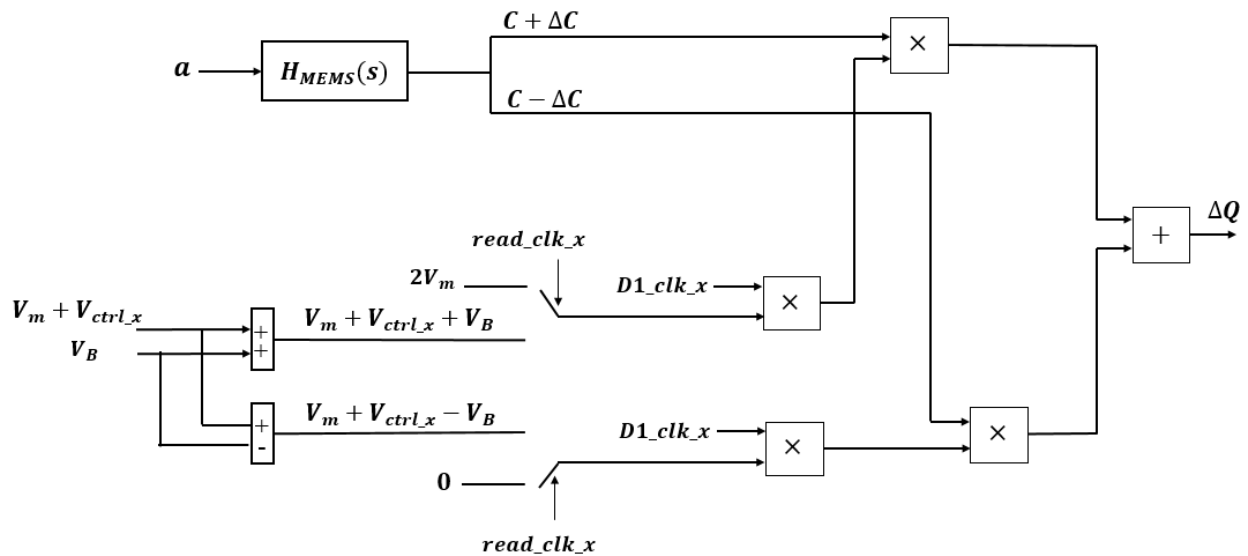


Figure 3.20 (b) Sensor model used in Figure 3.20 (a) to output the charge variation due to the acceleration variation

To measure only the charge variation due to the acceleration excitation, no electrostatic stimulus has to be applied on the mass during the reading phase. The $read_clk_x$ clock selects the voltage applied on the proof mass electrodes during the respective phase. And finally, to define the period of time corresponding to the damping phase of the $x$-axis, the $D1_clk_x$ selects this axis.

The charge variation is then sent to the C2V and amplified. Since the C2V is modeled using a constant gain, its output $V$ has to be read only at the end of the reading phase by the derivative block. Using the $damp_clk_x$ clock, the derivative samples the C2V output and calculates the control voltage. The new $V_{ctrl_x}$ value is applied on the proof mass electrodes during the $x$-axis damping phase but held during the entire $T_s$ period.

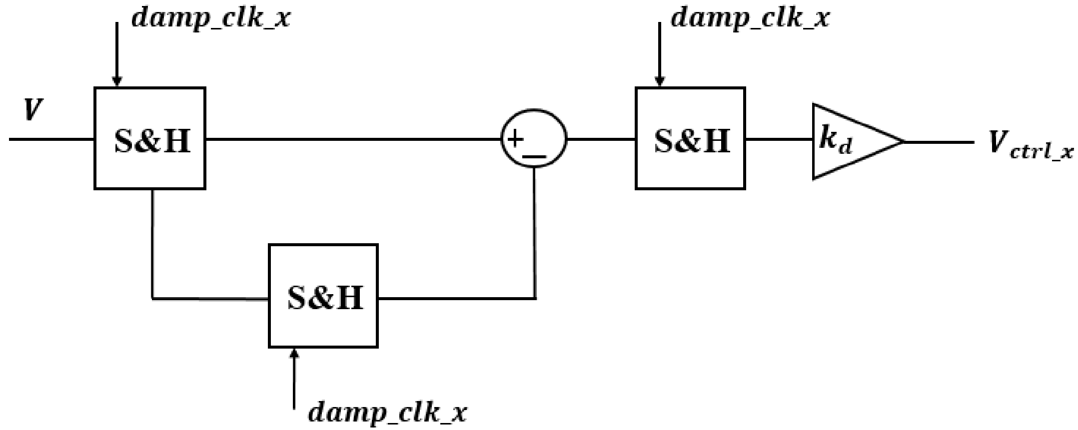


Figure 3.20 (c) Derivative model used in Figure 3.20 (a) to output the control voltage $V_{ctrl_x}$

The signals $read_clk_x$, $damp_clk_x$ and $D1_clk_x$ are non-overlapping clocks, active on rising edge, however one can approximate:

$$t_{read} = t_{damp} \tag{3.33}$$

$$T_s = 3(t_{read} + t_{damp}) \tag{3.34}$$

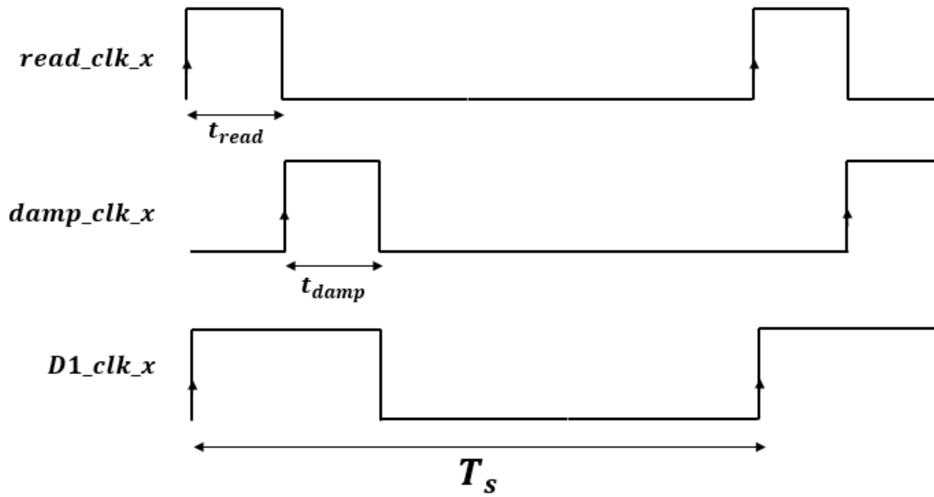


Figure 3.21 Clock chronograms used to control the closed loop system implementing successive damping

The net electrostatic force applied to the sensor during a sampling period $T_s$ is modulated by the damping duty cycle $\frac{t_{damp}}{T_s}$:

$$\Delta F_{D1} \cong \frac{t_{damp}}{T_s} \frac{2\varepsilon_0 \varepsilon_r A}{d_0^2} V_B V_{ctrl_x} \tag{3.35}$$

Supposing the MEMS parameters constant and a certain CMOS technology that limits $V_B$ and $V_{ctrl_x}$, it is clear that the ratio between $t_{damp}$ and $T_s$ is a design parameter and will play an important role on the damping efficiency. If $\frac{t_{damp}}{T_s}$ increases, the net electrostatic force increases also and the system ability to oscillate is diminished. On the other hand if $T_s$ increases a lot, the

system becomes slow and the velocity estimation applied to improve the damping is not more consistent with the actual proof mass movement and can drive the loop unstable.

For this reasons, a new damping approach was conceived to increase the electrostatic force applied to the MEMS during a sampling period $T_s$ without necessarily increasing the damping period $t_{damp}$ and slowing the system. This new damping method will be detailed in the next sub-section.

### 3.6.2 Simultaneous damping

A novel sequence, which optimizes the damping efficiency, has been designed and implemented. As for the successive damping, six separate phases can be distinguished in the same sampling period $T_s$. Figure 3.22 presents the simultaneous damping chronograms: for the 3-axis *x*, *y* and *z*, the system has three reading and three damping phases.

After an *x*-axis acceleration measurement during *Phase 1*, a new velocity estimation will be calculated and a new $V_{ctrl_x}$ sample is generated and used to apply a new electrostatic force value on the proof mass during *Phase 2*; during the same phase, the *y* and *z* damping values, that have been previously calculated in the $(n-1)T_s$ sampling period and stored, are applied on the *y* and *z* excitation electrodes respectively.

Next, the *y*-axis is measured and a new damping value is generated and applied on the *y* axis electrodes during *Phase 4*. However, since the damping value for the *x*-axis was stored due to the control block storing capacity from *Phase 2* and the *z*-axis damping value was stored since the $(n-1)T_s$ sampling period, the *x* and z axis will also be damped during *Phase 4*.

Finally, the *z* axis acceleration is measured and a new electrostatic force value is generated and applied on *z* axis electrodes during *Phase 6*. Simultaneously, the *x* and *y* damping values applied during *Phases 2* and *4*, will also be used to damp the *x* and *y* axis respectively.

| | Phase 1 | Phase 2 | Phase 3 | Phase 4 | Phase 5 | Phase 6 | Phase 1 | Phase 2 |
|---|---|---|---|---|---|---|---|---|
| X | Read x | Damp x[n] | - | Damp x[n] | - | Damp x[n] | Read x | Damp x[n+1] |
| Y | - | Damp y[n-1] | Read y | Damp y[n] | - | Damp y[n] | - | Damp y[n] |
| Z | - | Damp z[n-1] | - | Damp z[n-1] | Read z | Damp z[n] | - | Damp z[n] |

Figure 3.22 Novel sequence: simultaneous damping chronograms

Therefore, when one sampling period is complete, the three axes were measured and damped and three times more electrostatic force was thus applied to the transducer compared with the classical successive damping approach when sampling at the same frequency and without increasing the damping period $t_{damp}$ . The net electrostatic force applied to the mass during one sampling period $T_s$ when the 3-axis are damped simultaneously is:

$$\Delta F_{D2} \cong 3\frac{t_{damp}}{T_s}\frac{2\varepsilon_0\varepsilon_r A}{d_0^2}V_B V_{ctrl_x} \quad (3.36)$$

In order to model the novel simultaneous damping architecture, a similar block diagram as in Figure 3.20 will be used. The clock $D1_clk_x$ is replaced with $D2_clk_x$ to select the $x$-axis damping during the three damping periods. The control signals chronograms of the system implementing simultaneous damping are presented in Figure 3.23.

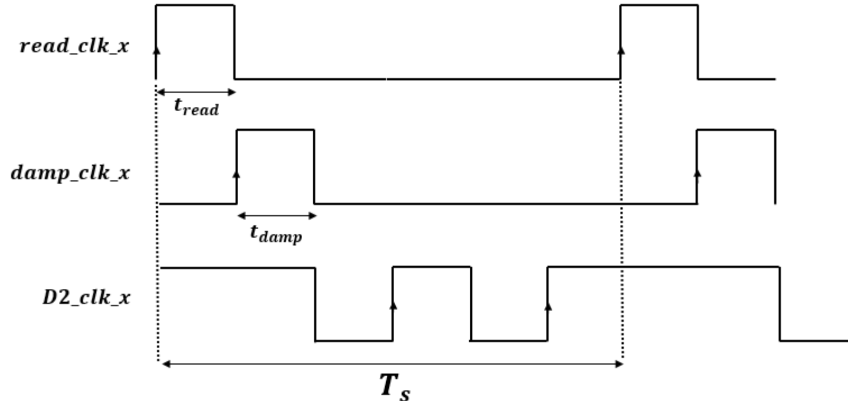


Figure 3.23 chronograms used to control the closed loop system implementing simultaneous damping

The Matlab-Simulink models for both damping architectures, successive and simultaneous, can be used, firstly, to check the electrostatic damping principle and secondly to compare the settling time performances. The approach with better results for the settling time will next be chosen for the CMOS implementation.

### 3.6.3 Performances and choice of architecture

The model simulation results are presented in this sub-section. The increased amount of electrostatic force for the simultaneous damping (3.36) compared with the classical approach (3.35) is normally translated into a transducer settling time reduction.

Both models have been simulated using several sampling periods $T_s$ and derivative gains $k_d$. Firstly, it is important to check the electrostatic force principle and the operating phases. One would expect one single damping phase per axis for the successive damping and three damping phases for the simultaneous damping. The electrostatic force applied on the mass has to be null during the non-damping phases for the respective axis. Additionally, when the proof mass reaches the steady state and the velocity estimation is 0, the net electrostatic force has to reach also a steady state of $0N$. Figure 3.24 presents the net electrostatic force waveforms for both damping architectures when the system input is a step acceleration that varies from $0g$ to $1g$. The simulation is performed for a quality factor of $Q = 2000$, a common mode voltage $V_m = 0.8\,V$ and $V_B = 0.4\,V$. The same sampling period $T_s = 21\mu s$ and derivative gain $k_d = 400$ are used for both cases. From Figure 3.24 one can notice the single damping phase for the successive damping approach and the three times application of the same electrostatic force level for the simultaneous damping.

One may also anticipate the simultaneous damping performances since it is this electrostatic force waveform that reaches firstly the steady state.

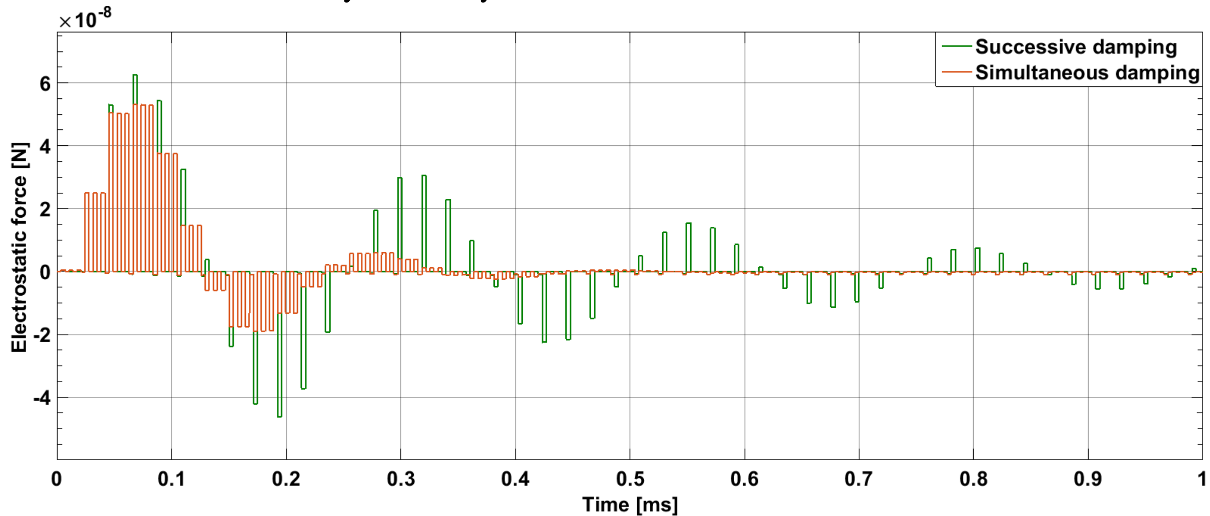


Figure 3.24 Electrostatic force waveforms for both approaches: successive and simultaneous damping

However, to quantify the performances in terms of settling time additional simulations have been performed. As stated previously, the settling time depends both on $T_s$ and on $k_d$ and consequently to check the settling performances, the sampling period has been varied between $6\ \mu s$ and $42\ \mu s$ and $k_d$ fixed to $600$. It is desired to obtain results compatible within a $1.6V$ power supply technology, therefore $V_B = \frac{V_m}{2} = 0.4V$ and the control voltage $V_{ctrl_x}$ is limited to $-0.4V < V_{ctrl_x} < 0.4V$. The settling time simulation results are presented in Figure 3.25.

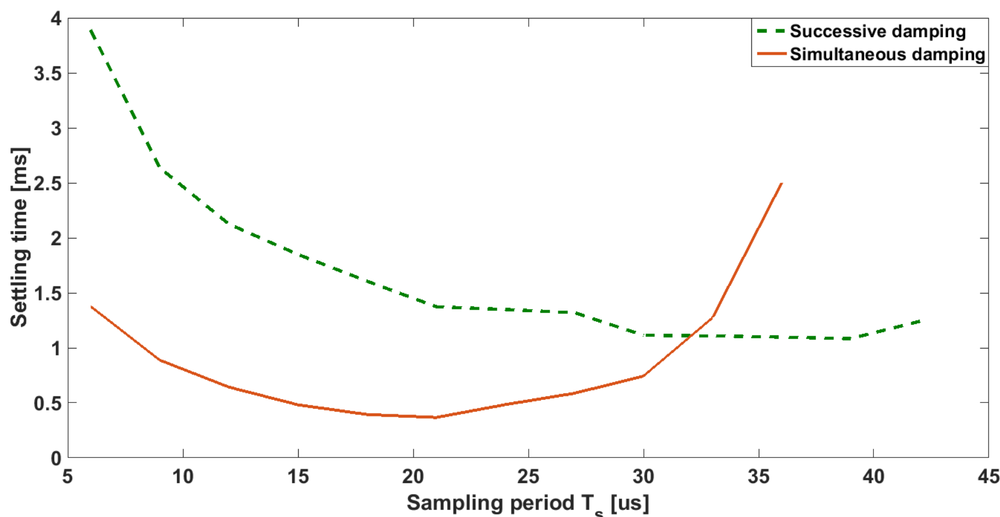


Figure 3.25 Settling time simulation results for both approaches: successive and simultaneous damping

It was also considered $t_{read} = t_{damp}$ and $T_s = 6t_{read}$. The sampling period limitations have two motivations: firstly, the system can't be faster than $f_s = 1/6\ \mu s = 166.66kHz$ because an acceleration measurement can't be performed faster than $1MHz$ and consequently $t_{read}$ is limited to $1\mu s$. Secondly, the lower sampling frequency is limited to the sensor bandwidth. If usually the design techniques advice for a sampling frequency $10$ to $20$ times higher than the cut-

off frequency, we have considered here a sampling frequency that can descend up to 6 times the sensor cut-off frequency.

The settling time has been measured within an 2% error range. From Figure 3.25 one can notice that the settling time performances for the simultaneous damping are better. When the sampling frequency is high, the simultaneous damping is very efficient and the settling time is roughly three times smaller than for the successive damping. Then, when the sampling frequency starts decreasing, the successive damping architecture can be a better choice. The intuitive explanation of the simultaneous damping performances degradation at low sampling frequencies is the incoherence of the electrostatic force value during the second and the third damping phase. When the sampling period is large, it is expected to apply on the excitation electrodes, during the second and the third damping phase, a velocity estimation which is no more corresponding to the real mass movement.

However, since sampling using a high frequency greatly improves the settling time compared with the classical approach, we are interested in further investigating the simultaneous damping architecture and in developing a mathematical model for the system, which is required to study the closed loop transfer function.

## 3.7 Multirate controller modeling in z-domain

The sampling period $T_s$ is considered to be the measurement rate for one axis or the period of time between two different C2V output samples for one axis. Nevertheless, it is clear that for the simultaneous damping approach, some signals are changing within this very same period $T_s$ (e.g. the electrostatic force). It is for this reason that one can say that the overall closed loop system is a multirate controller.

The architecture from Figure 3.20, implementing the simultaneous damping, can be discretized using two different sampling frequencies: $f_{s1}$ is the MEMS sensor frequency and $f_{s2}$ is the control block sampling rate. The block diagram of the simplified model is shown in Figure 3.26.

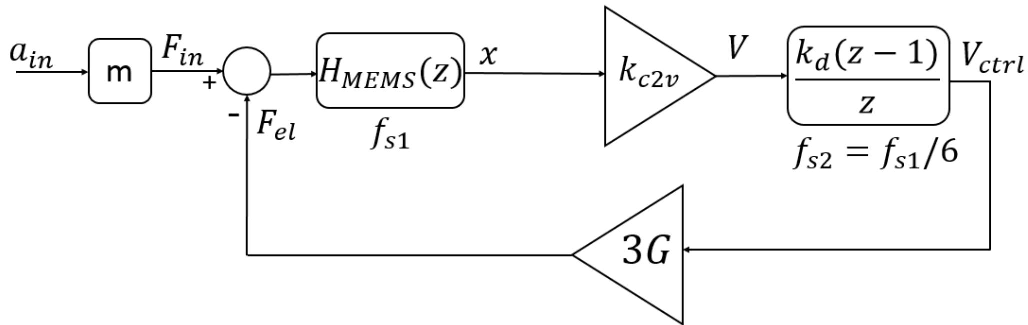


Figure 3.26 Simplified block diagram of the discretized system

Further, $f_{s1}$ is considered to be the fastest sampling frequency of the system in order to provide a better MEMS z-behavioral model and the ratio between $f_{s1}$ and $f_{s2}$ is 6 because there are 6 different phases per period.

In Figure 3.26, $H_{MEMS}(z)$ refers to the equation (3.12), $k_{c2v}$ is the C2V gain and $G$ is the voltage-to-force gain, defined as:

$$G = \frac{2\varepsilon_0\varepsilon_r A}{d_0^2} V_B \tag{3.37}$$

Since the damping is applied three times on the mass, there is a 3 coefficient for the voltage-to-force conversion $(3G)$.

Due to the fact that the system showed in Figure 3.26 has more than one sampling rate: $T_{s1}$ and $T_{s2}$, one will use the multirate signal processing theory to model it. Moreover, if $f_{s1}$ is the fastest sampling frequency, the blocks working at another sampling rate have to change it to $f_{s1}$ in order to allow the closed-loop study and to quantify the system operation using the same sampling frequency $f_{s1}$. The main operations that enable such transformations are signal down-sampling and up-sampling.

After introducing the up-sampling and down-sampling blocks, the simplified model becomes:

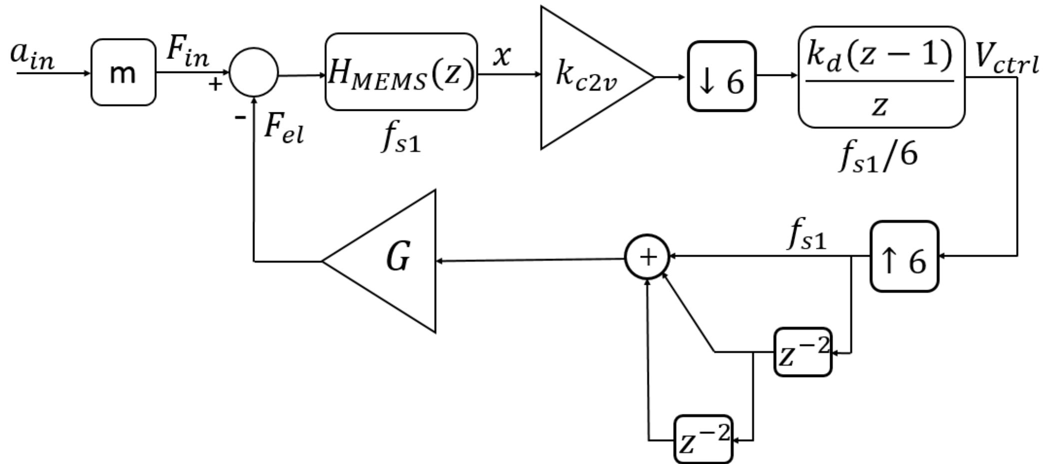


Figure 3.27 Simplified discrete model using up-sampling and down-sampling blocks

In Figure 3.27, the symbol $\downarrow M$ refers to down-sampling and $\uparrow M$ refers to up-sampling ($M = 6$. The Z Transform for a $M$ ratio up-sampling operation is reminded below (3.38):

$$u[k] - \uparrow M - v[n]$$
$$U(z) - \uparrow M - V(z)$$
$$V(z) = U(z^M) \tag{3.38}$$

where $v[n]$ is the up-sampled version of $u[k]$, and $V[z]$ and $U[z]$ the Z transforms of $v[n]$ and $u[k]$ respectively.

Furthermore, the down-sampling operation followed by an up-sampling, can be written in the z domain as:

$$u[n] - \downarrow M - v[k] - \uparrow M - u_M[n]$$

$$V(z) = \frac{1}{M}\sum_{m=0}^{M-1} U(e^{-\frac{j2\pi m}{M}} z^{\frac{1}{M}})$$

$$U_M(z) = \frac{1}{M}\sum_{m=0}^{M-1} U(e^{-\frac{j2\pi m}{M}} z) \quad (3.39)$$

where $u_M[n]$ is the up-sampled version of $v[k]$, and $U_M(z)$ its Z Transform.

Multirate signal processing theory uses the noble identities (3.40) to deal with up-sampling and down-sampling blocks:

$$\downarrow M - U(z) \equiv U(z^M) - \downarrow M$$
$$U(z) - \uparrow M \equiv \uparrow M - U(z^M) \quad (3.40)$$

Moreover, the discrete model can be one more time simplified and its representation is presented in Figure 3.28:

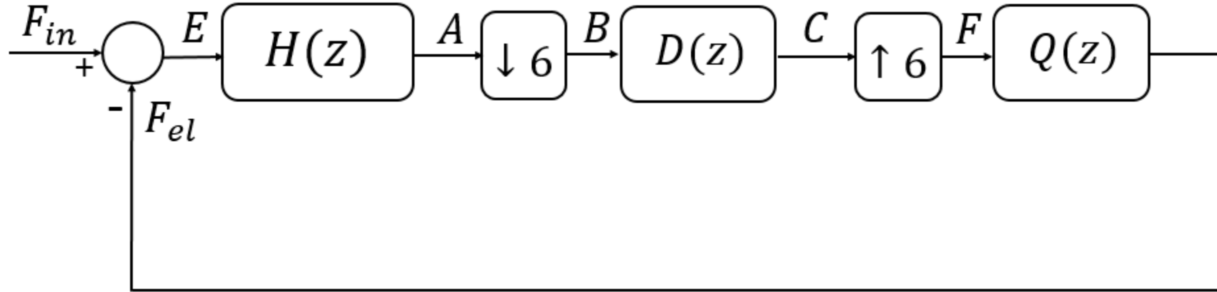


Figure 3.28 Simplified Discrete model for the multirate controller

where $H(z) = k_{c2v} \times H_{MEMS}(z)$ , $D(z) = \frac{k_d(z-1)}{z}$ and $Q(z) = G \times (1 + z^{-2} + z^{-4})$.

The model in Figure 3.28 is a fully z-domain representation of the simultaneous electrostatic damping architecture. To build this model, the continuous time elements (e.g. the sensor) have been transformed from s-to-z domain and the sampling frequency for certain discrete blocks have been changed to manage the closed loop analysis. The final result is a closed loop discrete time model with a unique sampling frequency, which was chosen to be the fastest of the system frequencies.

## 3.8 Closed-loop transfer function and stability study

To analyze the system presented in Figure 3.28, several methods have been proposed [Derk van der Laan, 1995], [Yamamoto, 1996] in the literature. The down-sampling and up-sampling processes transform this model into a time-variant system and consequently, an overall transfer function does not exist in the general case. The aim of this study is to find an input-output relationship in the z-domain from which the system stability can be estimated.

It can be noticed:

$F_{el}(z) = Q(z) \times F(z) = Q(z) \times C(z^6)$ (from 3.40)

$C(z) = D(z) \times B(z)$

$$B(z) = \frac{1}{6}\sum_{m=0}^{5} A(e^{-\frac{j2\pi m}{6}} z^{\frac{1}{6}})$$

$B(z^6)=\frac{1}{6}\sum_{m=0}^{5}A\left(e^{-\frac{j2\pi m}{6}}z\right)$ (from 3.34)

$A(z)=H(z)\times E(z)$

$E(z)=F_{in}(z)-F_{el}(z)$

$$C(z^6)=D(z^6)\times B(z^6)=D(z^6)\times\frac{1}{6}\sum_{m=0}^{5}A\left(e^{-\frac{j2\pi m}{6}}z\right)=$$

$$D(z^6)\times\frac{1}{6}\sum_{m=0}^{5}H\left(e^{-\frac{j2\pi m}{6}}z\right)\times E\left(e^{-\frac{j2\pi m}{6}}z\right)=$$

$$D(z^6)\times\frac{1}{6}\sum_{m=0}^{5}H\left(e^{-\frac{j2\pi m}{6}}z\right)\times\left(F_{in}\left(e^{-\frac{j2\pi m}{6}}z\right)-F_{el}\left(e^{-\frac{j2\pi m}{6}}z\right)\right)=$$

$$=D(z^6)\times\left[\left(\frac{1}{6}\sum_{m=0}^{5}H\left(e^{-\frac{j2\pi m}{6}}z\right)\times F_{in}\left(e^{-\frac{j2\pi m}{6}}z\right)\right)-\left(\frac{1}{6}\sum_{m=0}^{5}H\left(e^{-\frac{j2\pi m}{6}}z\right)\times F_{el}\left(e^{-\frac{j2\pi m}{6}}z\right)\right)\right] \quad (3.41)$$

Then:

$$\sum_{m=0}^{5}F_{el}(e^{-\frac{j2\pi m}{6}}z)=\sum_{m=0}^{5}Q(e^{-\frac{j2\pi m}{6}}z)\times C(e^{-\frac{j2\pi m}{6}\times 6}z^6) \quad (3.42)$$

But $C\left(e^{-j2\pi m}z^6\right)=C(z^6)$.

Replacing (3.42) in (3.41), equation (3.41) can be rewritten:

$$C(z^6)=D(z^6)\times\frac{1}{6}\left[\left(\sum_{m=0}^{5}H\left(e^{-\frac{j2\pi m}{6}}z\right)\times F_{in}\left(e^{-\frac{j2\pi m}{6}}z\right)\right)-C(z^6)\times\left(\sum_{m=0}^{5}H\left(e^{-\frac{j2\pi m}{6}}z\right)\times Q\left(e^{-\frac{j2\pi m}{6}}z\right)\right)\right]$$

$$C(z^6)=\frac{D(z^6)\times\frac{1}{6}\sum_{m=0}^{5}H(e^{-\frac{j2\pi m}{6}}z)\times F_{in}\left(e^{-\frac{j2\pi m}{6}}z\right)}{1+D(z^6)\times\frac{1}{6}\sum_{m=0}^{5}H\left(e^{-\frac{j2\pi m}{6}}z\right)\times Q\left(e^{-\frac{j2\pi m}{6}}z\right)}$$

$$F_{el}(z)=Q(z)\times C(z^6)=\frac{D(z^6)\times Q(z)\times\frac{1}{6}\sum_{m=0}^{5}H\left(e^{-\frac{j2\pi m}{6}}z\right)\times F_{in}\left(e^{-\frac{j2\pi m}{6}}z\right)}{1+D(z^6)\times\frac{1}{6}\sum_{m=0}^{5}H\left(e^{-\frac{j2\pi m}{6}}z\right)\times Q\left(e^{-\frac{j2\pi m}{6}}z\right)} \quad (3.43)$$

If we define $K(z)$ as:

$$K(z)=\frac{D(z^6)\times Q(z)}{1+D(z^6)\times\frac{1}{6}\sum_{m=0}^{5}H\left(e^{-\frac{j2\pi m}{6}}z\right)\times Q\left(e^{-\frac{j2\pi m}{6}}z\right)} \quad (3.44)$$

Then the equivalent system is represented in Figure 3.29.

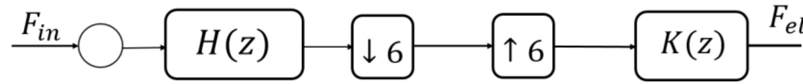


Figure 3.29 Equivalent open loop system

Equation (3.38) is the input-to-output relationship that describes the discrete multirate controller. The transfer function $K(z)$ can be used to conclude on the closed loop stability: the overall stability or instability can be deducted from $K(z)$ stability/instability [Derk van der Laan, 1995]. If $K(z)$ output is bounded for all bounded inputs, though stable, the overall system is stable. If $K(z)$ is unstable, the overall system will be unstable.

Next, the $K(z)$ transfer function stability has been studied. For a discrete system, the stability condition consists in imposing the poles placement inside the z-domain unity gain circle. If $K(z)$ has all its poles inside the unity gain circle, then, the overall system is be stable. The poles placement depends on the controller design parameters: $k_d$ and $T_s$, where $z = e^{j\omega T_s}$ in (3.44). For this reason, $k_d$ was varied between 20 and 1000 and $T_s$ between $8\ \mu s$ and $56\ \mu s$. The pairs $(k_d, T_s)$ that assure the system stability are presented in Figure 3.30.

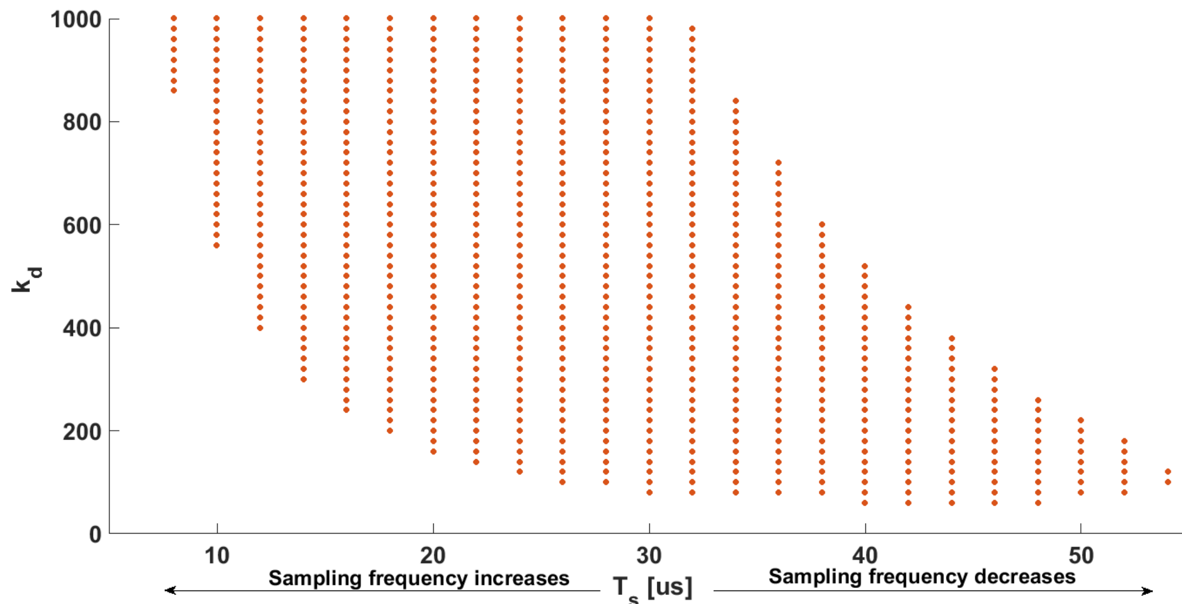


Figure 3.30. ($k_d$,$T_s$ ) stable points

It can be noticed from Figure 3.30 the values that assure the system stability. When the sampling frequency decreases, the derivative gain $k_d$ has to be carefully chosen. This novel approach, validated with behavioral models and simulations, allows to study the stability of a multirate controller for a 3-axis high Q capacitive MEMS accelerometer.

## 3.9 Summary

This chapter has proposed a new electrostatic damping architecture for a 3-axis underdamped accelerometer and presents a block by block modeling approach. Firstly, the system specifications and constraints have been set: single proof-mass mechanical sensing element common to the three-axis, single charge-to-voltage converter shared between the three-axis, no extra-damping electrodes, and no charge-pump circuit.

In this conditions, a new damping configuration based on the velocity estimation principle, allowing to improve the settling time has been developed, modeled and validated. The simultaneous damping approach is using the storing properties of the controller: by simply storing and applying the same amount of electrostatic force during the same sampling period, the settling time can be improved with a ratio of three compared with the classical damping approach.

Finally, a new approach that uses multirate signal processing techniques as the up-sampling and the down-sampling, has been introduced and validated. This method is required to determine the design parameters assuring a stable closed-loop operation.

Considering the settling time performances presented in Figure 3.25 and the stability simulation results showed in Figure 3.30, it was chosen for the system CMOS implementation a sampling period of $T_s = 24\ \mu s$ and a derivative gain $k_d = 300$. Increasing more the sampling frequency and the derivative gain values leads to a settling time reduction but the design challenges in terms of op-amp bandwidths and single stage gain architecture become notable.

Next chapter introduces the CMOS implementation of the architecture defined in this chapter. The overall accelerometer signal chain (C2V, derivative and analog gain stages) has been designed to fulfill the low power constraint of the system; the damping efficiency is assessed using closed loop simulations results and comparisons with Matlab-Simulink models.

# CHAPTER 4

# TOWARDS A CMOS ANALOG FRONT-END FOR A THREE-AXIS HIGH Q MEMS ACCELEROMETER WITH SIMULTANEOUS DAMPING CONTROL

Based on the previous analysis and successful modeling of the proposed closed loop accelerometer architecture, the corresponding CMOS analog front-end can now be designed. This chapter presents the block-by-block design of a low-power analog front-end for a three-axis underdamped MEMS accelerometer with simultaneous damping control. Using a top-down approach, a discrete-time switched-capacitor architecture is implemented in a $0.18\mu m$ CMOS TSMC process; the system architecture, already described and validated in Chapter 3, is translated into a transistor design using Cadence Environment. A new VerilogA-Spectre model has been developed for the three-axis MEMS accelerometer to enable the overall system simulation using the Cadence software. Finally, closed-loop simulations are performed and the settling time method is used to assess the damping efficiency.

## 4.1 System design of a low-power analog front-end for a three-axis underdamped MEMS accelerometer with simultaneous electrostatic damping control

The low-power specification of a consumer market sensor, as well as the electrodes multiplexing requirement, make the switched-capacitor circuit approach much more appropriate than the continuous time one. The sampling frequency is found using the stability analysis already presented in Chapter 3. The choice of each sub-system topology is based either on low-power or low-noise considerations.

The connection between the integrated circuit and the MEMS is ensured through the proof-mass itself. As a result, a fully-differential architecture can be designed for a fully differential MEMS with a two-mass transducer. For the sake of simplicity, in this study, a single mass will be connected to the C2V inverting input as presented in Figure 4.1; the common mode voltage of the C2V is set to $V_m = 0.8V$. Next, the derivative block estimates the proof mass velocity, $V_{ctrl}x$, and differentially outputs this quantity with respect to a common mode level which is $V_m + V_B = 1.2V$. Comparing the Derivative block outputs with equations (3.15), it can be noticed that the derivative gain $k_d$ is missing from the excitation signals expressions during the damping phase. It is for this reason that the next stage will add the derivative gain $k_d$. Finally, since during the reading phase different excitation signals are applied on the transducer electrodes ($V_{read\,x+}$ and $V_{read\,x-}$) an excitation block is added in the loop. The excitation signals block consists in an analog multiplexer controlled in such a way that either the reading or the damping excitation is applied on the sensor electrodes at a predefined moment and during a certain amount of time. The $y$ and $z$ electrodes are

connected to $V_m$ in order to create a null electrostatic force between these electrodes and the proof mass and also to not perturb the $x$-axis measurement. With such a system, an acceleration applied along the $x$-axis can be accurately measured even if the transducer has a high-quality factor. The circuit is designed for a sampling frequency of $T_s = 24\mu s$ and $k_d = 300$ (Section 3.8) and is working under an analog power supply of $V_{dda} = 1.6V$ and a digital power supply of $V_{ddd} = 1.75V$. Considering an ASIC implementation, the analog power supply is delivered by a bandgap circuit. If the bandgap has a supply of $1.75V$, a $V_{DS}$ of at least $0.15\ V$ has to be assured on the bandgap output p-channel transistor, resulting in an analog supply of $1.6V$. The digital supply doesn't have noise and perturbations sensitivity limitations and its value is decided by the embedded digital library; here $1.75V$.

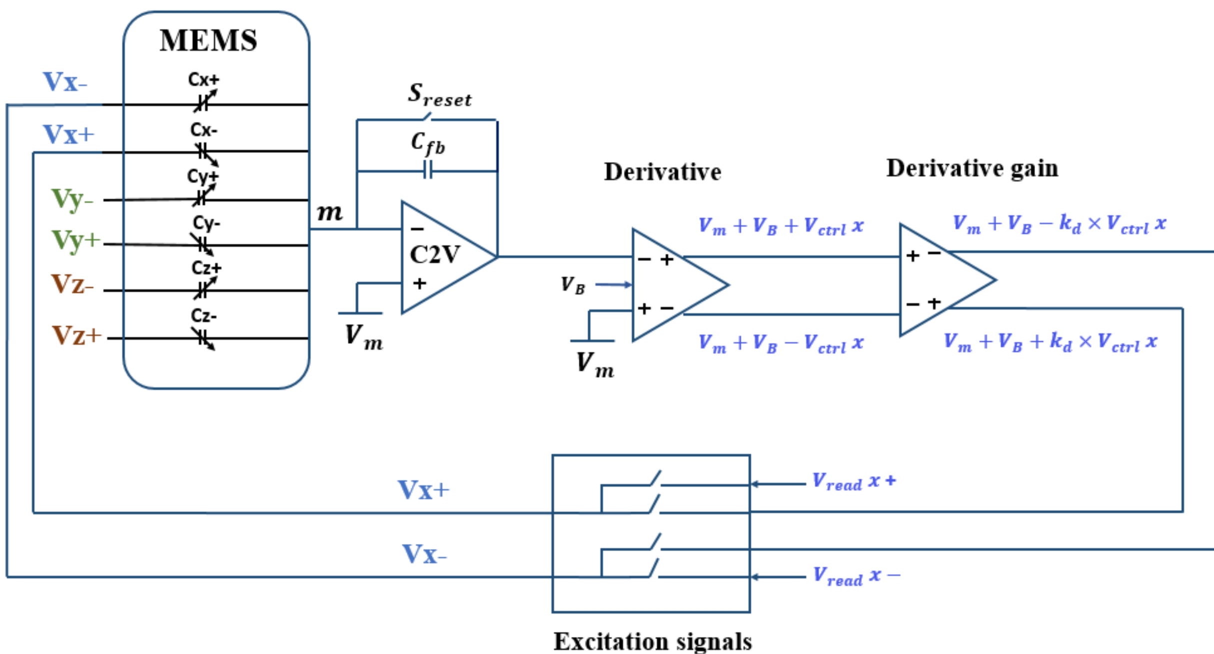


Figure 4.1. Block diagram of the accelerometer signal chain for x-axis

## 4.2 MEMS Accelerometer VerilogA – Spectre Model

In addition to the Matlab-Simulink models, a new MEMS accelerometer model is required for the CMOS implementation in order to run complete system simulations. The transducer, for which the design parameters have been presented in Table 3.1 and illustrated in Figure 3.2, was modeled using the VerilogA language and integrated in the Cadence'Spectre simulator. The modeling code is given in Appendices I and its associated symbol is shown in Figure 4.2.

The model pins purpose is either to enable the Analog-Front-End connection or for tests and validation. Firstly, the transducer can be stimulated along the three-directions $x$, $y$ and $z$ using the input pins $a_x$, $a_y$ and $a_z$ to apply an external acceleration. Depending on the test nature, the external acceleration can be a step, a sinusoidal acceleration or null, if for example, the self-test capabilities are used.

Further, the two moving masses can be accessed using the pins $m_1$ or $m_2$, which are connected to the C2V. Here, only $m_1$ pin is connected to the C2V inverted input. The current passing through the node $m_1$ reflects the charge variation induced by the acceleration applied on the mass. Then, each axis has two excitation plates, a positive and a negative one, that can be inverted since the design is symmetrical: $x_1$, $x_2$, $y_1$, $y_2$ and $z_1$, $z_2$. If needed, parasitical effects of the sensor shield or single-ended self-test modules can be modeled and implemented as well ($sub$ and $st$ are the associated pins for those capabilities).

The two excitation plates and two proof masses result in four variable capacitances per axis, twelve in total ($c_{x11}$, $c_{x12}$, $c_{x21}$, $c_{x22}$, $c_{y11}$, $c_{y12}$, $c_{y21}$, $c_{y22}$, $c_{z11}$, $c_{z12}$, $c_{z21}$, $c_{z22}$ ) that change their value under the effect of an external acceleration. The modeling convention is $1V$ for a $1fF$ of capacitance. The transducer sensitivity is $1.125\,fF/g$ per side or $4.5\,fF/g$ per axis.

Figure 4.2. An illustration of the MEMS accelerometer Cadence symbol

$Cst1b$ and $Cst2a$ refer to a one sided capacitor module for single ended self-test modules; $disp_{x1}$, $disp_{x2}$, $disp_{y1}$, $disp_{y2}$ can output the displacement of the proof masses $m_1$, $m_2$ when an acceleration occurs ($1V$ for a $1\mu m$ of displacement). Regarding the $z$-axis, the sensor has a teeter-tooter design and a rotational movement therefore the angle between the excitation plates and the proof mass measure the extern acceleration. $theta_{z1}$, $theta_{z2}$ are the output monitor pins for z-axis rotation ($1V$ for a 1 radian of displacement).

The model is built as follows: the VerilogA language is used to describe the transducer functioning. Then, the VerilogA model is included and appealed in a Spectre file. Parameters as

the sensor damping ratio, the sensitive area or the mass can be easily changed in the Spectre file, which makes the model adaptable to different designs or pressure conditions (damped or under-damped). The main VerilogA model modules are briefly presented here and detailed in Appendices I.

Firstly, to describe the translational proof mass motion and to calculate the displacement induced by an external acceleration, the second order mass-spring-damper system equations are implemented. The module is appealed in the Spectre file four times, once for each proof mass and each translational axis ($x$ and $y$). Regarding the z-axis, a VerilogA module has been developed to model the teeter-tooter rotational motion and to output the proof mass angle variation due to an external acceleration.

Furthermore, the displacement is converted into a capacitance using two separate modules, one for each type of motion; electrostatic forces modeling is also integrated within the sensed capacitances calculation modules.

The model has been tested and the theoretical parameters presented in Table 3.1, as the displacement sensitivity, the capacitance variation sensitivity as well as the resonance frequency have been checked. Figure 4.3 presents the transducer AC open-loop simulation results for two quality factors: $Q = 2$ (blue) and $Q = 2000$ (red).

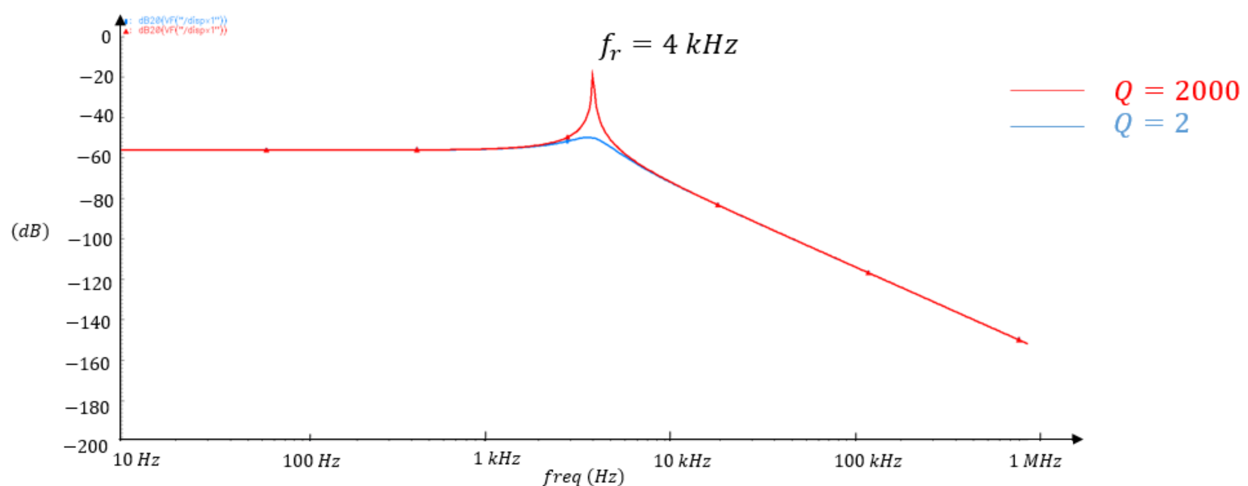

Figure 4.3 Open-loop MEMS displacement for Q=2 and Q=2000

In order to check the electrostatic forces implementation, the model has also been simulated with $0g$ input acceleration, and a slightly variation $\Delta V$ between the voltages on the proof mass and one of the fixed plates; the test bench configuration is shown in Figure 4.4.

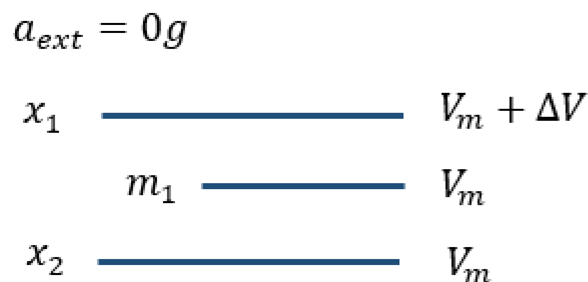

Figure 4.4 Open-loop plates configuration for electrostatic force test

The proof mass displacement induced by the electrostatic force that appears between the proof mass and the fixed electrode can be calculated using the equation (4.1):

$$x = \frac{\epsilon A}{2d_0^2}\frac{\Delta V^2}{k} \tag{4.1}$$

In this way, the displacement obtained either using the Simulink or Cadence models are compared to the theoretical value and the results are presented in Table 4.1. This test shows the coherence of proof mass displacement results obtained with different models.

| $\Delta V$ | Displacement ($x$) | | | | |
|---|---|---|---|---|---|
| | Calculation | Simulink | | Cadence | |
| | | Value $[nm]$ | Error (%) | Value $[nm]$ | Error (%) |
| $0.4V$ | $1.66\,nm$ | 1.67 | 0.67 | 1.69 | 1.8 |
| $0.5V$ | $2.6\,nm$ | 2.61 | 0.38 | 2.64 | 1.5 |
| $0.8V$ | $6.66\,nm$ | 6.71 | 0.75 | 6.81 | 1.8 |

Table 4.1 MEMS displacement under the effect of electrostatic forces and no extern acceleration

This section briefly presented a new VerilogA-Spectre three-axis MEMS model, developed for Cadence integration and overall system simulation. The sensor damping factor can be easily configured depending on the targeted application; further, several intermediary physical quantities (displacement, capacitance variation) can be observed; the connection to the C2V is performed through the proof mass itself.

## 4.3 Charge to voltage converter (C2V)

### 4.3.1 Block diagram and clock diagram

The analog front-end consists firstly, in a charge to voltage (C2V) amplifier that converts charge variations into voltage, during the reading phase. Note that the three axes share the same C2V. The front-end design must comply with a low-power and high resolution system specifications. As a result, a switched-capacitor architecture is implemented. The C2V amplifier requires two non-overlapping phases:

- *reset* (during which the damping is applied);
- *read* (not-reset);

However, the overall excitation control demands a more detailed clock diagram.

Figure 4.5 (a) and (b) shows the block diagram of the C2V and its chronograms, with the x-axis excitation signals, respectively. As it can be noticed, prior to the two excitation signals (during the reset phase), the C2V has a unity gain configuration to discharge the feedback capacitor $C_{fb} = 300fF$. For an input dynamic range of $[-8g; 8g]$ and a capacitance variation of $\Delta C = 2.25\,fF$ , the C2V requires an output dynamic range of $[752\,mV; 846\,mV]$ ($96\,mV$ peak to peak on a $800\,mV$ common mode).

The parasites between the proof mass and the ground are modeled using the capacitor $C_p = 3pF$ resulting in a feedback factor $\frac{1}{\beta} = 10$. When the reset switch $S_{reset}$ opens, the capacitance variation $\Delta C = C_1 - C_2$ is integrated into the C2V.

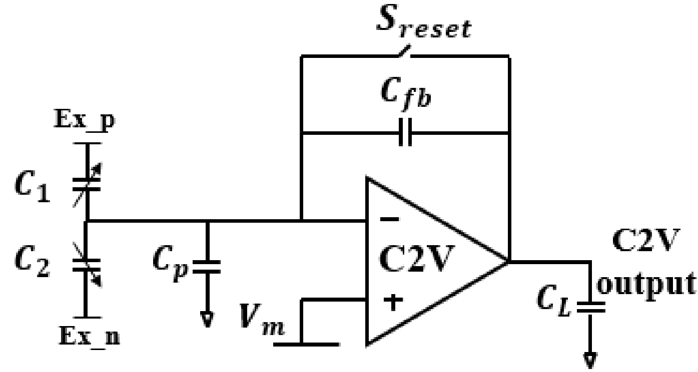


Figure 4.5 (a) Block diagram of the AFE's first stage (C2V)

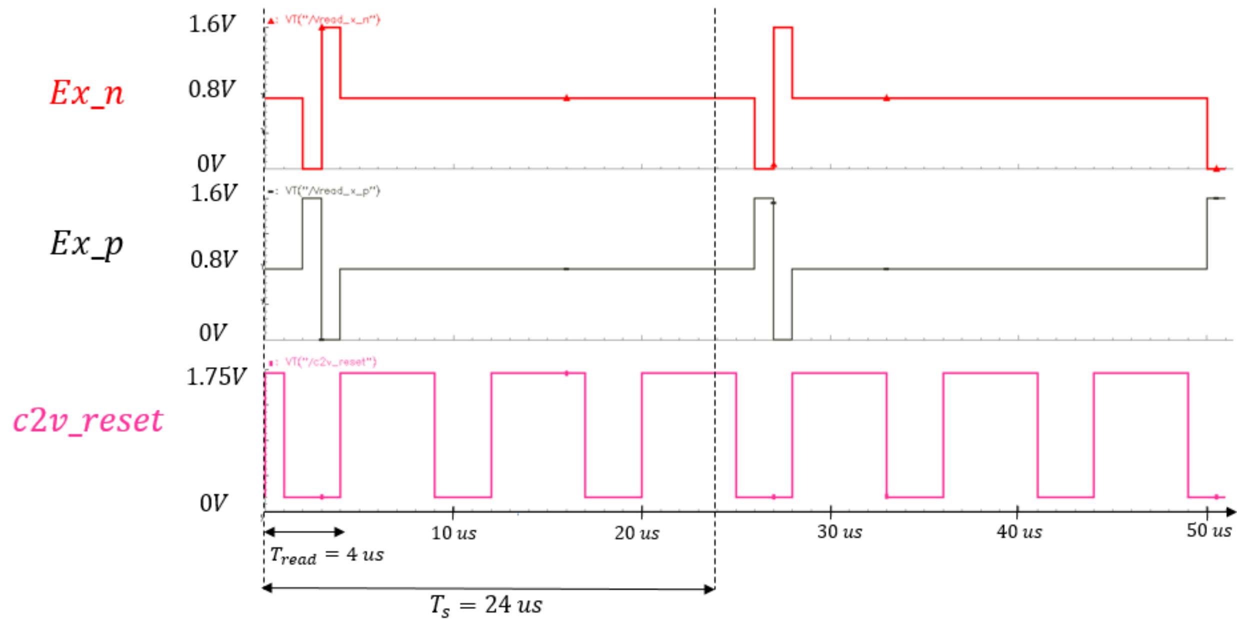


Figure 4.5 (b) Chronograms of the C2V block and x-axis excitation signals

The two opposite excitation signals of the measuring phase ($Ex_n$, $Ex_p$) are applied on the sensor fixed plates: two measurements are basically performed resulting in a differentiate C2V output.

The reading phase lasts $4\mu s$ and each of the excitation time duration is $1\mu s$. Therefore, the C2V amplifier bandwidth can be calculated using this information. If $\omega_{BW} = 2\pi f_{BW}$ is the closed-loop amplifier bandwidth, then $\tau_{BW}$ is its time constant and can be calculated using the relationship (4.2):

$$\tau_{BW} = \frac{1}{2\pi f_{BW}} \tag{4.2}$$

For a 0.1% amplifier output accuracy, it is usually considered [Demrow, 1970] that the amplifier requires $7\tau_{BW}$ to reach its steady state; the amplifier closed-loop bandwidth can thus be calculated as (4.3):

$$7\tau_{BW} = 1\mu s$$
$$f_{BW} = \frac{1}{2\pi\tau_{BW}} = 1.1MHz \quad (4.3)$$

If the C2V feedback factor is $\frac{1}{\beta} = 10$, then the amplifier gain bandwidth product $(GBW)$ is $f_{GBW} = \frac{1}{\beta} \times f_{BW} = 11MHz$.

To achieve the targeted output precision (0.1%), the amplifier should have a high open loop gain. Depending on the topology and on the amplifier bandwidth, a single stage or two-stages amplifier configuration can be used.

Using the above calculations, an operational amplifier architecture has been chosen and will next be detailed.

### 4.3.2 Basics of CMOS Analog Design and C2V Architecture choice

Nowadays, one of the most used configurations for an amplifier first stage is the cascode topology. It consists in a common-source transistor followed by a common-gate transistor. Figure 4.6 shows two cascode configurations: (a) one-stage telescopic cascode amplifier and (b) one stage folded cascode amplifier [Johns – Martin, 1997]. The main advantages of the cascode-amplifiers are the high impedance output node and thus, a very high gain compared with other single stages amplifiers but also high speed operation. Usually, to enable such high gain the current sources connected to the output node are designed using high quality cascode current mirrors. For easiness design considerations, same C2V amplifier could be used for the derivative block too. Hence, the folded-cascode architecture will be instead used since telescopic cascode amplifiers has a limited output swing.

The folded cascode principle can be summarized as follows: the input voltage is converted into a current by the common-source transistor; the output current is then applied to a common-gate transistor configuration. It is for this reason that the folded cascode amplifiers are often named Operational Transconductance Amplifiers (OTAs).

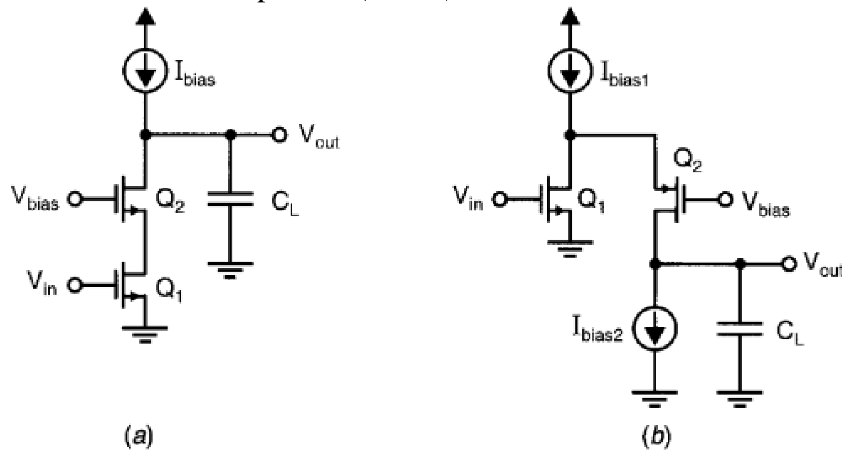


Figure 4.6 (a) Telescopic-cascode amplifier and (b) folded-cascode amplifier [Johns – Martin, 1997]

A first folded-cascode OTA architecture with PMOS differential input pair is shown in Figure 4.7 (a) [Razavi, 2001]. A simplified half-model is presented in Figure 4.7 (b) where $ro1$ and $ro5$ are the channel-length modulation resistors of the $M_1$ and $M_5$ transistor, respectively.

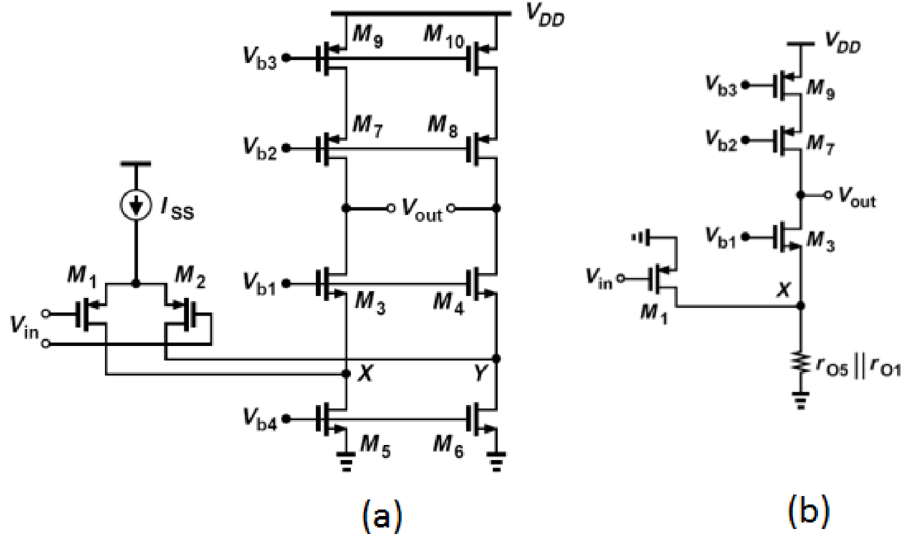


Figure 4.7 (a) Folded-cascode amplifier with PMOS differential input pair (b) simplified folded-cascode amplifier to calculate the voltage gain [Razavi, 2001]

This amplifier voltage gain can be derived from Figure 4.7 (b) using the MOS small-signal model [Razavi, 2001]; the result is presented in equation (4.4). By inspection, one can notice that the folded-cascode gain is significantly higher than other single stages configurations with minimum speed penalty.

$$A_v = \frac{v_{out}}{v_{in}} = g_{m1} \times [(g_{m3} \times ro5 || ro1 \times ro3) || (gm_7 \times ro9 \times ro7)] \tag{4.4}$$

where $g_m$ is the transistor transconductance defined as:

$$g_m = \frac{2I_D}{V_{GS} - V_{th}} \tag{4.5}$$

where $I_D$ is the DC current carried by the transistor, $V_{GS}$ the gate-source transistor voltage and $V_{th}$ the threshold voltage.

As stated previously, another issue to be addressed when designing a folded cascode is the current mirror connected to the output node. The current mirror operation is based on a perfect current copying from an ideal current source. Figure 4.8 (a) shows a basic current mirror where transistors $M_1$ and $M_2$ are supposed to operate in saturation region.

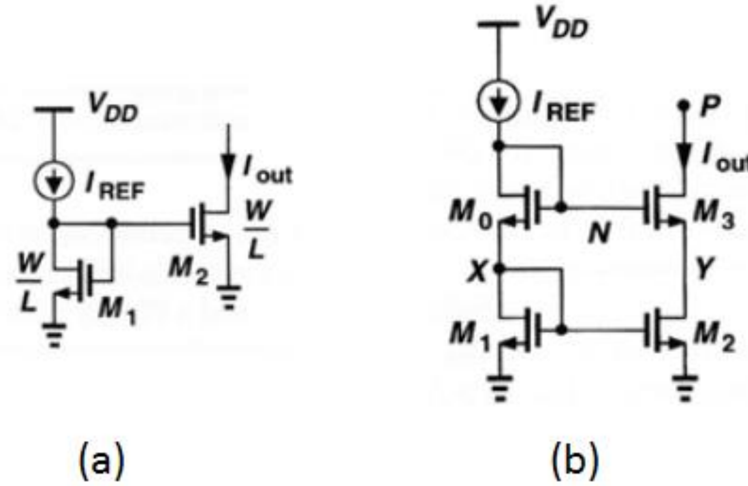


Figure 4.8 (a) Basic current mirror (b) cascode current mirror [Razavi, 2001]

Neglecting the channel length modulation effect [Steimle, 1991], one can thus write the current equations through $M_1(I_{ref})$ and $M_2(I_{out})$ as:

$$I_{ref} = \frac{1}{2}\mu_{n,p}C_{ox}\left(\frac{W}{L}\right)_1 (V_{GS} - V_{th})^2$$

$$I_{out} = \frac{1}{2}\mu_{n,p}C_{ox}\left(\frac{W}{L}\right)_2 (V_{GS} - V_{th})^2 \tag{4.6}$$

where $\mu_{n,p}$ is the mobility of charge careers, $C_{ox}$ is the gate oxide capacitance and $W$ and $L$ are the transistor channel width and length.

For identical devices and same process, the $I_{out}(I_{ref})$ dependency is reduced ideally to device dimensions $W$ and $L$ :

$$I_{out} = \frac{(W/L)_2}{(W/L)_1} I_{ref} \tag{4.7}$$

Further, the channel length modulation effect is no longer neglected and the currents flowing through $M_1$ and $M_2$ are rewritten as:

$$I_{D1} = \frac{1}{2}\mu_{n,p}C_{ox}\left(\frac{W}{L}\right)_1 (V_{GS} - V_{th})^2(1 + \lambda V_{DS1})$$

$$I_{D2} = \frac{1}{2}\mu_{n,p}C_{ox}\left(\frac{W}{L}\right)_2 (V_{GS} - V_{th})^2(1 + \lambda V_{DS2}) \tag{4.8}$$

where $\lambda$ is the channel-length modulation coefficient and $V_{DS}$ the drain-source voltage.

Hence, $I_{D2}$ depends now not only on the device dimensions but also on both drain-source voltages (4.9). For an identical current copying, the drain-source voltages must be equal.

$$I_{D2} = \frac{(W/L)_2}{(W/L)_1} \times \frac{(1+\lambda V_{DS2})}{(1+\lambda V_{DS1})} I_{D1} \tag{4.9}$$

Figure 4.8 (b) presents a customized current mirror which optimizes the current copying for non-negligible channel length modulation. The circuit idea is to assure $V_X = V_Y$ and hence $V_{GS3} = V_{GS0}$. This can be achieved by choosing:

$$\frac{(W/L)_3}{(W/L)_0} = \frac{(W/L)_2}{(W/L)_1} \tag{4.10}$$

However, the cascode mirror in 4.8 (b) requires a large headroom voltage to enable both $M_2$ and $M_3$ operation in saturation region. Other low-power cascode mirrors solutions can be found in [Razavi, 2001].

After a short overview of the folded-cascode amplifier and the basic current mirrors topologies, we will introduce now the C2V architecture chosen for this project.

### 4.3.3 Design and performances

For high gain considerations, the folded-cascode OTA architecture with a second stage has been chosen for the C2V amplifier (Figure 4.9). The second stage is a common-source configuration and a classical Miller compensation ($C_c$) is used to ensure the OTA stability.

The Miller compensation is critical in negative feedback amplifiers design. Here, a Miller capacitor has been added to split the two poles of the amplifier two stages and hence, to increase the phase margin. Other compensation methods suppose, for example, the addition of a nulling resistor in series with the Miller capacitor to eliminate or move the system right half plan zero, if exists.

One can calculate the Miller capacitance if knowing the amplifier output load. For an output capacitor load of $C_L = 800fF$, the Miller capacitor $C_c$ [Allen, Holberg, 2002] must fulfill the relationship:

$$C_c > 0.2C_L \tag{4.11}$$

For this design, it was chosen $C_c = 250fF$.

Next, considering the amplifier bandwidth previously calculated (4.3), one can deduct the input differential pair transconductance ($g_{m2} = g_{m3}$) as [Allen, Holberg, 2002]:

$$f_{BW} = \frac{g_{m2}}{2\pi C_c} \tag{4.12}$$

Hence, $g_{m2} = g_{m3} = 17.3\mu S$.

Since designing for low-power applications, the $g_m/I_D$ methodology [Jespers, 2010] can be used to calculate the optimal current flowing in $M_2$ and $M_3$. For this design, it was considered a $g_m/I_D$ ratio of 20 and thus a weak-inversion transistors operation. When in weak-inversion, transistors have a good current efficiency (low $V_{DS_{sat}}$) and a high output dynamic range [Boser, 2011]. In this conditions, one can write:

$$I_{D2} = I_{D3} = \frac{I_{D1}}{2} = 1\mu A \tag{4.13}$$

The bias voltage $V_{bp1}$ is generated as in Figure 4.10 to drive $2\mu A$ into $M_1$. Next, the n-channel current mirrors impose $3\mu A$ into $M_{10}$ and $M_{11}$ using the $V_{bn1}$ bias.

Therefore, $V_{bp2}$ and $V_{bn2}$, bias the $M_8$, $M_6$, $M_4$, $M_5$,$M_7$, $M_9$ folded-cascode and cascode current mirror to allow $2\mu A$ in each branch and saturation operation for each transistor.

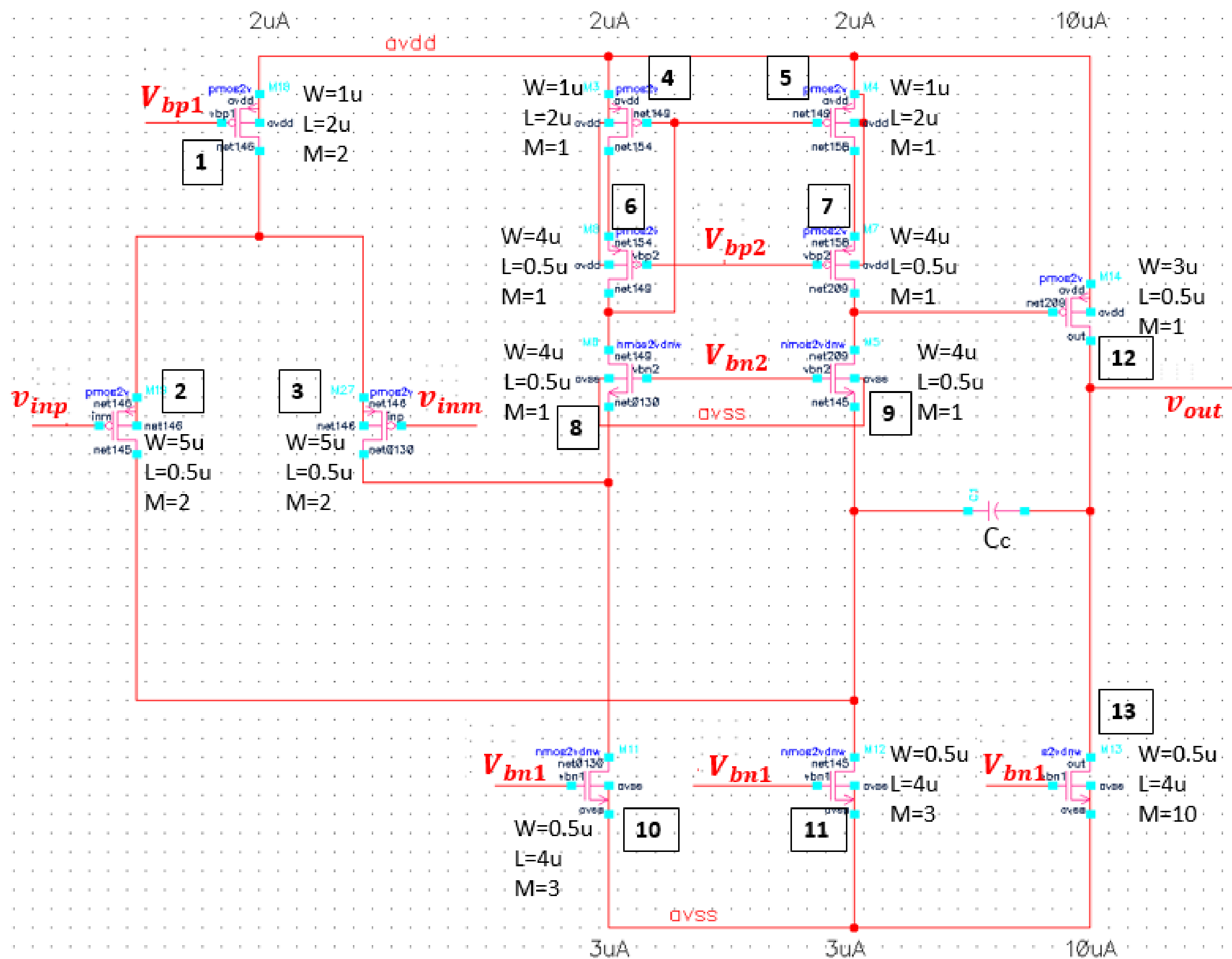

Figure 4.9 Folded-cascode OTA with second stage and Miller compensation

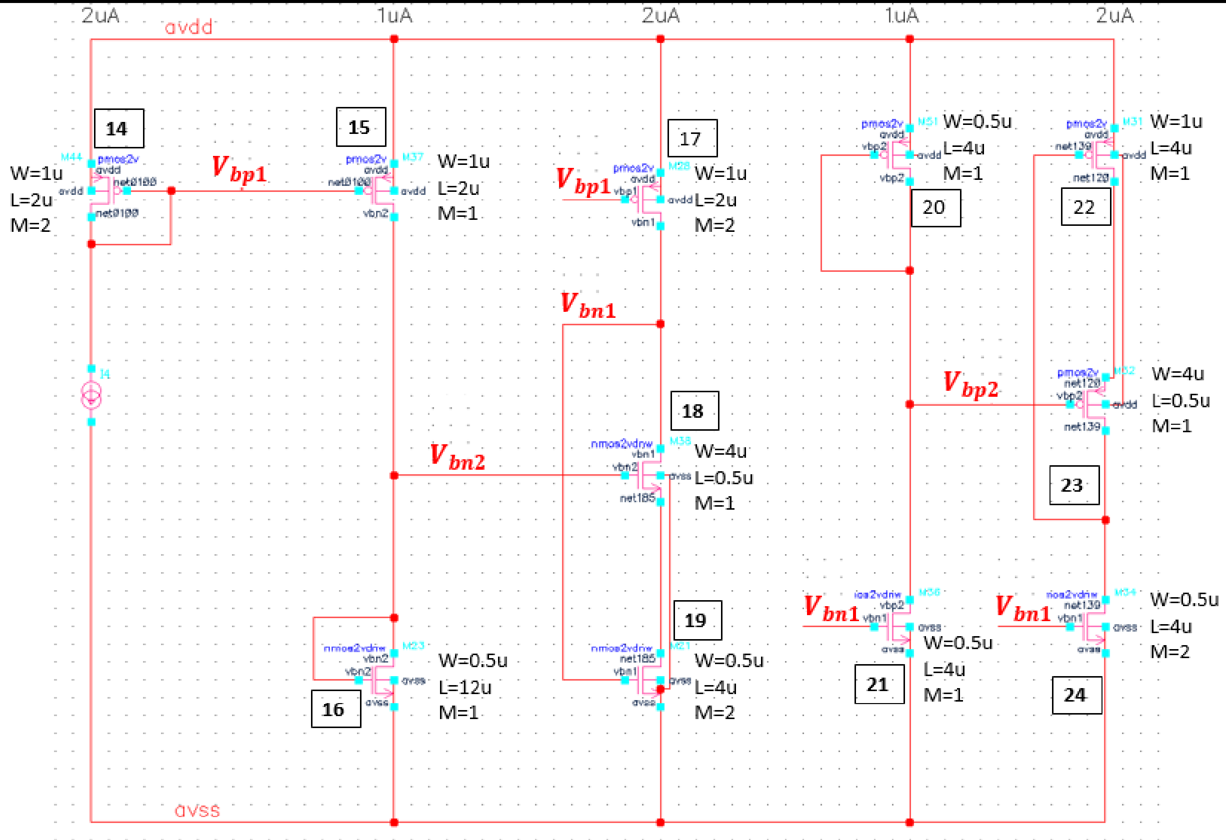

Figure 4.10 Two stages Folded-cascode amplifier – biases generation

To design the common-source output stage, one have to consider:

$$g_{m12} > 3g_{m2} \tag{4.14}$$

If $g_{m12} = 85\mu S$, at least $10\mu A$ should flow through the output stage. It results in a $16\mu A$ total current consumption for the amplifier and $8\mu A$ for the bias generation system.

A DC simulation is, at this stage, performed to check the devices operating point and the polarizations.

Next, the theoretical gain calculation was compared to the simulation results. Considering the channel length modulation effect, the overall input-output voltage gain is:

$$A_v = g_{m3}\times[(g_{m9}\times ro11||ro3\times ro9)||(g_{m7}\times ro7\times ro5)]\times g_{m12}\times(ro12||ro13) \tag{4.15}$$

Estimated calculation leads to an amplification factor of 38856, corresponding to a gain of 91.78 $dB$.Using this value, the C2V output accuracy can be calculated:

$$precision\ [\%] = \beta\left(\frac{1}{\beta} - \frac{A_v}{1+\beta A_v}\right) = 0.0025 \tag{4.16}$$

Which proves that the targeted precision of 0.1% is guaranteed.

An AC analysis is performed to validate the amplifier frequency response. In Figure 4.11, the amplifier module and phase are plotted. The simulated amplifier gain is 92 $dB$.

Further, Table 4.2 summarizes the amplifier performances; stability results show 89° of phase margin and a bandwidth of $1.38\,MHz\left(\beta=\frac{1}{10}\right)$ which is consistent with the amplifier specifications and theoretical designed values.

In this section, the C2V two stages folded-cascode amplifier design and validation were presented; next, the derivative block design is discussed.

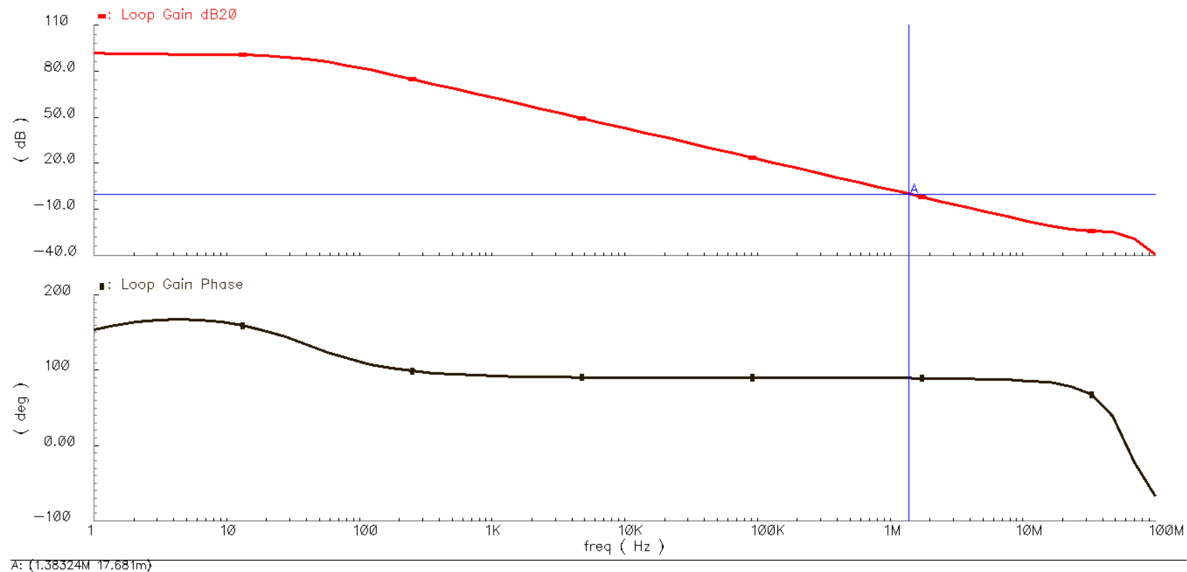


Figure 4.11 Amplifier Module and Phase – stability analysis

| | |
|---|---|
| Power supply ($V_{dda}$) | $1.6\,V$ |
| Current consumption ($I_{dd}$) | $24.3\,\mu A$ |
| Output precision | 0.025 % |
| Bandwidth ($\beta=\frac{1}{10}$) | $1.38\,MHz$ |
| Output dynamic range | [0.23 V; 1.42V] |

Table 4.2 C2V amplifier performances

## 4.4 Switched capacitor derivative block

The derivative block role is to process the C2V output and to deliver its derivative. By definition, a discrete signal derivative is obtained by subtracting two consecutive samples. In other words, the C2V output must be sampled and hold at least during two sampling periods. This is the very principle of operation of the derivative block designed and presented in this study. The circuit is using the switched capacitors technique to implement the derivative functionality. To obtain the differential output, the derivative inputs can be inversed (Figure 4.12 (a) and Figure 4.12 (b)). Since the derivative block is not faster than the C2V and the closed-loop gain is lower than for the C2V, the same amplifier designed for the C2V can be used to implement the switched capacitor derivative.

An illustration of the derivative block (Figure 4.12) and its associated chronograms (Figure 4.13) are shown next; the derivative block corresponding to the *x*-axis is presented and is assumed that the *y* and *z*-axis derivative blocks are identical to this one. The capacitance values are: $C_{INa} = C_{INb} = C_F = C_{Fa} = C_{Fb} = 500fF$.

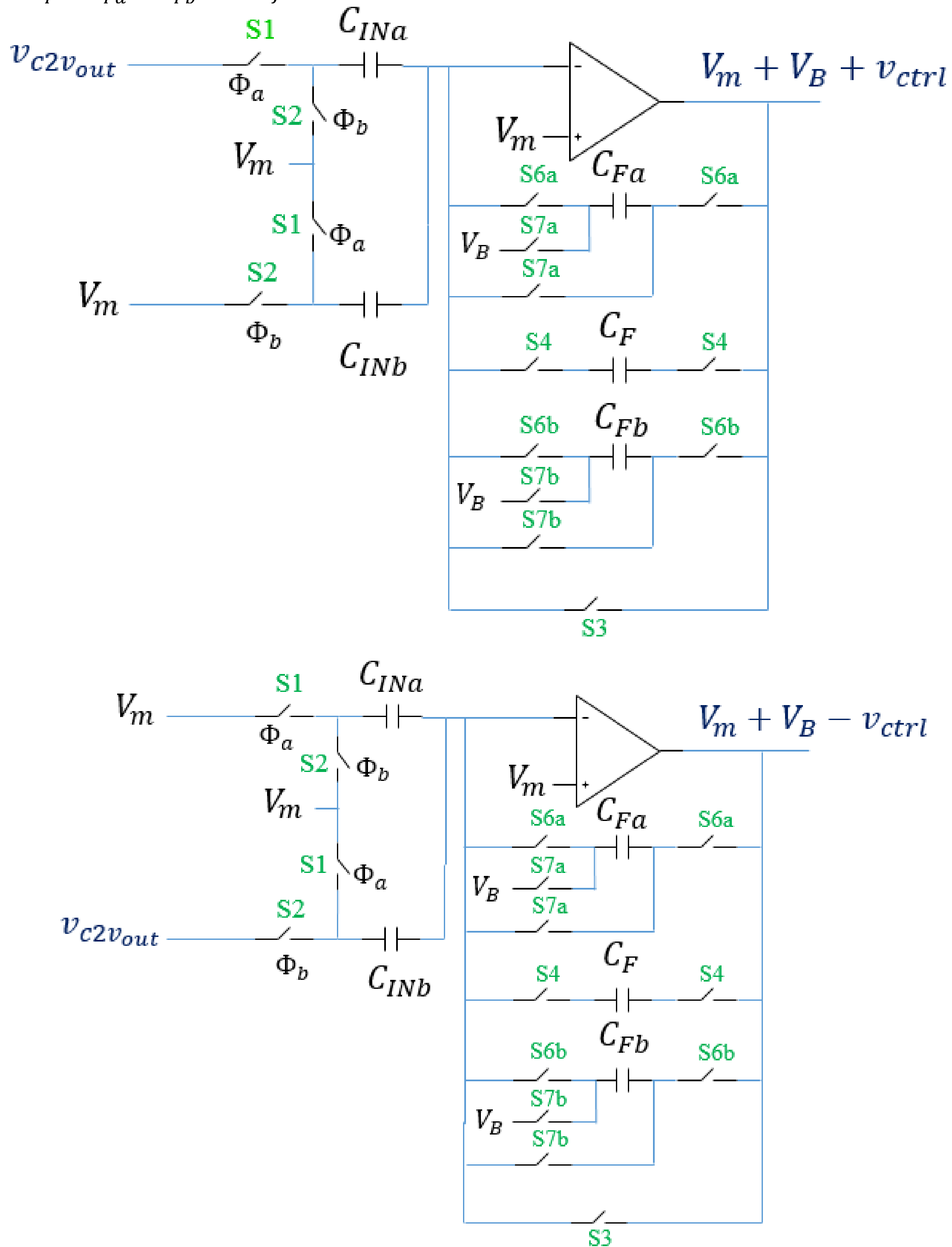


Figure 4.12 (a) and (b) An illustration of the derivative block

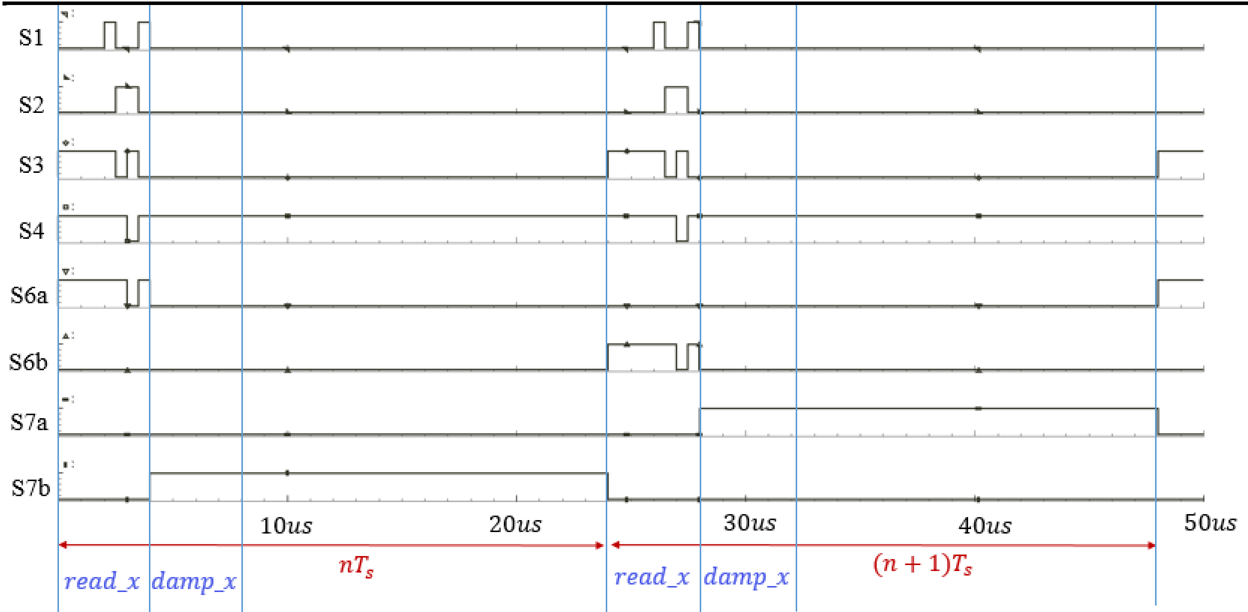


Figure 4.13 Chronograms of the derivative block

In Figure 4.13 the switches chronograms are given for two sampling periods. One sampling period lasts $24\mu s$ comprising one *x*-axis reading phase, one *y*-axis reading phase, one *z*-axis reading phase and three damping phases per axis. The reading and the damping phases are equal and they last 4 $\mu s$ each one.

The clocks are active on rising edge and accordingly, one can notice in Figure 4.13 that during the reading phases several clocks change state. A zoom on those clocks during the x-axis reading phase is shown in Figure 4.14; the reading excitation signals Ex_n and Ex_p are also illustrated in this figure. The reading phase has five sub-phases noted from 1 to 5 in Figure 4.14.

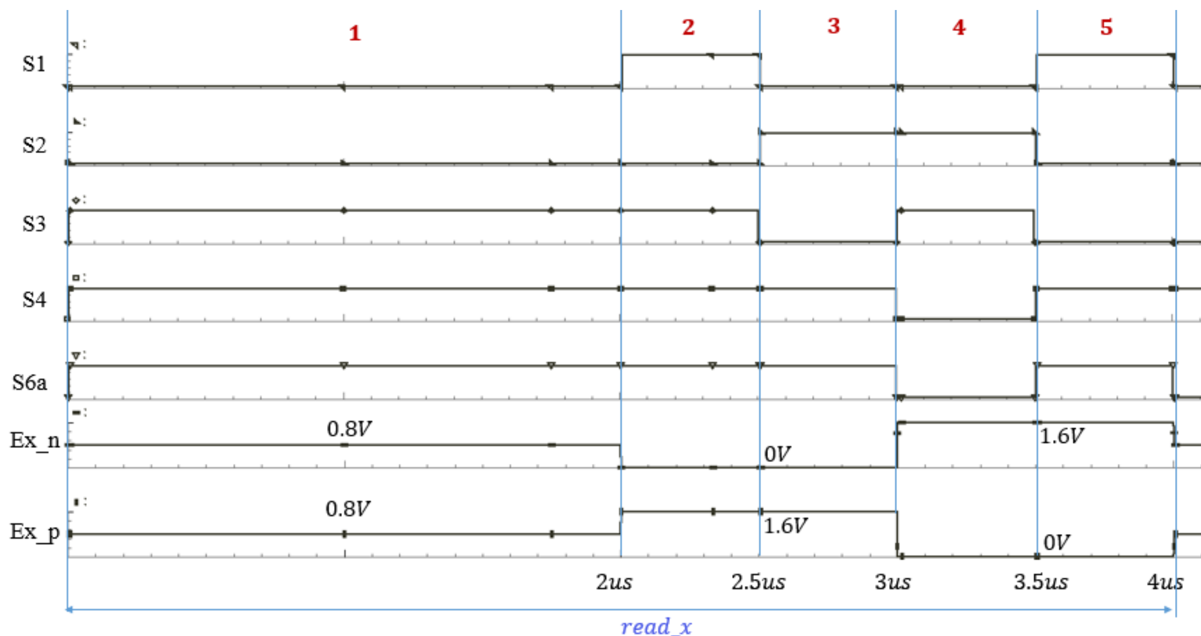


Figure 4.14 Chronograms of the derivative block

During the first sub-phase 1, the switches $S1, S2$ are open and the switches $S3$, $S4$ and $S6a$ are closed, resetting the capacitances $C_F$ and $C_{Fa}$. When sub-phase 2 occurs, $S1$ closes connecting $C_{INa}$ to the input and $C_{INb}$ to $V_m$. If $v_{os}$ is the amplifier offset, and $V$ the C2V output, the voltages stored in $C_{INa}$ and $C_{INb}$ in sub-phase 2 are:

$$V_{CINa} = V - V_m - v_{os}$$
$$V_{CINb} = -v_{os} \tag{4.17}$$

Where $V_{Cx}$ is the voltage across the capacitance $Cx$.

Then, during sub-phase 3, $S1$ and $S3$ are open and S2 closes connecting both $C_{INa}$ and $C_{INb}$ to $V_m$. The voltages sampled on $C_{INa}$ and $C_{INb}$ are:

$$V_{CINa} = -v_{os}$$
$$V_{CINb} = -v_{os} \tag{4.18}$$

Consequently, the voltage sampled and integrated in $C_F$ and $C_{Fa}$ is:

$$V_{(C_f||C_{Fa})} = \frac{1}{2}(V - V_m) \tag{4.19}$$

The $\frac{1}{2}$ ratio comes from the feedback factor since only $C_{INb}$ is connected to the amplifier input during this sub-phase.

Next, during sub-phase 4, $S4$ and $S6a$ open disconnecting $C_F$ and $C_{Fa}$; $S3$ closes in a unity-gain feedback configuration. $S1$ is still open and $S2$ closed (since the beginning of sub-phase 3) thus the voltages stored across $C_{INa}$ and $C_{INb}$ are:

$$V(C_{INa}) = -v_{os}$$
$$V_{CINb} = -v_{os} \tag{4.20}$$

During sub-phase 5, $S1$ closes and $S2$ opens as well as $S3$. $S4$ and $S6a$ are closed, reconnecting $C_F$ and $C_{Fa}$ to the circuit. The voltages sampled on $C_{INa}$ and $C_{INb}$ are:

$$V_{CINa} = V - V_m - v_{os}$$
$$V_{CINb} = -v_{os} \tag{4.21}$$

Finally, the voltage integrated in $C_F$ and $C_{Fa}$ during sub-phase 5 is:

$$V_{(C_f||C_{Fa})} = \frac{1}{2}(V_m - V) \tag{4.22}$$

Since $C_F$ and $C_{Fa}$ already integrated a sample during sub-phase 3, the total voltage across these capacitances when the reading phase ends is:

$$V_{(C_f||C_{Fa})} = V - V_m = V(nT_s) \tag{4.23}$$

When the next $x$-reading phase occurs (sampling period $(n+1)T_s$ ), the sequence is similar except that $C_{Fa}$ is replaced with $C_{Fb}$ and $S6a$ with $S6b$.

After the reading phase, the damping phase occurs by opening $S6a$ and disconnecting $C_{Fa}$ to hold the sample $V(nT_s)$ until the next reading cycle. In the same time, $S7b$ closes connecting $C_{Fb}$ to the circuit and to $V_B$. $C_{Fb}$ holds the sample $V(n-1)T_s$, thus, during the damping phase, the derivative block outputs $V_m + V_B + [V(nT_s) - V(n-1)T_s]$ or $V_m + V_B + V_{ctrl}$. This value is kept until the end of the sampling period and applied each time the damping is enabled. It is clear though

that the output common mode is $V_m$ during the reading phase and $V_m + V_B$ during the last phase of the sampling period.

The derivative block has been simulated to check its functionality. Figure 4.15 presents a zoom of the derivative block outputs during the reading phase: the C2V output (light blue line) and the differential derivative block waveforms (red and blackline) are shown; the five sub-phases can be noticed. During sub-phases 1, 2 and 4, the amplifier has a unity gain configuration while during the sub-phases 3 and 5, the derivative block samples the C2V output.

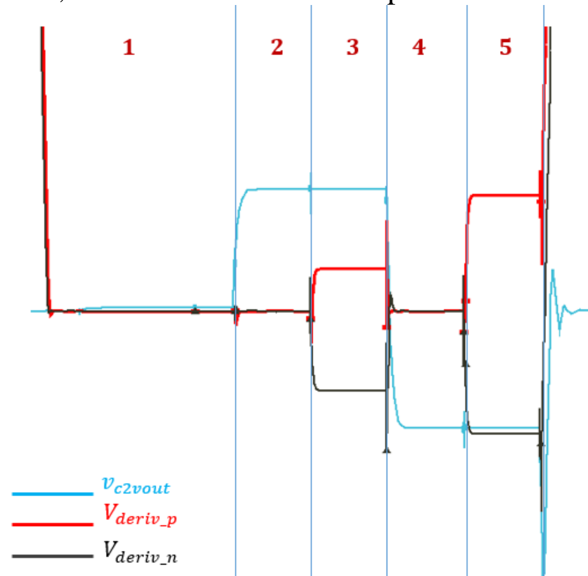


Figure 4.15 Derivative block simulation and illustration of the derivative block outputs during the reading phase

When zooming out on the derivative outputs waveform, out of the reading phases, one can notice the plots presented in Figure 4.16. The common mode change is obvious to $V_m + V_B = 1.2V$. The simulation is performed in closed-loop hence the system is progressively damped and the sensor velocity slows until becoming null when the system reaches the steady state. In steady state, and out of the reading phases, the derivative outputs $V_{deriv_p}$, $V_{deriv_n}$ are equal to $1.2V$.

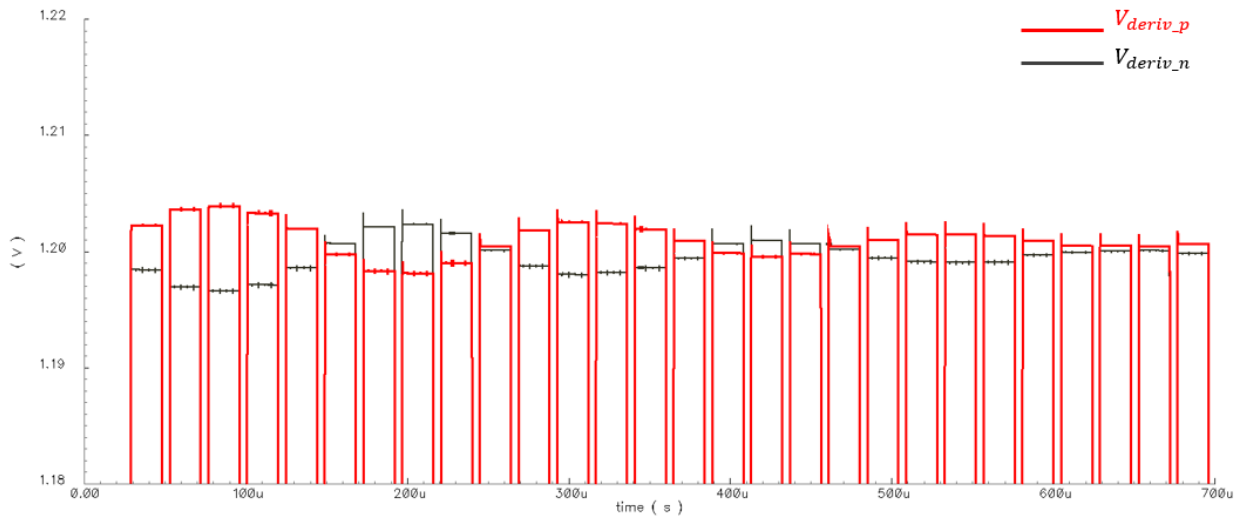


Figure 4.16 Derivative block simulation and illustration of the derivative outputs out of the reading phases

This section presented the derivative block design and chronograms.. The switched capacitor technique is used to output $V_{deriv_p} = V_m + V_B + V_{ctrl}$ and $V_{deriv_n} = V_m + V_B - V_{ctrl}$. An additional block will introduce the derivative gain $k_d$.

## 4.5 Derivative gain block

The derivative gain block aim is to multiply the control voltage $V_{ctrl}$, provided by the derivative block, by a certain gain value $k_d$, which was previously calculated (Chapter 3): $k_d = 300$. One can write the block input-to-output relationship as:

$$v_{gain_p} = V_m + V_B + k_d \times V_{ctrl}$$
$$v_{gain_n} = V_m + V_B - k_d \times V_{ctrl} \quad (4.24)$$

A representation of the switched-capacitors derivative gain block is shown in Figure 4.17 and its functioning will be next detailed. There are two gain stages: *Stage1* and *Stage2,* since a gain value of 300 seemed too large to be implemented using one amplifier. The overall voltage gain $A_v$ is:

$$A_v = A_{v_{stage1}} \times A_{v_{stage2}} \quad (4.25)$$

The first stage is a low-gain continuous-time fully-differential amplifier, while the second one is a switched-capacitors fully differential amplifier with common-mode feedback (CMFB) control; the derivative gain block has an output common mode of $V_{cm} = 1.2V$.

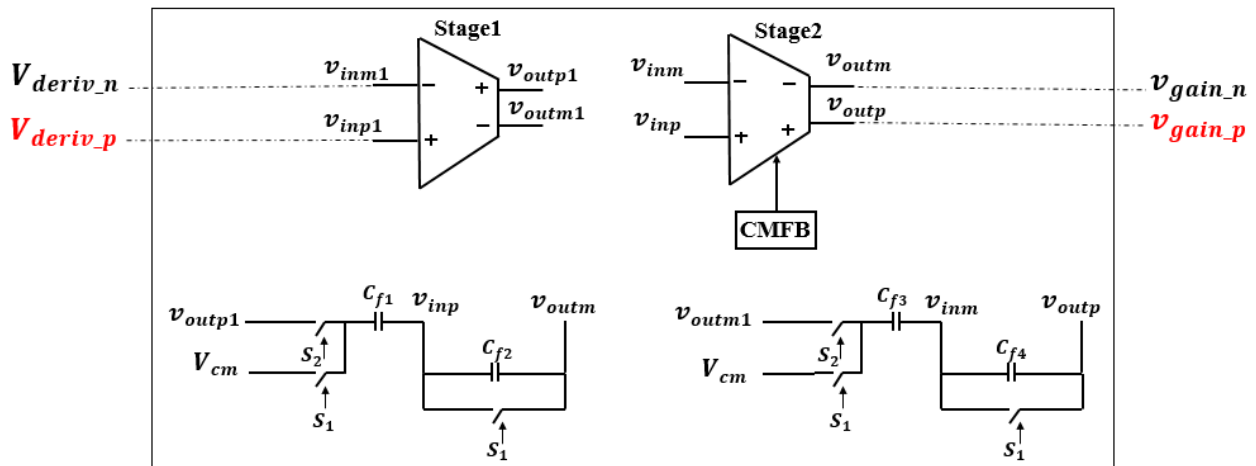


Figure 4.17 A representation of the switched-capacitors derivative gain block

The transistor level schema of the first gain stage is shown in Figure 4.18; the configuration is a common-source stage with diode-connected load. Transistors $M_3$ and $M_4$ are called diodes because their behavior is similar to a resistor since the gate is connected to the drain, keeping the transistor always in saturation. This configuration was chosen due to its low power consumption and high bandwidth.

One can find the first stage voltage gain as (4.26) or as (4.27) by neglecting the channel length modulation:

$$A_{v_{stage1}} = -g_{m1} \times \left(\frac{1}{g_{m3}} || ro1 || ro2\right) \tag{4.26}$$

$$A_{v_{stage1}} = \frac{-g_{m1}}{gm_3} \tag{4.27}$$

Further, since the same current is flowing both in the differential pair and in the diode load, the gain depends on the ratio between the two transistors ratio (10 in our case), on the charge carriers mobility and on the gate oxide capacitance:

$$A_{v_{stage1}} = -\sqrt{\frac{\mu_n C_{ox}(W/L)_1}{\mu_p C_{ox}(W/L)_3}} = -3.1 \tag{4.28}$$

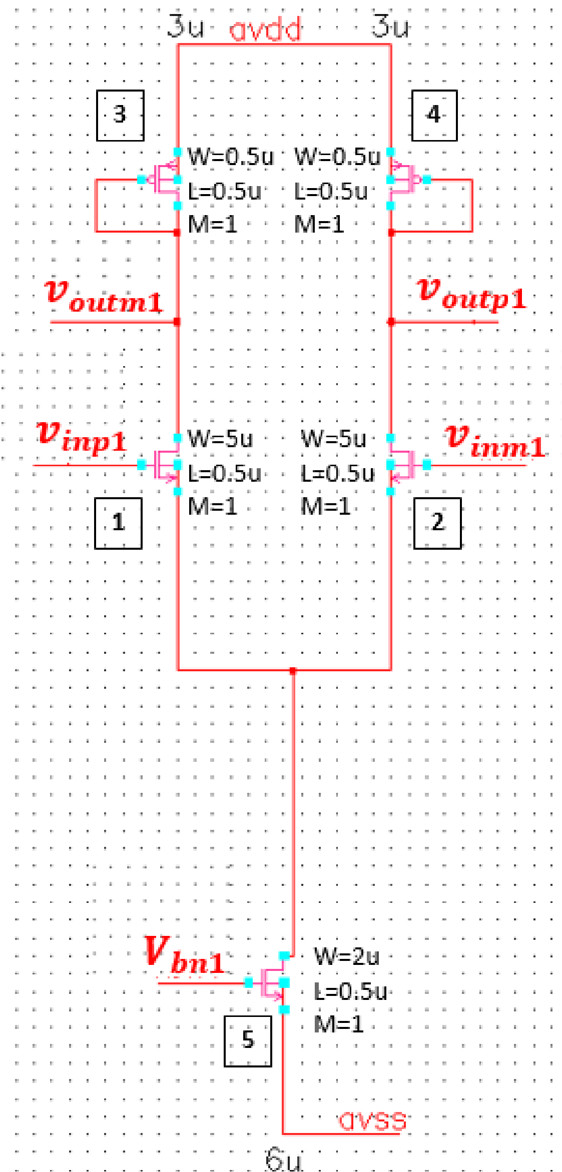


Figure 4.18 A representation of the single stage fully-differential amplifier

The design was checked using DC, transient and AC analyses. Simulation results revealed a $g_{m1}$ of $59.75\mu S$ and a $g_{m2}$ of $19.28\mu S$ ; thus, a gain of $A_{v_{stage1}} = -3.09$. The amplifier consumes $6\mu A$. The generation of bias $V_{bn1}$ will be next shown.

Going further, the second stage has to implement a gain of at least $k'_d = 100$. For the second stage a switched capacitor amplifier, as in Figure 4.17 has been implemented. It can be noticed that the first stage outputs $v_{outm1}$ and $v_{outp1}$ are the inputs of the second stage which has two non-overlapping phases: *reset* and *amplification*. The two clocks are represented in Figure 4.19.

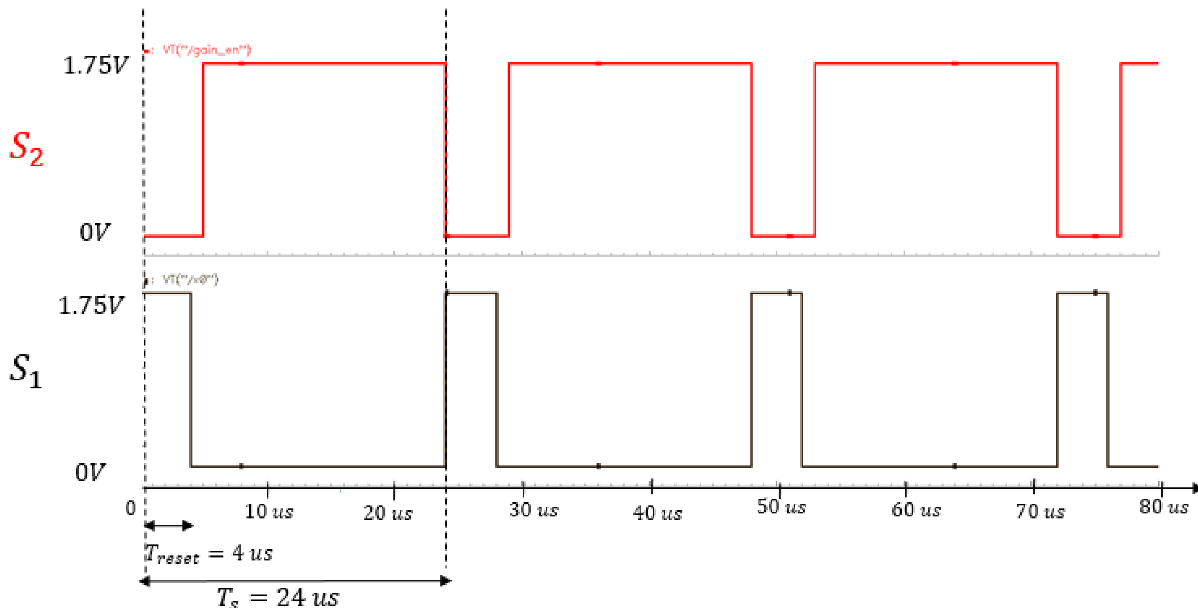


Figure 4.19. *Stage2* operating phases clocks: $S_1(reset)$ and $S_2(amplification)$

During the reset phase, switches $S_1$ are closed and $S_2$ open, allowing the reset of the capacitors $C_{f1}, C_{f2}, C_{f3}, C_{f4}$. Next, during the amplification phase, switches $S_2$ are closing, connecting the inputs $outm1$ and $outp1$to the $C_{f1}$ and $C_{f3}$, respectively.

If $C_{f2} = C_{f4} = 100fF$ and $C_{f1} = C_{f3} = k'_d * C_{f2}$ then the *Stage2* outputs during the amplification phase are:

$$v_{outm} = \frac{-C_{f1}}{C_{f2}} \times v_{outp1}$$
$$v_{outp} = \frac{-C_{f3}}{C_{f4}} \times v_{outm1} \quad (4.29)$$

The amplifier itself (*Stage2*) is a fully-differential structure with switched capacitors CMFB. Figure 4.20 shows the transistor level schema of the *Stage2* amplifier and in Figure 4.21 the bias generations are presented.

The two-stages amplifier presented in Figure 4.20 has a n-channel differential input pair and is a common source configuration. This first stage output is the node controlled by the common-mode feedback. The second stage is also a common source configuration. The amplifier is compensated using the *RC* method; the output charge is $C_L = 1pF$.

If it is to calculate the feedback-factor $\frac{1}{\beta}$, one should take in consideration the ratio between the capacitances $C_{f1}$ and $C_{f2}$, and between $C_{f3}$ and $C_{f4}$ which is $k'_d = 100$. Hence, $\frac{1}{\beta} = 100$.

To calculate the amplifier compensation capacitance $C_c$, equation (4.11) can be used. For this design $C_c = 300fF$ . Next, to calculate the GBW we have to specify how fast the amplifier has to be. Supposing that we expect a valid amplification value in $2\mu s$ , then $GBW = \frac{1}{\beta} \times 0.31\ MHz = 31\ MHz$ for a 1% amplifier output accuracy.

Equation (4.12) is used to calculate $g_{m1} = g_{m2} = 48\mu S$; thus we can estimate the current flowing into the differential input pair to $3\mu A$ in each branch.

For the output stage, $g_{m9} > 3g_{m2}$. Therefore, we have chosen $g_{m9} = 250\mu S$ and $I_{D9} = 24\mu A$. The compensation resistance is usually designed using equation (4. 30) [Razavi, 2001]:

$$R_c = \frac{1}{g_{m9}} \tag{4.30}$$

Thus, $R_c = 5k\Omega$.

The amplifier consumes $54\mu A$ and the biases generation circuit $3\mu A$.

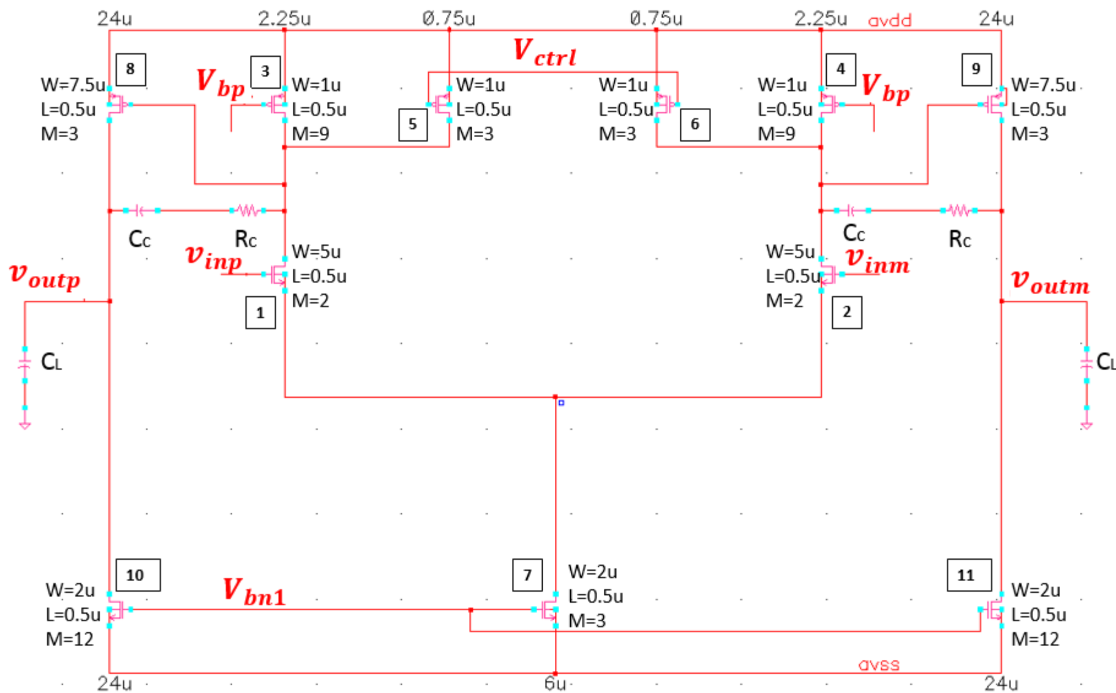

Figure 4.20. Transistor level schema of the *Stage2* fully-differential amplifier

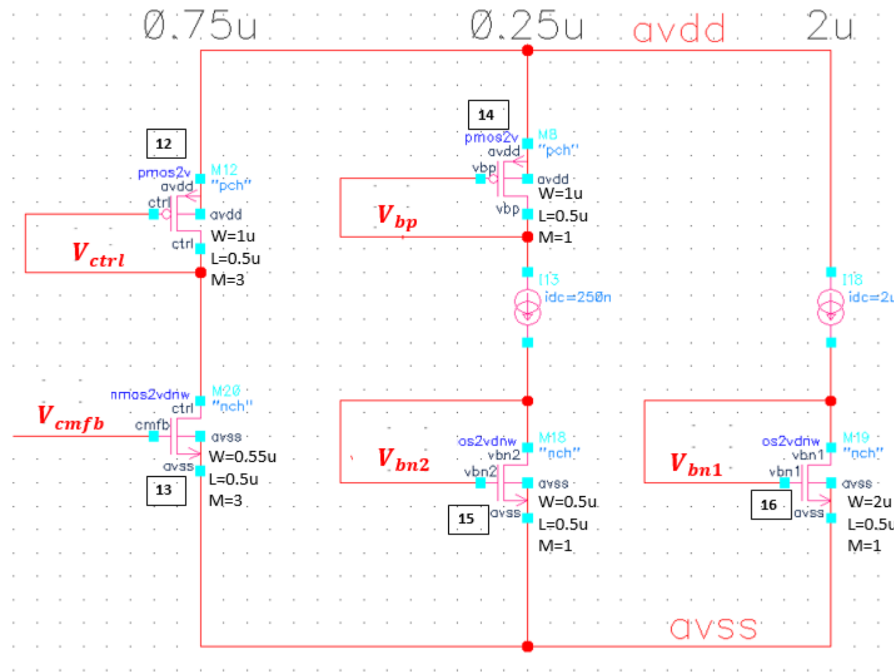


Figure 4.21. Biases generation of the derivative gain block

The frequency response of the amplifier was simulated and is presented in Figure 4.22. The measured frequency-unity-gain is $27\ MHz$ and the bandwidth gain $70dB$ with a phase margin of $60°$.

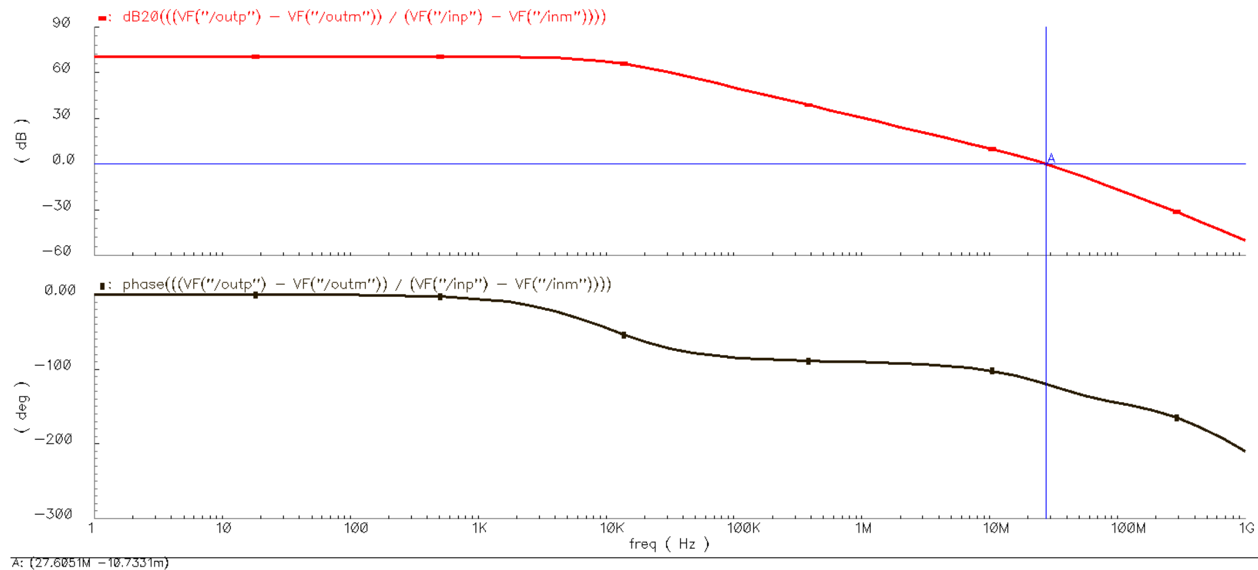


Figure 4.22. Modulus and phase waveforms – Amplifier AC simulation

Another issue to be addressed regarding this fully-differential amplifier is the output Common Mode Feedback Control. The CMFB is generally needed to control the common mode voltage at different nodes that can't be controlled by the amplifier negative feedback. In order to generate the specified common mode voltage, the CMFB structure senses the real amplifier common mode output voltage and compares it with a fixed-level common mode. The difference

between the sensed voltage and the fixed one is then used to balance the common mode level. For example, if the CMFB structure senses a diminution of the common mode, it will apply a higher control voltage to compensate; complementary, if the CMFB structure senses an increased common mode voltage, it will diminish the control voltage.

The switched capacitor CMFB used to control the amplifier shown in Figure 4.20 is presented in Figure 4.23 where $C_1 = C_2 = C_3 = C_4 = 500fF$. The topology is inspired from [Sansen, 2006] and works as follows: during phase 1, switches $S_1$ are closed and switches $S_2$ are open, thus, capacitors $C_1$ and $C_2$ provide CMFB while $C_3$ and $C_4$ are reset to a certain voltage $V_{vbn2}$. During phase 2, switches $S_1$ are open and switches $S_2$ are closed; capacitors $C_1$ and $C_2$ are reset to $V_{bn2}$ while $C_3$ and $C_4$ provide CMFB. By resetting the capacitors to a fixed and known voltage $V_{bn2}$, it allows to keep the $V_{cmfb}$ voltage to the desired voltage level. Then, the voltage $V_{cmfb}$ is used to control $M_{13}$ gate and to generate the desired current through $M_{12}$ and $M_{13}$, which is $0.75\mu A$. Same gate voltage as for $M_{12}$ ($V_{ctrl}$ is used to bias the amplifier p-channel transistors $M_5$ and $M_6$ and to control the $M_1$ and $M_2$ drain nodes.

If these nodes voltage level starts decreasing is because the current through $M_5$ and $M_6$ is increasing and because $V_{ctrl}$ increases. To solve, $V_{cmfb}$ must decrease to keep the same current level of $0.75\mu A$ through $M_{12}$ and $M_{13}$. The functioning is complementary when, the $M_1$ and $M_2$ drain voltages are increasing.

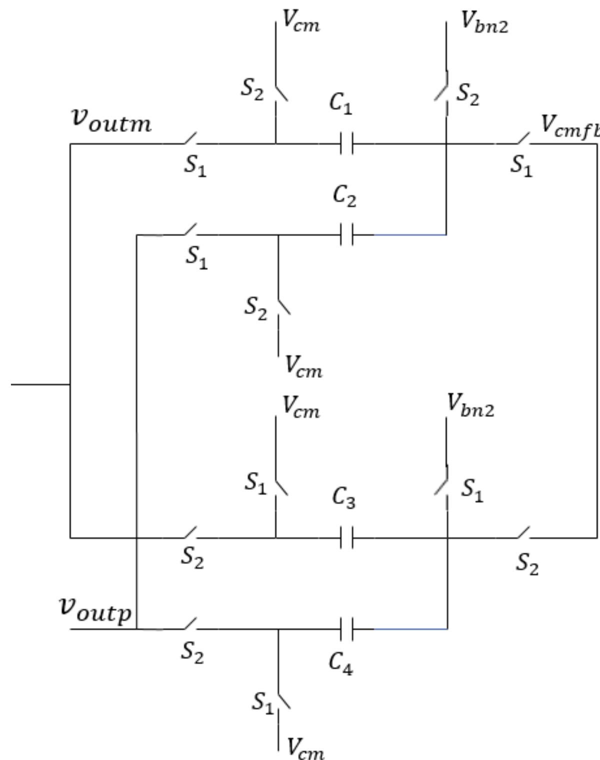


Figure 4.23 Switched-capacitors CMFB

Finally, the last point to be taken in consideration is the start-up condition. Considering an amplifier input that drives the n-channel differential pair transistors OFF, then the output common

mode is no longer predictable and controllable. This why, a forced common mode is imposed during at least one sampling period $T_s = 24\mu s$ as in Figure 4.24 using the PMOS switches $M_{17}$ and $M_{18}$; $V_{cm} = 1.2V$.

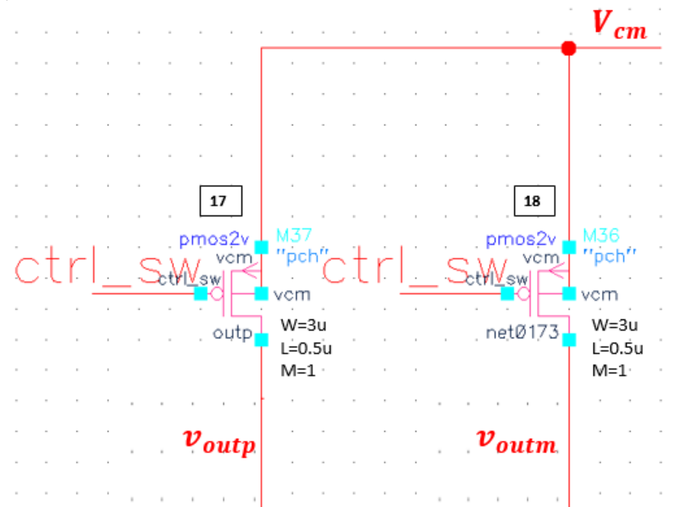


Figure 4.24 PMOS switches to force the start-up output common mode

The overall system presented in Figure 4.17 was simulated in order to check its functioning. For sin inputs with an amplitude of $2mV$ (peak-to-peak) and a common mode of $1.2V$, we are expecting an output of $600mV$. Figure 4.24 presents the transient simulation results; one can notice the common mode fixed at $1.2V$. The output amplitude is $591mV$ which results in a $k_d$ gain value of 295.5.

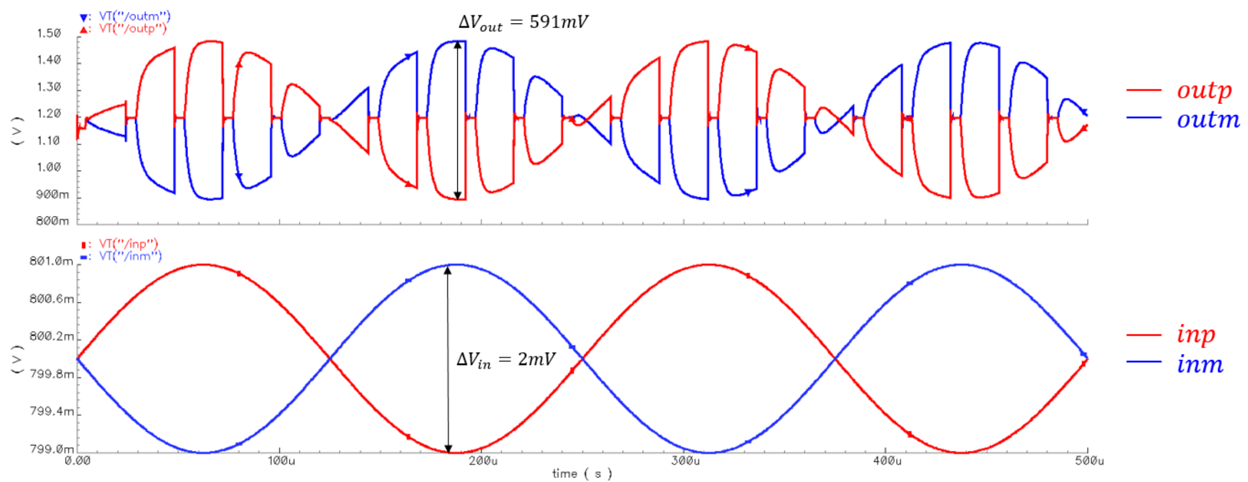


Figure 4.25 Transient analyze results of the overall derivative gain block

## 4.6 CMOS Switches

The architecture presented in this thesis implements the switched-capacitors technique for reasons already mentioned. Therefore, additionally to the amplifier, the switches have an important role.

CMOS switches are either single-transistors (p-channel or n-channel) or complementary switches ((p-channel and n-channel transistors). The performances of a CMOS switch are given by the speed and the accuracy. If the speed is determined by the transistor on-resistance and by the capacitors to be charged/discharged, for the accuracy, charge injection cancellations techniques [Razavi, 2001] can be used to improve the performances.

Considering a single transistor switch, its on-resistance can be expressed as:

$$R_{on} = \frac{1}{\mu_{n,p} C_{ox} \frac{W}{L}(V_{GS} - V_{th})} \tag{4.31}$$

The transistor is supposed to work in the linearized portion of the triode region (deep triode). From (4.31) it can be noticed that a small $R_{on}$ is achieved with a large $\frac{W}{L}$ ratio.

If $C_H$ is the switch load capacitor, then the time constant is:

$$\tau_{switch} = R_{on} C_H \tag{4.32}$$

Design practices usually consider at least $7\tau_{switch}$ for the switch charge/discharge duration.

Moreover, in the case of a complementary n-p switch, as in Figure 4.26, the two transistors on-resistances are connected in parallel. Thus, the equivalent on-resistance becomes:

$$R_{on,eq} = R_{on,n} || R_{on,p} = \frac{1}{\mu_n \, C_{ox} \frac{W}{L} (V_{GSn} - V_{thn})} || \frac{1}{\mu_p \, C_{ox} \frac{W}{L} (V_{GSp} - V_{thp})} \tag{4.33}$$

Which is obviously smaller than $R_{on}$ and therefore $\tau_{switch}$ is smaller.

Since the load capacitances in this work range from $300fF$ to $1pF$ and the desired speed has same orders of magnitudes (switches charge/discharge duration superior to $1\mu s$), same switch presented in Figure 4.26 has been used for all the system blocks: C2V, derivative. derivative gain block and excitation signals block.

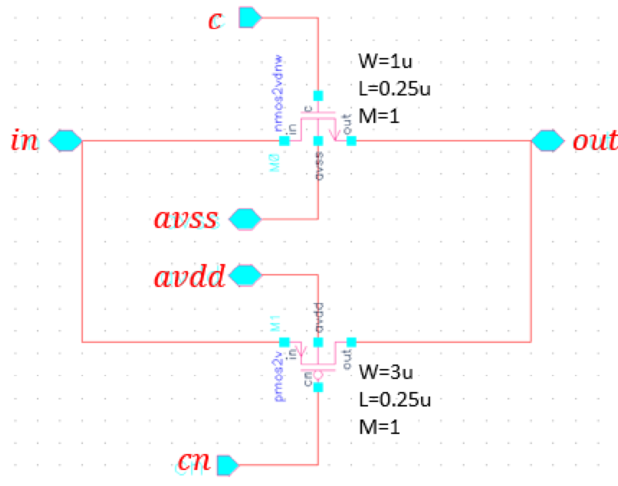


Figure 4.26 Complementary CMOS switch

To check the switch performances, the $R_{on}$ resistance was simulated. The result is presented in Figure 4.27; the maximum $R_{on}$ resistance is $3.14k\Omega$. Afterwards, the switch was added in each system block and its functioning validated.

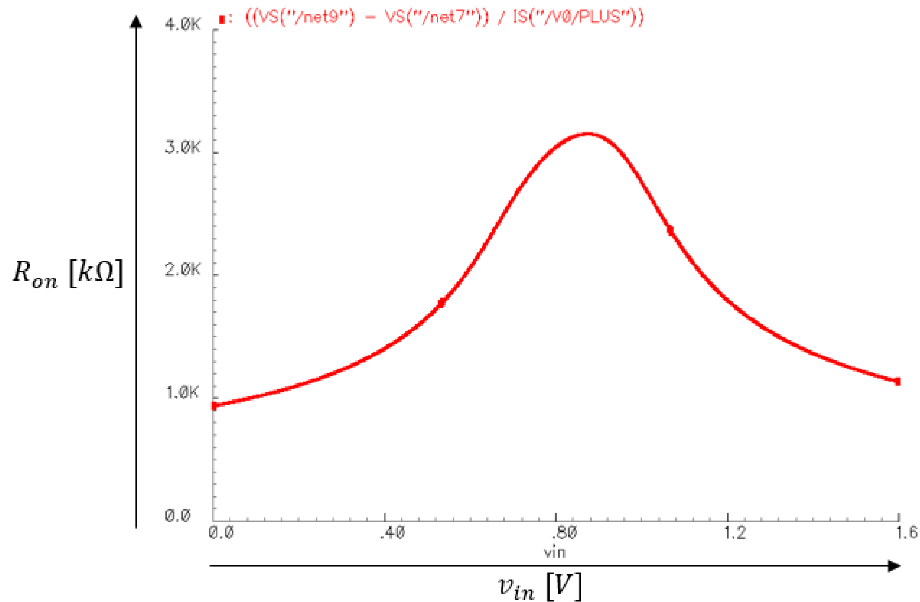


Figure 4.27 Switch $R_{on}$ resistance simulation

## 4.7 Excitation signals block

The block presented in section 4.5 amplifies the derivative output, which is available and useful only during the damping phases; otherwise, the excitation signals in Figure 4.5 (b) have to be applied on the MEMS fixed plates. To enable this operation, an additional block was added to apply the corresponding signals depending on the system functioning phase, as in Figure 4.28.

There are two non-overlapping phases that control switches $S_r$ and $S_d$ (Figure 4.29); when $S_r$ is closed, $Ex_p$ and $Ex_n$ are applied on x-axis fixed plates. Then, when $S_d$ closes the derivative gain amplifier outputs are applied on x-axis fixed plates.

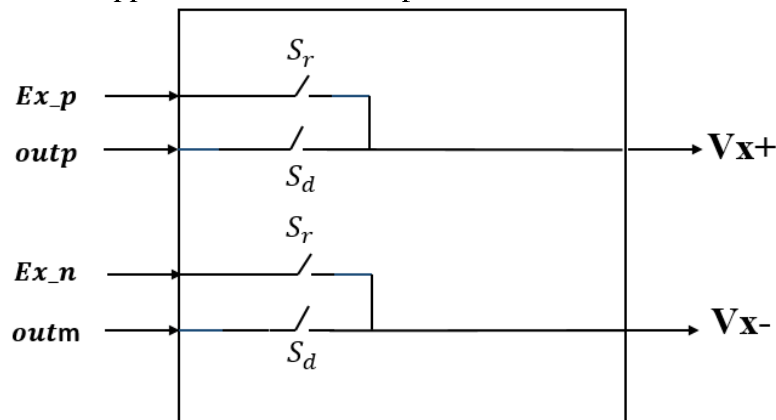


Figure 4.28 A representation of the excitation signals block

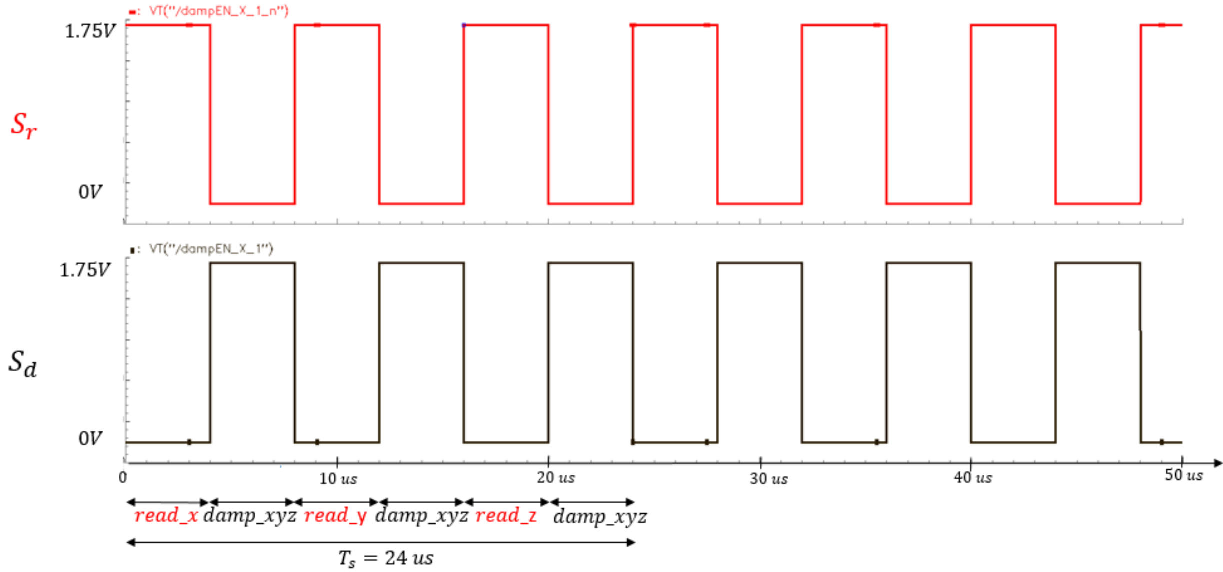


Figure 4.29 $S_r$ and $S_d$ control signals

This block is the last one from the loop and its outputs are directly applied on the MEMS. A full-system closed loop simulation and validation can now be performed.

## 4.8 Closed-loop system validation

To validate the closed-loop operation using the Cadence tool, a test bench comprising all the blocks detailed in this chapter has been built. In order to control the proof mass movement along the x-axis using the simultaneous damping method, the chronograms have been designed to allow a sampling period of $T_s = 24\mu s$ with a reading phase equal to the damping phase, each one of $4\mu s$. The *Stage2* derivative gain block has a gain of $k'_d = 100$ and thus an overall gain of $k_d = 300$.

The sensor quality factor is $Q = 2000$. The external acceleration of $9.8\, m/s^2$ was simulated using a voltage step varying from 0 to $9.8V$ with a rising time of $1ns$.

We are interested in validating the electrostatic damping principle and checking the simultaneous damping efficiency by measuring the system settling time. Further, the Cadence simulated settling time will be compared with the result obtained using the Matlab-Simulink model.

The proof mass displacement transient simulation result is presented in Figure 4.30. The simulation is performed in closed loop and the settling time is reduced to $800\mu s$ instead of $400\ ms$ in an open-loop, without electrostatic damping, configuration. Same set up for the Matlab-Simulink model lead to a settling time value of $680\mu s$. The difference can come from the non-idealities of the CMOS blocks, charge injections but also from the start-up condition imposed for the fully-differential *Stage2* gain block; during this reset phase the voltage applied on the sensor plates is not in concordance with the real proof mass movement.

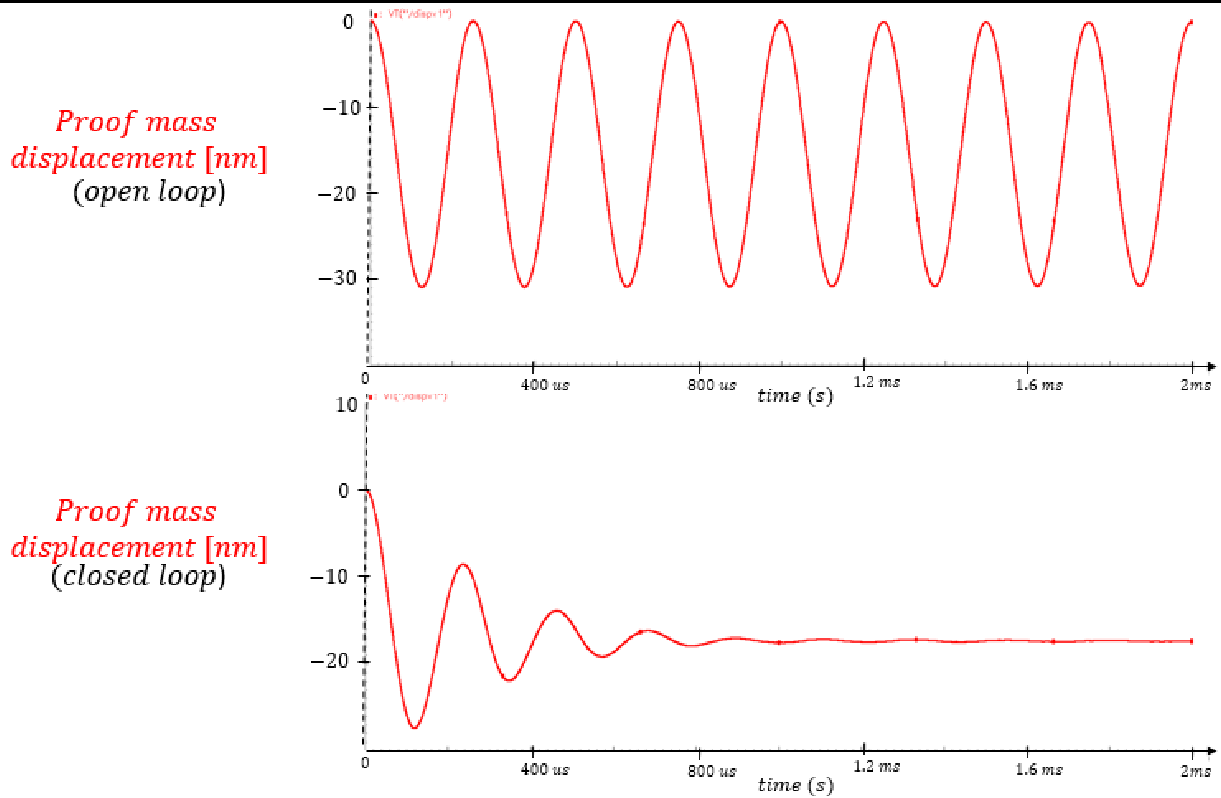


Figure 4.30 Transient simulation results comparison between the open loop displacement response (no damping) and the closed loop displacement response (damping enabled)

In terms of performances, the CMOS interface presented in this work has a power consumption of $0.2\,mW$ for a one-axis accelerometer and $0.48\,mW$ for the three-axis architecture. Table 4.3 presents a performances comparison of several closed-loop accelerometers presented in the literature that implement either a $\sum\Delta$ loop or an analog control. The power consumption as well as the surface of the CMOS interface implementing only a Derivative controller are improved over the state of the art performances.

| | [Yucetas, 2012] | [Ye, 2013] | [Xu, 2015] | [Petkov, 2005] | [Pastre, 2009] | [Zhao, 2016] | This work |
|---|---|---|---|---|---|---|---|
| Topology | PD controller | PID controller | $3th$ $order$ $\sum\Delta$ | $4th$ $order$ $\sum\Delta$ | $5th$ $order$ $\sum\Delta$ | PI controller | D controller |
| Power supply/ Power consumption (one-axis) | $3.6\,V/$ $3.6\,mW$ | $5\,V/$ $58\,mW$ | $7\,V/$ $23\,mW$ | $5V$ $/\,13mW$ | $\pm 9V$ $and$ $3.3V$ $12\,mW$ | $15V$ $and$ $3V/$ $174\,mW$ | $1.6V/$ $0.2\,mW$ (1 axis) $0.48\,mW$ (3-axis) |
| CMOS | $0.35\mu m$ | $0.35\mu m$ | $0.5\mu m$ | $0.5\mu m$ | $0.6\mu m$ | $0.35\mu m$ | $0.18\mu m$ |
| Surface (one-axis) | $6.66\,mm^2$ | $0.5\,mm^2$ | $7.8\,mm^2$ | $0.9\,mm^2$ | $9.7\,mm^2$ | $11.75$ $mm^2$ | $\approx 1\,mm^2$ *(3-axis* |
| Input range | $\pm 1.15g$ | $\pm 1.2g$ | $\pm 1.2g$ | $\pm 2g$ | $\pm\,11g$ | $\pm 50g$ | $\pm 8g$ |

Table 4.3 CMOS interface performances

In order to experimentally validate the electrostatic damping principle, a discrete components implementation of the architecture presented in Chapter 4 has been developed. The transducer, the read-out interface and other analog stages are placed on a two-layer PCB while the STM32F4 discovery board is used for the signal processing operation. The C-code developed for the excitation signals generation is attached in Appendices II and the discrete components architecture design is presented in Appendices III.

## 4.9 Summary

This chapter introduced a novel switched capacitor architecture implementing simultaneous damping control, adapted for a three-axis low power MEMS accelerometer.

The system was designed in a $0.18\mu m$ CMOS TSMC process and is compatible with a fully-integrated ASIC solution. Each section deals with a loop block, concluding with the closed loop simulation and system validation. The system operation was validated and the settling time results prove the damping efficiency. However, further improvements can be achieved in terms of noise and charge injection reduction.

# Conclusions and perspectives

Recently, consumer electronics industry has known a spectacular growth that would have not been possible without pushing the integration barrier further and further. In this context, MEMS have known an exponential growth and are, nowadays, embedded in most consumer applications. In addition, sensing multiple DoF with a unique integrated circuit has become the new trend in the Internet of Things era since both power and cost reductions are the keys of this continuously developing industry.

Capacitive MEMS inertial sensors, as the accelerometers and the gyroscopes, have won their places in consumer electronics and are currently subject to various research topics. Here, the accelerometer-gyroscope fusion research topic has been addressed and this thesis had as main objective the design of the analog front-end circuits to drive and sense an underdamped three-axis accelerometer efficiently.

Firstly, the issue related to the native underdamped architecture of the accelerometer, has been stated: long transducer settling time and weak control over the sensor behavior. Several control methods have been investigated and the proposed architecture choice has been designed and optimized to suit the MEMS designed by NXP Semiconductors. The transducer is here a dual-mass three-axis capacitive accelerometer, the proof mass of which is common to the three axes. Consequently, an acceleration measurement along the three axes can be only performed sequentially.

The analog control which implements electrostatic damping for this system, is based on the linear relationship between the net electrostatic force and the proof mass velocity estimation. As far as the acceleration measurement itself is concerned, the damping should be applied sequentially to not perturb different axes operation.

The main goal of the thesis is the design of an analog control architecture achieving low power consumption. In this context, the novel system proposed in this work has as main features the analog first stage shared among the three axes, the switched-capacitor technique used in the main loop blocks but also the analog blocks operation under a low power supply. Furthermore, no additional charge-pump block or high voltage CMOS process are required for a successful damping control. Finally, the thesis presents the development of a new damping chronogram (simultaneous damping) which improves the damping efficiency compared to the state of the art damping methodology (successive damping).

The simultaneous damping technique is based on the artificial damping generation starting from the proof mass velocity estimation and on sampling, holding and applying this very same damping value three times within the same sampling frequency. The mathematical modeling of the simultaneous damping technique has been very challenging since the overall discrete closed-loop transfer function couldn't be developed using the classical z-transform method. The simultaneous damping requires at least two different operating sampling frequencies and thus, provides a multirate control over the MEMS behavior. Using down sampling and up sampling signal processing techniques, a mathematical model that develops the multirate controller properties has been designed to give more insight in the loop stability and provide a mean to assess

the impact of the sampling frequency and gain of the loop on its stability. Using this method together with the model, the sampling frequency and the loop gain value have been determined for the CMOS implementation.

The thesis describes also each block modeling (Matlab-Simulink) and the closed loop simulations along with the concept validation. For the transducer, the read-out interface and the control block (derivative), several behavioral models have been developed and the settling time method has been used to assess the damping efficiency. Finally, the simultaneous damping architecture has been implemented in this work due to its higher performances in term of settling time.

The transistor-level design of the accelerometer signal chain is based on switched-capacitor techniques and can be further integrated within an ASIC. The design operation as well as the damping efficiency have been validated using Cadence Spectre simulations. Lastly, a discrete components architecture has been designed to experimentally validate the simultaneous damping concept.

In perspective, a fully ASIC design together with the microfabrication and the characterization is necessary to experimentally validate the integrated circuit solution. To do so, already available analog blocks such as the bandgap or the oscillator can be used; however, additional digital design is required to conceive the CMOS logic used to control the analog operation. Finally, ASIC top cell verification must be performed to validate both analog and digital operation.

Going further, a fully-differential (using both transducer masses) system solution can be imagined. Since the two masses are oppositely moving under the effect of same acceleration value and the fixed electrodes are shared between the two masses, the control voltage can no longer be applied on the fixed excitation plates. Otherwise, it will cause the desired damping effect for one of the proof masses but will drive the other mass even more instable. Two solutions can be imagined to solve these issues: firstly, the transducer fixed electrodes can be separated (one for each proof mass) if a MEMS design review is possible. In this way, different electrostatic forces can be applied on each mass and both can be controlled. Secondly, the bias voltage $V_B$ can be differentially applied on the proof masses during the damping phase and the damping effect will be in concordance with each mass motion as a result. However, another issue that may arise, is the electrostatic forces apparition between the sensor shield and the masses, which can perturb the operation. The MEMS Verilog-A Spectre model can be adjusted in order to take into account the phenomenon and to validate this possible implementation. In addition, design improvements in terms of noise and charge injections can be further achieved by employing low-noise and charge injection reduction techniques.

In conclusion, the thesis presented a novel simultaneous damping architecture adapted for a three-axis capacitive transducer, that considerably reduces the settling time compared with the state of the art approach (2 times smaller, for a sampling time of $24\ \mu s$ ) and 500 times smaller compared with an open loop operation. The system stability can now be studied using a new method that certifies the closed loop stability for a certain sampling time and loop gain value. Transistor-level design validated the overall mathematical and behavioral modeling.

# Bibliography

1. [Aaltonen, 2007] – L. Aaltonen, P. Rahikkala, M. Saukoski, K. Halonen “Continuous Time Interface for $\pm$1.5 g Closed-Loop Accelerometer” IEEE International Conference on Integrated Circuit Design and Technology, September 2007.

2. [Allen, 2009] – J. Allen “Micro-System Inertial Sensing Technology Overview” Sandia National Laboratories, April 2009.

3. [Allen, Holberg, 2002] - Phillip E. Allen, Douglas R. Holberg “CMOS Analog Circuit Design”, Oxford University Press, 2002.

4. [Amini, 2004] - B. Amini, F. Ayazi, “A 2.5-V 14-bit ΣΔ CMOS SOI capacitive accelerometer,” IEEE Journal of Solid-State Circuits, vol. 39, pp. 2467–2476, Dec. 2004.

5. [Atre, 2006] – A. Atre, "Analysis of out-of-plane thermal microactuators", Journal of Micromechanics and Microengineering, pp. 250-213, 2006.

6. [Borovic, 2005] - B Borovic, A. Q. Liu, D. Popa, H. Cai, F. L. Lewis “Open-loop versus closed-loop control of MEMS devices: choices and issue” Journal of Micromechanics and Microengineering 15, pp. 1917-1924, Aug. 2005.

7. [Bose, 2014] – S. Bose, A. Raychowdhury, M. Jatolia, T. Bhattacharyya “Design of PID controller for ultra-sensitive Nano-g resolution MEMS tunneling accelerometer” IEEE International Conference on Control System, Computing and Engineering (ICCSCE), Nov. 2014.

8. [Boser, 1996] – B. Boser, R. Howe “Surface micromachined accelerometers,” IEEE Journal of Solid-State Circuits, vol. 31, pp. 366–375, Mar. 1996.

9. [Boser, 2011] – B.E. Boser “Analog Design Using gm/Id and ft metrics” https://people.eecs.berkeley.edu/~boser/presentations/2011-12%20OTA%20gm%20Id.pdf

10. [Cagdaser, 2005] – B. Cagdaser, B. E. Boser, "Resonant drive for stabilizing parallel-plate actuators beyond the pull-in point", the 13th International Conference on Solid-State Sensors Actuators and Microsystems Transducers’05, vol. 1, pp. 688-692, 2005.

11. [Cannon, 2014] – M. Cannon “A2 Discrete Systems” Oxford University online teaching material, 2014, [web] http://www.eng.ox.ac.uk/~conmrc/dcs/notes.html

12. [Chan, 2000] - E. Chan, R. Dutton “Electrostatic micromechanical actuator with extended range of travel” Journal of Microelectromechanical Systems, vol. 9, No. 3, pp. 321-328, Sept. 2000.

13. [Chan, 2000] - E. K. Chan, R. W. Dutton, "Electrostatic micromechanical actuator with extended range of travel", Journal of Microelectromechanical Systems, vol. 9, pp. 321-328, 2000.
14. [Chatterjee, 2016] – G. Chatterjee "Développement d'une unité de mesure inertielle à base de smart-MEMS" Ph.D. Thesis, Université de Montpellier, December 2016.
15. [Chen, 1997] – H. Chen, M. Bao, H. Zhu, S. Shen, "A piezoresistive accelerometer with a novel vertical beam structure," Proceedings of IEEE International Conference of Solid State Sensors and Actuators, vol. 2, pp. 1201–1204, Jun. 1997.
16. [Chen, 2014] – F. Chen, W. Yuan, H. Chang, I. Zeimpekis, M. Kraft "Low noise vacuum MEMS closed-loop accelerometer using sixth-order multi-feedback loops and local resonator sigma delta modulator" IEEE 27th International Conference on Micro Electro Mechanical Systems (MEMS), March 2014.
17. [Chowdhury, 2003] – S. Chowdhury, M. Ahmadi, W. C. Miller "Nonlinear Effects in MEMS Capacitive Microphone Design" Proceedings of IEEE International Conference on MEMS, NANO and Smart Systems, July 2003.
18. [Cole, 1994] – B.E. Cole et al., "512x512 infrared scene projector array for low-background simulations" Solid-State Sensor and Actuator Workshop, pp. 7-12, June 1994.
19. [Dean, 2006] – R.N. Dean "A technique for the measurement of relative velocity between parallel plate electrodes in micromachined structures" Ph.D. dissertation, Auburn University, Alabama, 2006.
20. [Demrow, 1970] – R. Demrow "Settling time of Operational amplifiers" Analog Dialogue Journal, analog Devices, June 1970. http://www.analog.com/media/en/analog-dialogue/volume-4/number-1/articles/volume4-number1.pdf.
21. [Denghua, 2010] – L. Denghua, X. Gao, F. Zhou, Z. Zhang "Research on nonlinearity property of piezoelectric vibration accelerometer based on cymbal transducer" Proceedings of the IEEE International Conference on Information and Automation, June 2010.
22. [Derk van der Laan, 1995]- Marten Derk van der Laan "Signal Sampling Techniques for Data Acquisition in Process Control" Ph.D. Thesis, University of Groningen, 1995 http://www.rug.nl/research/portal/files/3266743/thesis.pdf!null
23. [DeVoe, 1997] - D. DeVoe, A. Pisano, "A fully surface-micromachined piezoelectric accelerometer," in Proceedings of IEEE International Conference Solid State Sensors and Actuators, vol. 2, pp. 1205–1208, Jun. 1997.
24. [DeVoe, 2001] – D. L. DeVoe, A.P. Pisano "Surface Micromachined Piezoelectric Accelerometers (PiXLs), Journal of Microelectromechanical Systems, vol. 10, No. 2, June 2001.

25. [Doll, 2011] - J.C. Doll, E.A. Corbin, W.P. King, B.L. Pruitt "Self-heating in piezoresistive cantilevers" Applied Physics Letter 98, May 2011.

26. [Domingues, 2013] – C. Domingues, Dolphin Integration, "Challenges for integrating high performance Inertial performance Inertial Measurement Unit (IMU)" IP-SOC 2013, Nov. 2013.

27. [Doncescu, 2014] – A. Doncescu "Stabilité des Systèmes Discrets et Echantillonnés", 2014, [web]

28. [Dong, 2008]– P. Dong, X. Li, H. Yang, H. Bao, W. Zhou, S. Li, S. Feng, "High performance monolithic triaxial piezoresistive shock accelerometers," Sensors and Actuators A: Physical, vol. 141, pp. 339–346, Feb. 2008.

29. [Enz, 1996] – C. Enz, G.Temes " Circuit Techniques for Reducing the Effects of Op-Amp Imperfections: Autozeroing, Correlated Double Sampling and Chopper Stabilization" Proceedings of the IEEE, vol. 84, No.11, Nov. 1996.

30. [French, 1996] - P. J. French "Development of surface micromachining techniques compatible with on-chip electronics" Journal of Micromechanics and Microengineering, vol.6, pp. 197–211, 1996.

31. [French, 1998] – P.J. French, P.M. Sarro "Surface versus bulk micromaching: the contest for suitable applications" Journal of Micromechanics and Microengineering, vol. 8, pp 45-53, 1998.

32. [Garcia-Valenzuela, 1994] - A. Garcia-Valenzuela, M. Tabib-Azar, "Comparative study of piezoelectric, piezoresistive, electrostatic, magnetic, and optical sensors" Proceedings SPIE, vol. 2291, pp. 125–142, July 1994.

33. [Han, 2003] - K.H. Han, Y.H. Cho, "Self-balanced navigation-grade capacitive microaccelerometers using branched finger electrodes and their performance for varying sense voltage and pressure," Journal of Microelectromechanical Systems, vol. 12, pp. 11–20, Feb. 2003.

34. [He, 2008] – L. He, Y.P. Xu, M. Palaniapan "A CMOS Readout Circuit for SOI Resonant Accelerometer With 4 $\mu g$ Bias Stability and 20 $\mu g/\sqrt{Hz}$ Resolution" IEEE Journal of Solid-State Circuits, vol.43, No.6, pp. 1480, June 2008.

35. [Henrion, 1990] – W. Henrion, L. DiSanza, M. Ip, S. Terry, H. Jerman, "Wide dynamic range direct accelerometer" in IEEE 4th Solid-State Sensor and Actuator Workshop, pp. 153–157, June 1990.

36. [Hewa-Kasakarage, 2013] – N. N. Hewa-Kasakarage, D. Kim, M.L. Kuntzman, N.A. Hall "Micromachined Piezoelectric Accelerometers via epitaxial silicon cantilevers and bulk silicon proof masses" Journal of Microelectromechanical Systems, vol. 22, No. 6, Dec. 2013.

37. [Huang, 2005] - S. Huang, X. Li, Z. Song, Y. Wang, H. Yang, L. Che, J. Jiao, “A high-performance micromachined piezoresistive accelerometer with axially stressed tiny beams” Journal of Micromechanics and Microengineering, vol. 15, pp. 993, May 2005.

38. [Iseki, 2006] – T. Iseki, M. Okumura, T. Sugawara, "Two-Dimensionally Deflecting Mirror Using Electromagnetic Actuation", Optical Review, pp. 189-194, 2006.

39. [IVC102] - PRECISION SWITCHED INTEGRATOR TRANSIMPEDANCE AMPLIFIER, Texas Instruments, http://www.ti.com/lit/ds/symlink/ivc102.pdf.

40. [Jespers, 2010] – P. Jespers “The gm/ID Methodology, a sizing tool for low-voltage analog CMOS Circuits” Springer, 2010.

41. [Jiang, 2000] - X. Jiang, J. I. Seeger, M. Kraft, B. E. Boser, “A monolithic surface micromachined Z-axis gyroscope with digital output,” Symposium on VLSI Circuits, Digest of Technical Papers, pp. 16–19, 2000.

42. [Jiangfeng, 2002] – W. Jiangfeng, G. K. Fedder, L. R. Carley, “A low-noise low-offset chopper-stabilized capacitive-readout amplifier for CMOS MEMS accelerometers” IEEE International Solid-State Circuits Conference, pp. 428–478, Feb. 2002.

43. [Johns-Martin, 1997] – D. Johns, K. Martin “Analog Integrated Circuit Design”, John Wiley & Sons, 1997.

44. [Kajita, 2000] - T. Kajita, M. Un-Ku, and G. C. Temes, “A noise-shaping accelerometer interface circuit for two-chip implementation,” Proceedings of IEEE International Symposium Circuits and Systems, pp. 337–340, 2000.

45. [Keil] - https://www.keil.com/boards2/stmicroelectronics/stm32f4_discovery/

46. [Kempe, 2011] – Volker Kempe, Sensor Dynamics AG “Inertial MEMS: Principles and Practice”, 2011.

47. [Kim, 1983] – S.C. Kim, K.D. Wise, “Temperature sensitivity in silicon piezoresistive pressure transducers” IEEE Transactions Electron Devices 30, pp. 802–810, 1983.

48. [Kobayashi, 2009] - T. Kobayashi, H. Okada, M. Akiyama, R. Maeda, T. Itoh “A digital output piezoelectric accelerometer using CMOS-compatible ALN thin film” International Transducers 2009 Solid-State Sensors, Actuators and Microsystems Conference, June 2009.

49. [Kraft, 1998] - M. Kraft, C.P. Lewis, T.G. Hesketh “Closed-loop silicon accelerometers” IEEE Proceedings on Circuits, Devices and Systems, vol. 145, issue 5, Oct. 1998.

50. [Kulah, 2002] - H. Kulah, A. Salian, N. Yazdi, K. Najafi, “A 5 V closed-loop second order sigma-delta Micro-G microaccelerometer,” Proceedings Solid-State Sensor, Actuator and Microsystems Workshop, pp. 219–222, 2002.

51. [Kulah, 2003a] - H. Kulah, C. Junseok, N. Yazdi, K. Najafi, “A multi-step electromechanical sigma-delta converter for micro-G capacitive accelerometers” IEEE International Solid-State Circuits Conference, 2003.

52. [Kulah, 2006] – H. Kulah, J. Chae, N. Yazdi, K. Najafi, “Noise analysis and characterization of a sigma-delta capacitive microaccelerometer,” IEEE Journal of Solid-State Circuits, vol.41, issue 2, Feb. 2006.

53. [Kyynäräinen, 2001] - J. M. Kyynäräinen, A. S. Oja, H. Seppa, "Increasing the Dynamic Range of a Micromechanical Moving-Plate Capacitor", Analog Integrated Circuits and Signal Processing 29, pp. 61-70, 2001.

54. [Lajevardi, 2012] - P. Lajevardi, V. Petkov, B. Murmann, “A ΔΣ interface for MEMS accelerometers using electrostatic spring-constant modulation for cancellation of bondwire capacitance drift,” IEEE International Solid-State Circuits Conference Digest Technical Papers, pp. 196–198, Feb. 2012.

55. [Lang, 1999] - C. Lang, R. Tielert, “A low noise accelerometer with digital pid-type controller and multibit force feedback,” Proceedings of 25th European Solid-State Circuits Conference (ESSCIRC), pp. 250–253, Sep. 1999.

56. [Lee, 2006] – S.H. Lee “Multirate digital control system design and its application to computer disk drives” IEEE Transactions on Control Systems Technology, vol. 14, issue 1, pp. 124-133, Jan. 2006.

57. [Lemkin, 1999] - M. Lemkin, B. Boser, “A three-axis micromachined accelerometer with a CMOS position-sense interface and digital offset-trim electronics” IEEE Journal of Solid-State Circuits, vol. 34, no. 4, pp. 456–468, Apr. 1999.

58. [Li, 2012] – J. Li, S. Fan, Z. Guo “Design and Analysis of Silicon Resonant Accelerometer” Research Journal of Applied Sciences, Engineering and Technology, 5(3): 970-974, July 2012.

59. [Lian, 2010] – F.L. Lian “Design of Real-Time Control Systems - Controller Design of Digital Control Systems”, 2010, [web] http://cc.ee.ntu.edu.tw/~fengli/Teaching/RTCS/982_rtcs24_DTDesign4.pdf

60. [LM6154] - Dual and Quad 75 MHz GBW Rail-to-Rail I/O Operational Amplifiers, Texas Instruments, http://www.ti.com/lit/ds/symlink/lm6154.pdf.

61. [Lu, 1995] - C. Lu, M. Lemkin, B. Boser, “A monolithic surface micromachined accelerometer with digital output” IEEE International Solid-State Circuits Conference, Digest of Technical Papers, Feb. 1995.

62. [Luo, 2002] - H. Luo, G. Zhang, L. Carley, G. Fedder, “A post-cmos micromachined lateral accelerometer,” Journal of Microelectromechanical Systems, vol. 11, pp. 188–195, June 2002.

63. [Maithripala, 2003] - D. H. S. Maithripala, J. M. Berg, W. P. Dayawansa, "Capacitive stabilization of an electrostatic actuator: Output feedback viewpoint", American Control Conference 2003, vol. 5, pp. 4053-4058, 2003.
64. [Matteis, 2015] - M. De Matteis, A. Pezzota, M. Sabatini, M. Grassi, M. Croce, P. Malcovati, A. Baschirotto “A 0.13µm-CMOS 90µW 51dB-SNR Continuous-Time Accelerometer Front-End with 10b SAR-ADC” IEEE Sensors, Nov.2015.
65. [Milanovic, 2010] – V. Milanovic, Mona E. Zaghloul, Nim H. Tea, John S. Suehle, Beverly Payne, Michael Gaitan “Micromachined convective accelerometers in standard integrated circuits technology” Applied physics letters vol. 76, no. 4, Jan. 2010.
66. [Mukherjee, 2011] - B. Mukherjee, K. B. M Swamy, S. Kar, S. Sen “Effect of voltage induced electrostatic forces on MEMS capacitive accelerometer” IEEE Students' Technology Symposium (TechSym), Jun. 2011.
67. [Nguyen, 2014] - H. B. Nguyen, L. Latorre, P. Nouet “A new monolithic 3-axis thermal convective accelerometer: principle, design, fabrication and characterization” Microsystem Technologies, Volume 21, Issue 9, pp 1867–1877, September 2015.
68. [Ning, 1995] – Y. Ning, Y. Loke, G. McKinnon, “Fabrication and characterization of high g-force, silicon piezoresistive accelerometers” Sensors and Actuators A: Physical, vol. 48, pp. 55–61, May 1995.
69. [Paavola, 2007] – M. Paavola, M. Kamarainen, J. Jarvinen, M. Saukoski, M. Laiho, K. Halonen “A Micropower Interface ASIC for a Capacitive 3-Axis Micro-Accelerometer” IEEE Journal of Solid-State Circuits, vol. 42, no. 12, pp. 2651-2665, Dec. 2007.
70. [Paavola, 2009] - M. Paavola, M. Kämäräinen, E. Laulainen, M. Saukoski, L. Koskinen, M. Kosunen, K. Halonen, “A Micropower ΔΣ-based interface ASIC for a capacitive 3-axis micro-accelerometer,” IEEE Journal of Solid-State Circuits, vol. 44, pp. 3193–3210, Nov. 2009.
71. [Park, 2011] – S. Park “Low Voltage Electrostatic Actuation and Displacement Measurement through Resonant Drive Circuit” Ph.D. dissertation, University of Waterloo, Canada, 2011.
72. [Partridge, 2000] - A. Partridge, J.K. Reynolds, B.W. Chui, E.M. Chow, A.M. Fitzgerald, L.Zhang, N.I. Maluf, T. W. Kenny “A High-Performance Planar Piezoresistive Accelerometer” Journal of Microelectromechanical Systems, Vol. 9, No. 1, March 2000.
73. [Pastre, 2009] - M. Pastre, M. Kayal, H. Schmid, A. Huber, P. Zwahlen, A.-M. Nguyen,Y. Dong, “A 300Hz 19b DR capacitive accelerometer based on a versatile front end in a 5th-order ΔΣ loop” Proceedings of 35th European Solid-State Circuits Conference (ESSCIRC), pp. 288–291, Sep. 2009.

74. [Petkov, 2005] - V. Petkov, B. Boser “A Fourth-Order ΣΔ Interface for Micromachined Inertial Sensors” IEEE Journal of Solid-State Circuits, vol. 40, issue 8, pp. 1602 – 1609, Aug. 2005.

75. [Petkov, 2014] – V. Petkov, G. Balachandran, J. Beintner “A Fully Differential Charge-Balanced Accelerometer for Electronic Stability Control” IEEE Journal of Solid-State Circuits, vol. 49, issue 1, pp. 262 – 270, Jan. 2014.

76. [Razavi, 2001] – B. Razavi “Design of CMOS Analog Integrated Circuits”, McGraw-Hill International edition, 2001.

77. [Renaut, 2013] – F. Renaut “MEMS Inertial Sensors Technology”, Swiss Federal Institute of Technology Zurich, 2013.

78. [Robbins, 1991] - Robbins, William P. "High-Displacement Piezoelectric Actuator Utilizing a Meander-Line Geometry-Part II:Therory", IEEE Transactions on Ultrasonics, Ferroelectrics, and Frequency Control, pp. 461-467, 1991.

79. [Robert, 2009] – Ph. Robert, V. Nguyen, S. Hentz, L. Duraffourg, G. Jourdan, J. Arcamone ,S. Harrisson “M&NEMS: A new approach for ultra-low cost 3D inertial sensor”, IEEE Sensors 2009.

80. [Roberts, 2006] – S. Roberts “Design of digital filters” [web] http://www.robots.ox.ac.uk/~sjrob/Teaching/SP/l6.pdf

81. [Roessig, 2002] - T.A. Roessig, R.T. Howe, A.P. Pisano, J.H. Smith “Surface micromachined accelerometer” International Conference on Solid State Sensors and Actuators, 1997.

82. [Roland, 1981] - JJ Roland, GP Agrawal “Optical gyroscopes” Optics & Laser Technology, 13(5):239–244, 1981.

83. [San-Andres, 2015] – L. San-Andres “Dynamic response of second order mechanical systems (1 DOF systems) - Free response to initial conditions: viscous and coulomb damping systems. Forced response: impulse and step loads” [web] http://rotorlab.tamu.edu/me617/handout2a_2008.pdf

84. [Sansen, 2006] – W. Sansen “Analog Design Essentials” The Springer International Series in Engineering and Computer Science, Nov.2006.

85. [Scheeper, 1996] - P. Scheeper, J. O. Gullov, L. M. Kofoed, “A piezoelectric triaxial accelerometer,” Journal of Micromechanics and Microengineering, vol. 6, p. 131, Mar. 1996.

86. [Seeger, 1997] - J. Seeger, S. Crary, “Stabilization of electrostatically actuated mechanical devices “ Proceedings of Transducers ‘97, vol. 2, pp. 1133-1136, June. 1997.

87. [Seeger, 2003] - J.I. Seeger, B.E. Boser, “Charge control of parallel-plate, electrostatic actuators and the tip-in instability”, Journal of Microelectromechanical Systemes, vol. 12, no. 5, pp. 656-671, 2003.

88. [Selvakumar, 1998] – A. Selvakumar, K. Najafi “A high-sensitivity z-axis capacitive silicon microaccelerometer with a torsional suspension” Journal of Microelectromechanical Systems, vol. 7, no. 2, pp. 192–200, June 1998.

89. [Seo, 2005] – Y. H. Seo, D.S. Choi, J.H. Lee, T.M. Lee, T.J. Je and K.H. Whang "Piezoelectric Actuator Based on Stiffness Control and Stroke Amplication for Large Lateral Actuation", IEEE International Conference on Micro Electro Mechanical Systems, pp. 383-386, 2005.

90. [Sherman, 1992] - S. Sherman, W. Tsang, T. Core, R. Payne, D. Quinn, K.-L. Chau, J. Farash, S. Baum, “A low cost monolithic accelerometer; product/technology update”, Proceedings of IEEE International Electron Devices Meeting, pp. 501–504, Dec. 1992.

91. [Sim, 1997] - J.H. Sim, S.H. Hahm, J.H. Lee, I.S. Yu, and J.S. Kim, “Eight beam piezoresistive accelerometer fabricated by using a selective porous silicon etching method” in Proceedings of IEEE International Conference on Solid State Sensors and Actuators, vol. 2, pp. 1193–1196, Jun. 1997.

92. [Smith, 1994] – T. Smith, O. Nys, M. Chevroulet, Y. DeCoulon, M. Degrauwe “A 15 b electromechanical sigma-delta converter for acceleration measurements” IEEE International Solid-State Circuits Conference, Feb. 1994.

93. [Snyder, 2016] – C. Snyder “Part 3: Degrees of Freedom” http://www.leadingones.com/articles/intro-to-vr-4.html

94. [Steimle, 1991] – M. Steimle, H.Muhlhoff “Limitations of Digital CMOS-Processes for Analog Applications doe to Channel Length Modulation and Hot Carrier Degradation” Solid State Device Research Conference, 1991. ESSDERC '91. 21st European, Sept. 1991.

95. [STM32F4] - http://www.st.com/content/ccc/resource/technical/document/user_manual/70/fe/4a/3f/e7/e1/4f/7d/DM00039084.pdf/files/DM00039084.pdf/jcr:content/translations/en.DM00039084.pdf

96. [Sugiyama, 1994] – S. Sugiyama, O. Tabata, K. Shimaoka “Micromachined sensors using polysilicon sacrificial layer etching technology” IEEE International Electron Devices Meeting, pp. 127-130, Dec. 1994.

97. [Sun, 2010] - C.-M. Sun, M.-H. Tsai, Y.-C. Liu, and W. Fang, “Implementation of a monolithic single proof-mass tri-axis accelerometer using CMOS-MEMS technique,” IEEE Trans. Electron Devices, vol. 57, no. 7, pp. 1670–1679, July 2010.

98. [Sun, 2010] - H. Sun, D. Fang, K. Jia, F. Maarouf, H. Qu, and H. Xie, “A low-power low noise dual chopper amplifier for capacitive CMOS-MEMS accelerometers,” IEEE Sensors Journal, vol. 11, pp. 925–933, Apr. 2010.

99. [Tan, 2012] - T.D. Tan “A Piezoresistive Acceleration sensor: from System to Physical Levels”, Sensors & Transducers Journal, vol.145, issue 10, pp. 86-95, Oct. 2012.

100. [Tez, 2015] – S. Tez, U. Aykutlu, M. M. Torunbalci, T. Akin “A Bulk-Micromachined Three-Axis Capacitive MEMS Accelerometer on a Single Die” Journal of Microelectromechanical Systems, vol. 24, no. 5, pp. 1264–1274, Oct. 2015.

101. [Tingting, 2012] - [Z. Tingting, L. Haojiong, H. Jingqing, Z. Meng, H. Lichen, Z. Yacong, L. Wengao, C. Zhongjian “An s-z Domain Transformation Method for the Readout Circuit Design of Closed-Loop Micromechanical Capacitive Accelerometer” IEEE International Conference on Electron Devices and Solid State Circuit (EDSSC) Dec. 2012.

102. [Tsai, 2012] - M.H. Tsai, Y.C. Liu, W. Fang, “A three-axis CMOS-MEMS accelerometer structure with vertically integrated fully differential sensing electrodes,” Journal of Microelectromechanical Systems, vol. 21, no. 6, pp. 1329–1337, Dec. 2012.

103. [Wang, 2003] – L.P. Wang, R.A. Wolf Jr., Y, Wangpaalang, K. K. Deng, L. Zou, R. J. Davis, S. Trolier-McKinstry “Design, fabrication and measurement of high sensitivity piezoelectric microelectromechanical systems accelerometers” Journal of Microelectromechanical Systems, vol. 12, No. 4, Aug. 2003.

104. [Wang, 2006] – L.P Wang, E. Ginsburg, F. Gerfers, D. Samara-Rubio, B. Weinfeld, Q. Ma, V. Rao “Sputtered AIN Thin Films for Piezoelectric MEMS Devices” IEEE Sensors, Oct. 2006.

105. [Wang, 2007] - C. Wang, M.-H. Tsai, C.-M. Sun, and W. Fang, “A novel CMOS out-of plane accelerometer with fully-differential gap-closing capacitance sensing electrodes,” Journal of Micromechanical Microengineering, vol. 17, no. 7, pp. 1275–1280, Jun. 2007.

106. [Wang, 2015] – C. Wang, J. Lan, J. Luo, D. Nag, K. Chai, B. Grinberg “A ultra-low-power sensor signal processor for high-performance close-loop MEMS accelerometer” IEEE International Conference on Electron Devices and Solid-State Circuits (EDSSC), Jun. 2015.

107. [Williams, 2010] - M. D. Williams, B. A. Griffin, T. N. Reagan, J. R. Underbrink, M. Sheplak, “An AlN MEMS piezoelectric microphone for aeroacoustic applications,” Journal of Microelectromechanical Systemes, vol. 21, no. 2, pp. 270–283, Apr. 2012.

108. [Wu, 2002] – J. Wu, Ph.D. Thesis “Sensing and Control Electronics for Low-Mass Low-Capacitance MEMS Accelerometers” Carnegie Institute of Technology.

109. [Wu, 2004] – J. Wu, G. K. Fedder, L.R. Carley “A low-noise low-offset capacitive sensing amplifier for a $50-\mu g/\sqrt{Hz}$ monolithiv CMOS MEMS Accelerometer” IEEE Journal of Solid-State Circuits, vol. 39, no. 5, pp. 722-730, May 2004.

110. [Xie, 2003] – H.K. Xie “Principles of MEMS Transducers” (Fall 2003) EEL5225 course, Lecture 22, University of Florida, Oct. 2003.

111. [Xu, 2015] – H. Xu, X. Liu, L. Yin "A Closed-Loop ΣΔ Interface for a High-Q Micromechanical Capacitive Accelerometer With 200 ng/√Hz Input Noise Density" IEEE Journal of Solid-State Circuits, vol. 50, issue 9, pp. 2101-2112, 56–468, Sept. 2015.

112. [Yamamoto, 1996] – Y. Yamamoto "A Retrospective View on Sampled-Data – Control Systems" Kyoto University, 1996 http://citeseerx.ist.psu.edu/viewdoc/download?doi=10.1.1.46.3308&rep=rep1&type=pdf

113. [Yazdi, 2000] – N. Yazdi, K. Najafi, "An all-silicon single-wafer micro-g accelerometer with a combined surface and bulk micromachining process," IEEE Journal of Microelectromechanical Systems, vol. 9, pp. 544–550, Dec. 2000.

114. [Yazdi, 2003] – N. Yazdi, K. Najafi, A. Salian, "A high-sensitivity silicon accelerometer with a folded-electrode structure," Journal of Microelectromechanical Systems, vol. 12, pp. 479–486, Aug. 2003.

115. [Ye, 2013] - Z.Ye, Haigang Yang, Tao Yin, G. Huang, F. Liu "High-Performance Closed-Loop Interface Circuit for High-Q Capacitive Microaccelerometers" IEEE Sensors Journal, vol. 13, issue 5, pp. 1425 – 1433, May 2013.

116. [Yin, 2009] – L. Yin, X. Liu, W. Chen, W. Chen, Z. Zhou "A low-noise CMOS interface circuit for closed-loop accelerometer" IEEE International Conference on Nano/Micro Engineered and Molecular Systems, Jan. 2009.

117. [Yole, 2014] - Status of the MEMS Industry 2014 (Yole Development) http://www.yole.fr/6_9_AXIS.aspx#.WHX3NNIrKM8

118. [Yole, 2016] – Status of the MEMS Industry 2016 (Yole Development) http://www.slideshare.net/Yole_Developpement/status-of-the-mems-industry-2016-report-by-yole-developpement

119. [Yucetas, 2010] – M. Yücetaş, A. Kalanti, J. Salomaa, L. Aaltonen, K. Halonen "An analog closed-loop SC accelerometer interface for a capacitive high-Q sensor element" Conference on Ph.D. Research in Microelectronics and Electronics (PRIME), July 2010.

120. [Yucetas, 2010b] – M. Yücetaş, L. Aaltonen, K. Halonen "Linearity study of a self-balancing capacitive half-bridge sensor interface" An analog closed-loop SC accelerometer interface for a capacitive high-Q sensor element" 12th Biennial Baltic Electronics Conference (BEC 2010), Oct. 2010.

121. [Yucetas, 2012] – M. Yucetas, M. Pulkkinen, A. Kalanti, J. Salomaa, L.Aaltonen, K. Halonen " A high resolution accelerometer with electrostatic damping and improved supply sensitivity" IEEE Journal of Solid-State Circuits, vol. 47, no. 7, pp. 1721-1730, July 2012.

122. [Yucetas, 2013] – M. Yucetas “Capacitive Accelerometer Interfaces Utilising High-Q Microelectromechanical Sensor Elements” Ph.D. dissertation, Aalto University, 2013.

123. [Zhao, 2008] - D. Zhao, M. Zaman, F. Ayazi, “A chopper-stabilized lateral-BJT-input interface in 0.6 µm CMOS for capacitive accelerometers,” IEEE International Solid-State Circuits Conference, pp. 584–637, Feb. 2008.

124. [Zhao, 2009] – D. Zhao “A low-noise CMOS interface for capacitive microacceleroemeters” Ph.D. dissertation, Georgia Institute of Technology, Dec. 2009.

125. [Zhao, 2016] – M. Zhao, Z. Chen, Y. Yang, Y. Niu, G. Chen, W. Lu, Y. Zhang “A low-noise closed-loop interface for high-G capacitive micro-accelerometer” IEEE International Symposium on Circuits and Systems (ISCAS), May 2016.

126. [Zotov, 2015] – S. Zotov, B.Simon, A.Trusov, A. Shkel “High Quality Factor Resonant MEMS Accelerometer With Continuous Thermal Compensation” IEEE Sensors Journal, Vol. 15, no.9, September 2015.

127. [Zou, 2008] – Q. Zou, W. Tan, E. S. Kim, G.E. Loeb “Single- and triaxis piezoelectric-bimorph accelerometers” Journal of Microelectromechanical Systems, vol. 17, No. 1, Febr. 2008.

128. [Zou, 2015] – X. Zou, A. Seshia “A high-resolution resonant MEMS accelerometer” 18th International Conference on Solid-State Sensors, Actuators and Microsystems (TRANSDUCERS), June 2015.

# Appendices I

## Model MEMS Accelerometer VerilogA – Spectre

- Module trans_1dof (accel, mover, disp)

- The module aim is to calculate the proof mass displacement (*disp*) due to an input acceleration (*accel*) using the second order mass-sprint-damper system equations;
- *mover* is just an intermediate state for the proof mass position;
- For each axis (with translational movement) and each proof mass, the module trans_1dof is appealed in the Spectre file:
  adutmechx1 (ax moverx1 dispx1) trans_1dof
  adutmechx2 (ax moverx2 dispx2) trans_1dof
  adutmechy1 (ay movery1 dispy1) trans_1dof
  adutmechy2 (ay movery2 dispy2) trans_1dof

- Module cpp_trans2 (mover, xp, mid, xn, cpo, cpi, cno, cni)

- The module aim is to output the sensed capacitances for the translational devices
- *Mover* – node that represents the proof mass state;
- *Xp, mid, xn* – electrical nodes representing excitation electrodes: p for the positive side and n for the negative one , *mid* is connected to the proof mass;
- *Cpo, cpi* – electrical nodes for the positive capacitance pins;
- *Cno, cni* – electrical nodes for negative capacitance pins;
- This module contains the sensed capacitances calculations and the electrostatic forces modeling;
- Real proof mass position (*mover*) is calculated previously, using the trans_1dof module;
- This VerilogA module is required twice for each axis
  asensecapx1 (moverx1 x2 m1 x1 cx11 0 cx12 0) cpp_trans2
  asensecapx2 (moverx2 x2 m2 x1 cx21 0 cx22 0) cpp_trans2
  asensecapy1 (movery1 y2 m1 y1 cy11 0 cy12 0) cpp_trans2
  asensecapy2 (movery2 y2 m2 y1 cy21 0 cy22 0) cpp_trans2

- Module rot_1dof (accel, rotator, theta)

- The module aim is to calculate the proof mass angle (*theta*) due to an input acceleration (*accel*) using the second order system equations for a rotational motion;
- *Rotator* – intermediate state for the proof mass position. As for « mover », *rotator* contains all the force/displacement equations;
- This module appears twice in the Spectre file (once for each proof mass):
  adutmech1 (az rotator1 theta1) rot_1dof.

adutmech2 (az rotator2 theta2) rot_1dof

- Module cpp_rot_bigap (rotator, vp, vmid, vn, cpo, cpi, cno, cni)

- This module describes a differential bigap rotating parallel plate capacitor;
- *Rotator* is the proof mass position calculated using the module *rot_1dof* ;
- *Vp, vn* are the model excitation electrodes and *vmid* is the proof mass node;
- *Cpo, cpi* – electrical nodes for the positive capacitance pins;
- *Cno, cni* – electrical nodes for the negative capacitance pins;
- Simpson's rule of integration is used to calculate capacitances and electrostatic forces:
- $\int_a^b f(x) \approx \frac{b-a}{6}\left[f(a) + 4f\left(\frac{a+b}{2}\right) + f(b)\right]$
- This is being implemented for convergence/stable solutions
- The module is used in the Spectre file (once for each proof mass):
  asensecap1 (rotator1 z2 m1 z1 cz11 0 cz12 0) cpp_rot_bigap
  asensecap2 (rotator2 z2 m2 z1 cz 21 0 cz22 0) cpp_rot_bigap

## A. model_heka.scs

```
simulator lang=spectre

library heka_model

//**********************************************************
section base
//**********************************************************
modelOptions options scale=1u gmin=1e-12 tnom=(27)

parameters
+    sDOTpercent         = (0)
+    sDOTmult            = (1)
+    sDOTmult2           = (1)
+    pi4models           = (3.141592654)
+    nil                 = (0)

real mod(real a, real b) {
   return a-b*int((a+0.5)/b);    // a and b must be positive
}

real sgn(real a) {
   return ((a>0)-(a<0));
}

real shrnk(real udr, real sDOTmult) {
   return (udr*sDOTmult) ;
```

adutmech2 (az rotator2 theta2) rot_1dof

- Module cpp_rot_bigap (rotator, vp, vmid, vn, cpo, cpi, cno, cni)

- This module describes a differential bigap rotating parallel plate capacitor;
- *Rotator* is the proof mass position calculated using the module *rot_1dof* ;
- *Vp, vn* are the model excitation electrodes and *vmid* is the proof mass node;
- *Cpo, cpi* – electrical nodes for the positive capacitance pins;
- *Cno, cni* – electrical nodes for the negative capacitance pins;
- Simpson's rule of integration is used to calculate capacitances and electrostatic forces:
- $\int_a^b f(x) \approx \frac{b-a}{6}\left[f(a) + 4f\left(\frac{a+b}{2}\right) + f(b)\right]$
- This is being implemented for convergence/stable solutions
- The module is used in the Spectre file (once for each proof mass):
  asensecap1 (rotator1 z2 m1 z1 cz11 0 cz12 0) cpp_rot_bigap
  asensecap2 (rotator2 z2 m2 z1 cz 21 0 cz22 0) cpp_rot_bigap

## B. model_heka.scs

```
simulator lang=spectre

library heka_model

//**********************************************************
section base
//**********************************************************
modelOptions options scale=1u gmin=1e-12 tnom=(27)

parameters
+   sDOTpercent          = (0)
+   sDOTmult             = (1)
+   sDOTmult2            = (1)
+   pi4models            = (3.141592654)
+   nil                  = (0)

real mod(real a, real b) {
   return a-b*int((a+0.5)/b);    // a and b must be positive
}

real sgn(real a) {
   return ((a>0)-(a<0));
}

real shrnk(real udr, real sDOTmult) {
   return (udr*sDOTmult) ;
```

```
}
real pwr(real x, real y) {
   return (x**y) ;
}

//*********************************************************
endsection base
//*********************************************************

//*********************************************************
section hdpoly_process_params
//*********************************************************

parameters
+    nom_tt              = (25)
+    nom_cd              = (-0.2)
+    nom_psg1            = (0.9)
+    nom_psg2            = (1.8)
+    nom_dela_cd         = (0)
+    nom_delr_tt         = (1.0)
+    nom_delr_psg1       = (1.0)
+    nom_delr_psg2       = (1.0)
+    nom_dela_x1o        = (0.0)
+    nom_dela_x2o        = (0.0)
+    nom_dela_y1o        = (0.0)
+    nom_dela_y2o        = (0.0)
+    nom_dela_z1o        = (0.0)
+    nom_dela_z2o        = (0.0)
+    sig_dela_cd         = (0.045)
+    sig_delr_tt         = (0.033)
+    sig_delr_psg1       = (0.033)
+    sig_delr_psg2       = (0.033)
+    sig_dela_x1o        = (0.01)
+    sig_dela_x2o        = (0.01)
+    sig_dela_y1o        = (0.01)
+    sig_dela_y2o        = (0.01)
+    sig_dela_z1o        = (1e-6)
+    sig_dela_z2o        = (1e-6)

//*********************************************************
endsection hdpoly_process_params
//*********************************************************

//*********************************************************
section typ_mems_process_params
//*********************************************************
```

```
parameters
+    nsig_dela_cd                 = (0)
+    nsig_dela_x1o                = (0)
+    nsig_dela_x2o                = (0)
+    nsig_dela_y1o                = (0)
+    nsig_dela_y2o                = (0)
+    nsig_dela_z1o                = (0)
+    nsig_dela_z2o                = (0)
+    nsig_delr_tt                 = (0)
+    nsig_delr_psg1               = (0)
+    nsig_delr_psg2               = (0)

//********************************************************
endsection typ_mems_process_params
//********************************************************


//********************************************************
section mems
//********************************************************
```

**ahdl_include "$WORKAREA_DIR/veyron_sim/models/genericmems_heka.va"**

```
parameters
+    dela_cd                      = (nom_dela_cd+nsig_dela_cd*sig_dela_cd)
+    dela_z1o                     = (nom_dela_z1o+nsig_dela_z1o*sig_dela_z1o)
+    delr_tt                      = (nom_delr_tt*(1+nsig_delr_tt*sig_delr_tt))
+    delr_psg1                    =(nom_delr_psg1*(1+nsig_delr_psg1*sig_delr_psg1))
+    delr_psg2                    =(nom_delr_psg2*(1+nsig_delr_psg2*sig_delr_psg2))
+    cdval                        = nom_cd+dela_cd
+    ttval                        = (nom_tt*delr_tt)
+    psg1val                      = (nom_psg1*delr_psg1)
+    psg2val                      = (nom_psg2*delr_psg2)

subckt heka (ax ay az z1 y1 x1 m1 m2 x2 y2 z2 sub cx11 cx12 cx21 cx22
cy11 cy12 cy21 cy22 cz11 cz12 cz21 cz22 cst1b cst2a dispx1 dispx2
dispy1 dispy2 theta1 theta2)

parameters
+    wfactor                      = ((2.0+cdval)^3)/((2.0+nom_cd)^3)

adutmechy1 (ay movery1 dispy1) trans_1dof
+ ks=(3.5*delr_tt*wfactor)
+ mass=(5.52e-9)
+ damp_ratio=(0.53)
+ orient=(1.0)
```

```
+ offset=(0)
adutmechy2 (ay movery2 dispy2) trans_1dof
+ ks=(3.5*delr_tt*wfactor)
+ mass=(5.52e-9)
+ damp_ratio=(0.53)
+ orient=(-1.0)
+ offset=(0)

asensecapy1 (movery1 y2 m1 y1 cy11 0 cy12 0) cpp_trans2
+ g0=(1.5-cdval)
+ cf=(35)
+area0= (23800)
asensecapy2 (movery2 y2 m2 y1 cy21 0 cy22 0) cpp_trans2
+ g0=(1.5-cdval)
+ cf=(35)
+area0= (23800)

adutmechx1 (ax moverx1 dispx1) trans_1dof
+ ks=(3.5*delr_tt*wfactor)
+ mass=(5.52e-9)
+ damp_ratio=(0.00025)
+ offset=(0)
+ orient=(-1.0)
adutmechx2 (ax moverx2 dispx2) trans_1dof
+ ks=(3.5*delr_tt*wfactor)
+ mass=(5.52e-9)
+ damp_ratio=(0.00025)
+ orient=(1.0)
+ offset=(0)

asensecapx1 (moverx1 x2 m1 x1 cx11 0 cx12 0) cpp_trans2
+ g0=(1.5-cdval)
+ cf=(55)
+ area0= (23800)
asensecapx2 (moverx2 x2 m2 x1 cx21 0 cx22 0) cpp_trans2
+ g0=(1.5-cdval)
+ cf=(55)
+ area0= (23800)

adutmech1 (az rotator1 theta1) rot_1dof
+ kr=(0.112e-6*delr_tt*wfactor)
+ mass=(2.330e-15*(35790+0.5*6536*cdval)*ttval)
+ l_cg=(302.0)
+ irot=(2.42e-16)
+ damp_ratio=(0.1)
+ thetaoff=(dela_z1o)
```

```
+ orient=(1.0)
adutmech2 (az rotator2 theta2) rot_1dof
+ kr=(0.112e-6*delr_tt*wfactor)
+ mass=(2.330e-15*(35790+0.5*6536*cdval)*ttval)
+ l_cg=(+302.0)
+ irot=(2.42e-16)
+ damp_ratio=(0.1)
+ thetaoff=(dela_z1o)
+ orient=(-1.0)

asensecap1 (rotator1 z2 m1 z1 cz11 0 cz12 0) cpp_rot_bigap
+ areafill_cap1=(0.84)
+ areafill_cap2=(0.875)
+ width0=(150.0)
+ l1=(60.0)
+ l2=(162.0)
+ l3=(233.0)
+ g1=(psg1val)
+ g2=(psg2val)
+ cf=(7)
asensecap2 (rotator2 z2 m2 z1 cz21 0 cz22 0) cpp_rot_bigap
+ areafill_cap1=(0.84)
+ areafill_cap2=(0.875)
+ width0=(150.0)
+ l1=(60.0)
+ l2=(162.0)
+ l3=(233.0)
+ g1=(psg1val)
+ g2=(psg2val)
+ cf=(7)

ends

//***********************************************************
endsection mems
//***********************************************************

endlibrary heka_model
```

### C. genericmems_heka.va

```
`include "discipline.h"
`include "constants.h"

////////////////////////////////////////////////////////////////////////////////////////////////////////////////////////////////////////////////////////////////////////////
```

```
`define pi              3.14159265   // Ratio of circle circumference to diameter
`define eps0um          8.854e-18    // Permittivity of air / vacuum [F/um]
`define eps0m           8.854e-12    // Permittivity of air / vacuum [F/m]
`define k_boltz         1.38065e-23  // Boltzmann's constant [J/K]


`ifdef insideADMS
   `ifdef notInsideADMS
      `undef  notInsideADMS
   `endif
`else
   `define notInsideADMS
`endif

`ifdef __VAMS_COMPACT_MODELING__
   `ifdef not__VAMS_COMPACT_MODELING__
      `undef  not__VAMS_COMPACT_MODELING__
   `endif
`else
   `define not__VAMS_COMPACT_MODELING__
`endif



`ifdef __VAMS_COMPACT_MODELING__

`ifdef insideADMS
      `define IPRcc(nam,def,uni,lwr,upr,des) (*units=uni, type="instance", ask="yes",
desc=des*) parameter real    nam=def from[lwr:upr];
      `define IPRco(nam,def,uni,lwr,upr,des) (*units=uni,type="instance", ask="yes", desc=des*)
parameter real    nam=def from[lwr:upr);
      `define IPRoc(nam,def,uni,lwr,upr,des) (*units=uni, type="instance", ask="yes",
desc=des*) parameter real    nam=def from(lwr:upr];
      `define IPRoo(nam,def,uni,lwr,upr,des) (*units=uni,type="instance", ask="yes", desc=des*)
parameter real    nam=def from(lwr:upr);
      `define IPRnb(nam,def,uni,        des) (*units=uni, type="instance", ask="yes", desc=des*)
parameter real    nam=def;
      `define IPIcc(nam,def,uni,lwr,upr,des) (*units=uni,type="instance", ask="yes", desc=des*)
parameter integer nam=def from[lwr:upr];
      `define IPIco(nam,def,uni,lwr,upr,des) (*units=uni,type="instance", ask="yes", desc=des*)
parameter integer nam=def from[lwr:upr);
      `define IPIoc(nam,def,uni,lwr,upr,des) (*units=uni,type="instance", ask="yes", desc=des*)
parameter integer nam=def from(lwr:upr];
      `define IPIoo(nam,def,uni,lwr,upr,des) (*units=uni,type="instance", ask="yes", desc=des*)
parameter integer nam=def from(lwr:upr);
```

```
    `define IPInb(nam,def,uni,        des) (*units=uni,type="instance", ask="yes", desc=des*)
parameter integer nam=def;
    `define IPIsw(nam,def,uni,        des) (*units=uni,type="instance", ask="yes", desc=des*)
parameter integer nam=def from[ 0:  1];
  `else // notInsideADMS

    `define IPRcc(nam,def,uni,lwr,upr,des) (*units=uni,desc=des*) parameter real    nam=def
from[lwr:upr];
    `define IPRco(nam,def,uni,lwr,upr,des) (*units=uni,desc=des*) parameter real    nam=def
from[lwr:upr);
    `define IPRoc(nam,def,uni,lwr,upr,des) (*units=uni,desc=des*) parameter real    nam=def
from(lwr:upr];
    `define IPRoo(nam,def,uni,lwr,upr,des) (*units=uni,desc=des*) parameter real    nam=def
from(lwr:upr);
    `define IPRnb(nam,def,uni,        des) (*units=uni,desc=des*) parameter real    nam=def;
    `define IPIcc(nam,def,uni,lwr,upr,des) (*units=uni,desc=des*) parameter integer nam=def
from[lwr:upr];
    `define IPIco(nam,def,uni,lwr,upr,des) (*units=uni,desc=des*) parameter integer nam=def
from[lwr:upr);
    `define IPIoc(nam,def,uni,lwr,upr,des) (*units=uni,desc=des*) parameter integer nam=def
from(lwr:upr];
    `define IPIoo(nam,def,uni,lwr,upr,des) (*units=uni,desc=des*) parameter integer nam=def
from(lwr:upr);
    `define IPInb(nam,def,uni,        des) (*units=uni,desc=des*) parameter integer nam=def;
    `define IPIsw(nam,def,uni,        des) (*units=uni,desc=des*) parameter integer nam=def
from[  0:  1];
  `endif

`else // not__VAMS_COMPACT_MODELING__

  `define IPRcc(nam,def,uni,lwr,upr,des) parameter real    nam=def from[lwr:upr];
  `define IPRco(nam,def,uni,lwr,upr,des) parameter real    nam=def from[lwr:upr);
  `define IPRoc(nam,def,uni,lwr,upr,des) parameter real    nam=def from(lwr:upr];
  `define IPRoo(nam,def,uni,lwr,upr,des) parameter real    nam=def from(lwr:upr);
  `define IPRnb(nam,def,uni,        des) parameter real    nam=def;
  `define IPIcc(nam,def,uni,lwr,upr,des) parameter integer nam=def from[lwr:upr];
  `define IPIco(nam,def,uni,lwr,upr,des) parameter integer nam=def from[lwr:upr);
  `define IPIoc(nam,def,uni,lwr,upr,des) parameter integer nam=def from(lwr:upr];
  `define IPIoo(nam,def,uni,lwr,upr,des) parameter integer nam=def from(lwr:upr);
  `define IPInb(nam,def,uni,        des) parameter integer nam=def;
  `define IPIsw(nam,def,uni,        des) parameter integer nam=def from[  0:  1];

`endif
//////////////////////////////////////////////////////////////////////////////////////////////////////////////////////////////////////////////

//////////////////////////////////////////////////////////////////////////////////////////////////////////////////////////////////////////////
```

```
// Begin Module Definitions

//////////////////////////////////////////////////////////////////////////////////////////////////////////////////////////////////////////////

//  TRANSLATIONAL

//////////////////////////////////////////////////////////////////////////////////////////////////////////////////////////////////////////////
// This model describes the translation motion of a 1-dof damped mechanical system
//////////////////////////////////////////////////////////////////////////////////////////////////////////////////////////////////////////////

module trans_1dof (accel, mover, disp);
inout accel;        // Applied acceleration - this is still an electrical state
inout mover;             // Node that represents proof mass state in the x-direction
inout disp;

electrical   accel;      // Input acceleration in [m/s^2]
electrical   mover;       // [um]
electrical   mov_vel;     // [um/s]
electrical   disp;       // 1V = 1um

branch(mov_vel) vel_int;     // Dummy node for mica topology checker


`IPRcc( damp_ratio        ,  1.5     ,""      , 0.0001,   5,    "damping ratio")
`IPRoo( mass              ,  1e-9    ,"kg"    ,1e-10,   1e-7,   "mass of mover")
`IPRoo( ks                ,  5       ,"N/m"   , 0.5,    100,    "spring constant")
`IPRoo( tcs1              ,  0       ,"N/m/K"   , -1e-1,  1e-1,   "tc1 of spring constant")
`IPRoo( tcs2              ,  0       ,"N/m/K^2"  , -1e-3,  1e-3,   "tc2 of spring constant")
`IPRoo( tnom              ,  25.0    ,"C"     , 0,      200,    "nominal temperature")
`IPRcc( orient            ,  1.0     ,"C"     ,-1.0,    1.0,    "relative orientation")
`IPRoo( offset            ,  0       ,"um"    ,-0.5,    0.5,    "initial displacement")
`IPRoo( tco1              ,  0       ,"N/m/K"   , -1e-1,  1e-1,   "tc1 of offset")
`IPRoo( tco2              ,  0       ,"N/m/K^2"  , -1e-3,  1e-3,   "tc2 of offset")

real D_coef;
real ks_t, deltat,offset_t;
real Q_fact,natural_fo,rolloff_fo;

analog begin

`ifdef notInsideADMS
  @(initial_step) begin
`endif

  begin :  initializeInstance
    deltat      = ($temperature-273.15-tnom);
```

```
    ks_t          = ks*(1+tcs1*deltat+tcs2*deltat*deltat);
    offset_t      = offset*(1+tco1*deltat+tco2*deltat*deltat);
    D_coef        = damp_ratio * 2* sqrt(ks*mass);
    Q_fact        = 1/(2*damp_ratio);
    natural_fo    = (sqrt(ks_t/mass) /(2*`pi)) * 1e-3;
    rolloff_fo    = sqrt( sqrt(pow(2*pow(damp_ratio,2)-1.0,2)+1) -(2*pow(damp_ratio,2)-1.0) )*
natural_fo;
    //$strobe ("natural_fo\n", natural_fo);
    //$strobe ("rolloff_fo\n", rolloff_fo);
  end // initializeInstance

`ifdef notInsideADMS
  end //intial step
`endif

  begin : dynamicBlock

   I(vel_int)      <+  1.0*V(mov_vel);
   V(mov_vel)      <+  ddt(V(mover));
   I(mover)        <+  orient*mass*V(accel)* 1.0e6 ;          // Force of acceleration
   I(mover)        <+ -ks_t*V(mover);                                 //Spring restoring force
   I(mover)        <+ -ks_t*offset_t;                                //Spring restoring force
   I(mover)        <+ -D_coef*V(mov_vel);           // Damping
   I(mover)        <+ -mass*ddt(V(mov_vel), 1.0e-6);  // Acceleration of mover substracts from
//total force
   I(mover)       <+white_noise(4.0e12*`k_boltz*$temperature*D_coef, "Brownian");
// Brownian noise

  end // DynamicBlock

   V(disp) <+ V(mover);   // Monitor node for displacement
end // analog

endmodule //trans_1dof
////////////////////////////////////////////////////////////////////////////////////////////////////////////////////////////////
////////////////////////////////////////////////////////////////////////////////////////////////////////////////////////////////

// This module can be used for the sense and selftest capacitors on translational devices
// This approach uses linearization of electrostatic force to limit behavior instead of force
clamping
//////////////////////////////////////////////////////////////////////////////////////////////////////////////
////////////////////////////////////////////////////////////////////////////////////////////////////////////////////////////////////
module cpp_trans2 (mover, xp, mid, xn, cpo,cpi, cno,cni);

inout mover;                       // Node that represents proof mass state
in the x-direction
```

```
inout xn,mid,xp;
inout cno, cpo;
inout cni, cpi;


electrical      mover;          // [um]
electrical    xn,mid,xp;
electrical    cno,cpo;          // 1V = 1fF
electrical    cni,cpi;          // 1V = 1fF
voltage       qn,qp;
voltage       cnval,cpval;

`IPRcc( cf          ,   10    ,""       , 0.000000,   200,   "parasitic capacitance")
`IPRoo( g0          ,   1.5   ,"kg"     ,0.2,         5,     "initial gap")
`IPRoo( tco1        ,   0     ,"um/K"   ,-1e-1,       1e-1,  "tc1 of offset")
`IPRoo( tco2        ,   0     ,"um/K^2" ,-1e-3,       1e-3,  "tc2 of offset")
`IPRoo( tnom        ,   25    ,"C"      ,  0,         200,   "nominal temperature")
`IPRoo( nom_off     ,   0     ,"C"      ,-2e-1,       2e-1,  "nominal temperature")
`IPRoo( area0       ,   0     ,"C"      ,1e-9,        38000, "nominal temperature")

real mm_t, deltat;
real gap_p,gap_n;
real gap_p_tmp,gap_n_tmp;
real gap_p0,gap_n0;
real gap_min;

analog begin

`ifdef notInsideADMS
    @(initial_step) begin
`endif


  begin :  initializeInstance

    // area0 um^2
        //$strobe("area0    \t= %g (kg) \n", area0);

   begin : temperatureCoefficient
     deltat = ($temperature-273.15-tnom);
     mm_t   = (nom_off+deltat*tco1+deltat*deltat*tco2);
   end

   gap_p0  = (g0 * (1-mm_t));
   gap_n0  = (g0 * (1+mm_t));
   gap_min = (0.01*g0);
```

```
    end // initializeInstance

`ifdef notInsideADMS
      end //intial step
`endif

    begin : dynamicBlock

            gap_p_tmp  = gap_p0 + V(mover);
            gap_n_tmp  = gap_n0 - V(mover);

            gap_p = gap_p_tmp;
            gap_n = gap_n_tmp;

            if (gap_p > gap_min) begin
              I(mover)  <+-0.5*`eps0um*1e12*area0*(V(xp,mid)*V(xp,mid)/(gap_p*gap_p));
              V(cpval)   <+  (`eps0um*area0*1e15/gap_p)+cf;
            end else begin
             I(mover)  <+-0.5*`eps0um*1e12*area0*(V(xp,mid)*V(xp,mid)/(gap_min*gap_min));
             V(cpval)   <+((`eps0um*area0*1e15/gap_min)*(2-gap_p/gap_min))+cf;
            end

            if (gap_n > gap_min) begin
              I(mover)  <+0.5*`eps0um*1e12*area0*(V(xn,mid)*V(xn,mid)/(gap_n*gap_n));
              V(cnval)   <+ (`eps0um*area0*1e15/gap_n)+cf;
            end else begin
              I(mover)  <+0.5*`eps0um*1e12*area0*(V(xn,mid)*V(xn,mid)/(gap_min*gap_min));
              V(cnval)   <+((`eps0um*area0*1e15/gap_min)*(2-gap_n/gap_min))+cf;

            end
            V(qn) <+ V(xn,mid)*V(cnval);
            V(qp) <+ V(xp,mid)*V(cpval);

    end // DynamicBlock

    V(cno,cni)   <+ V(cnval);
    V(cpo,cpi)   <+ V(cpval);

    I(xn,mid)   <+ ddt(V(qn))*1e-15;
    I(xp,mid)   <+ ddt(V(qp))*1e-15;

end // analog

endmodule //cpp_trans2
```

```
///////////////////////////////////////////////////////////////////////////////////////////////////////////////////
///            This is a one-sided capacitor module for single ended self-test modules
///////////////////////////////////////////////////////////////////////////////////////////////////////////////////
module cpp_trans_1side (mover, xst, mid, csto,csti);

inout mover;                    // Node that represents proof mass state
in the x-direction
inout xst,mid;
inout csto, csti;

electrical      mover;              // [um]
electrical     xst,mid;
electrical     csto,csti;                // 1V = 1fF
voltage        qst;
voltage        cstval;

`IPRcc( tt              ,    25       ,""      , 0.05,     5000,    "nominal capacitance")
`IPRcc( tf              ,    0.85     ,""      , 0.05,     5000,    "nominal capacitance")
`IPRcc( lf              ,    10       ,""      , 0.05,     5000,    "nominal capacitance")
`IPRcc( nf              ,    1        ,""      , 1.00,     5000,    "nominal capacitance")
`IPRcc( cf              ,    10       ,""      , 0.000000,   200,    "parasitic capacitance")
`IPRoo( g0              ,    1.5      ,"kg"    ,0.2,         5,    "initial gap")
`IPRoo( orient          ,    1        ,"C"     ,-2,          2,    "nominal temperature")
`IPRoo( tnom            ,    25       ,"C"     ,0,         200,    "nominal temperature")

real area0;
real mm_t, deltat;
real gap_st;
real gap_st_tmp;
real gap_st0;
real gap_min;

analog begin

`ifdef notInsideADMS
     @(initial_step) begin
`endif

    begin :  initializeInstance

      area0    = (tt+2*tf)*lf*nf; // um^2

      begin : temperatureCoefficient
        deltat = ($temperature-273.15-tnom);
      end
```

```
      gap_st0  = g0 ;
      gap_min = (0.1*g0);

    end // initializeInstance

`ifdef notInsideADMS
      end //intial step
`endif

    begin : dynamicBlock

            gap_st_tmp  = gap_st0 - V(mover)*orient;
            gap_st = gap_st_tmp;

            if (gap_st > gap_min) begin
           I(mover) <+0.5*`eps0um*1e12*area0*orient*(V(xst,mid)*V(xst,mid)/(gap_st*gap_st));
               V(cstval)  <+  (`eps0um*area0*1e15/gap_st)+cf;
            end else begin
       I(mover)<+0.5*`eps0um*1e12*area0*orient*(V(xst,mid)*V(xst,mid)/(gap_min*gap_min));
               V(cstval)   <+((`eps0um*area0*1e15/gap_min)*(2-gap_st/gap_min))+cf;
            end

           V(qst) <+ V(xst,mid)*V(cstval);
    V(csto,csti) <+ V(cstval);
    I(xst,mid)   <+ ddt(V(qst))*1e-15;

    end // DynamicBlock
end // analog

endmodule //cpp_trans_1side
////////////////////////////////////////////////////////////////////////////////////////////////////////////////////////////////////////////////

module stop_trans (mover);

inout mover;                // Node that represents proof mass state

electrical mover;
electrical mov_vel;

`IPRoo( gap_stop       ,    0.70       ,"um"          ,0.000001,    inf,            "Gap between stopper
and proof mass")
`IPRoo( ks_stop        ,    100        ,"N/m"         ,    0, inf,            "Stiffness of mechanical stop")
`IPRoo( dmp_stop       ,    0.8        ,"N/m"         ,    0,inf,            "Stiffness of mechanical stop")

parameter real eps = 1e-6;
real delta_p, delta_n;
```

```
real mod_delta_p, mod_delta_n;

analog begin

`ifdef notInsideADMS
   @(initial_step) begin
`endif

   begin : initializeInstance

   end//  initializeInstance

`ifdef notInsideADMS
   end //intial step
`endif

begin : dynamicBlock

    V(mov_vel)  <+ ddt(V(mover));
    delta_n = (V(mover)-gap_stop);
    delta_p = (V(mover)+gap_stop);
    mod_delta_n = 0.5*(delta_n+sqrt((delta_n)*(delta_n)+eps*eps));
    mod_delta_p = 0.5*(delta_p-sqrt((delta_p)*(delta_p)+eps*eps));
 I(mover) <+-ks_stop*(mod_delta_n+mod_delta_p)-ddt(mod_delta_n+mod_delta_p)*dmp_stop;

end // dynamicBlock
end // analog
endmodule
////////////////////////////////////////////////////////////////////////////////////////////////////////////////////////////////////////////

// ROTATIONAL

////////////////////////////////////////////////////////////////////////////////////////////////////////////////////////////////////////////
// This model describes a differential bigap rotating parallel plate capacitor
////////////////////////////////////////////////////////////////////////////////////////////////////////////////////////////////////////////

module cpp_rot_bigap (rotator, vp, vmid, vn, cpo,cpi, cno,cni);

inout rotator;        // Node that represents proof mass rotation
about pivot point
inout vn,vmid,vp;     // Electrodes
inout cno, cpo;       // Monitoring nodes for capacitance
inout cni, cpi;       // Monitoring nodes for capacitance
                      // Monitoring nodes are set up to be "stackable"
for parallel capacitances
```

```
electrical     rotator;                  // [rad]
electrical     vn,vmid,vp;
electrical     cpo,cno;                  // 1V = 1fF
electrical     cpi,cni;                  // 1V = 1fF
voltage        qp,qn;
voltage        cpvalv,cnvalv;

//branch (rotator) rot_int;

//////////////////////////////////////////////////////////////////////////////////////////////////////////////
// Model parameters
//////////////////////////////////////////////////////////////////////////////////////////////////////////////

`IPRcc( width0            ,   200      ,""     , 0.05,   50000,    "drawn area um^2")
`IPRcc( areafill_cap1      ,   1        ,""     ,0.05,      1,     "fill factor for capacitance")
`IPRcc( areafill_cap2 ,   areafill_cap1 ,""   , 0.05,      1,     "fill factor for electrostatic force")
`IPRcc( l1  ,   200   ,""   ,0.05,    5000,    "inner distance from pivot to center of electrode ")
`IPRcc( l2 ,   300   ,""    , 0.05,    5000,    "bigap distance from pivot to center of electrode ")
`IPRcc( l3   ,   400   ,""     , 0.05,    5000,    "outer distance from pivot to center of electrode")
`IPRcc( cf      ,   10       ,""     , 0.00,    200,    "parasitic capacitance")
`IPRoo( g1      ,   0.9      ,"kg"    , 0.2,      5,    "initial inner gap")
`IPRoo( g2               ,   1.8      ,"kg"    , 0.2,      5,     "initial outer gap")
`IPRoo( tc1             ,   0        ,"rad/K"   ,-1e-1,   1e-1,    "tc1 of gap mismatch")
`IPRoo( tc2             ,   0        ,"rad/K^2"  ,-1e-3,   1e-3,    "tc2 of gap mismatch")
`IPRoo( nom_g0_mm    ,   0     ,"C"      ,-2e-1,    2e-1,    "nominal offset Positive Cp >Cn ")
`IPRoo( tnom              ,   25       ,"C"      , 0,    200,     "nominal temperature")

real mm_t, deltat;
real gap_p1_tmp1,gap_n1_tmp1;
real gap_p1_tmpm,gap_n1_tmpm;
real gap_p1_tmp2,gap_n1_tmp2;
real gap_p1_max1,gap_n1_max1;
real gap_p1_maxm,gap_n1_maxm;
real gap_p1_max2,gap_n1_max2;
real gap_p2_tmp1,gap_n2_tmp1;
real gap_p2_tmpm,gap_n2_tmpm;
real gap_p2_tmp2,gap_n2_tmp2;
real gap_p2_max1,gap_n2_max1;
real gap_p2_maxm,gap_n2_maxm;
real gap_p2_max2,gap_n2_max2;
real gap_p10,gap_n10;
real gap_p20,gap_n20;
real gap_min1,gap_min2;
real thetamax1,thetamax2,thetamax;
real lm1,lm2;
real cnval,cpval;
```

```
real taup,taun;
real cnval1,cpval1;
real taup1,taun1;
real cnval2,cpval2;
real taup2,taun2;
real vfacp,vfacn;
real cpval_int1, cnval_int1;
real cpval_max1, cnval_max1;
real cpval_int2, cnval_int2;
real cpval_max2, cnval_max2;

analog begin

`ifdef notInsideADMS
    @(initial_step) begin
`endif

  begin :  initializeInstance

    lm1 = (l1+l2)/2.0;
    lm2 = (l2+l3)/2.0;
    gap_min1 = (0.1*g1);
    gap_min2 = (0.1*g2);
    thetamax1     = (g1-gap_min1)/l2;
    thetamax2     = (g2-gap_min2)/l3;
    // Determine which is the limiting gap
    if (thetamax2 < thetamax1) begin
      thetamax = thetamax2;
    end else begin
      thetamax = thetamax1;
    end

    begin : temperatureCoefficient
     deltat = ($temperature-273.15-tnom);
     mm_t   = (nom_g0_mm*(1+deltat*tc1+deltat*deltat*tc2));
    end

    gap_p10  = (g1 * (1-mm_t));
    gap_n10  = (g1 * (1+mm_t));
    gap_p20  = (g2 * (1-mm_t));
    gap_n20  = (g2 * (1+mm_t));
    // Calculate min gap at "integration" points for simpson's method
      gap_p1_max1    = gap_p10 - thetamax*l1;
      gap_p1_maxm    = gap_p10 - thetamax*lm1;
      gap_p1_max2    = gap_p10 - thetamax*l2;
      gap_n1_max1    = gap_n10 - thetamax*l1;
```

```
        gap_n1_maxm    = gap_n10 - thetamax*lm1;
        gap_n1_max2    = gap_n10 - thetamax*l2;

        gap_p2_max1    = gap_p20 - thetamax*l2;
        gap_p2_maxm    = gap_p20 - thetamax*lm2;
        gap_p2_max2    = gap_p20 - thetamax*l3;
        gap_n2_max1    = gap_n20 - thetamax*l2;
        gap_n2_maxm    = gap_n20 - thetamax*lm2;
        gap_n2_max2    = gap_n20 - thetamax*l3;

cpval_int1    = (l1/(gap_p1_max1*gap_p1_max1)+4*lm1/(gap_p1_maxm*gap_p1_maxm) +
l2/(gap_p1_max2*gap_p1_max2));
cnval_int1    = (l1/(gap_n1_max1*gap_n1_max1)+4*lm1/(gap_n1_maxm*gap_n1_maxm) +
l2/(gap_n1_max2*gap_n1_max2));
cpval_max1    =(`eps0um*width0*(l2-l1)*1e15/6)*areafill_cap1*(1/gap_p1_max1
+4/gap_p1_maxm + 1/gap_p1_max2);
 cnval_max1    =(`eps0um*width0*(l2-l1)*1e15/6)*areafill_cap1*(1/gap_n1_max1
+4/gap_n1_maxm + 1/gap_n1_max2);

 cpval_int2    = (l2/(gap_p2_max1*gap_p2_max1)+4*lm2/(gap_p2_maxm*gap_p2_maxm) +
l3/(gap_p2_max2*gap_p2_max2));
 cnval_int2    = (l2/(gap_n2_max1*gap_n2_max1)+4*lm2/(gap_n2_maxm*gap_n2_maxm) +
l3/(gap_n2_max2*gap_n2_max2));
cpval_max2=(`eps0um*width0*(l3-l2)*1e15/6)*areafill_cap2*(1/gap_p2_max1
+4/gap_p2_maxm + 1/gap_p2_max2);
 cnval_max2    =(`eps0um*width0*(l3-l2)*1e15/6)*areafill_cap2*(1/gap_n2_max1
+4/gap_n2_maxm + 1/gap_n2_max2);

    end // initializeInstance
`ifdef notInsideADMS
      end //intial step
`endif

    begin : dynamicBlock
            gap_p1_tmp1    = gap_p10 - V(rotator)*l1;
            gap_p1_tmpm    = gap_p10 - V(rotator)*lm1;
            gap_p1_tmp2    = gap_p10 - V(rotator)*l2;
            gap_n1_tmp1    = gap_n10 + V(rotator)*l1;
            gap_n1_tmpm    = gap_n10 + V(rotator)*lm1;
            gap_n1_tmp2    = gap_n10 + V(rotator)*l2;

            gap_p2_tmp1    = gap_p20 - V(rotator)*l2;
            gap_p2_tmpm    = gap_p20 - V(rotator)*lm2;
            gap_p2_tmp2    = gap_p20 - V(rotator)*l3;
            gap_n2_tmp1    = gap_n20 + V(rotator)*l2;
            gap_n2_tmpm    = gap_n20 + V(rotator)*lm2;
```

```
            gap_n2_tmp2    = gap_n20 + V(rotator)*l3;

            vfacp      = 0.5*(V(vp,vmid)*V(vp,vmid));
            vfacn      = 0.5*(V(vn,vmid)*V(vn,vmid));

        // Calculate theta value to begin linearization of capacitance
        // Use Simpson's rule of integration to calculate capacitances and electrostatic forces
        // This is being done to avoid "exact" solution which has 1/theta term
   // Create a linearization of the capacitance and electrostatic force above a certain value of theta
   // This is being implemented for convergence/stable solutions in a spice-like circuit simulator
            if (V(rotator) > thetamax) begin

                cpval1   =(`eps0um*width0*(l2-l1)*1e15/6)*areafill_cap1*cpval_int1*(V(rotator)-
thetamax)+cpval_max1   ;
                cnval1   =(`eps0um*width0*(l2-l1)*1e15/6)*areafill_cap1*(1/gap_n1_tmp1
+4/gap_n1_tmpm + 1/gap_n1_tmp2) ;
                taup1    =vfacp*(`eps0um*width0*(l2-
l1)/6)*areafill_cap1*(l1/(gap_p1_max1*gap_p1_max1)+4*lm1/(gap_p1_maxm*gap_p1_maxm)
+ l2/(gap_p1_max2*gap_p1_max2));
                taun1    =vfacn*(`eps0um*width0*(l2-
l1)/6)*areafill_cap1*(l1/(gap_n1_tmp1*gap_n1_tmp1)+4*lm1/(gap_n1_tmpm*gap_n1_tmpm) +
l2/(gap_n1_tmp2*gap_n1_tmp2));

                cpval2 =(`eps0um*width0*1e15*(l3-l2)/6)*areafill_cap2*cpval_int2*(V(rotator)-
thetamax)+cpval_max2   ;
                cnval2   =(`eps0um*width0*1e15*(l3-l2)/6)*areafill_cap2*(1/gap_n2_tmp1
+4/gap_n2_tmpm + 1/gap_n2_tmp2) ;
                taup2    =vfacp*(`eps0um*width0*(l3-l2)/6)*areafill_cap2* (l2/(gap_p2_max1*
gap_p2_max1)+4*lm2/(gap_p2_maxm*gap_p2_maxm) + l3/(gap_p2_max2*gap_p2_max2));
                taun2    =vfacn*(`eps0um*width0*(l3- l2)/6)*areafill_cap2 *(l2/(gap_n2_tmp1*
gap_n2_tmp1)+4*lm2/(gap_n2_tmpm*gap_n2_tmpm) + l3/(gap_n2_tmp2*gap_n2_tmp2));

                cpval    = cpval1 + cpval2 +cf;
                cnval    = cnval1 + cnval2 +cf;
                taup     = taup1 + taup2;
                taun     = taun1 + taun2;

            end else if (V(rotator) < -1*thetamax) begin
                cpval1      =(`eps0um*width0*1e15*(l2-l1)/6)*areafill_cap1*(1/gap_p1_tmp1
+4/gap_p1_tmpm + 1/gap_p1_tmp2) ;
                cnval1      =-1.0*(`eps0um*width0*1e15*(l2-l1)/6)*areafill_cap1* cnval_int1*
(V(rotator)+thetamax)+cnval_max1;
                taup1  =vfacp*(`eps0um*width0*(l2-l1)/6)*areafill_cap1* (l1/(gap_p1_tmp1*
gap_p1_tmp1)+4*lm1/(gap_p1_tmpm*gap_p1_tmpm) + l2/(gap_p1_tmp2*gap_p1_tmp2));
                taun1       =vfacn*(`eps0um*width0*(l2-l1)/6)* areafill_cap1* (l1/(gap_n1_max1*
gap_n1_max1)+4*lm1/(gap_n1_maxm*gap_n1_maxm) + l2/(gap_n1_max2*gap_n1_max2));
```

```
                cpval2  = (`eps0um*width0*1e15*(l3-l2)/6)*areafill_cap2*(1/gap_p2_tmp1
+4/gap_p2_tmpm + 1/gap_p2_tmp2) ;
                cnval2 = -1.0*(`eps0um*width0*1e15*(l3-l2)/6)*areafill_cap2* cnval_int2*
(V(rotator)+thetamax)+cnval_max2;
                taup2      =vfacp*(`eps0um*width0*(l3-l2)/6)*areafill_cap2* (l2/(gap_p2_tmp1*
gap_p2_tmp1)+4*lm2/(gap_p2_tmpm*gap_p2_tmpm) + l3/(gap_p2_tmp2*gap_p2_tmp2));
                taun2   = vfacn*(`eps0um*width0*(l3-l2)/6)*areafill_cap2* (l2/(gap_n2_max1*
gap_n2_max1)+4*lm2/(gap_n2_maxm*gap_n2_maxm) + l3/(gap_n2_max2*gap_n2_max2));

                cpval    = cpval1 + cpval2 +cf;
                cnval    = cnval1 + cnval2 +cf;
                taup     = taup1 + taup2;
                taun     = taun1 + taun2;

            end else begin
                cpval1      =(`eps0um*width0*1e15*(l2-l1)/6)*areafill_cap1*(1/gap_p1_tmp1
+4/gap_p1_tmpm + 1/gap_p1_tmp2);
                cnval1      =(`eps0um*width0*1e15*(l2-l1)/6)*areafill_cap1*(1/gap_n1_tmp1
+4/gap_n1_tmpm + 1/gap_n1_tmp2);
                taup1       = vfacp*(`eps0um*width0*(l2-l1)/6)*areafill_cap1* (l1/(gap_p1_tmp1*
gap_p1_tmp1)+4*lm1/(gap_p1_tmpm*gap_p1_tmpm) + l2/(gap_p1_tmp2*gap_p1_tmp2));
                taun1    = vfacn*(`eps0um*width0*(l2-
l1)/6)*areafill_cap1*(l1/(gap_n1_tmp1*gap_n1_tmp1) +4*lm1/(gap_n1_tmpm*gap_n1_tmpm)
+ l2/(gap_n1_tmp2*gap_n1_tmp2));

                cpval2   =(`eps0um*width0*1e15*(l3-l2)/6)*areafill_cap2*(1/gap_p2_tmp1
+4/gap_p2_tmpm + 1/gap_p2_tmp2);
                cnval2  =(`eps0um*width0*1e15*(l3-l2)/6)*areafill_cap2*(1/gap_n2_tmp1
+4/gap_n2_tmpm + 1/gap_n2_tmp2);
                taup2      =vfacp*(`eps0um*width0*(l3-l2)/6)*areafill_cap2* (l2/(gap_p2_tmp1*
gap_p2_tmp1)+4*lm2/(gap_p2_tmpm*gap_p2_tmpm) + l3/(gap_p2_tmp2* gap_p2_tmp2));
                taun2      =vfacn*(`eps0um*width0*(l3-l2)/6)*areafill_cap2*(l2/(gap_n2_tmp1*
gap_n2_tmp1)+4*lm2/(gap_n2_tmpm*gap_n2_tmpm) + l3/(gap_n2_tmp2*gap_n2_tmp2));

                cpval    = cpval1 + cpval2 +cf;
                cnval    = cnval1 + cnval2 +cf;
                taup     = taup1 + taup2;
                taun     = taun1 + taun2;

            end

   end // DynamicBlock

   V(cpvalv) <+  (cpval);
   V(cnvalv) <+  (cnval);
```

```
   V(qn)    <+ V(vn,vmid)*V(cnvalv);
   V(qp)    <+ V(vp,vmid)*V(cpvalv);

   // This configuration is used to allow capacitance modules to be stacked in parallel and
provide total capacitance calculations
   V(cno,cni)    <+ V(cnvalv);
   V(cpo,cpi)    <+ V(cpvalv);

   I(rotator)    <+  (taup-taun);

   I(vn,vmid)    <+ ddt(V(qn))*1e-15;
   I(vp,vmid)    <+ ddt(V(qp))*1e-15;


end // analog

endmodule //cpp_rot_bigap

//////////////////////////////////////////////////////////////////////////////////////////////////////////////////////////////////////////////////
// This model describes a differential single rotating parallel plate capacitor
//////////////////////////////////////////////////////////////////////////////////////////////////////////////////////////////////////////////////

module cpp_rot (rotator, vp, vmid, cpo,cpi);

inout rotator;        // Node that represents proof mass rotation
about pivot point
inout vmid,vp;     // Electrodes
inout cpo;       // Monitoring nodes for capacitance
inout cpi;       // Monitoring nodes for capacitance
                 // Monitoring nodes are set up to be "stackable"
for parallel capacitances


electrical     rotator;                  // [rad]
electrical     vmid,vp;
electrical     cpo;                 // 1V = 1fF
electrical     cpi;                 // 1V = 1fF
voltage        qp;
voltage        cpvalv;

//branch (rotator) rot_int;

//////////////////////////////////////////////////////////////////////////////////////////////////////////////////
// Model parameters
//////////////////////////////////////////////////////////////////////////////////////////////////////////////////
```

```
`IPRcc( width0              ,    200        ,""       , 0.05,    50000,     "drawn area um^2")
`IPRcc( areafill_cap         ,    1          ,""       ,0.05,      1,     "fill factor for capacitance")
`IPRcc( l1  , 200   ,""      , 0.05,     5000,     "inner distance from pivot to center of electrode ")
`IPRcc( l2     ,  300  ,""     ,0.05,    5000,     "bigap distance from pivot to center of electrode ")
`IPRcc( cf                  ,    10         ,""       , 0.00,     200,     "parasitic capacitance")
`IPRoo( g0                  ,    1.5        ,"kg"     ,  0.2,       5,     "initial gap")
`IPRoo( tc1                 ,    0          ,"rad/K"    ,-1e-1,    1e-1,     "tc1 of gap mismatch")
`IPRoo( tc2                 ,    0          ,"rad/K^2"  ,-1e-3,    1e-3,     "tc2 of gap mismatch")
`IPRoo( nom_g0_mm    ,    0    ,"C"      ,-2e-1,     2e-1,    "nominal offset Positive Cp > Cn ")
`IPRoo( tnom                ,    25         ,"C"      ,    0,     200,     "nominal temperature")
`IPRoo( pol                 ,     1         ," "      ,    -2,      2,     "polarity")

real mm_t, deltat;
real gap_p_tmp1;
real gap_p_tmpm;
real gap_p_tmp2;
real gap_p_max1;
real gap_p_maxm;
real gap_p_max2;
real gap_p0;
real gap_min;
real thetamax;
real lm;
real cpval;
real taup;
real vfacp;
real cpval_int;
real cpval_max;

analog begin

`ifdef notInsideADMS
    @(initial_step) begin
`endif


  begin :  initializeInstance

    lm      = (l1+l2)/2.0;
    gap_min = (0.1*g0);
    thetamax     = (g0-gap_min)/l2;
    begin : temperatureCoefficient
      deltat = ($temperature-273.15-tnom);
      mm_t   = (nom_g0_mm*(1+deltat*tc1+deltat*deltat*tc2));
    end
```

```
      gap_p0  = (g0 * (1-mm_t));
      // Calculate min gap at "integration" points for simpson's method
         gap_p_max1    = gap_p0 - thetamax*l1;
         gap_p_maxm    = gap_p0 - thetamax*lm;
         gap_p_max2    = gap_p0 - thetamax*l2;
       cpval_int    = (l1/(gap_p_max1*gap_p_max1)+4*lm/(gap_p_maxm*gap_p_maxm) +
l2/(gap_p_max2* gap_p_max2));
       cpval_max    =(`eps0um*width0*1e15*(l2-l1)/6)*areafill_cap*(1/gap_p_max1
+4/gap_p_maxm + 1/gap_p_max2);

    end // initializeInstance

`ifdef notInsideADMS
      end //intial step
`endif

    begin : dynamicBlock
            gap_p_tmp1    = gap_p0 - pol*V(rotator)*l1;
            gap_p_tmpm    = gap_p0 - pol*V(rotator)*lm;
            gap_p_tmp2    = gap_p0 - pol*V(rotator)*l2;

            vfacp      = 0.5*(V(vp,vmid)*V(vp,vmid));

          // Calculate theta value to begin linearization of capacitance

          // Use Simpson's rule of integration to calculate capacitances and electrostatic forces
          // This is being done to avoid "exact" solution which has 1/theta term


    // Create a linearization of the capacitance and electrostatic force above a certain value of theta
     // This is being implemented for convergence/stable solutions in a spice-like circuit simulator

            if (V(rotator) > thetamax) begin

                 cpval   =(`eps0um*width0*1e15*(l2-l1)/6)*areafill_cap*cpval_int*(V(rotator)-
thetamax)+cpval_max       + cf;
                 taup    =-vfacp*(`eps0um*width0*(l2-l1)/6)*areafill_cap* (l1/(gap_p_max1*
gap_p_max1)+4*lm/(gap_p_maxm*gap_p_maxm) + l2/(gap_p_max2*gap_p_max2));

            end else if (V(rotator) < -1*thetamax) begin
                 cpval      =(`eps0um*width0*1e15*(l2-l1)/6)*areafill_cap*(1/gap_p_tmp1
+4/gap_p_tmpm + 1/gap_p_tmp2)+cf;
                 taup       =vfacp*(`eps0um*width0*(l2-l1)/6)*areafill_cap*(l1/(gap_p_tmp1*
gap_p_tmp1)+4*lm/(gap_p_tmpm*gap_p_tmpm) + l2/(gap_p_tmp2*gap_p_tmp2));
            end else begin
                 cpval      =(`eps0um*width0*1e15*(l2-l1)/6)*areafill_cap*(1/gap_p_tmp1
```

```
+4/gap_p_tmpm + 1/gap_p_tmp2)+cf;
                taup      = -vfacp*(`eps0um*width0*(l2-l1)/6)*areafill_cap*(l1/(gap_p_tmp1
*gap_p_tmp1)+4*lm/(gap_p_tmpm*gap_p_tmpm) + l2/(gap_p_tmp2*gap_p_tmp2));
            end

   V(cpvalv) <+  (cpval);
   V(qp)     <+  (V(vmid,vp)*V(cpvalv));

   // This configuration is used to allow capacitance modules to be stacked in parallel and
provide total capacitance calculations
   V(cpo,cpi)    <+ V(cpvalv);
   I(rotator)    <+    (pol*taup);
   I(vmid,vp)    <+ ddt(V(qp))*1e-15;
   end // DynamicBlock

end // analog

endmodule //cpp_rot

/////////////////////////////////////////////////////////////////////////////////////////////////////////////////////////////////////////////////////////////////
// Travel stop for rotational devices
/////////////////////////////////////////////////////////////////////////////////////////////////////////////////////////////////////////////////////////////////
module stop_rot (rotator);

inout     rotator;              // Node that represents proof mass state
electrical rotator;


`IPRoo( gap_stop       ,    0.90       ,"um"     ,    0.1,inf,   "Gap between stopper and proof mass")
`IPRoo( l_stop    ,    300        ,"um"          ,    0.1,inf,           "Distance of stop from pivot point")
`IPRoo( kr_stop   ,    1000e-6     ,"uN-m/rad "    ,    0, inf,            "Stiffness of mechanical stop")
`IPRoo( dmp_stop       ,    0.1        ," "      ,    1e-12, 1e20,         "Damping of mechanical stop")

real theta_stop;
real del_theta_n, del_theta_p;
real gap_n, gap_p;

parameter real eps = 1e-18;

analog begin

`ifdef notInsideADMS
  @(initial_step) begin
`endif

  begin : initializeInstance
```

```
    theta_stop=gap_stop/l_stop;
  end//  initializeInstance

`ifdef notInsideADMS
  end //intial step
`endif

 begin : dynamicBlock
   theta_stop     = gap_stop/l_stop;
   del_theta_n    = theta_stop - V(rotator);
   del_theta_p    = theta_stop + V(rotator);
   gap_n          = 0.5*(del_theta_n-sqrt((del_theta_n*del_theta_n)+eps*eps));
   gap_p          = 0.5*(del_theta_p-sqrt((del_theta_p*del_theta_p)+eps*eps));

   I(rotator) <+kr_stop*l_stop*(gap_n-gap_p)-ddt(gap_n-gap_p)*dmp_stop*1e3;
 //Force applied to rotator by travel stop

end // dynamicBlock

end // analog

endmodule
////////////////////////////////////////////////////////////////////////////////////////////////////////////////////////////////

////////////////////////////////////////////////////////////////////////////////////////////////////////////////////////////////
module rot_1dof(accel, rotator, theta);

inout accel;                    // Applied acceleration -
this is still an electrical state
inout rotator;                          // Node that represents
proof mass state in the x-direction
inout theta;

electrical        accel;              // Input acceleration in [m/s^2]
electrical      rotator;              // Rotation angle [rad]
electrical   rotator_vel;               // Rotational velocity [rad/s]
electrical        theta;              // 1V = 1rad - output
monitor pin for rotation

branch(rotator_vel) vel_int;

///////////////////////////////////////////////////////////////////////////////////////////////////////////////////////////////
// Model parameters
////////////////////////////////////////////////////////////////////////////////////////////////////////////////////////////////

`IPRcc( damp_ratio              ,    1.5        ,""          ,   0.000001,        5,     "damping ratio")
```

```
`IPRoo( mass          ,  4.2e-9   ,"kg"     ,  1e-10,   1e-7,   "mass of heavy end ")
`IPRoo( l_cg          ,  300      ,"um"     ,  -1000,   1000,   "center of gravity")
`IPRoo( irot  ,  2.42e-4  ,"kg-um^2"   ,  1e-16,  1,   "moment of inertia about pivot point")
`IPRoo( kr           ,  1.13e-6   ,"uN-m/rad",   1e-9,    100,   "spring constant")
`IPRoo( tcs1     ,  0        ,"uN-m/rad*K"  ,  -1e-1,   1e-1,   "tc1 of spring constant")
`IPRoo( tcs2      ,  0        ,"N-um/rad*K^2" ,  -1e-3,   1e-3,   "tc2 of spring constant")
`IPRoo( tnom     ,  25.0     ,"C"       ,    0,    200,   "nominal temperature")
`IPRcc( orient        ,  1.0      ,""        ,  -1.0,    1.0,   "relative orientation")
`IPRoo( thetaoff    ,  0        ,"uN-m/rad*K"  ,  -1e-3,   1e-3,   "initial offset angle")
`IPRoo( tco1          ,  0        ,"uN-m/rad*K"  , -1e-1,   1e-1,   "tc1 of offset angle")
`IPRoo( tco2     ,  0        ,"N-um/rad*K^2" , -1e-3,   1e-3,   "tc2 of offset angle")

real D_coef;
real kr_t, deltat,theta0_t;
real Q_fact,natural_fo,rolloff_fo;

analog begin

`ifdef notInsideADMS
     @(initial_step) begin
`endif

    begin :  initializeInstance
      begin : temperatureCoefficient
        deltat       = ($temperature-273.15-tnom);
        kr_t         = kr*(1+tcs1*deltat+tcs2*deltat*deltat);
        theta0_t     = thetaoff*(1+tco1*deltat+tco2*deltat*deltat);

      end
      begin : calculateDampingCoefficient
        D_coef       = damp_ratio * 2* sqrt(kr_t*irot);
      end
      begin : nominalMechanicalParameters
        Q_fact       = 1/(2*damp_ratio);
        natural_fo    = 1e-3*(sqrt(kr_t/irot*1e6) /(2*`pi)) ;
rolloff_fo  = sqrt( sqrt(pow(2*pow(damp_ratio,2)-1.0,2)+1)- (2*pow(damp_ratio,2)-1.0) ) *
natural_fo;

      end //nominalMechanicalParameters
    end // initializeInstance

`ifdef notInsideADMS
      end //intial step
`endif

    begin : dynamicBlock
```

```
V(rotator_vel)       <+ ddt(V(rotator),1.0e-9);
I(vel_int)           <+ 1*V(rotator_vel);
I(rotator)           <+1.0*orient*l_cg*mass*(V(accel))*1e-6;                    //
//Torque from acceleration N um - cg is length from rotation center
I(rotator)           <+  -irot*ddt(V(rotator_vel),1.0e-9);
                     // Resulting angular acceleration
I(rotator)           <+ -1.0*kr_t*theta0_t;
                     // Torque creating initial offset
I(rotator)           <+ -1.0*kr_t*V(rotator);
                     // Torque from the rotational stiffness
I(rotator)           <+ -1.0*D_coef*V(rotator_vel);
                     // Torque from the rotational damping
I(rotator)           <+ white_noise(4.0e12*`k_boltz*$temperature*D_coef, "Brownian");
// Brownian noise


  end // DynamicBlock

  V(theta) <+ V(rotator);

end // analog

endmodule //rot_1dof
//////////////////////////////////////////////////////////////////////////////////////////////////////////
```

# Appendices II

## STM32F4 Discovery Board programing

<main.c>

```
#include <stm32f4xx.h>
#include "stdio.h"
#include "stm32f4_discovery.h"
#include "tm_stm32f4_dac.h"
#include "defines.h"
#include "stm32f4xx_tim.h"
#include "stm32f4xx_rcc.h"
#include "misc.h"

void RCC_Config(void);
void RCC_Configuration(void)
{
  RCC_AHB1PeriphClockCmd(RCC_AHB1Periph_GPIOC, ENABLE);
  RCC_APB2PeriphClockCmd(RCC_APB2Periph_ADC1, ENABLE);
          RCC_APB1PeriphClockCmd(RCC_APB1Periph_TIM2, ENABLE);
          RCC_APB1PeriphClockCmd(RCC_APB1Periph_TIM5, ENABLE);

}
 /**************************************************/
//Initialisation des timer

void InitializeTimer2()  // Timer to create the period of 24us (41.6 kHz)
{
    TIM_TimeBaseInitTypeDef timerInitStructure;
    timerInitStructure.TIM_Prescaler = 84 - 1;   //1Mhz because clk_stm = 84Mhz because the formule is clk_timer2=clk_stm/((Prescaler+1)*(period+1))
    timerInitStructure.TIM_CounterMode = TIM_CounterMode_Up;
    timerInitStructure.TIM_Period = 24-1;       //Divide 1Mhz by 24 to have 41.6kHz
    timerInitStructure.TIM_ClockDivision = TIM_CKD_DIV1;
    timerInitStructure.TIM_RepetitionCounter = 0;
    TIM_TimeBaseInit(TIM2, &timerInitStructure);
    TIM_Cmd(TIM2, ENABLE);
            TIM_ITConfig(TIM2, TIM_IT_Update, ENABLE);
}
void InitializeTimer5()  // Timer to create the period of 4us (250 KHz)
{
```

```
   TIM_TimeBaseInitTypeDef timerInitStructure;
   timerInitStructure.TIM_Prescaler = 84 - 1;
   timerInitStructure.TIM_CounterMode = TIM_CounterMode_Up;
                   timerInitStructure.TIM_Period = 2-1;
                   timerInitStructure.TIM_ClockDivision = TIM_CKD_DIV1;
   timerInitStructure.TIM_RepetitionCounter = 0;
   TIM_TimeBaseInit(TIM5, &timerInitStructure);
   TIM_Cmd(TIM5, ENABLE);
           TIM_ITConfig(TIM5, TIM_IT_Update, ENABLE);
}

void Output_voltage_config(void) //Configure Inputs outputs
{
         GPIO_InitTypeDef GPIO_InitStruct;
         RCC_AHB1PeriphClockCmd(RCC_AHB1Periph_GPIOB, ENABLE); //GPIOB
indicates the use of ports B
         GPIO_InitStruct.GPIO_Pin = GPIO_Pin_6 | GPIO_Pin_8 | GPIO_Pin_3 | GPIO_Pin_5;
//corresponding to PB6 PB8 PB3 PB5
  GPIO_InitStruct.GPIO_OType = GPIO_OType_PP;
  GPIO_InitStruct.GPIO_PuPd = GPIO_PuPd_NOPULL;
  GPIO_InitStruct.GPIO_Mode = GPIO_Mode_OUT;
  GPIO_Init(GPIOB, &GPIO_InitStruct);
}

void GPIO_Configuration(void) //GPIO config for the ADC
{
  GPIO_InitTypeDef GPIO_InitStructure;

  /* ADC Channel 11 -> PC1 */

  GPIO_InitStructure.GPIO_Pin = GPIO_Pin_1; //corresponding to PC1
  GPIO_InitStructure.GPIO_Mode = GPIO_Mode_AN;
  GPIO_InitStructure.GPIO_PuPd = GPIO_PuPd_NOPULL ;
  GPIO_Init(GPIOC, &GPIO_InitStructure);
}

void ADC_Configuration(void) //ADC config this function was found on stm32f4-
discovery.com
{
  ADC_CommonInitTypeDef ADC_CommonInitStructure;
  ADC_InitTypeDef ADC_InitStructure;
 /* ADC Common Init */
```

```
  ADC_CommonInitStructure.ADC_Mode = ADC_Mode_Independent;
  ADC_CommonInitStructure.ADC_Prescaler = ADC_Prescaler_Div2;
  ADC_CommonInitStructure.ADC_DMAAccessMode = ADC_DMAAccessMode_Disabled;
  ADC_CommonInitStructure.ADC_TwoSamplingDelay = ADC_TwoSamplingDelay_5Cycles;
  ADC_CommonInit(&ADC_CommonInitStructure);

  ADC_InitStructure.ADC_Resolution = ADC_Resolution_12b;
  ADC_InitStructure.ADC_ScanConvMode = DISABLE; // 1 Channel
  ADC_InitStructure.ADC_ContinuousConvMode = DISABLE; // Conversions Triggered
  ADC_InitStructure.ADC_ExternalTrigConvEdge = ADC_ExternalTrigConvEdge_None; //
Manual
  ADC_InitStructure.ADC_ExternalTrigConv = ADC_ExternalTrigConv_T2_TRGO;
  ADC_InitStructure.ADC_DataAlign = ADC_DataAlign_Right;
  ADC_InitStructure.ADC_NbrOfConversion = 1;
  ADC_Init(ADC1, &ADC_InitStructure);

/* ADC1 regular channel 11 configuration */
  ADC_RegularChannelConfig(ADC1, ADC_Channel_11, 1, ADC_SampleTime_144Cycles); //
PC1

  /* Enable ADC1 */
  ADC_Cmd(ADC1, ENABLE);
}

/******************************************************************************
*********/

uint16_t ADC_X1 = 0;
uint16_t calcul = 0;
uint16_t vitesse_X;
uint16_t ADCConvertedValue;

int main(void)
{
  int j;

        /* Initialize system */
    RCC_Configuration();
    GPIO_Configuration();
    SystemInit();

    /* Initialize DAC channel 2, pin PA5 */
 TM_DAC_Init(TM_DAC2);
```

```
            /* Initialize DAC channel 1, pin PA4 */
    TM_DAC_Init(TM_DAC1); //PA4
            //Init timer
            InitializeTimer2();
            InitializeTimer5();
                    //Init ADC
                    ADC_Configuration();

                    //Output init
                    Output_voltage_config(); //config output voltage

                    while (1) //infinite loop
    {
                              ADC_SoftwareStartConv(ADC1); //this enables ADC
                              while(ADC_GetFlagStatus(ADC1, ADC_FLAG_EOC) == RESET);
          if (TIM_GetITStatus(TIM2, TIM_IT_Update) != RESET)
//we manage the frequency 37kHz with the flag of timer2
    {
                              for (j=1;j<13;j++){
                                        while(TIM_GetITStatus(TIM5, TIM_IT_Update) == RESET){};
//If the flag of the timer 660kHz doesn't change, we do nothing
                                        TIM_ClearITPendingBit(TIM5, TIM_IT_Update);
                              //we clear the flag

                                        switch(j){
case 1: //acquisition de la valeur de electrode_X
ADCConvertedValue = ADC_GetConversionValue(ADC1);
//We save the value of ADC
vitesse_X = ADCConvertedValue - ADC_X1;
//We calculate the "speed"
ADC_X1 = ADCConvertedValue;
//We save the value of ADC for the next passage in the loop
          TM_DAC_SetValue(TM_DAC1, 0); //On envoie 0 pour X
          //Outputs :
          TM_DAC_SetValue(TM_DAC2, 0);    //DAC2
          TM_GPIO_SetPinLow(GPIOB,GPIO_Pin_6); //PWM3
          TM_GPIO_SetPinLow(GPIOB,GPIO_Pin_8); //PWM4
          TM_GPIO_SetPinHigh(GPIOB,GPIO_Pin_3); //PWM1
          TM_GPIO_SetPinLow(GPIOB,GPIO_Pin_5); //PWM2
          break;

case 2:
TM_DAC_SetValue(TM_DAC1, 0);  //DAC1
```

```
TM_DAC_SetValue(TM_DAC2, 0);    //DAC2
TM_GPIO_SetPinLow(GPIOB,GPIO_Pin_6); //PWM3
TM_GPIO_SetPinLow(GPIOB,GPIO_Pin_8); //PWM4
TM_GPIO_SetPinLow(GPIOB,GPIO_Pin_3); //PWM1
TM_GPIO_SetPinHigh(GPIOB,GPIO_Pin_5); //PWM2
break;

case 3:
calcul =  2048+vitesse_X; //VB=2048 (1.5V)
TM_DAC_SetValue(TM_DAC1, calcul);
TM_DAC_SetValue(TM_DAC2, 2048);    //DAC2
TM_GPIO_SetPinHigh(GPIOB,GPIO_Pin_6); //PWM3
TM_GPIO_SetPinHigh(GPIOB,GPIO_Pin_8); //PWM4
TM_GPIO_SetPinLow(GPIOB,GPIO_Pin_3); //PWM1
TM_GPIO_SetPinLow(GPIOB,GPIO_Pin_5); //PWM2
break;

case 4 :
TM_DAC_SetValue(TM_DAC1,calcul);
TM_DAC_SetValue(TM_DAC2, 2048);    //DAC2
TM_GPIO_SetPinHigh(GPIOB,GPIO_Pin_6); //PWM3
TM_GPIO_SetPinHigh(GPIOB,GPIO_Pin_8); //PWM4
TM_GPIO_SetPinLow(GPIOB,GPIO_Pin_3); //PWM1
TM_GPIO_SetPinLow(GPIOB,GPIO_Pin_5); //PWM2
 break;

case 5 :
TM_DAC_SetValue(TM_DAC1, 0); //read y
TM_DAC_SetValue(TM_DAC2, 0);    //DAC2
TM_GPIO_SetPinLow(GPIOB,GPIO_Pin_6); //PWM3
TM_GPIO_SetPinLow(GPIOB,GPIO_Pin_8); //PWM4
TM_GPIO_SetPinLow(GPIOB,GPIO_Pin_3); //PWM1
TM_GPIO_SetPinLow(GPIOB,GPIO_Pin_5); //PWM2
break;

case 6 :
TM_DAC_SetValue(TM_DAC1, 0); //read y
TM_DAC_SetValue(TM_DAC2, 0);    //DAC2
TM_GPIO_SetPinLow(GPIOB,GPIO_Pin_6); //PWM3
TM_GPIO_SetPinLow(GPIOB,GPIO_Pin_8); //PWM4
TM_GPIO_SetPinLow(GPIOB,GPIO_Pin_3); //PWM1
TM_GPIO_SetPinLow(GPIOB,GPIO_Pin_5); //PWM2
break;
```

```
case 7 :
TM_DAC_SetValue(TM_DAC1, calcul);
TM_DAC_SetValue(TM_DAC2, 2048);    //DAC2
TM_GPIO_SetPinHigh(GPIOB,GPIO_Pin_6); //PWM3
TM_GPIO_SetPinHigh(GPIOB,GPIO_Pin_8); //PWM4
TM_GPIO_SetPinLow(GPIOB,GPIO_Pin_3); //PWM1
TM_GPIO_SetPinLow(GPIOB,GPIO_Pin_5); //PWM2
break;

case 8 :
TM_DAC_SetValue(TM_DAC1, calcul);
TM_DAC_SetValue(TM_DAC2, 2048);    //DAC2
TM_GPIO_SetPinHigh(GPIOB,GPIO_Pin_6); //PWM3
TM_GPIO_SetPinHigh(GPIOB,GPIO_Pin_8); //PWM4
TM_GPIO_SetPinLow(GPIOB,GPIO_Pin_3); //PWM1
TM_GPIO_SetPinLow(GPIOB,GPIO_Pin_5); //PWM2
break;

case 9 :
TM_DAC_SetValue(TM_DAC1, 0); //read z
TM_DAC_SetValue(TM_DAC2, 0);    //DAC2
TM_GPIO_SetPinLow(GPIOB,GPIO_Pin_6); //PWM3
TM_GPIO_SetPinLow(GPIOB,GPIO_Pin_8); //PWM4
TM_GPIO_SetPinLow(GPIOB,GPIO_Pin_3); //PWM1
TM_GPIO_SetPinLow(GPIOB,GPIO_Pin_5); //PWM2
break;

case 10 :
TM_DAC_SetValue(TM_DAC1, 0); //read z
TM_DAC_SetValue(TM_DAC2, 0);    //DAC2
TM_GPIO_SetPinLow(GPIOB,GPIO_Pin_6); //PWM3
TM_GPIO_SetPinLow(GPIOB,GPIO_Pin_8); //PWM4
TM_GPIO_SetPinLow(GPIOB,GPIO_Pin_3); //PWM1
TM_GPIO_SetPinLow(GPIOB,GPIO_Pin_5); //PWM2
break;

case 11:
TM_DAC_SetValue(TM_DAC1, calcul);
TM_DAC_SetValue(TM_DAC2, 2048);    //DAC2
TM_GPIO_SetPinHigh(GPIOB,GPIO_Pin_6); //PWM3
TM_GPIO_SetPinHigh(GPIOB,GPIO_Pin_8); //PWM4
TM_GPIO_SetPinLow(GPIOB,GPIO_Pin_3); //PWM1
```

```
        TM_GPIO_SetPinLow(GPIOB,GPIO_Pin_5); //PWM2
        break;

        case 12 :
        TM_DAC_SetValue(TM_DAC1, calcul);
        TM_DAC_SetValue(TM_DAC2, 2048);    //DAC2
        TM_GPIO_SetPinHigh(GPIOB,GPIO_Pin_6); //PWM3
        TM_GPIO_SetPinHigh(GPIOB,GPIO_Pin_8); //PWM4
        TM_GPIO_SetPinLow(GPIOB,GPIO_Pin_3); //PWM1
        TM_GPIO_SetPinLow(GPIOB,GPIO_Pin_5); //PWM2
        break;

        default:
        TM_GPIO_SetPinLow(GPIOB,GPIO_Pin_6); //PWM3
        TM_GPIO_SetPinLow(GPIOB,GPIO_Pin_8); //PWM4
        TM_GPIO_SetPinLow(GPIOB,GPIO_Pin_3); //PWM1
        TM_GPIO_SetPinLow(GPIOB,GPIO_Pin_5); //PWM2
                                }
                        }
    TIM_ClearITPendingBit(TIM2, TIM_IT_Update);
   }
  }
}

#ifdef  USE_FULL_ASSERT
/**
  * @brief  Reports the name of the source file and the source line number
  *         where the assert_param error has occurred.
  * @param  file: pointer to the source file name
  * @param  line: assert_param error line source number
  * @retval None
  */
void assert_failed(uint8_t* file, uint32_t line)
{
  /* Infinite loop */
  while (1)
  {
  }
}
#end
```

# Appendices III

To experimentally validate the novel simultaneous electrostatic damping approach, a printed circuit board (PCB) has been developed. The integrated circuit presented in Chapter 4 was converted into an equivalent discrete components implementation using available IC's on the market. Additional work implied the design of a suitable vacuum chamber circuit since no underdamped MEMS accelerometer was fabricated.

Generally, the same loop-structure as described in Chapter 4, is employed and includes: the transducer, a read-out input stage and a signal processing unit and control block; note that gain stages or summing amplifiers have also been added. The signal processing is embedded in the STM32F407 discovery board ( $168\,MHz$ STM32F407VGT6 microcontroller – 32-bit ARM Cortex) [STM32F4]. The two-layer printed circuit is placed in a vacuum chamber under a pressure of $100Torr$ to make the accelerometer underdamped.

This chapter presents the printed circuit design as well as the microcontroller configuration and the overall system simulations and experimental results.

## III.1 Introduction

A block diagram of the designed circuit is shown in Figure 5.1. The transducer is placed on the PCB and the proof mass displacement is measured using a discrete charge to voltage amplifier [IVC102]. Its output is then amplified to increase the signal level sent to the microcontroller. This additional stage is required because the discrete circuit has a much larger feedback capacitor ( $1pF$ compared to only $300fF$ for the integrated circuit) but also larger parasitic capacitors and thus, less C2V output signal gain.

The analog gain stages can also help to adjust the common mode level as we are no longer limited by the CMOS technology supplies. The microcontroller has a 3V power supply and can thus output a maximum voltage of $3V$. In these conditions, the excitation signals applied on the MEMS electrodes can be increased to $\pm 3V$ ($V_m = 0V$). This results in a differential C2V output voltage with a common mode output voltage of $V_m = 0V$ which must be shifted up to 1.5V because the microcontroller ADC can convert only positive voltages.

The microcontroller ADC converts the C2V output at the end of the measuring phases and calculates the difference between two successive samples. The microcontroller DAC, together with other pulse-width-modulated (PWM) microcontroller outputs are then summed using two amplifiers to deliver the final excitation signals to be applied on the MEMS fixed electrode plates.

If an x-axis acceleration is willing to be measured, the y- and z-axis fixed electrodes are biased at the same DC voltage $V_m$. If the acceleration direction changes, the fixed electrodes excitation signals can be easily interchanged.

Each discrete circuit block and functionality will be further detailed in the following sections.

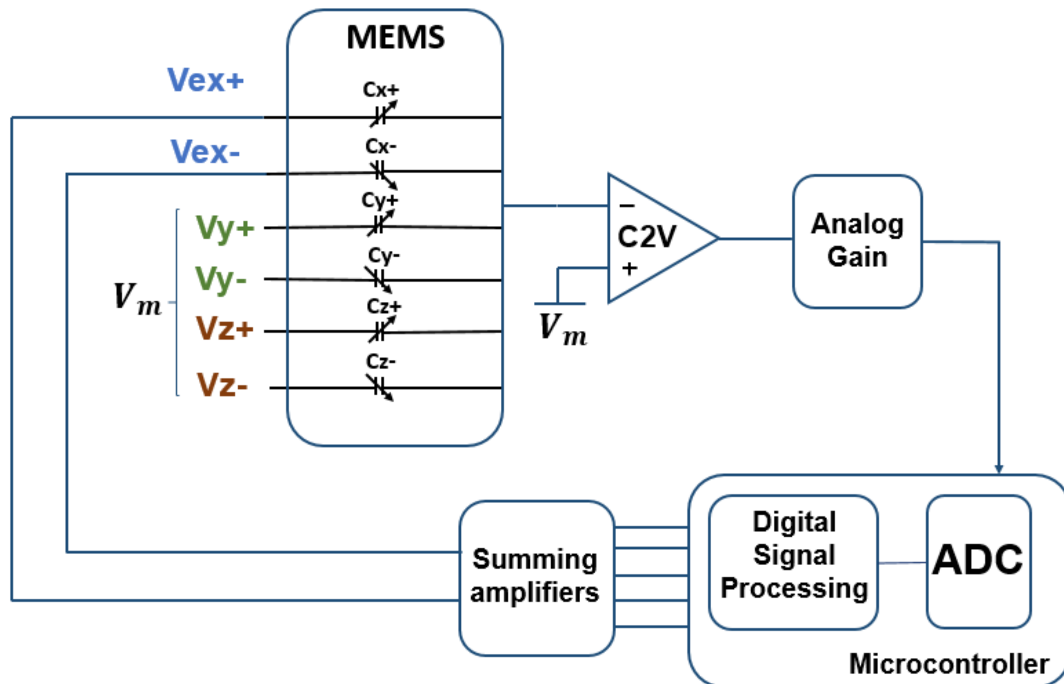


Figure 5.1 Block diagram of the discrete circuit (printed board and microcontroller)

## III.2 Discrete charge to voltage converter

When an acceleration occurs and the fixed electrodes are correctly biased, a charge to voltage amplifier can be used to measure the sensor charge variation. Based on the sampling frequency and sensitivity requirements, the Texas Instruments IVC102 switched capacitor transimpedance amplifier (Figure 5.2) was identified as a suitable candidate for this application.

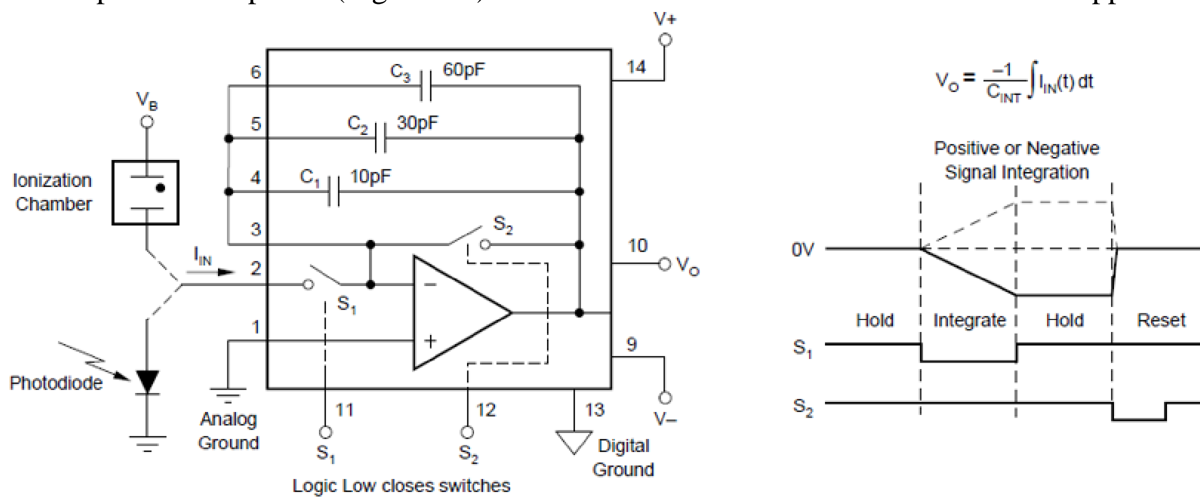


Figure 5.2 Switched capacitor transimpedance amplifier (Texas Instruments, IVC102) [IVC102]

The amplifier is a 14-pin device operating under a $\pm15V$ power supply. The non-inverting input is internally connected to the analog ground while the inverting input connectivity can be externally configured.

There are three feedback capacitors: $C_1 = 10pF$, $C_2 = 30pF$ and $C_3 = 60pF$ that can be connected either separately or in parallel, resulting in a $(10 + 30 + 60)pF = 100pF$ feedback capacitor. The capacitors can be reseted via internal switches and controlled using the $S_1$ and $S_2$ pins, thus the amplifier has two mainly configurations: reset and integration.

Since the capacitance variation to be measured is in the order of several $fF$, even the lower feedback capacitor value of $10pF$ appears to be too large nevertheless.

Equation (5.1) reminds the C2V basic functioning:

$$V_O = \frac{-\Delta C}{C_{fb}} V_{ex} \tag{5.1}$$

where $V_O$ is the C2V amplifier output voltage, $\Delta C$ the capacitance variation to be measured, $C_{fb}$ the amplifier feedback capacitor and $V_{ex}$ the excitation voltage applied across the capacitor to be measured.

As it can be noticed in (5.1), to increase $V_O$, two options are possible: decreasing $C_{fb}$ or increasing $V_{ex}$. The maximum voltage applied on the sensor fixed plates is limited by the microcontroller capabilities and thus fixed to $3V$. The minimum integrated feedback capacitor is $C_1 = 10pF$; when $C_2$ and $C_3$ are not used, internal capacitor pins should be connected to the analog ground. An external capacitor $C_{ext} = 1pF$ can be connected between pins 3 and 4, in series with $C_1$. The resulting equivalent feedback capacitor can be calculated as follows:

$$C_{eq} = \frac{C_1 C_{ext}}{C_1 + C_{ext}} \sim 1pF \tag{5.2}$$

In these conditions, if the sensor capacitance variation is $\Delta C = 2.25\, fF/g$ and $V_{ex} = V_{ex_p} - V_{ex_n} = 3V - (-3V) = 6V$, the C2V peak to peak expected output voltage sensitivity is $13.5\, mV/g$.

Furthermore, the two switches $S_1$ and $S_2$, in Figure 5.2, can perturb the measurement due to their charge injections. Figure 5.3. presents the charge injection dependency on the input capacitance, for both switches.

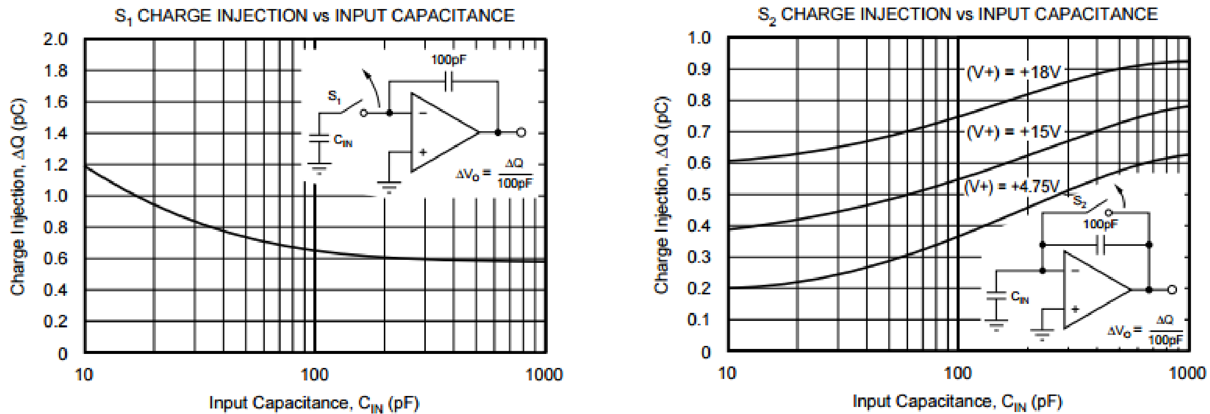

Figure 5.3. $S_1$ charge injection vs. input capacitance (left) and $S_2$ charge injection vs. input capacitance (right) [IVC102]

Considering $S_1$, for an input capacitance of $C_{in} = 10pF$, the output voltage offset generated by the $S_1$ charge injections is:

$$\Delta V_O(S_1) = \frac{\Delta Q}{10pF} = 0.12V \quad (5.3)$$

which is far from being negligible compared to the C2V sensitivity.

Moreover, if $C_{in}$ is smaller (as in our case), $\Delta V_O$ is even larger. Similarly, for $S_2$, if the amplifier is powered to $\pm 15V$, the C2V output voltage offset is:

$$\Delta V_O(S_2) = \frac{\Delta Q}{10pF} = 0.04V \quad (5.4)$$

Comparing (5.3) and (5.4) with the C2V sensitivity ($0.135\, V/g$) it is clear that the charge injection effect is too important and can't be neglected.

The C2V operating phases have been described in Chapter 4, section 4.3. It is reminded that the C2V is common to the three-axis and the feedback capacitor must be reset after each measuring phase to not perturb the other axes measurements. If it is decided not to operate both $S_1$ and $S_2$ and to keep them closed (in order to avoid the charges injection effect), a method to reset the feedback capacitor should be conceived.

Device specifications guarantee a $2MHz$ gain-bandwidth [IVC102] and the system sampling period is $T_s = 24\mu s (f_s = 41{,}7kHz)$. However, the C2V feedback capacitor should be reset every $8\mu s$ (the time between two reading phases – Figure 4.29). If the amplifier has a time constant $\tau_A$ much larger than $8\mu s$ then the feedback capacitor is cleared and a new acceleration can be measured without operating the internal switches $S_1$ and $S_2$.

To increase $\tau_A$, a large resistance value $R_{fb}$ can be placed in parallel with the feedback capacitor as in Figure 5.4.

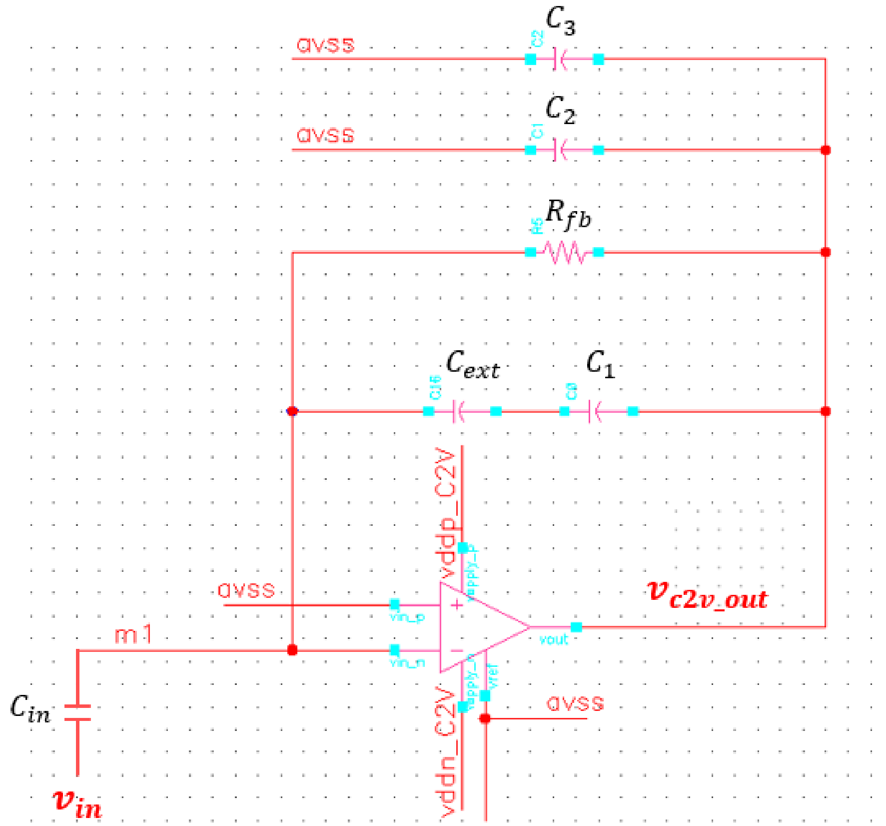


Figure 5.4. IVC102 configuration

In Figure 5.4, the amplifier inverting input is connected to the sensor proof mass and $C_{in}$ is the capacitance to be measured. The C2V transfer function can be written as:

$$H_{C2V}(s) = -\frac{-sR_{fb}C_{in}A_0}{(1+A_0)+s(A_0R_{fb}C_{eq}+R_{fb}C_{in}+R_{fb}C_{eq}+\tau_{A_0})+s^2(R_{fb}C_{in}\tau_{A_0}+R_{fb}C_{eq}\tau_{A_0})} \quad (5.5)$$

where $C_{eq}$ is defined in (5.2) and $s$ the Laplace variable. The amplifier typical transfer function is $H_0(s) = \frac{-A_0}{1+\tau_{A_0}s}$ where $A_0$ is its open loop gain and $\tau_{A_0}$ the characteristic time constant related to the opamp open loop bandwidth.

From (5.5) one can notice that the resulting transfer function is a combination between an integrator and a differentiator; its frequency response is plotted in Figure 5.5.

If $R_{fb} = 20M\Omega$, the two filter cut-off frequencies can be calculated as:

$$f_1 = \frac{1}{2\pi R_{fb}C_{eq}} = 8.8kHz$$
$$f_2 = \frac{1}{2\pi R_{fb}C_{in}} \quad (5.6)$$

$f_2$ is limited by the design specifications to 2 $MHz$. However, the measurement phases last no longer than $2\mu s$ each one and thus the measurement frequency is 125 $kHz$ which is placed in the amplifier functioning bandwidth $[8.8kHz; 2MHz]$.

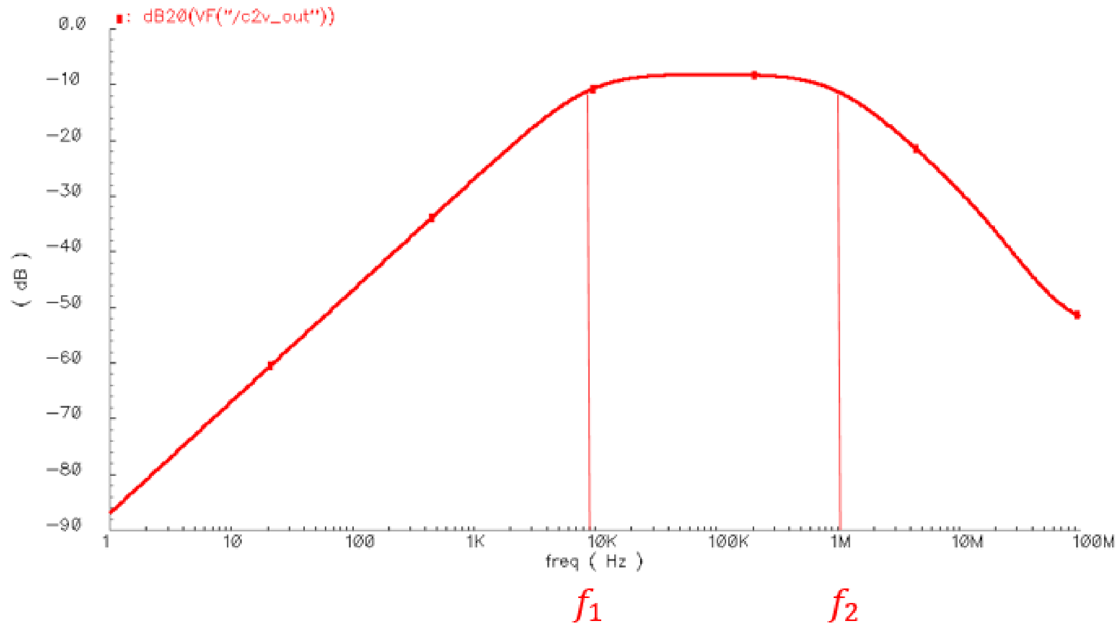


Figure 5.5. IVC102 frequency response with $R_{fb} = 20M\Omega$ connected between the amplifier inverting input and its output

The configuration developed for the IVC102 device meets the specifications and its charge to voltage converter operation was validated; the device will be next used as the analog front-end first stage in the discrete implementation.

## III.3 Analog gain stage

The IVC102 ideally outputs $13.5mV$ in steady state; however, parasitic capacitances on the PCB can perturb its output. For this reason, an additional analog gain stage is added. The analog gain stage output, which has a $0V$ common mode, is directly connected to the microcontroller ADC. Therefore, a common mode shift should be applied to allow an only-positive voltages ADC conversion.

The STM32F407 microcontroller has an analog supply of $3V$; hence, a convenient common mode of $1.5V$ has been chosen for the analog gain stage. The topology proposed for the analog gain stage is shown in Figure 5.6. where $Vcm_{gain} = 1.5V$, $R_1 = 1k\Omega$ and $R_a$ is a potentiometer.

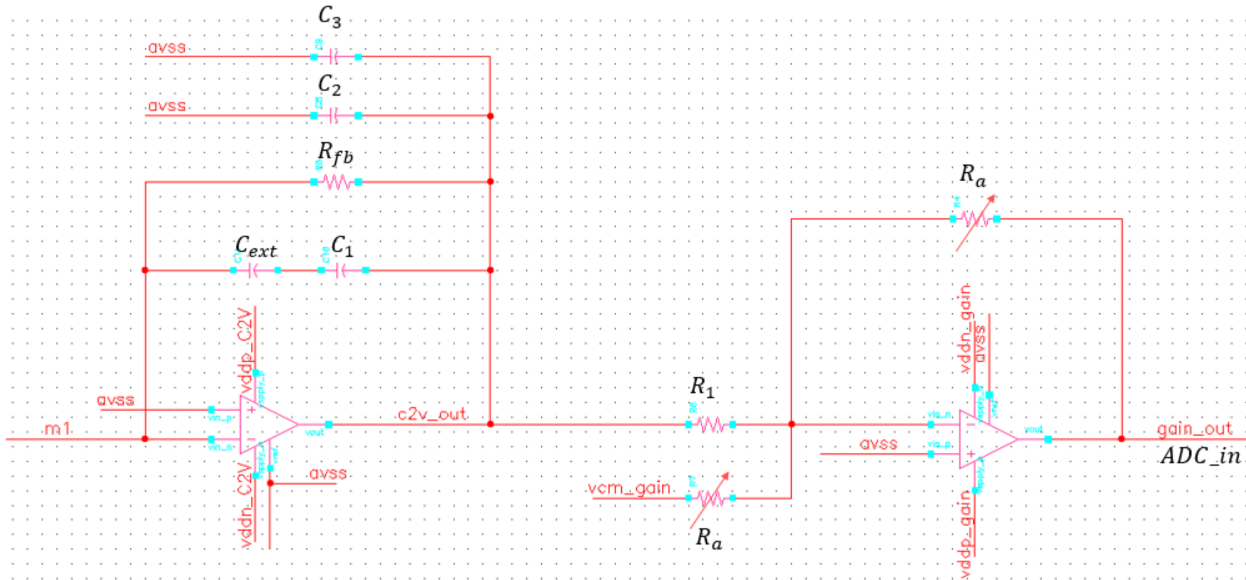

Figure 5.6. IVC102 and analog gain stage configuration

This stage transfer function can be written as:

$$V_{gain_{out}}(s) = \frac{-R_a}{R_1} v_{c2v_{out}}(s) + Vcm_{gain} \tag{5.7}$$

The gain is given by the ratio between $R_a$ and $R_1$ and since the stage has a continuous-time operation the main parameters to be considered when choosing the analog gain device are the highest slew-rate and gain-bandwidth product. The LM6154 Texas Instruments amplifier ($5\ V/\mu s$, $75MHz$) [LM6154] was selected for this application.

## III.4 STM32F4 Discovery Board configuration

The damping excitation signals sequence was generated using the STM32F4 discovery board; the board programming was implemented within the Keil uVision 5 software tool [Keil] and the C-language.

Figure 5.7 presents the entire excitation sequence during a sampling period, comprising six phases. $V_{ex+}$ and $V_{ex}-$. are the signals applied on the MEMS fixed plates and should be generated by the [STM32F4]. The main limitations of the board are: a power supply of $3V$ and two Digital to Voltage converters $(DAC)$ - two. Complementary to the two DACs, three board pulse-width-modulated (PWM) outputs can be programmed. The PWM have a digital behavior, can be set either low or high while the DACs can output any positive value.

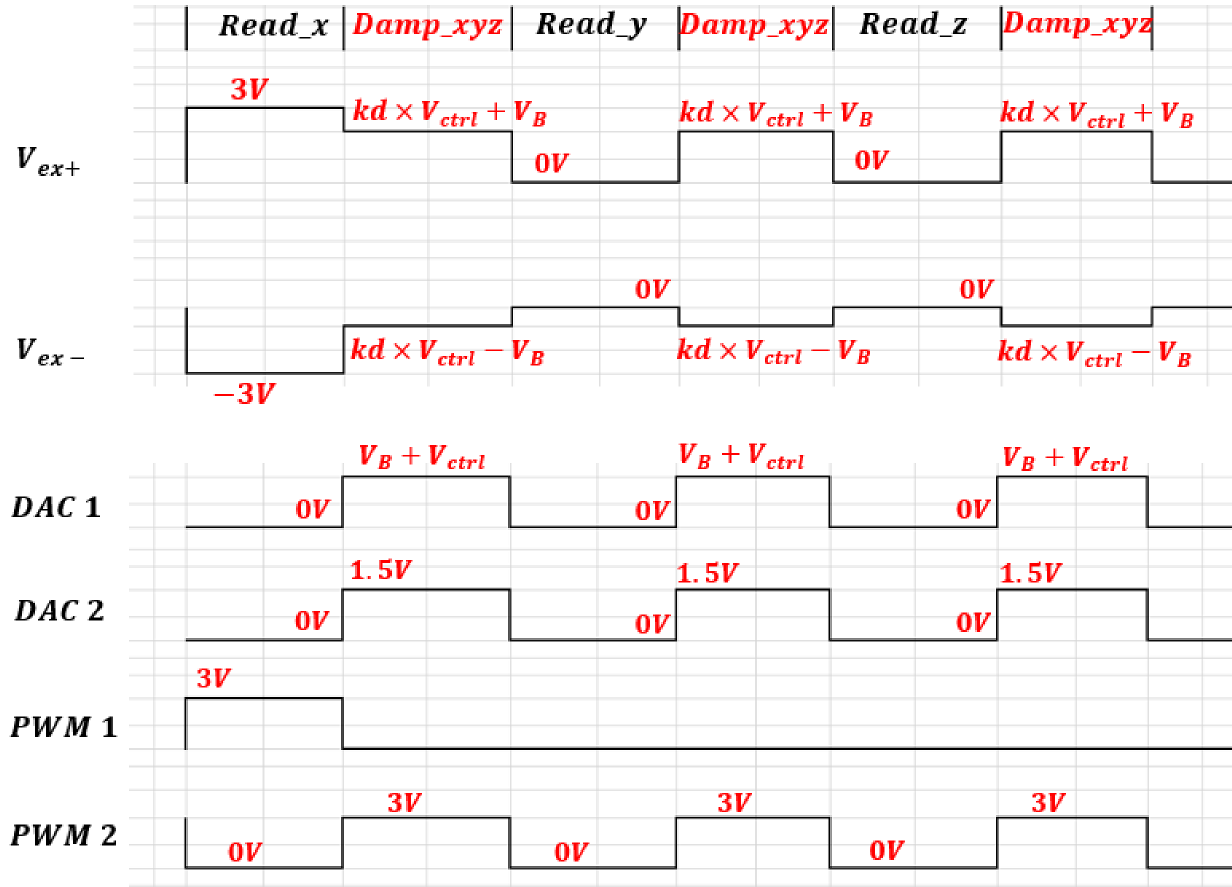


Figure 5.7. Excitation signals chronograms

The ADC converts the analog gain stage output into a digital value. This value is then used to calculate the velocity as the differences between two successive ADC conversions and then shifted by $V_B = 1.5V$.The obtained result is provided through the $DAC1$ functionality. In addition, the second converter $DAC2$ generates $V_B$ during the damping phases as illustrated in Figure 5.7.

The C-code developed for the excitation signals ($DAC1$, $DAC2$, $PWM1$, $PWM2$, $PWM3$) generation is attached in Appendices II. However, these waveforms must be processed to obtain $V_{ex+}$ and $V_{ex}-$. The following section proposes a signal processing configuration in order to apply the $V_{ex+}$ and $V_{ex}-$ on the MEMS fixed plates.

## III.5 Summing amplifiers

To obtain $V_{ex+}$ and $V_{ex}-$. from $DAC1$, $DAC2$, $PWM1$, $PWM2$ and $PWM3$ microcontroller outputs, several operations should be performed. The first one is related to the derivative gain $k_d$; the velocity estimation $V_{ctrl}$ delivered by $DAC1$ can be multiplied with $k_d$ using the configuration presented in Figure 5.8 where $k_d$ is the ratio between the two amplifiers resistances and $R = 1k\Omega$. The output, $S_1$, can be expressed during the damping phase as:

$$S_1 = V_B - k_d \times V_{ctrl} \tag{5.8}$$

Similarly, to generate the negative measuring excitation $(-3V)$, the configuration in Figure 5.8 can be used. Both amplifiers can be implemented using the [LM6154] devices.

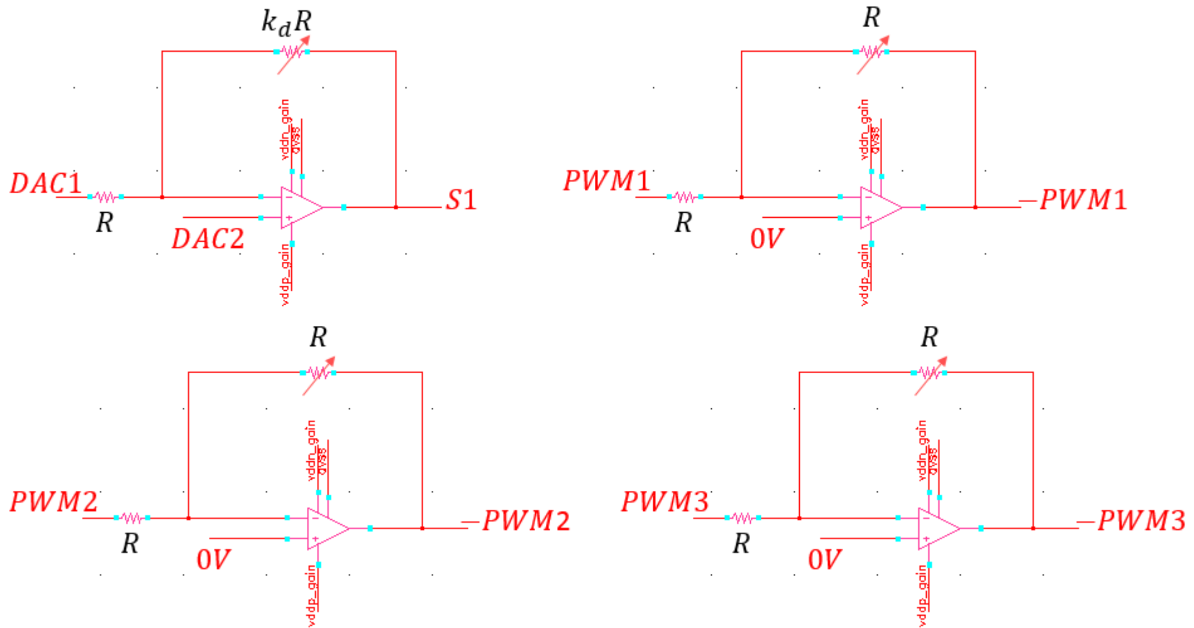


Figure 5.8. $S_1$, $-PWM1$, $-PWM2$ and $-PWM3$ signals generation

Further, using two summing amplifiers, $V_{ex}+$ (Figure 5.9 (a)) and $V_{ex}-$ (Figure 5.9 (b)) can be generated. The summing amplifiers are also [LM6154] devices.

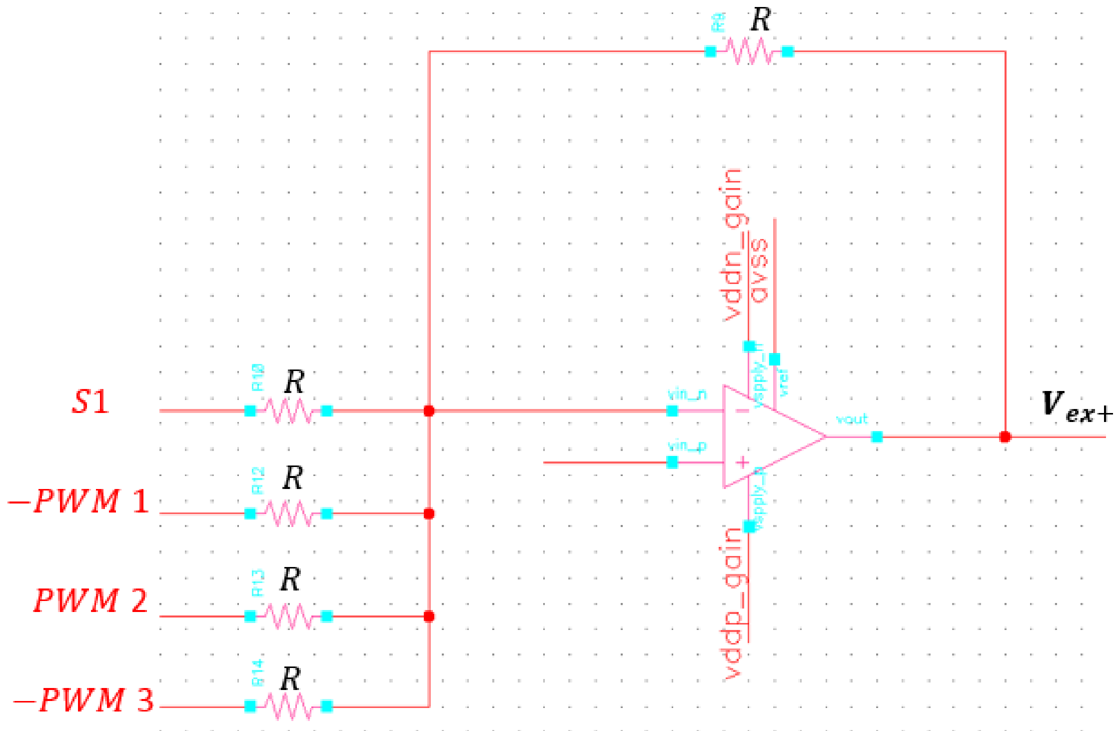


Figure 5.9 (a) $V_{ex+}$ Excitation signal generation

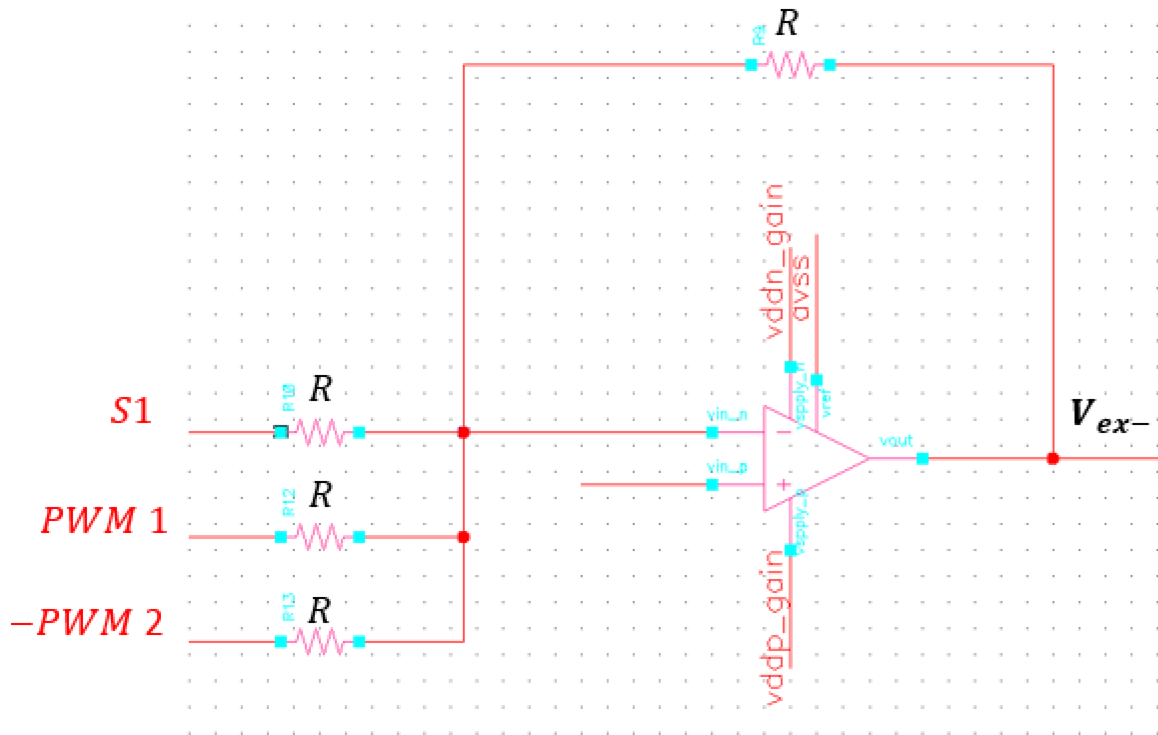


Figure 5.9 (b) $V_{ex-}$ Excitation signal generation

## III.6 Experimental set-up and results

### III.6.1 C2V validation

To validate the C2V functioning, the amplifier is firstly tested using an external capacitor $C_{in} = 1pF$ . We are expecting, a closed-loop gain of $\frac{C_{in}}{C_{eq}} \sim 1$. The amplifier input and output voltages are plotted in Figure 5.10. One can notice that the ratio between the two waveforms is roughly 1 for a frequency of $68kHz$.

Using this configuration, the two amplifier cut-off frequencies can also be measured: $f_1 = 8.8kHz$ and $f_2 = 127kHz$ (Figure 5.11). The $f_2$ value, which is smaller than the expected datasheet specification, can be explained by the parasitical capacitances and the different test configuration.

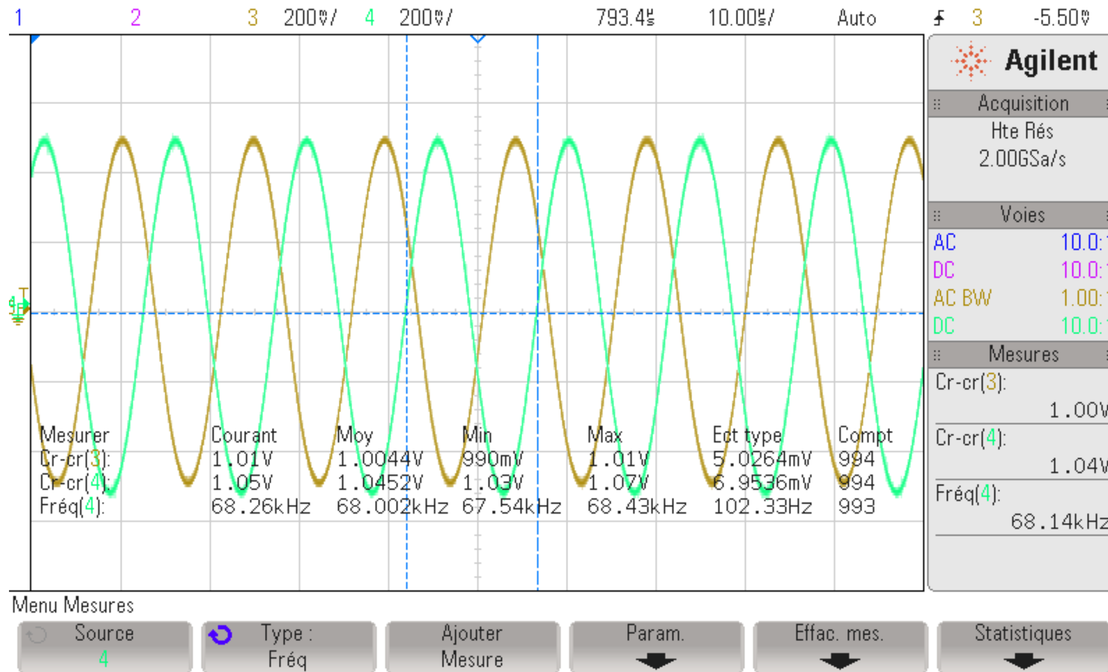

Figure 5.10 C2V gain measurement when $C_{in} = 1pF$

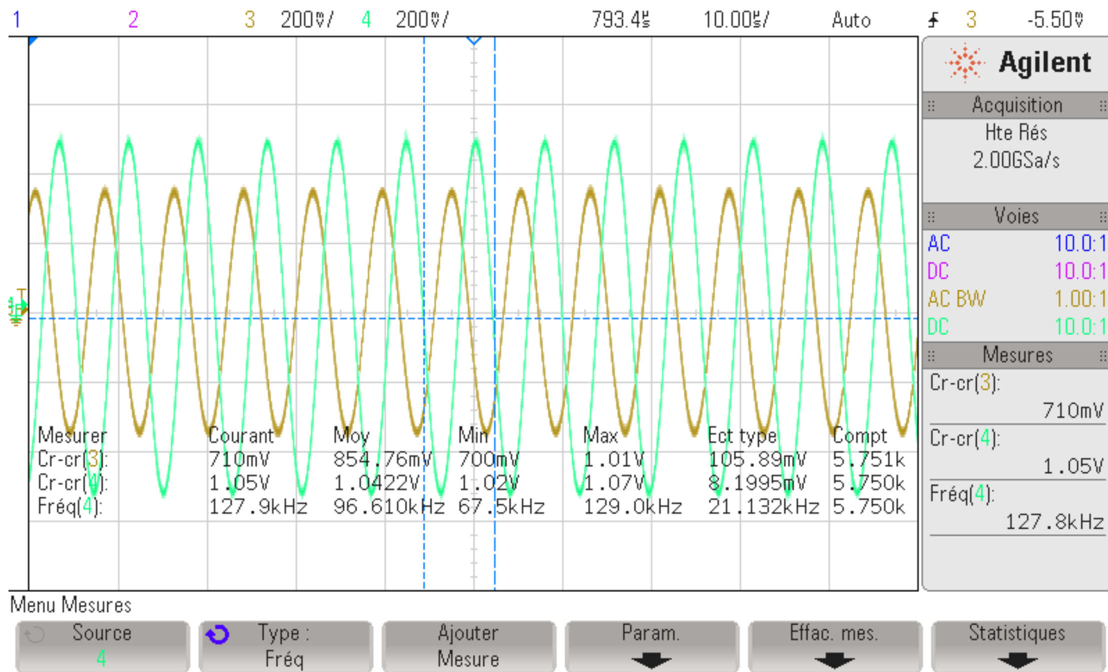

Figure 5.11 C2V high cut-off frequency measurement

## III.6.2 Signals generation using the STM32F4 discovery board

To test the microcontroller signals generation, the code presented in Appendices II is used. Figure 5.12 shows the digital outputs $PWM1, PWM2$ and $PWM3$ while Figure 5.13 illustrates the

excitation signal to be applied on MEMS negative electrodes. The generation of each phase is in concordance with the chronograms presented in Figure 5.7.

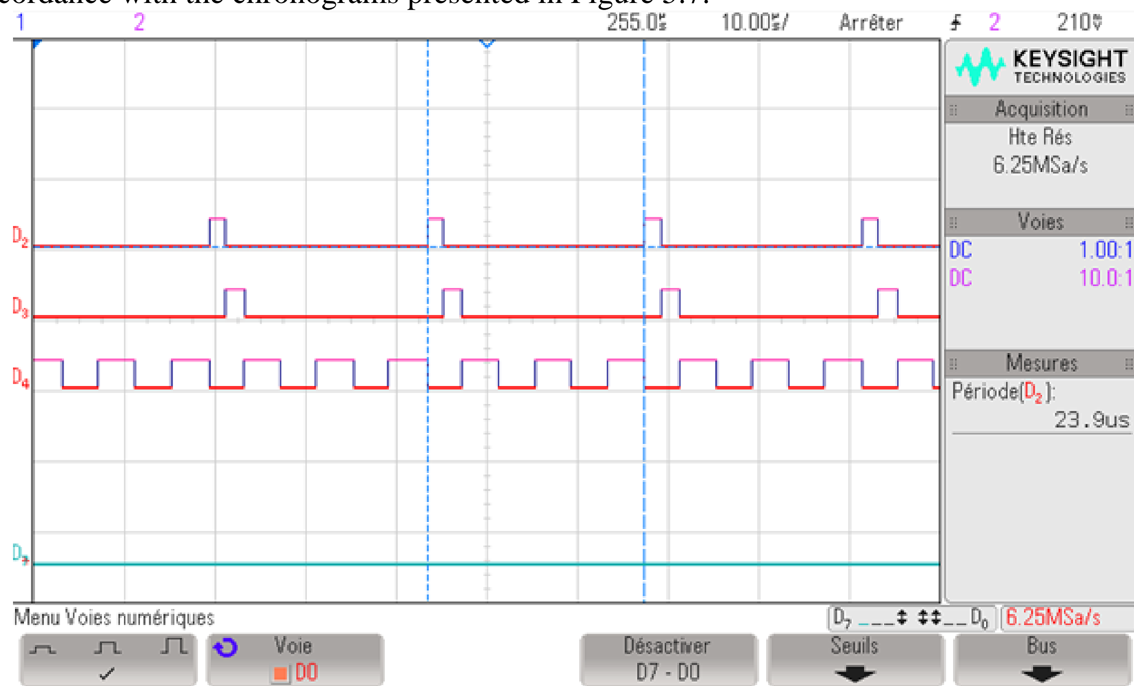


Figure 5.12 $PWM1, PWM2$ and $PWM3$ signals generation

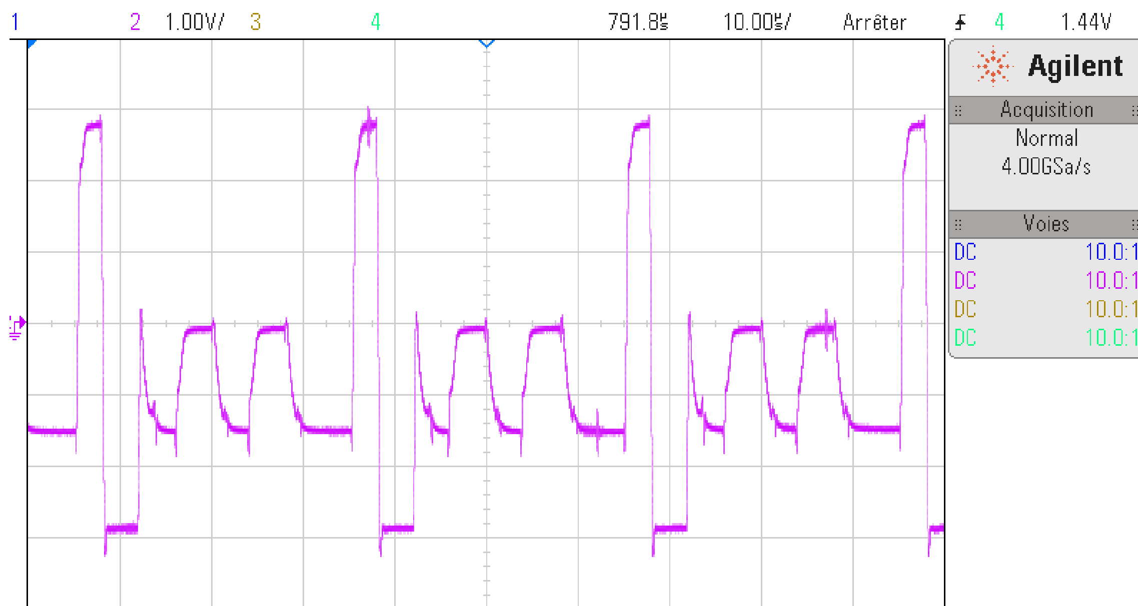


Figure 5.13 $V_{ex-}$ excitation signal to be applied on MEMS negative electrode

## III.7 Summary

This chapter introduced a discrete implementation approach of the architecture designed and validated theoretically in Chapters 3 and for 4. The discrete components implementation is intended for experimental validation only.

A two-layers PCB has been developed to host the transducer, the C2V and other analog processing while the digital signal processing is performed using the STM32F407 discovery board; the system was block by block validated.

.

# List of publications

1. Ciotirca Lavinia Elena, Thierry Cassagnes, Jérôme Enjalbert, Bernal Olivier, Hélène Tap « A MICROELECTROMECHANICAL DEVICE AND A METHOD OF DAMPING A MASS THEREOF » Freescale Semiconductor US Patent SA25488EC-WO, Filled March 1, 2016.
2. Ciotirca Lavinia, Olivier Bernal, Jérôme Enjalbert, Thierry Cassagnes, Hélène Tap. « 3-axis high Q MEMS accelerometer with simultaneous damping control » NEWCAS June 26-29 2016, Vancouver, BC, Canada.
3. Chong Li, Ciotirca Lavinia Elena, Robert N. Dean, George T. Flowers « A MEMS PPA Based Active Vibration Isolator » 12th International Conference and Exhibition on Device Packaging, March 15-17, 2016 Austin, AZ, USA.